UC-25
LBL-18411
c.1

Lawrence Berkeley Laboratory
UNIVERSITY OF CALIFORNIA

Materials & Molecular Research Division

RECEIVED
LAWRENCE
BERKELEY LABORATORY
JAN 7 1985
LIBRARY AND
DOCUMENTS SECTION

DENSIFICATION AND DEFORMATION IN THE PRESENCE OF A LIQUID PHASE

J.E. Marion II
(Ph.D. Thesis)

July 1984

For Reference
Not to be taken from this room

LBL-18411
c.1

Prepared for the U.S. Department of Energy under Contract DE-AC03-76SF00098

DISCLAIMER

This document was prepared as an account of work sponsored by the United States Government. While this document is believed to contain correct information, neither the United States Government nor any agency thereof, nor the Regents of the University of California, nor any of their employees, makes any warranty, express or implied, or assumes any legal responsibility for the accuracy, completeness, or usefulness of any information, apparatus, product, or process disclosed, or represents that its use would not infringe privately owned rights. Reference herein to any specific commercial product, process, or service by its trade name, trademark, manufacturer, or otherwise, does not necessarily constitute or imply its endorsement, recommendation, or favoring by the United States Government or any agency thereof, or the Regents of the University of California. The views and opinions of authors expressed herein do not necessarily state or reflect those of the United States Government or any agency thereof or the Regents of the University of California.

LBL-18411

DENSIFICATION AND DEFORMATION IN THE PRESENCE OF A LIQUID PHASE

John Edward Marion II

Ph.D. Thesis

Lawrence Berkeley Laboratory
University of California
Berkeley, California 94720

July 1984

This work was supported by the Director, Office of Energy Research, Office of Basic Energy Sciences, Materials Sciences Division of the U.S. Department of Energy under Contract No. DE-AC03-76SF00098.

DENSIFICATION AND DEFORMATION IN THE PRESENCE OF A LIQUID PHASE

John Edward Marion II

Materials and Molecular Research Division
Lawrence Berkeley Laboratory
University of California
Berkeley, CA 94720

Abstract

The mechanisms for creep and sintering of solid materials in the presence of a liquid phase are explored. In Part 1, the sintering behavior of a simple ceramic/glass system is studied. Densification involves concurrent viscous flow and solution/reprecipitation processes for which physical expressions are proposed. A comparison of these equations with microstructural observations suggests that thin equilibrium grain boundary films, which continuously separate the solid grains, are capable of supporting gradients in normal stresses, as required for diffusive matter transport through the liquid. Experimental evidence is presented for the existance of significant structure within the thin grain boundary films giving it unique physical properties which are neither entirely like an amorphous solid, nor are they completely crystalline. The final stage in the liquid-phase sintering process, the closure of pores, is modeled using an extreme value distribution to describe the sizes of the shrinking pores. These expressions are compared to microstructural and kinetic measurements from several liquid-phase sintered systems.

In Part 2, the investigation focuses on high temperature deformation in the presence of a liquid phase. At low stress levels, continuous deformation, without failure, is possible by matter transport through the liquid phase. At higher local stress levels, cavities form within the liquid, and permit more rapid deformation leading to eventual failure. Results of a transmission electron microscopy characterization of creep damage in several liquid-phase sintered ceramic alloys exposed to creep strains at elevated temperatures are used to propose a sequence for the early stages of cavitation damage. Interface failure time models are generated for each step in the sequence. Specifically, physical expressions are derived for the growth and coalescence times for oblate holes in thin glass films along two grain interfaces. Additionally, the times for formation of spherical holes along three grain channel glass pockets and their subsequent growth to full-facet sized cavities, by viscous flow and solution/reprecipitation mechanisms, are evaluated.

TABLE OF CONTENTS

ABSTRACT iii

TABLE OF CONTENTS. v

1. GENERAL INTRODUCTION 1

1.1 Research Outline. 1

1.2 Background. 2

1.3 Terminology 7

PART I. SINTERING IN THE PRESENCE OF A LIQUID PHASE. 10

1. INTRODUCTION 10

1.1 Transmission Electron Microscopy. 12

1.2 Sintering Experiments 13

2. DENSIFICATION BY CONCURRENT VISCOUS FLOW AND SOLUTION/REPRECIPITATION 16

2.1 Introduction. 16

2.2 Viscous Flow. 16

2.3 Solution/Reprecipitation. 18

2.4 Comparison of Rate Equations. 19

3. THE STRUCTURE OF THE INTERGRANULAR PHASE 21

3.1 Introduction. 21

3.2 Experimental Procedure. 21

3.3 Results of the Diffraction Experiments. 24

3.4 Discussion. 25

4. PORE CLOSURE 30

4.1 Introduction. 30

4.2 Sintering 31

4.3 Experimental Results. 36

4.4 Pore Closure Statistical Model. 37

4.5 Discussion. 43

5. CONCLUSIONS. 46

REFERENCES 50

FIGURE CAPTIONS. 55

FIGURES. 61

APPENDICES, PART I 103

App. I. The Capillary Force 103

App. II. Densification by Solution/Reprecipitation 105

App. III. Thermodynamic Stability of the Intergranular Phase Under a Stress. 109

App. IV. Liquid Phase Sintering: Related Phenomena. 110

A. Sintering of Jagged Particles: The Origin of Low Angle Boundaries 110

B. Density Relations During Particle Rearrangement. 114

C. Initial Stage Sintering Rate Equations 115

App. V. Wetting and Penetration 117

A. Penetration. 117

B. Two-Sphere Sintering: Penetration Behavior. . . 117

C. Wetting of Alumina: An Estimate of the Surface Energy Anisotropy. 119

App. VI. Characterization of Microstructures 121

A. Liquid Phase Sintered Alumina. 121

B. Pure Alumina 122

References 125

Figure Captions. 127

Figures. 131

PART II. DEFORMATION IN THE PRESENCE OF A LIQUID PHASE. 151

1. INTRODUCTION 151

2. EXPERIMENTAL PROCEDURE 152

3. DAMAGE OBSERVATIONS. 154

4. MODELS FOR DEFORMATION IN THE PRESENCE OF A LIQUID PHASE . . . 157

4.1 Introduction. 157

4.2 Steady State Creep by Solution/Reprecipitation. 158

4.3 Hole Nucleation 158

4.4 Cavity Evolution. 165

5. DISCUSSION AND IMPLICATIONS. 180

REFERENCES 184

FIGURE CAPTIONS. 187

FIGURES. 190

APPENDICES, PART II. 206

App. I. The Origin of the Strengthening Effect of Silicon Nitride by Oxidation 206

App. II. Creep Rate Due to Solution/Reprecipitation. 214

App. III. Related Observations. 216

App. IV. The Final Stage of Hole Depletion 218

References 220

Figure Captions. 221

Figures. 222

ACKNOWLEDGMENT 228

1. GENERAL INTRODUCTION

1.1 Research Outline

Understanding the effects of a minority liquid phase on the deformation and densification behavior of solids is critical for the development of modern materials for high performance applications. Current descriptions of sintering and creep in the presence of a liquid phase are inadequate to form predictive models. Here, a theoretical foundation is proposed by developing models for deformation based on cavitation observations and by deriving physical expressions for the sintering mechanisms; these models are correlated with experimental data.

The first part of the thesis describes three related aspects of the liquid-phase sintering problem. All three are connected by the common objective of gaining insight into the continuous chemical potential gradient that must exist within the liquid phase in order for sintering to occur. Prior research has merely stated that potential differences exist between various locations in the sintering body (due to differences in stress or chemical composition) but no attempt has been made to understand how the potential gradient is established or maintained. The present approach to this issue firstly considers a dynamic situation for establishing the chemical potential gradient, based on the continuous flow of liquid out of the layer between grains. This study concludes that an adequate potential gradient cannot be established in this manner. Instead, it is proposed that the second phase develops a partially ordered structure that in turn allows a

sufficient stress gradient to be maintained statically, similar to the situation for grain boundaries in a single phase system. This notion is assessed by a TEM investigation of the structural state of the second phase layer between the grains. The results indicate that the thin two grain boundaries are indeed partially ordered, inferring that mass flow analyses for sintering based on grain boundary diffusion models can be applied (as modified for an increased diffusion thickness). These insights finally permit densification models to be developed for liquid phase sintering systems. The models can then be compared with results from sintering experiments. In this instance, a simple two phase system—alumina/anorthite-glass—is studied and correlations between theory and experiment are established.

The second part of the thesis examines the initiation and accumulation of creep damage in liquid-phase-sintered systems. Damage formation, manifest as holes in the second phase, is known to proceed creep rupture. Furthermore, the growth and coalescence of the damage induces the final failure. Hence, the initial step in comprehending high temperature failure in liquid-phase sintered materials, entails the characterization and understanding of damage formation. The present study uses TEM for the characterization of the initial creep damage. Then, based on these observations, physical models for the initiation and growth of cavities are developed. Subsequent studies will examine the coalescence of the cavities into rupture cracks.

1.2 Background

Sintering describes the process by which discrete ceramic or metal particles in a compact coalesce to form a dense body at high

temperatures. If pressure is also used, the process is hot-pressing. Four primary diffusion mechanisms are available for matter transport in the solid state at the sintering temperature; diffusion of atoms along the solid surface, evaporation (and condensation) of atoms between the solid and the vapor, diffusion of atoms through the crystal lattice, and diffusional transport along grain boundaries. For densification, material must be removed from the neck area between the particles, permitting the particle centers to approach. Only the latter two mechanisms, lattice and grain boundary diffusion permit removal of material from the neck, giving center approach and hence densification. Evaporation/condensation and surface diffusion give neck growth and lead to particle coarsening without densification.

For systems in which a liquid phase is present at the sintering temperature, a fifth matter transport path, solution/reprecipitation (S/R) is available wherein matter is dissolved in, and transported by the liquid phase. For penetrating liquids (i.e., the presence of the liquid phase along grain boundaries is energetically favored over solid/solid contacts) this diffusional path is similar to grain boundary diffusion in that it permits matter transport of solid atoms out from between adjoining particles, and leads to densification. Several examples illustrate these principles.

In silicon nitride, a modern engineering ceramic, matter transport in compacts of small sized particles is dominated by surface diffusion.[1] When these particles coarsen, evaporation/condensation is the fastest transport mechanism. A liquid phase appears to be required for

sintering in order to elevate the rate of matter transport along grain boundaries (by S/R) above that of the non-densifying mechanisms. Aluminum oxide, another important technological ceramic, is frequently fabricated by pressureless sintering at low temperatures in the presence of a liquid phase. Furthermore, in many alloys, impurities that form a penetrating liquid are already present in the partially refined material, hence it is often economical for a variety of reasons to sinter in the presence of a liquid phase.

Unfortunately, the same matter transport mechanisms obtain during creep deformation at elevated temperatures. A number of high technology ceramic materials have recently emerged that are prepared with small amounts of additives that (in combination with elements from the solid phase) become viscous liquids at the processing temperature and enhance densification. Many of these liquid-phase sintered materials are being developed for high temperature applications, yet the additives are often sufficient to form impurity grain boundary phases[2] which appear to be necessary for reasonable sintering kinetics, but significantly increase the deformation rate in creep situations.[3] This study is focussed on understanding the role of a minority liquid phase on the densification and deformation properties of a solid compact.

Several fields of science have encountered related problems. The earliest descriptions of solid deformation by matter transport through the liquid phase come from geology.[4] In this field researchers described the deformation of rock in the presence of thin capillaries

of water at some distance below the surface of the earth. These "pressure-solution" models, in part, form the basis for current theories on crustal deformation and intercontinental drift.[5,6] On the other end of the particle size scale, colloid chemists have long been interested in describing the interaction of small particles separated by a liquid. In 1886, Reynolds[7] derived the equation for the approach of two disks separated by a liquid, but this type of expression is unsuitable for the analysis of very small particles. The treatment by Derjaguin and Landau[8] of the van der Waals attraction at close particle separation and the formulation of the electrostatic repulsion due to electrical double layer overlap by Verwey and Overbeek[9] has been combined to form the DLVO theory which describes particle interactions in electrolytes, but has some shortcomings, particularly when extended to very small separation distances.[10]

The term <u>liquid phase sintering</u> was introduced by Hoyt in 1930[11] during his address to the AIME annual meeting to describe the processing technique that was being developed for sintering tungsten carbide in the presence of liquid cobalt, producing the now common cemented carbides. The early compacts contained a large volume fraction of liquid (.25 to .35); the quoted mechanism of sintering was simply melting and penetration of the liquid between the solid grains.

Several years later, success in sintering to full density with much less liquid[12] obviated the existence of at least one other densification mechanism, and the hypothesis was advanced that solid particles were being dissolved and transported in the liquid phase.

Interest in liquid-phase sintering intensified, and it was soon discovered that many other common systems were being processed in the presence of a liquid (e.g., the alumina based sanitary and dinner ware are sintered with a silicate liquid phase). A host of phenomenological models for the sintering behavior were advanced[13] but a reasonable theoretical treatment of the problem of liquid phase sintering awaited the publication of Kingery's classic paper "Densification During Sintering in the Presence of a Liquid Phase" in 1959.[14]

Kingery proposed three steps for liquid phase sintering: the close-packing and redistribution of the solid as the liquid begins to melt (rearrangement); transport of solid matter through the liquid phase (solution/reprecipitation); and the formation of solid necks between the grains (coalescence). Further, three requirements for liquid-phase sintering, originally proposed by Jones in 1938,[15] were explicitly expressed as: appreciable amounts of liquid are required; the solid must be partially soluble in the liquid; and the liquid must completely penetrate between the solid grains. The latter requirement has been the subject of considerable debate and will be explored extensively in the discussion here.

Investigators modelling sintering or creep in the presence of a liquid phase are presented with a paradox: for moderate and small amounts of liquid, the primary mechanism for densification in sintering (and for deformation during creep) is by solution/reprecipitation. The process requires a stress gradient to be maintained in the liquid, yet liquids are normally incapable of supporting the required stress

gradient. Previous investigators have either chosen not to address this difficulty,[14] or have remedied the problem by incorporating into their models a solid/solid contact between the grains.[16-19] One objective of the present study is to provide further information regarding this paradox.

1.3 Terminology

The term wetting is commonly applied to the thermodynamical equilibrium of the interfacial energies of a liquid on a solid in the presence of a vapor (Fig. 1A). The well known Youngs-Laplace equation describes the horizontal components of the interfacial tensions at the liquid drop edge as:

$$\gamma_{sv} = \gamma_{\ell s} + \gamma_{sv} \cos\theta \tag{1}$$

where subscripts s, ℓ and v stand for solid, liquid and vapor, respectively, and θ will be called the contact angle here. The vertical components can be satisfactorily ignored for most situations involving elastic solids. The systems for which $\theta > 90^\circ$ are often described as non-wetting, and for cases where $\theta < 90^\circ$ as wetting. $\theta = 0$ is commonly referred to as the condition for spreading.

The situation at the solid/liquid boundary (Fig. 1B) is now considered where equilibrium is characterized by

$$\gamma_{ss} = 2\gamma_{s\ell} \cos\psi/2 \tag{2}$$

for finite dihedral angle, ψ. The term wetting is commonly used also to describe the situation where

$$\gamma_{ss} \geq 2\gamma_{s\ell} \tag{3}$$

(i.e., $\psi = 0$) in which penetration of the liquid along the grain boundaries is energetically favorable. A comparison of Eqs. (1) and (2) reveals that, although there is a common term, $\gamma_{s\ell}$, there is no fundamental inter-relation between these two "wetting" expressions. Situations commonly exist where the dihedral angle is zero, and the liquid penetrates the grain boundaries yet the contact angle is finite. With the present terminology, it is not clear whether this situation should be described as wetting or as non-wetting. Standard sessile drop "wetting" experiments thus have no direct application to the study of the grain boundary penetration phenomenon. Here it is preferred to adopt the term wetting to describe the solid/liquid/vapor interfacial energy relation, and the term penetrating to describe the situation illustrated by Eq. (3) in which the liquid is energetically favored to exist between the solid grains.

The term liquid-phase sintering has been used to describe a variety of system in which a liquid is present during at least part of the sintering process and in some way enhances the densification rate. In systems where the room temperature phases are all solids, a liquid may still be present at the processing temperature and will then participate in the sintering process in a beneficial way. Subsequently it may somehow become incorporated into the solid matrix. This process, called transient liquid-phase sintering, is not as common as one might expect because substantial kinetic barriers exist to the required

reactions of the liquid which is constrained in the narrow channels separating the solid grains. Consequently a remnant of the liquid phase often persists after sintering.

For systems where the liquid is in equilibrium with the solid, small and moderate amounts of liquid will give rise to a capillary pressure which acts to pull the particles together, if the contact angle, θ, is less than 90°. Systems in which $\theta > 0°$ are said to have a partially wetting liquid, because there is some contribution to the interparticle force due to the pendular ring of liquid (Appendix I). It is emphasized, however, that since the liquid is energetically prohibited from penetrating the interface between the solid particles, it is incapable of providing a diffusion path which leads to particle center approach. In these systems, the beneficial role of the liquid is limited mainly to the initial stages during particle rearrangement. Liquid phase sintering should be reserved for cases where the dihedral angle is zero; the liquid completely penetrates between the solid contacts and extends along the two grain channels.

PART I

SINTERING IN THE PRESENCE OF A LIQUID PHASE

1. INTRODUCTION

The objective of this section of the thesis is to define how the chemical potential gradient required for sintering can be established and maintained and to propose appropriate sintering models. The study begins by considering a kinetic situation wherein an appropriate gradient arises by the continuous flow of the second phase from between the grains. The structure of the thin second phase film is then examined as a basis for establishing an alternate static mechanism for sustaining the required gradient. Based on these results, densification models for liquid phase sintering are proposed and compared with experimental sintering data.

Sophistication in high resolution and analytical electron microscopy has permitted direct observation and identification of grain boundary phases in sintered ceramics[2,20,21] and cermets.[22] These observations suggest that impurities or additives form thin liquid films along the grain boundaries at the processing temperature which significantly enhance sintering rates. The relatively recent experimental verification that many important high technology ceramics contain an integranular phase[2,23-26] has stimulated interest in understanding the effect of a small amount of liquid on the densification and deformation processes. The research presented here is concerned with this issue.

This liquid film is considered to act as a rapid diffusion path for atoms of the solid species, and thereby allow enhanced densification. However, the specific chemical potential gradients that govern the mass transport through the liquid have not been comprehensively addressed. Fundamental understanding of this process is thus deficient and requires further study. The intent of the present section is to address this deficiency.

It is widely accepted that the curvature of the liquid meniscus (Appendix I) induces a tensile pressure in the liquid. It is then presumed that this process provides a chemical potential gradient in the liquid which causes atoms of the solid phase to diffuse toward the meniscus. Such atom transport, accompanied by solution and precipitation processes occurring in series, results in the continuous flux of atoms needed to enhance sintering rates. An important omission, however, in most prior studies concerns the precise nature of the chemical potential gradient in the liquid that governs the atom flux. A chemical potential gradient implies the existence of gradients in normal stress and/or in the concentration of the solid species dissolved in the liquid. The nature of these gradients is now examined.

The existence of stress gradients in the liquid has frequently been discounted, because viscous flow of the liquid would normally be expected to equilibrate the pressure. However, viscous flow in very thin films is restricted and some gradients in stress may be expected to persist for considerable duration. The role of viscous flow in the establishment of the chemical potential gradient is examined in a subsequent section. The concern regarding the ability of the liquid

to sustain an adequate chemical potential gradient has resulted in the suggestion that small solid/solid contacts invariably exist[16-19] and that these either support the stress or provide a site of high local chemical potential (which yields a chemical potential difference between the contact and the liquid meniscus). An important facet of the present study entails the experimental assessment of the presence of solid contacts in partially sintered, liquid-phase containing materials. These studies complement several prior investigations of fully sintered bodies, which provide direct evidence that no solid contacts exist between grains, other than low angle grain boundaries.

The experimental studies are followed by detailed consideration of the chemical potentials in the liquid and of viscous flow properties. The possible existence of structure in the liquid phase constrained along narrow capillaries is examined. Models for pore closure, considered to be the final stage in the sintering process are derived and compared to sintering data. Finally, some implications and suggestions for further research are presented.

1.1 Transmission Electron Microscopy

To date nearly all reported images of high angle boundaries in fully dense liquid-phase sintered ceramics exhibit a continuous grain boundary film. Reported images which appear to have a solid/solid contact have either been for special low energy boundaries, or have been imaging artifacts produced because the rigid conditions for proper high resolution imaging of grain boundaries were not adhered to. The possibility remains, however, that solid/solid contacts could

persist between the grains throughout the sintering process until local regions reach full density at which time the capillary pressure between the solid grains becomes zero; the grain boundary phase could then erode the solid neck. This would result in the observation of a continuous grain boundary film in the fully dense materials, while a dry contact had actually persisted throughout the sintering process. This scenario is believed to be unlikely, due to energetic reasons, but the possibility that solid/solid contacts exist during sintering is explored here by examining grain boundaries in samples taken from compacts which had just begun to sinter and then were water quenched to preserve microstructural features.

It should be noted that, traditionally, the presence or absence of a grain boundary film has been addressed by optical, or scanning electron microscopy—both of those techniques lack the spatial resolution to resolve very thin intergranular films. The high resolution afforded by TEM is therefore required.

1.2 Sintering Experiments

The alumina/anorthite system was chosen for liquid phase sintering densification rate experiments, and to provide the required samples for microscopy. The powder preparation, sintering methods and microscopy techniques are discussed in detail in a latter section, but are briefly described here.

A high purity alumina powder was mixed with anorthite glass frit which had been prepared from reagent grade $CaCO_3$, 99.99% pure SiO_2 and high purity Al_2O_3. After casting, the glass was broken with a mortar

and pestle, and then milled and sifted to <10 μm. Dispersions of the frit were allowed to settle and the superanate was drawn off and dryed to provide a 0.8 μm micron mean particle size glass powder. Alumina/anorthite glass mixtures were prepared by ball milling with alumina balls, drying and sieving. After cold pressing, pellets of the mixture were quickly inserted into a vertical quench furnace heated to a temperature about 50°C above the required sintering temperature. This approach permitted very rapid sample heating so that short term sintering data could be collected. After the appropriate sintering time, pellets were quenched directly from the furnace into water to preserve microstructural features. Density was determined by the Archimedes method, modified to account for open porosity. TEM specimens were prepared in the standard manner except that the fragile, low-density samples were impregnated with epoxy and thinned from one side only in the ion-mill.

Microstructural characterization of these samples is covered in Appendix VII, but the observations pertinent to the present discussion are now given; of interest here is the assessment of grain boundary structures in samples that have just begun to sinter. Microscopy results are presented for a sample that had been sintered at 1555°C for thirty seconds and had increased in density from 60 to 63% of theoretical density. The composition was Al_2O_3/10% $CaO-Al_2O_3-2SiO_2$ by weight.

In these samples, high resolution electron microscopy reveals a continuous glassy grain boundary film with a thickness of approxi-

mately 1.2 nm (Figs. 2,3).† Sample preparation difficulties precluded making sufficient observations to completely substantiate this claim, but in two high resolution images (Fig. 2) and in the six diffuse dark field images (e.g., Fig. 3) of grain boundaries in the very early stages of sintering, solid contacts are absent and the thickness of the glassy layer is about 1.2 nm.

---

†Similar observations have been widely reported on dense materials, yet the possibility remains that a wetting liquid only enters the capillaries as the material becomes dense, and the capillary tension is relieved. Hence, observations on "barely" sintered samples are relevant.

2. DENSIFICATION BY CONCURRENT VISCOUS FLOW AND SOLUTION/ REPRECIPITATION

2.1 Introduction

After the majority of the rearrangement process has been completed* the densification is governed by the rate of approach of adjoining grains which are separated by a liquid. Grain center approach is permitted by viscous flow from between the grains and by matter transport by solution/reprecipitation which itself consists of series processes wherein the solid is dissolved into the liquid, diffuses through the liquid, and is reprecipitated onto the crystal. A kinetic model is now proposed for concurrent viscous flow and solution/ reprecipitation, appropriate for the intermediate stage of liquid-phase sintering.

2.2 Viscous Flow

The model assumes a fluid layer sandwiched between two parallel flat plates which are moving together under the influence of a force. This geometry corresponds to the common situation of two approaching particles, separated by a liquid capillary, where an area on each particle has begun to dissolve at the point of highest chemical potential permitting contact flattening (Appendix I). The analysis commences with the expression for the pressure distribution that

---

*Rearrangement continues throughout sintering, but is the primary contributor to the densification rate only in the early stages.

develops between parallel side disks containing a flowing viscous fluid given by[7]

$$\frac{d}{dr}\left[r\left(\frac{d\sigma}{dr}\right)\right] = -\frac{12\ \eta_a r}{\delta^3}\left(\frac{d\Delta}{dt}\right) \tag{4}$$

where σ is the stress developed at a radial distance, r, from the grain center (Fig. 4), η_a is the apparent viscosity of the flowing liquid, which, in thin layers, may differ appreciably from bulk viscosity, δ is the fluid thickness separating the grains, and $\frac{d\Delta}{dt}(\equiv\dot{\Delta}_f)$ is the rate of grain center approach allowed by viscous fluid flow. The boundary conditions required to solve the equation are: symmetry at the grain centers specifies that $d\sigma/dr = 0$, at $r = 0$, and chemical potential continuity at the meniscus interface dictates that $\sigma = \gamma_{lv}(\frac{1}{\rho} + \frac{1}{x})$ at $r = x$, where x is the meniscus radius, γ_{lv} is the liquid/vapor energy and ρ is the meniscus radius of curvature.

Integration gives the stress distribution between approaching grains as:

$$\sigma(r) = -\frac{3\eta\dot{\Delta}_f}{\delta^3}(r^2 - x^2) + \gamma(\frac{1}{\rho} + \frac{1}{x}) \tag{5}$$

This equation is now integrated over the area of the neck to obtain an explicit expression for the force distribution on the neck; the net force is set to zero, as required for free sintering, yielding the expression for the rate of grain center approach due to viscous flow:

$$\dot{\Delta}_f = \frac{-2\delta^3\gamma}{3\eta x^2}\left(\frac{1}{\rho} + \frac{1}{x}\right) \tag{6}$$

2.3 Solution/Reprecipitation

The rate of grain center approach due to matter transport of the solid species away from the contact area of the approaching grains is governed by a series process involving the rate at which matter can be dissolved (and subsequently reprecipitated) and by the rate at which the solid species can diffuse through the fluid. Commonly the rate of one of these two processes, either the interface reaction, or diffusion, is much slower than the other and consequently governs the total series rate. Sintering equations for the important case where diffusion is the rate limiting step are derived here. Expressions are also developed which simultaneously treat both the interface reaction and the diffusion step (Appendix III) but are unwieldy, and must be solved numerically and are, thus, unsuitable for general comparison with the viscous flow model.

The analysis for densification by diffusion-controlled solution/reprecipitation commences with the standard expression for the rate of mass transport along a grain channel, given by the differential equation

$$\frac{d^2\sigma(x)}{dx^2} = \frac{-kT\dot{\Delta}_{S/R}}{\Omega Dc\delta} \tag{7}$$

where $\dot{\Delta}_{S/R}$ is the rate of grain center approach allowed by the

solution/reprecipitation process. Symmetry requires that $d\sigma/dx = 0$ at the midpoint along the grain channel and that the stress at the liquid meniscus equal the surface tension stress given by the relation

$$\sigma = \gamma\left(\frac{1}{\rho} + \frac{1}{x}\right)$$

Integration of Eq. (7) then gives the stress distribution

$$\sigma = \frac{kT\dot{\Delta}_{S/R}}{\Omega Dc\delta}\left(x^2 - r^2\right) + \gamma\left(\frac{1}{\rho} + \frac{1}{x}\right) \tag{8}$$

The requirement that the net stress along the neck be zero for sintering gives the densification rate allowed by solution/reprecipitation as;

$$\dot{\Delta}_{S/R} = \frac{-3\Omega Dc\delta\gamma}{2kT\ x^2}\left(\frac{1}{\rho} + \frac{1}{x}\right) \tag{9}$$

2.4 Comparison of Rate Equations

Comparison of Eqs. (6) and (9) indicates that

$$\frac{\dot{\Delta}_f}{\dot{\Delta}_{S/R}} = \frac{4kT\delta^2}{9\Omega Dc\eta} \tag{10}$$

This expression can be simplied by using the Stokes-Einstein equation

$$D = \frac{kT}{6\pi\Omega^{2/3}\eta} \tag{11}$$

such that the ratio of the two parallel densification processes becomes

$$\frac{\dot{\Delta}_f}{\dot{\Delta}S/R} = \frac{8\pi\delta^2}{3c\Omega^{2/3}} \tag{12}$$

For values of these variables pertinent to the Al_2O_3/Anorthite system used for this study (δ = 1.2 nm, $\Omega = 4\times10^{-29}$ m^2, $c_\ell = 0.3$) this ratio is ~3 x 10^2. A survey of several other liquid phase sintered systems yields similarly high values for this ratio.

This comparison leads to a general conclusions from this kinetic model: **even for very narrow channels, the rate at which liquid flows out from between the grains is rapid compared to the rate of matter transport by S/R.** Consequently the liquid layer is squeezed out rather quickly to a thickness dictated by some other phenomenon, such as short range structural order. Evidence for this order and the way in which it arises is discussed in the next section.

Equilibrium calculations of the stress required to eliminate an impurity grain boundary phase are given in Appendix IV. In all cases, the stress required to form a solid/solid contact is large (~500 MPa); far in excess of stresses expected in any normal hot pressing (50 MPa) or creep situation (<100 MPa) and several orders of magnitude higher than a typical sintering stress exerted by the capillary force (~5 MPa). For a wetting liquid there are thus, compelling energetic reasons for a liquid layer to remain continuously separating the solid grains.

3. THE STRUCTURE OF THE INTERGRANULAR PHASE

3.1 Introduction

In the previous chapter, models were proposed for densification in the presence of a liquid phase. A comparison of the sintering rate predictions for viscous flow and solution/reprecipitation illustrate that the grain boundary film observed throughout the sintering process is apparently in equilibrium; the thickness of the two grain boundary seems to be quickly reduced to about 1nm and then remains at that thickness for the remainder of the sintering process. The question persists, however: how does this liquid film support the stress gradient required for matter transport by solution/reprecipitation? One possibility is that the intergranular phase undergoes a stress-induced structural change; that possibility is explored here. Anamolous properties have been been reported in thin liquid films including structural ordering[27] and phase separation[28] but these concepts have yet to be applied to explaining how the thin films separating ceramic grains in liquid-phase sintered materials are capable of supporting the required stress gradients.

3.2 Experimental Procedure

To investigate the possibility that the thin films along two grain boundaries exist at a structural state more ordered than the bulk phase, an electron microscope study was conducted in which electron diffraction data produced by the glass residing in three grain enclaves is compared to diffraction information generated by the glass along the two grain boundaries.

Diffuse dark field (DDF) micrographs were obtained by selectively imaging electrons that had been diffusely scattered into the aperture by the intergranular phase in the alumina/anorthite alloys. In this imaging mode, scattering from an amorphous material are nearly uniform with only minor fluctuations in the scattered intensities having maxima in the diffraction pattern corresponding to spacings which are an integer multiple of the mean inter-atomic separation within the sample. For somewhat more ordered materials, the electron scattering becomes more coherent and the maxima in the diffraction pattern are more apparent. In the limit, an ordered crystal diffracts coherent electrons primarily along specific Bragg angles giving rise to the well-known spot diffraction patterns.

In order to investigate the nature of the two grain boundary structure, a systematic series of DDF micrographs were obtained at increasingly higher diffraction angles from regions of the microstructure containing a three grain pocket (expected to have essentially bulk properties) and of least one two-grain boundary oriented edge-on to the electron beam (e.g., Fig. 2). Diffracted intensities measured by microdensitometer traces from the images of three grain and from two-grain boundaries were then compared as a function of diffracted angle.*

---

*The use of microdensitometer traces on diffuse dark field images to determine the grain boundary width was pioneered by Krivanek, Shaw and Thomas[20]. The suggestion that a similar technique could be used to generate radial distribution functions for the intergranular phase was suggested by L.C. De Jonghe.

Care was taken to ensure similar exposure conditions for each image. The beam was permitted to stabilize prior to beginning the experiment and for each series, the same exposure time and condenser defocus setting was used; the negatives were processed simultaneously. Data from several trial runs was rejected because it was suspected that not all of the exposure information on these negatives fell within the linear range of the emulsion.

A small condenser aperture was used so that inelastic scattering around the transmitted beam did not affect data at high d spacings. For each series of DDF micrographs, the direction traversed for the transmitted beam was chosen specifically to avoid interaction with coherent Bragg orders from adjoining crystals, because scattered intensities from these grains (if included in the DDF) gave false background readings in the microdensitometer traces. Similarly, the direction perpendicular to the grain boundary (in reciprocal space) was avoided for the traces in order to ensure that any diffraction effects due to the boundary itself would not lead to an incorrect interpretation of the data. Finally, the general problem of statistical variation in the results was addressed by obtaining, for each area examined, four series of micrographs; two sets at different angles, with each set having two series extending from opposite sides of the transmitted beam. Three areas were examined, in all, giving twelve total series of traces.

As a control, several thin foils of anorthite glass were studied. The method for preparation of anorthite is discussed in the next chapter. A number of foils were prepared from the quenched glass

casting, these were amorphous. Several of these foils were annealed at 1500°C (50°C below the melting temperature of anorthite) for various times (0.5, 2 and 24 hrs) in order to produce varying degrees of crystallization. High magnification weak beam images and electron diffraction patterns were obtained so that diffraction information generated by the DDF traces could be compared both to check the position of the diffracted intensity maxima, as well as to estimate the degree of crystallinity along three grain channels and within two grain boundaries.

3.3 Results of the Diffraction Experiments

The diffraction data are plotted in Figs. 5-7. The abscissa is the calculated d-spacing for the intensity recorded from each diffuse-dark field image by a microdensitometer. This relative intensity is plotted as the ordinate. The d-spacing is calculated by Braggs' law using the value of the diffraction angle found by measuring the displacement of the objective aperture from the optic axis for each diffuse dark field micrograph, and by knowing the energy of the electrons and the camera length. Broad maxima, as expected from amorphous glass, are observed in both the DDF traces obtained from three grain pockets as well as from diffraction patterns from the unannealed bulk anorthite glass specimen. However, the maxima from the two grain boundary spectra are considerably sharper, suggesting that these regions are not entirely amorphous. Statistical variations are unlikely to account for this result, despite scatter in the data, because the sharp peaks are consistent over the twelve sets of DDF spectrum obtained, and more

importantly the d-spacings of the maxima in the DDF traces are in the same positions as those obtained in diffraction patterns of bulk anorthite specimens. Finally, as a basis for estimating the degree of crystallinity, electron diffraction data from two grain boundaries in alumina/anorthite are compared with patterns generated by the bulk anorthite glass specimens that have been annealed (Fig. 7).

3.4 Discussion

The electron diffraction data indicates that the two grain boundary film in the alumina/anorthite material is apparently more highly ordered than the anorthite glass in the triple grain pockets. A comparison of data from two grain boundaries with data from a partially crystallized bulk anorthite glass sample suggests that the degree of crystallization in both systems is about the same; the diffraction spectra match. Several descriptive models are now hypothesized to describe the structure and properties of the film that separates the solid boundaries.

3.4.1 Model for Microcrystallites. The density of vitreous silica has been found to increase under modest pressure[29,30] and unless the compressed silica is annealed, this increase is permanent. Anomalies in the density vs. molar refraction curves occur at points corresponding to trydimite and α-crystobalite and have been interpreted as indicating the formation of micro-crystallites within the disorderd matrix.[31] This suggests that the capillary pressure in the grain boundaries of the two phase materials of interest here, which is present during sintering, may lead to a pressure induced

structural change in the glassy phase along the grain boundaries resulting in regions of micro-crystallinity. In addition, recent x-ray work by Konnert and D'Antonio[32] compares computed and observed radial distribution functions for amorphous silica. These investigators found that the experimental data correlate best with a theoretical model of a random packing of ordered 1.2 nm trydimite crystals. On the basis of these experiments and the diffraction data generated here, one can hypothesize a boundary layer having a thickness similar to that observed in which there is some specific short range order within micro-crystalline regions, yet no long range order (Fig. 8).

High magnification images of the partially annealed bulk anorthite specimen support this hypothesis; randomly oriented microcrystals are visible (Fig. 9), having a mean size of about 2 nm. If the bulk specimen reflects the situation in the two grain boundaries, then these data suggest a boundary structure in which microcrystals are packed in between the solid alumina grains. Two rigid ceramic crystals separated by a row of marble-like crystallites of the second phase are envisioned (Fig. 8).

3.4.2 Layer Model. A second theory is based on molecular dynamical calculations for freezing liquids at a solid interface.[33] Here it is suggested that the first several liquid layers are in strict registry with the solid surface with respect to the position and distance from the surface, yet appear disordered parallel to the surface. Applying this concept to the intergranular phase in the alumina/anorthite system, the grain boundary appears to be essentially amorphous when the grain boundary is viewed edge-on, but is crystalline

when viewed parallel to the grain faces (Fig. 10). Several layers of a two dimensional crystal with weak bonding between layers is thus proposed as a second model that is also consistent with the diffraction data. These hypotheses are now examined in light of published macroscopic studies on this class of materials.

Internal friction measurement on hot-pressed silicon nitride[34] which is known to contain a thin intergranular phase, indicate that the grain boundary phase located along the two grain boundaries has properties very similar to a bulk glass of the same composition in its response to shear stresses. Both models proposed here would indeed resist shear stresses in a manner similar to a bulk glass. In the first model solid grains slide across the loosely bonded crystallite "marbles"; in the second model grain boundary sliding would simply involve the shearing of essentially amorphous layers in the intergranular film, in a manner analogous to shearing of graphite along its weakly bonded planes. However, both models for the intergranular phase would resist viscous fluid flow out of the capillary in a manner similar to the behavior of a crystal, and would be capable of sustaining substantial normal stress gradients as required for solution/reprecipitation. In both models, normal stresses and viscous flow (requiring shear along planes oriented 45° to the plane of the boundary) would act on the model boundary layer in a direction in which it appears essentially crystalline.

3.4.3 Phase Separation. For several liquid-phase sintered systems, phase separation has been observed within the glassy phase at

triple points. X-ray spectroscopy on a hot-pressed silicon nitride indicates that phase separation can occur in which the glassy phase separates into regions of crystalline enstatite, surrounded by nearly pure SiO_2.[28,35] This tendency has been noted particularly in the three grain pockets and has lead to the suggestion that the three grain enclaves are acting as impurity sinks and that the two grain boundaries are becoming increasingly pure SiO_2. Since pure silica is difficult to crystallize, this tendency supports the model of two dimensional layers in preference to the model hypothesizing randomly oriented microcrystals.

However, the system investigated here is fundamentally different than magnesia fluxed silicon nitride. Anorthite is in equilibrium with alumina and hence no phase separation would be expected. Diffraction patterns generated by the crystallites in the three grain boundaries can be indexed as crystalline anorthite within amorphous anorthite. X-ray diffraction on bulk anorthite indicates that the crystallizing phase is anorthite. Furthermore, the morphology of the small crystals are neither spherulitic nor are they lath-like as is the case in the non-equilibrium $MgSiO_2$ glasses within silicon nitride.[36] For the alumina/anorthite system, no evidence for phase separation exists.

One important difference between the two models proposed for the boundary film in alumina/anorthite is their prediction of the diffusion coefficient, D_ℓ. For the marble theory, a diffusion rate would be predicted similar to diffusion along solid/solid grain boundaries

in a crystallized sample of the same composition as the intergranular phase. On the other hand, the two dimensional crystal theory would lead to the expectation of a diffusion coefficient similar to an amorphous bulk glass except that D_ℓ might well be reduced by perhaps one third due to a decrease in the possible directions for atom jumps (from six to four) because of the two dimensionality of the intergranular film.

It is stressed that the models proposed here are speculative. At the same time, they consistently explain the observed behavior in these materials and are in accordance with the principles of mechanics and surface chemistry. Whether or not the specifics of these schemes are correct, the experimental data indicate that the thin films that exist along the grain boundaries have unique properties and are neither entirely amorphous, nor are they completely crystalline.

4. PORE CLOSURE

4.1 Introduction

The final stage in the sintering of compacts in the presence of a liquid phase is the closure of remnant pores. Current theories for LPS assume the formation of solid contacts as the final stage and do not address pore closure specifically.[14,16,17] Models for solid-state sintering assume a homogeneous distribution of pores having a uniform size and are unsuitable for adaptation to liquid-phase sintering for several reasons. As pores shrink, the closure rate increases exponentially so that uniform pore size models predict a rapidly increasing sintering rate for high density bodies, yet the opposite trend is observed in sintering behavior. Furthermore, in LPS systems, experimental evidence and energetic arguments[37,38] suggest that the smallest coordination number (CN) pores (which are generally the small primary* pores) close completely, before the larger pores shrink significantly. Presumably, the diffusion rate of material along two grain boundaries limits the rate of material transport to fill these pores. Simultaneously, the chemical potential gradient generated by the radius of curvature of the large pores is much smaller than the gradient for the smaller pores. Hence the mean pore diameter actually increases during sintering until the final stages. Since powder

*The void space between the individual (primary) particles in a compact are primary pores. Secondary pores are the void space between packed agglomerates which are themselves made up of primary particles and primary pores.

compacts typically contain a broad pore size distribution, models predicting a uniform pore shrinkage rate give a poor physical simulation.

A number of experiments are described which have been performed to explore the sintering behavior of materials in the presence of a liquid phase. Models are then proposed for the pore closure stage that use an extreme value function to describe the pore size distribution. The rational for adopting this approach is to give a physically accurate model that properly predicts the observed trends in sintering behavior.

4.2 Sintering

4.2.1 Experimental method. Several studies have examined shrinkage rates for sintering in the presence of a liquid phase.[13,29,30] Of particular interest in this investigation was the assessment of microstructural evolution during sintering so that bulk density, pore size and morphology, and kinetic data could all be correlated with the sintering models derived here. Sintering studies of a well-characterized model system were thus undertaken to obtain sintering rate data, as well as to generate samples as required for microscopy.

The system chosen for the sintering studies was alumina/anorthite; alumina is partially soluble in anorthite glass (Al_2O_3 - CaO - $2SiO_2$), the glass is in equilibrium with alumina (Fig. 11)[39] and anorthite penetrates between the alumina grains above the eutectic temperature of 1552°.[40]

The anorthite was prepared from reagent grade $CaCO_3$, high purity SiO_2 and ultrahigh purity alumina. The source and impurity levels

of these materials are given in Table 1. The proper amount of each constituent was mixed for 24 hours in alcohol, dryed, calcined and fired for 20 hours at 1600°C in a platinum crucible. After firing the crucible was lowered rapidly from the furnace and quenched into a water bath. X-ray diffraction showed no trace of crystallinity; the spectrum had no peaks. Transmission electron microscopy on a thin film prepared from the glass was also performed. No crystallites were visible even at the highest magnification and the diffraction patterns consisted of a single broad ring, typical of amorphous materials. Annealing of these specimens did result in crystallization as discussed in Section 3.2.

The glass was broken with a mortar and pestle, milled in an alumina ball mill, using alumina milling media and alcohol for three days, stir dried and sieved to less than 10 μm. The particle size distribution was measured from SEM micrographs (Fig. 12). For some of the sintering studies, a finer glass frit was desired. Suspensions of the <10 μm anorthite powder were prepared by mixing alcohol, acetic acid and the powder, and adjusting the pH to two. The dispersion was allowed to settle (~14 hours) and the superanate was drawn off with a pipette and dried. This resulted in a much finer glass particle size (Fig. 13).

A number of alumina/glass mixtures were prepared by mixing the glass frit with various alumina powders. Several different powders were used in order to assess the effect of particle size and morphology on the sintering rate. The jagged alumina had a mean

Table 1. Powder Impurities

Designation	Jagged Alumina	Semispherical Alumina	Spherical Alumina	$CaCO_3$	SiO_2
Manufacturer	Engineered Materials[1]	Sumitomo[2]	UC Berkeley[3]	Allied Chemical[4]	Apache Chemical[5]
Morphology	Jagged	Potato-shaped	Spherical	Unknown	Needles
Crystal Structure	α	α	Unknown	Un	Un
Mean Particle Size	1.2	.39	20	Un	.03
Quoted Purity	99.99	>99.99	Unknown	>99.0	>99.99
Weight Percent[6] Impurities					
Si	.02	.0006	-	-	P
Al	P	P	P	-	.002
K	-	-	-	.01	-
Ca	.005	-	-	P	.001
Na	-	.0002	-	.002	.001
Fe	.03	.0006	-	.002	.001
Mg	.003	.0002	-	.02	.002
Ca	.001	.002	-	-	-
C	-	-	-	.001	.002

[1]GEM 241, Ultrahigh Purity Alumina, Engineered Materials, P.O. Box 363, Church St. Station, New York, NY 10008

[2]AKP-30-High Purity Alpha alumina five powder. Sumitoma Chemical Company, Ltd.

[3]Spherodized in a DC Plasma generator.

[4]Allied Chemicals, General Chemical Division, New York, NY 10010

[5]No. 6846 SiO_2, Apache Chemicals Inc., P.O. Box 126, Seward, IL 61077

[6]Weight percent from mass spectrometry; dash indicates no measurement performed, P indicates principle constituent.

particle size of 0.8 μm; the morphology and size distribution are described by Fig. 14. Impurity levels for the powders are given in Table 1.

Electron diffraction patterns generated from these particles were identified as α-alumina in agreement with x-ray diffraction which gave only peaks attributable to α-alumina. The semi-spherical alumina had a mean particle size of 0.3 μm (Fig. 15). Alumina spheres with a 20 μm mean size (Fig. 16) were also used in the study. Alumina/glass mixtures were prepared by a variety of methods. It was of interest to assess the sintering characteristics of compacts that had been optimally mixed with the finest glass frit and to contrast those results with compacts that had been prepared with relatively large glass frit and had been poorly mixed. The finest alumina powder (0.3 μm, semi-spherical) and the collodial glass frit (0.5 μm) were mixed with teflon media in isopropyl alcohol and nitric acid (total pH = 2) for 12 hours, and rapidly stir dried. The jagged alumina powder was mixed with coarse (10 μm) glass frit for 2 hours in alcohol and dried without agitation. Between these extremes a number of intermediate mixtures were prepared, as listed in Table 2.

As controls, glass-free powder compacts were sintered in air for each of the three alumina powders. For sintering, small pellets (0.3 cm x 0.9 cm dia.) were cold pressed to about 60% density. These pellets were thrust into a furnace (Fig. 17) which was preheated approximately 50°C above the sintering temperature to insure that the sample reached the sintering temperature quickly (<10 seconds) as

Table 2. Compact Mixtures for Sintering Studies

Designation	Alumina	Glass	Wt Ratio	Mixing	Liquid	pH	Media	Method
Poorly mixed jagged	jagged	10 μm	90/10	2 hrs	isopropyl alcohol	6.5	teflon	evaporation
Poorly mixed jagged	jagged	10 μm	95/5	2 hrs	isopropyl alcohol	6.5	teflon	evaporation
Well mixed jagged	jagged	1 μm	90/10	72 hrs	isopropyl acetic acid	4	alumina	stir dried
Pure jagged	jagged	none	100	-	-	-	-	-
Well-mixed semispherical	semi-spherical	0.5 μm	90/10	72 hrs	isopropyl nitric acid	2	alumina	stir dried
Pure semi-spherical	semi-spherical	none	100	-	-	-	-	-
Well-mixed semispherical w/10 μm pores[1]	semi-spherical	0.5 μm	86/10/4	dry	-	-	teflon	-
Spherical	spherical	1 μm	90/10	4 hrs	isopropyl acetic acid	4	alumina	stir dried
Pure spherical	spherical	none	100	-	-	-	-	-

[1]Prepared as mixture 5, except that after drying four weight percent 10 μm poly vinyl alcohol was added.

indicated by a thermocouple in contact with the pellet. After the appropriate sintering time, the pellet was dropped into water to preserve the microstructural features.

Density was determined by the modified Archimedes method. Briefly, the standard water displacement technique was used, except that open porosity is accounted for with a measurement of the amount of water which had penetrated the sample. This was accomplished by drying and weighing the well-soaked sample in air and comparing that to the dry weight in air.

4.2.2 Sample preparation for SEM. Reasonably dense ($\rho_f > 0.8$) alumina samples were prepared for examination in the scanning electron microscope (SEM) by slicing the sample with a diamond saw, and then mounting the cross section in bakelite and mechanically polishing on successively finer grits to a 1 μm polish. The sample was coated with a thin layer of gold to prevent charging in the electron beam.

Samples that had inadequate structural integrity to withstand the stresses of preparation ($\rho_f < 0.8$), including the as-pressed powders, were vacuum impregnated with epoxy prior to cutting and mounting.

4.3 Experimental Results

A variety of alumina powders were sintered with various amounts of a liquid phase as shown in Table 2. The sintering rate diagrams (density vs time plots) are shown in Figs. 18-23. Generally, the trends for these curves follow expectations: jagged particles sinter less quickly than semispherical particles even in the presence of a liquid phase; compacts with a higher volume fraction of glass sinter more quickly than samples with less glass; small particles sinter more

quickly than large particles. One interesting generalization is that compacts in which the glass frit is significantly larger than the alumina particles sinter more slowly than alumina with no glass phase presumably because when the glass melts and enters the capillaries between the solid particles, and a void is created where the glass has melted (Fig. 24). When the glass frit is coarse these voids are quite large, and take a significant amount of time to close. Even though well packed pure alumina does not have the rapid transport path provided by the continuous grain boundary films, this is apparently more than compensated for because the pores are very much smaller and have an associated higher chemical potential. To investigate this hypothesis one further experiment was performed. Four weight percent of a 10 μm polymer powder (poly-vinyl-alcohol) was added to the dried semi-spherical alumina and 10% collodial glass mixture to provide 10 μm holes in a microstructure with a well-mixed, homogeneously distributed glass phase. Initial densification of this compact was slow but the sintering rate curve eventually intersected and joined the poorly mixed compact in which 10 μm glass frit had been used (Fig. 22).

In order to compare the measured sintering rate with the theoretical models, selected samples from the sintering studies were sectioned and examined in the SEM. Representative micrographs are presented in Figs. 25-30; the pore size and separation were measured from these micrographs.

4.4 Pore Closure Statistical Model

For powders that are well mixed and carefully processed, the shrinkage rate behavior is expected to be dominated by the rate of

closure of primary pores which are located at multiple grain junctions. A typical pore closure model is developed in which a continuous intergranular phase along two grain boundaries is assumed to connect cylindrical pores encapsulated in liquid at three grain junctions (Fig. 31). The analysis given here is the first theory applied to sintering, in which a distribution function is used to describe the change in pore size with time. Previous theories assumed all pores were of the same size, were shrinking at an equal rate, and disappeared simultaneously. The distribution function was used here to give physically correct theoretical models which predict heterogeneous pore closure, in agreement with observations. The pore volume can be filled either by viscous flow of the liquid phase into the void space, or by diffusion of atoms from the solid through the liquid phase to multiple grain corners. The latter case is appropriate when relatively small amounts of a liquid phase are present and substantial redistribution of atoms from the crystalline grains (by solution/reprecipitation) is required to achieve full density. In cases where a large volume fraction of liquid is available, however, simple penetration of the liquid into the solid skeleton can fill most or all of the void space.

For poorly-mixed powders, the post-rearrangement sintering rate is dominated by the closure of large isolated pores. These secondary and tertiary large CN pores result from the relatively voluminous void space between packed agglomerates or can be developed when a solidified particle of the liquid phase melts and enters the capillaries between the crystalline particles, leaving a void space behind. The sintering behavior of this type of microstructure is addressed by

modelling the densification rate of a compact that is locally dense, but has fairly large, well-separated pores (Fig. 32). As before, these pores can be filled either by excess liquid phase, or by diffusion of atoms from the crystalline grains into the pore space.

The analysis for each of these models is similar. Hence, the complete derivation is given for the typical pore closure model appropriate to the case where the pores fill by diffusion of solid atoms through the liquid phase.

The analysis for typical pore closure commences with the derivation of the local pore size shrinkage rate; the rate of change in the density of the compact is then derived explicitly. The stress distribution along a boundary containing a liquid phase which can transport matter by liquid phase diffusion is:

$$\frac{d^2\sigma}{dr^2} = \frac{-\dot{y}\,kT}{c_\ell \delta_\ell D_\ell \Omega} \tag{13}$$

where σ is the stress as a function of distance r along the boundary, $\dot{y}$ is the grain center approach rate, c_ℓ is the solubility of the solid in the liquid, δ_ℓ is the boundary layer thickness, D_ℓ is the diffusivity of the solid through the liquid and Ω is the atomic volume. Symmetry requires that $d\sigma/dr = 0$ at $r = 0$ and chemical potential continuity dictates that the stress of the pore surface ($r = \ell - a$) be γ/a. Here, a is the pore radius and γ is the liquid/vapor interfacial energy. Integration of Eq. (13) subject to these boundary conditions gives the stress between two cylindrical pores as:

$$\sigma(r) = -\frac{\dot{y}\,kT}{2c_\ell\delta_\ell D_\ell\Omega}\left(r^2 - (\ell-a)^2\right) + \gamma/a \tag{14}$$

The average stress on the boundary is zero for sintering and hence,

$$\frac{\dot{y}\,kT}{c_\ell D_\ell\delta_\ell\Omega} = \frac{6\gamma}{a(\ell-a)^2} \tag{15}$$

For a unit thickness, volume conservation dictates that $\ell\dot{y} = 2\pi a\dot{a}$. The pore shrinkage rate is then

$$\dot{a} \approx \frac{3c_\ell D_\ell\delta_\ell\gamma\Omega}{\pi kT\,a^2\ell} \tag{16}$$

The assumption that $\ell >> a$ restricts application of the model to microstructures in which the distance separating the pores is large compared to the pore radius. Integration gives

$$a = (a_o^3 - \alpha_d t)^{1/3} \tag{17}$$

where a_o is the initial pore size and

$$\alpha_d = \frac{3c_\ell D_\ell\delta_\ell\gamma\Omega}{\pi kT\ell}$$

An extreme value distribution is now assumed for the initial pore size:

$$G(a_o) = 1 - \exp(-(a_o/a^*)^{k^*}) \tag{18a}$$

or,

$$g(a_o)da_o = \frac{k^*(a_o)^{k^*-1}}{a^{*k^*}} \exp\left[-\left(\frac{a_o}{a^*}\right)^{k^*}\right] da_o \tag{18b}$$

where k* and a* are the shape and scale parameters, which may be determined from microstructural measurements.

Substituting a_o from Eq. (17) with Eq. (18b) the pore size distribution at time, t, becomes;

$$g(a)\ da = e^{-u}\ du \tag{19}$$

where

$$u \approx \left(\frac{a^3 + \alpha_d t}{a^{*k^*}}\right)^{k^*/3}$$

The average pore size <a> at time t can thus be obtained as;

$$\langle a\rangle = a^* \int_{u_o}^{\infty} e^{-u}(u-u_o)^{1/k^*}\ du \tag{20a}$$

$$= a^*\ e^{-u_o}\ \Gamma(1 + 1/k^*) \tag{20b}$$

where

$$u_o \equiv \left(\alpha_t t/a_*^3\right)^{k^*/3}$$

and Γ is the gamma function. Furthermore a_* can be related to the initial average pore size, $\langle a_o\rangle$, using

$$\langle a_o \rangle = \frac{k_*}{a_*^{k_*}} \int_0^\infty a_o^{k^*} \exp\left[- (a_o/a_*)^{k_*} \right] da_o \tag{21}$$

which, upon integration becomes

$$\langle a_o \rangle = a_* \ (1 + 1/k_*) \tag{22}$$

Hence, from Eq. (20b),

$$\langle a \rangle = \langle a_o \rangle \, e^{-u_o} \tag{23}$$

It is now required that the void size be expressed in terms of the density, ρ, viz

$$\dot{\rho} = 2\pi \langle a \rangle \langle \dot{a} \rangle / 3\sqrt{3}^{\ 2} \tag{24}$$

or,

$$\rho = \rho_o + \frac{2\pi \langle a_o \rangle^2}{6\sqrt{3}\,\ell^2} \left[1 - \exp\left(\frac{-2\alpha_d \beta t}{\langle a_o \rangle^3} \right) \right] \tag{25}$$

where $\beta = \Gamma^3 (a + 1/k_*)$ and ρ_o is the initial density (at $t = 0$).

If the pores close by viscous flow, α_d is replaced by

$$\alpha_v \equiv \frac{\gamma \delta^3}{4\pi\eta\ell}$$

where η is the viscosity of the viscous phase.

For the geometry in which the local microstructure is dense, except for large pores having radius a, separated by a distance, z, (Fig. 29), the corresponding expression for pores filling by diffusion through the liquid phase is:

$$\rho = \rho_0 + \frac{2\pi\langle a_0\rangle^2}{6\sqrt{3}z^2}\left[1 - \exp\left(\frac{-2\alpha_i \beta x t}{\langle a_0\rangle^3}\right)\right] \tag{26}$$

where

$$\alpha_i \equiv \frac{3c_\ell D_\ell \delta_\ell \gamma \Omega}{\pi k T z}$$

and x is the number of multiple paths available for diffusion between the pores.

When sufficient liquid phase is present to permit the isolated pores to fill by viscous flow, the density relation is again given by Eq. (26) with α_i replaced by

$$\lambda_i \equiv \frac{\gamma\delta^3}{4\pi\eta z}$$

4.5 Discussion

The models are now compared to experimental data (Fig. 33). Measurements taken from SEM micrographs of microstructures at various stages in the sintering process provide the values for the pore size and separation at the measured density of the sample. Data from the sintering curves (Figs. 18–23) give the experimental points.

The general trend illustrated by a comparison between experimental data and theory for the mixtures studied, has the following features. At high densities the theory and experiment correlate well. The favorable comparison at high density is consistent with the aim of the theory, which is to model the closure rate of pores, and consequently predict the sintering rate as full density is approached. At low density the measured sintering rate exceeds the predicted rate. This discrepency is presumed to arise because at low density, rearrangement processes are active ad significantly enhance the measured sintering rate. Such effects are beyond the scope of current densification models.

It is noted the densification data from compacts of alumina powders of vastly different morphologies and particle sizes have been used to obtain the data plotted in Figs. 33-38. The favorable application of the theory at high density is, thus, independent of the specifics of the original grain sizes and shapes. However, the sintering rates at low density vary considerably with different powder morphologies and sizes, within the identical alloy system, underscoring the immense difficulty associated with physical modeling of the rearrangement process.

Finally, these pore closure models can be compared with the analyses of viscous flow kinetics, given in Section 2. There it was found that viscous flow does not permit the required chemical potential to be maintained. The densification models given here similarly predict that viscous flow processes significantly overestimate the

measured sintering rate. Consequently, it appears that a viscous flow process cannot be sustained during sintering and diffusive mechanisms must prevail.

5. CONCLUSIONS

Densification mechanisms for sintering in the presence of a liquid phase have been examined. Previous studies had identified thin grain boundary films which act as rapid diffusion paths for atoms of the solid species, but the specific chemical potential gradients (which are required in order to motivate this matter transport) had not been comprehensively examined. The curvature of the liquid meniscus induces a tensile pressure in the liquid, yet this in itself is not adequate to provide the required stress gradient because viscous flow of the liquid would normally prevent a gradient from being maintained. Previous studies have thus focussed on small solid/solid contacts as a means to support the stress or as a site of high chemical potential. However, published high resolution micrographs of grain boundaries in dense liquid phase sintered materials, and particularly, similar micrographs given here for partially sintered materials provide no evidence for solid contacts: continuous grain boundary films are observed separating every high angle grain boundary throughout the sintering process.

In seeking possible mechanisms by which the chemical potential gradient can be maintained, kinetic models for concurrent viscous flow and solution/reprecipitation have been developed. A comparison of these expressions yields the result that viscous flow is quite rapid compared to solution/reprecipitation. Kinetic arguments based on viscous flow of the glassy phase from between the grains are thus inadequate to explain how the required stress gradient is maintained. In fact, grain boundary observations on partially sintered materials

suggest (in agreement with the analysis of the kinetic model) that the solid grains approach rapidly by the flow of liquid from between the grains until the separation distance is quite small, between one and two nanometers. Further densification then is by mass transport through the liquid phase.

In the absence of a viable kinetic argument, possible static mechanisms for maintaining the stress gradient are explored. Thermodynamic calculations indicate that a thin intergranular film would be expected to remain in equilibrium between the solid grains for the stress levels encountered during sintering. Phase separation or other chemical changes can occur, but a thin intergranular film is consistently observed. The situation is rationalized as follows: as the grain centers approach, a balance is established between squeezing as much liquid as possible out of the grain boundary and still having enough remanent liquid to maintain the energetically beneficial configuration of two solid/liquid boundaries rather than one solid/solid boundary. This phenomenon requires rather unique properties for the thin film viz., a film that supports a stress gradient.

To address the nature of the structure within the thin intergranular films, an electron diffraction experiment was conducted in which the thin two grain boundary films were found to be more crystalline than the amorphous three grain channels. These observations lead to the proposal of several possible models for the grain boundary structure. One model, based on published Xray studies, predicted short range order within the boundary layer, in which the solid grains were

separated by a layer of microcrystals. In the second model, several weakly-bonded layers of a two-dimensional crystal were envisioned separating the grains. For planar boundaries, both models predict a thin layer which behaves similarly to a liquid in its resistance to shear stresses (in agreement with published data) yet is capable of sustaining substantial gradients in normal stresses, in a manner similar to a crystal, as required for matter transport by solution/reprecipitation.

The observations of partially ordered second phase films along the two grain boundaries permitted a diffusion model to be developed for the final stage of sintering; pore closure. Expressions were derived for the closure of small pores homogeneously distributed at three grain junctions, and for larger isolated pores heterogeneously distributed throughout the microstructure. These models used an extreme value distribution to describe the sizes of the shrinking pores in order to correctly simulate the microstructural evolution. Pores filled by viscous flow of the liquid phase or by matter transport of solid atoms through the liquid.

Sintering rate diagrams coupled with knowledge of the pore sizes and morphology enabled a comparison with these models in order to elucidate densification trends during the sintering process. As powder compacts reached high densities, the measured sintering rate matched the theoretical prediction for sintering dominated by diffusion along two grain boundaries. Viscous flow predictions substantially overestimated the measured sintering rate, in agreement with the kinetic

analysis. The favorable correlation between the diffusion theory and experiment was found to be independent of the morphology and particle size of the ceramic starting powder. At low densities, rearrangement processes apparently contributed significantly to the measured densification rate and thus the theory underestimated the measured rate. Consequently, the initial sintering behavior varied widely within compacts of the same composition, but different powder particle shapes and sizes. Thus further research into the microstructural evolution during the early stages of sintering emerges as a prime area for future investigations.

REFERENCES

1. R.M. Cannon and U. Chowdhry, "Deformation and mass transport mechanisms in Si_3N_4," Report No. 4, Ceramics Processing Research Laboratory, MIT, 1976.
2. D.R. Clarke and G. Thomas, "Grain boundary phases in a hot pressed MgO fluxed silicon nitride," J. Amer. Ceram. Soc. 60, p. 491 (1977).
3. J.E. Marion, A.G. Evans, D.R. Clarke and M.D. Drory, "Overview No. 28: High Temperature Failure Initiation in Liquid-Phase-Sintered Materials," Acta Metall. 31, p. 1445 (1983).
4. H.C. Sorby, "On slaty cleavage, as exhibited by the Devonian Limestones of Devonshire," Phil. Mag. 11, p. 20 (1855).
5. R.L. Stocker and M.F. Ashby, "On the rheology of the upper Mantle," Rev. Geophys. and Space Phys. 11, p. 39 (1973).
6. E.H. Rutter, "The kinetics of rock deformation by pressure solution," Phil. Trans. R. Soc. Lond. A 283, p. 203 (1976).
7. R. Reynolds, "Flow of liquid from between approaching bodies," Phil. Trans. 177, p. 157 (1886).
8. B.V. Derjaquin, Zeits f. Physik 84, p. 657 (1933), Isz. AN-SSR, OMEN, Ser. Khim. 5, p. 1153 (1937) and B.V. Derjaquin and L. Landu, Acta Phys. Chim. URSS 14, p. 633 (1941).
9. E.J.W. Verwey and J. Th. G. Overbeek, "Theory of the Stability of Lyophobic Colloids, Elsever, Amsterdam (1948).
10. B.W. Ninham, "Long-Range vs. Short-Range Forces. The Present State of Play," J. Phys. Chem. 84, 1423 (1980).

11. S.L. Hoyt, "Hard Metal Carbides and Cemented Tungsten Carbides," Trans. AIME 89, 9 (1930).

12. G.H.S. Price, C.J. Smithells, and S.V. Williams, "Sintered Alloys, Part I: Copper-Nickel Tungsten Alloys Sintered with a Liquid Phase Present," J. Inst. Metals 62, 239 (1938).

13. F.V. Lenel, "Sintering in the Presence of a Liquid Phase," Trans. AIME 175, 878 (1948).

14. W.D. Kingery, "Densification During Sintering in the Presence of a Liquid Phase I Theory," J. Appl. Physics, 30, 301 (1959).

15. W.D. Jones, Discussion to Price Smithells and Williams (1938), J. Inst. Metals 62, 263 (1938), and
W.D. Jones, "Manufacturing of Non-porous Alloys from Powders," Metal Treatment, 5, 13 (1939).

16. R.B. Heady, and J.W. Cahn, "An Analysis of the Capillary Forces in Liquid-Phase Sintering of Spherical Particles," Met. Trans., 1, 185 (1970).

17. J.W. Cahn and R.B. Heady, "Analyses of Capillary Forces in Liquid-Phase Sintering of Jagged Particles," J. Amer. Ceram. Soc., 53, 406 (1970).

18. R. Raj and C.K. Chyung, "Solution/Reprecipitation Creep in Glass Ceramics," Acta Metall. 29, p. 159 (1980).

19. G.M. Pharr and M.F. Ashby, "On the Creep Enhanced by a Liquid Phase," Acta Metall. 31, p. 29 (1983).

20. The two important techniques for imaging the grain boundary phase are diffuse dark field imaging and lattice fringe imaging. The

earliest published images of the grain boundary film using the diffuse dark field technique were by M. Ruhle, C. Springer, L.T. Gaukler and M. Wilkens; "TEM studies of phases in Si-Al-O-Alloys," Proc. Fifth Int. Conf. on High Voltage Electron Microscopy, Japan Society of Electron Microscopy, ed. Mura and Hashimoto, 1977. Concurrent work on this technique was being performed at U.C. Berkeley by D.R. Clarke. He submitted a paper which briefly discussed the technique to Phil. Mag. in May 1977, but it was rejected and later appeared in Ultramicroscopy in 1979. The first paper to describe the diffuse-dark field technique in detail and to use the method for grain boundary width determinations was by O.L. Krivanek, T.M. Shaw and G. Thomas, "Imaging of thin intergranular phases by high resolution electron microscopy," J. Appl. Phys. 50, p. 4223 (1979).

21. The first published micrograph of the intergranular phase by the lattice fringe technique is by D.R. Clarke and appeared on the back cover of the American Ceramics Society journal, Vol. 60, No. 9-10, 1977. The first paper to report the detection of thin intrgranular films by lattice fringe images is by D.R. Clarke and G. Thomas, 1977 (Ref. 2).

22. V. Jayaram and R. Sinclair, "Detection of thin intergranular cobalt layers in WC-Co composites by lattice imaging," J. Amer. Ceram. Soc. 66, p. C137 (1983).

23. J. Blanc, C.J. Buiocchi, M.S. Abrahams and W.E. Ham, "The Si/SiO_2 interface examined by cross-sectional transmission electron microscopy," Appl. Phys. Lett. 30, p. 120 (1977).

24. L.M. Levinson and J.R. Phillips, "The Physics of Metal Oxide Varisistors," J. Appl. Phys. 46, p. 1332 (1975).

25. O.L. Krivanek, T.T. Sheng, and D.C. Tsai, "A high resolution electron microscopy study of the Si-SiO_2 interface," Appl. Phys. Lett. 32, p. 437 (1978).

26. S.C. Hansen, Y.R. Shiue and D.S. Phillips, "Grain boundary microstructures in a commercial alumina ceramic," Advances in Ceramics, 6, M.F. Yan and A.H. Heuer, eds., p. 163 (1982).

27. B. Ninham, "Short Range Order in Thin Films," J. Phys. Chem. 85, 1091 (1981).

28. G. Thomas, C. Ahn, and T. Weiss, "Characterization and Crystallization of Y-Si-Al-O-N Glass, J. Amer. Ceram. Soc. 65, p. C185 (1982).

29. R. Bruckner, "High pressure effects in vitreous SiO_2," J. Non-Crystalline Solids 5, p. 177 (1970).

30. S. Sakka, and J.D. MacKenzie, "Densification Phenomenon in Glasses," ibid. 1, p. 107 (1969).

31. A.G. Revesz, "Pressured induced conformational changes in vitreous silica," ibid. 7, p. 77 (1972).

32. J.H. Konnea, P. D'Antonia and J. Karle, "Analysis and interpretation of diffraction data from amorphous materials," from Advances in X-ray Analysis, Vol. 24, Plenum, p. 63 (1981).

33. A. Geiger, A. Rahman and F.H. Stillinger, "Molecular Dynamics Study of the Hydration of Lennard-Jones Solutes," J. Chem. Phys. 70, p. 263 (1979).

34. R. Raj and M.F. Ashby, "On grain boundary sliding and diffusional creep," Met. Trans. 2, p. 1113 (1971).

35. D.R. Clarke, N.J. Zaluzec and R.W. Carpenter, "The Intergranular Phase in Hot-Pressed Silicon Nitride: II. Evidence for Phase Separation and Crystallization," J. Amer. Ceram. Soc. 64, p. 608 (1981).

36. T.M. Shaw, "The Crystallization of Glasses in the Mg-Si-O-N System," Ph.D. Thesis, U.C. Berkeley (1980).

37. V.K. Singh, "Densification of alumina and silica in the presence of a liquid phase," J. Amer. Ceram. Soc. 64, C133 (1981).

38. T.M. Shaw, private communication (1984).

39. W.D. Kingery and M.D. Narasimhan, "Densification During Sintering in the Presence of a Liquid Phase, II. Experiment," J. Appl. Phys. 30, p. 307 (1959).

40. P.L. Flaitz, "Some Aspects of Liquid Phase Sintering of Alumina," Ph.D. Thesis, U.C. Berkeley (1982).

FIGURE CAPTIONS

Fig. 1. (a) Schematic for wetting angle measurements.

(b) Schematic for grain boundary penetration and dihedral angle measurements. When $\psi = 0^\circ$, the liquid can penetrate the grain boundary.

Fig. 2. (a) High resolution transmission electron micrograph of a grain boundary in 63% dense alumina/anorthite, showing a continuous intergranular phase with a thickness of about 1.2 nm.

(b) HREM of a three grain pocket (G) and a two grain boundary in the 63% dense alumina/anorthite.

Fig. 3. (a) Bright field and (b) Diffuse dark field transmission electron micrographs of 63% dense alumina/anorthite sample. The light contrast in the DDF micrograph is the glassy phase. (Bar = 50 nm)

Fig. 4. Geometry assumed for the sintering models. Although spheres are shown, the expressions derived here are general.

Fig. 5. (a) Graph of the percent light transmitted versus "d" the reciprocal distance from the optic axis for microdensitometer traces from the diffuse dark field negatives. Only the extremes in the data are shown for $d < 2$Å, because of the large number of data points. The arrow indicates the d-spacing at which the objective aperture began to intercept a portion of the transmitted beam; data to the right of the arrow is meaningless.

(b) Similar plot obtained from DDF images of the two grain boundaries.

Fig. 6. (a) Graph of percent light transmitted versus d-spacing from the negative of a diffraction pattern obtained from amorphous anorthite. The maxima is the (100) plane.

(b) Plot from partially crystallized anorthite (diffraction pattern inset in Fig. 8).

(c) Plot from nearly-completely crystallized anorthite. Direction (A) in the pattern was the scan direction for the microdensitometer trace which intercepts the Bragg spots and is shown in the plot as a solid line. Direction (B) is for a trace that did not intercept the Bragg spots and is shown as a dotted line in the plot.

Fig. 7. (a) Comparison between data obtained for electron diffraction from three grain channels by the diffuse-dark field technique (dots) with traces from a diffraction pattern of amorphous anorthite (solid line). The comparison illustrates the amorphous nature of the glassy phase lying along three grain channels.

(b) Comparison between DDF data from two grain boundaries (dots) with the diffraction pattern from a partially crystallized anorthite sample (solid line). The position and relative intensity of the peaks in the DDF plot indicate a good match with the diffraction pattern, illustrating the

presence of some crystallinity in the intergranular phase along two grain boundaries.

Fig. 8. Schematic of "marble" grain boundary model, showing two solid grains separated by a row of randomly oriented microcrystals.

Fig. 9. High magnification dark-field TEM micrograph of microcrystals in the partially crystallized anorthite sample, annealled 30 minutes at 1500°C. Inset; the diffraction pattern from this sample. Approximate position of the objective aperature is indicated by the circle. (Bar = 2 nm)

Fig. 10. Schematic of "layer" grain boundary model showing (A) an amorphous like structure when viewed edge-on to the grain boundary and (B) a crystalline-like structure when viewing perpendicular to the grain faces.

Fig. 11. Phase diagram for the alumina/anorthite system.

Fig. 12. (a) Scanning electron micrograph of 10 μm anorthite glass (bar = 2 μm) and (b) plot of the particle size distribution estimated from SEM micrographs.

Fig. 13. (a) SEM of collodial anorthite (bar = 2 μm) and (b) particle size distribution.

Fig. 14. (a) SEM of jagged alumina (bar = 1.5 μm) and (b) particle size distribution.

Fig. 15. (a) SEM of semi-spherical alumina (bar = 1 μm) and (b) particle size distribution.

Fig. 16. (a) SEM of spherical alumina (bar = 50 μm) and (b) particle size distribution.

Fig. 17. Schematic of quench furnace used for the sintering experiments.

Fig. 18. Density vs. time sintering rate diagrams for:

(a) 90/10, jagged alumina/1 μm anorthite, well mixed.

(b) 90/10 jagged alumina/10 μm anorthite, poorly-mixed.

(c) Pure jagged alumina.

(d) 95/5 jagged alumina/10 μm anorthite, poorly mixed.

Fig. 19. (a) 90/10 spherical alumina with 1 μm anorthite.

(b) Pure spherical alumina.

Fig. 20. (a) 90/10 semi-spherical alumina/0.5 μm anorthite, well mixed.

(b) Pure semi-spherical alumina.

(c) Mixture in (20a) with 4 weight percent 10 μm polyvinyl alcohol (PVA) particles. This burned out on heat up, giving approximately 10 μm holes, which then sintered slowly.

Fig. 21. (a) Pure semi-spherical alumina ($\bar{d}$ = 0.3 μm).

(b) Pure jagged alumina ($\bar{d}$ = 1.5 μm).

(c) Pure spherical alumina ($\bar{d}$ = 20 μm).

Fig. 22. (a) 90/10 jagged with 10 μm anorthite, poorly mixed.

(b) 90/10 semi-spherical/0.5 μm anorthite and 4% PVA. The curves intersect at about 10^5 seconds. Further sintering for both mixtures appear to be governed by the rate of closure of the large pores caused by the large glass

particles melting (in a) and by closure of the intentional pores introduced by the PVA (in b).

Fig. 23. Spare number

Fig. 24. (a) SEM micrograph of an exceptionally large glass particle amongst collodial glass frit. When these large glass particles melt during the early stages of sintering they leave a large residual void (b), that accounts for the slow sintering rate in the final stages (bars = 10 μm).

Figs. 25-30. SEM micrographs of polished sections used for pore size and pore separation measurements.

Fig. 25. 90/10 jagged alumina/1 μm anorthite, well mixed, sintered 15% seconds at 1555°C, density is 72% (bar = 5 μm).

Fig. 26. Semi-spherical alumina with 10% 0.5 μm anorthite, well mixed, sintered 15 seconds at 1555°C; 85% dense (bar = 5 μm).

Fig. 27. Jagged alumina with 10% 1 μm anorthite, well mixed, sintered $4x10^3$ seconds at 1555°C; 88% dense (bar = 5 μm).

Fig. 28. Jagged alumina with 10%, 10 μm anorthite, poorly mixed, sintered at 1555°C for $8x10^5$ seconds, 91% dense (bar = 10 μm).

Fig. 29. Semi-spherical alumina with 10% 0.5 μm anorthite, well-mixed, sintered at 1555°C for $3x10^2$ seconds, 96% dense (bar = 10 μm).

Fig. 30. Jagged alumina with 10% 1 μm anorthite, well mixed, sintered at 1555°C for $3x10^5$ seconds, 98% dense (bar = 4 μm).

Fig. 31. Schematic of the geometry assumed for the typical pore closure model.

Fig. 32. Schematic of the geometry assured for the isolated pore closure model.

Fig. 33. to 38. Comparison of experimental data with the models derived using pore size and separation measurements from Figs. 25-30, respectively. The plots compare the change in density (from the measured starting density to final density) with the time elapsed during the densification. Models for two grain boundary diffusion agree well with experimental measurements for high densities (>90%); rearrangement processes contribute to densification at low densities and thus the pore closure models underestimate the sintering rate..

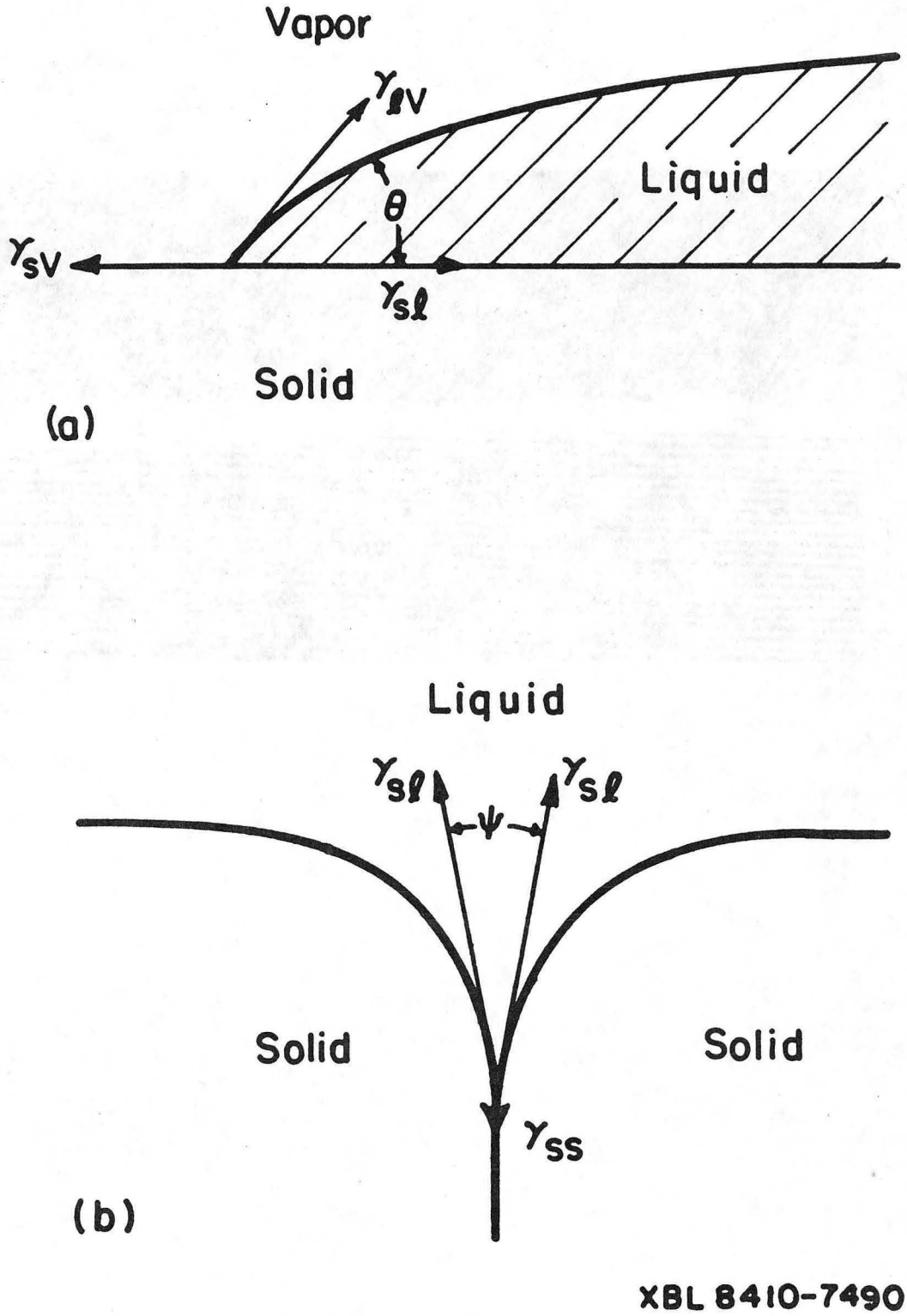
Vapor
$\gamma_{\ell V}$
Liquid
θ
γ_{sV}
$\gamma_{s\ell}$
Solid
(a)
Liquid
$\gamma_{s\ell}$
$\gamma_{s\ell}$
ψ
Solid
Solid
γ_{ss}
(b)
XBL 8410-7490

Figure 1

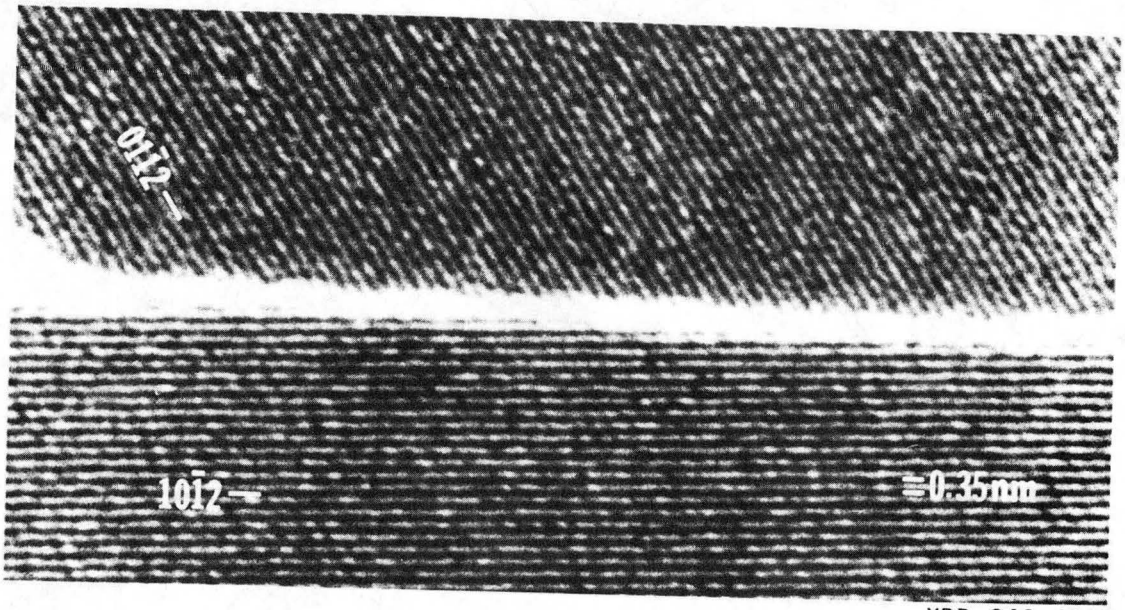

XBB 848-6452

Figure 2a

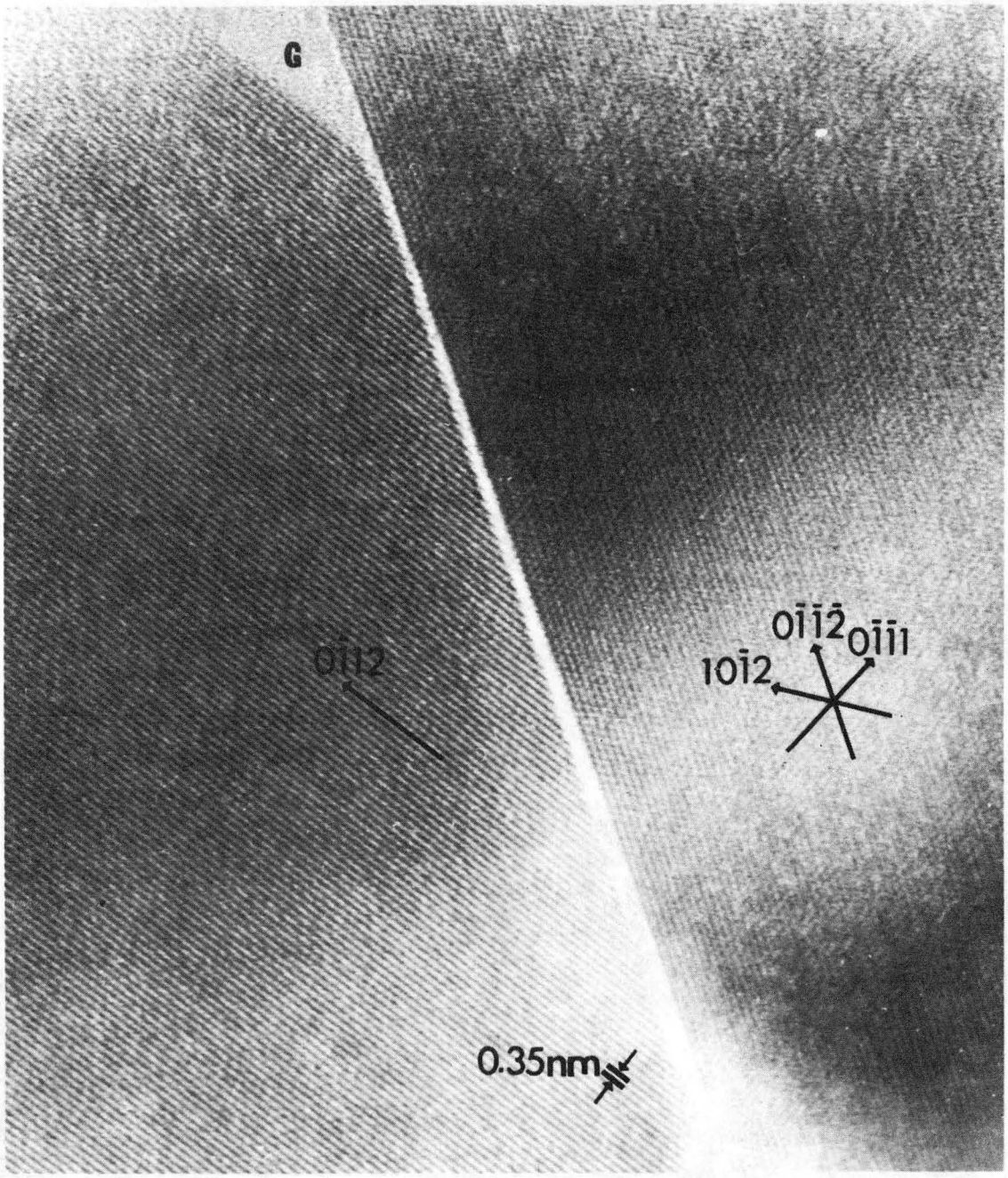

XBB 848-6459

Figure 2b

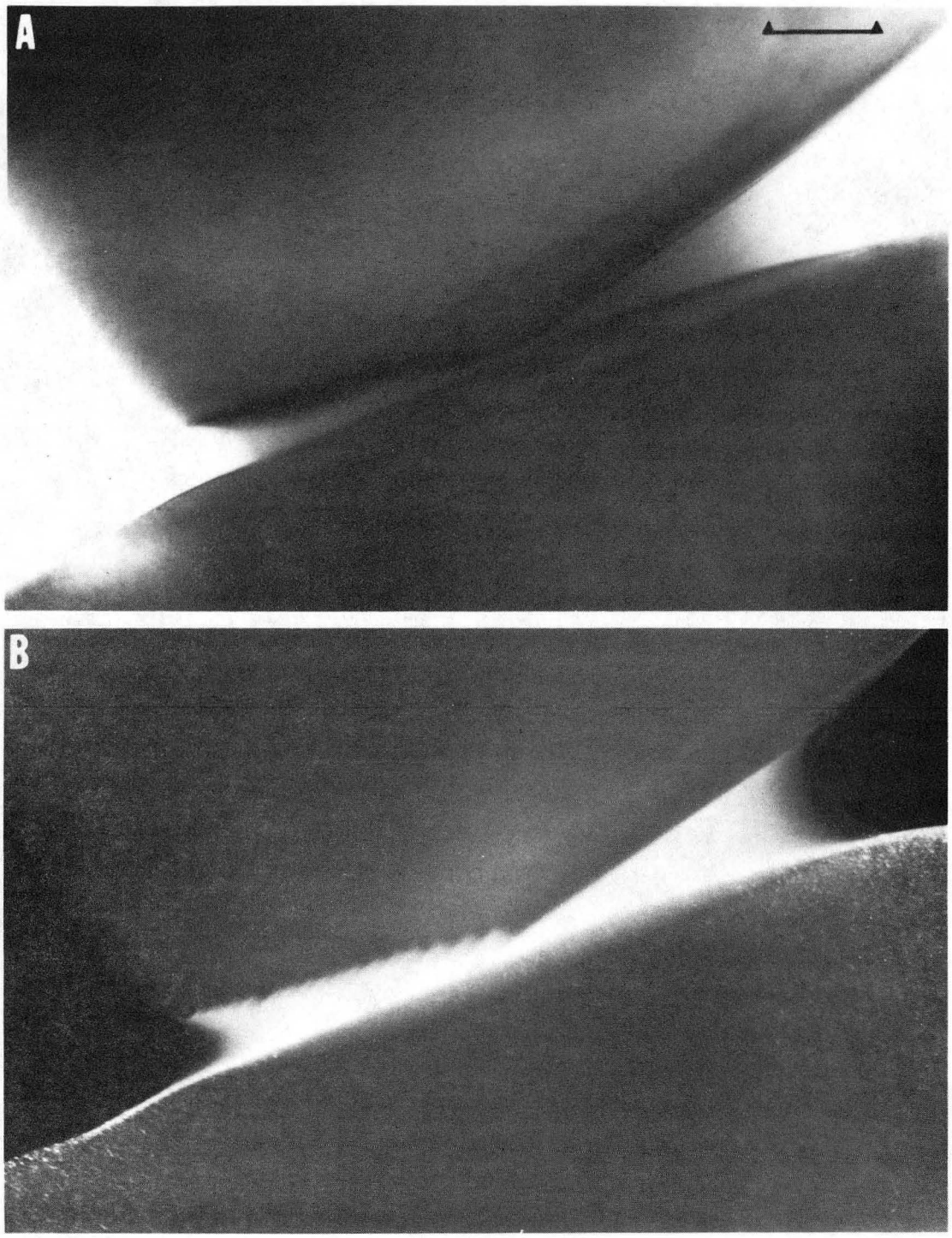

XBB 848-6449

Figure 3

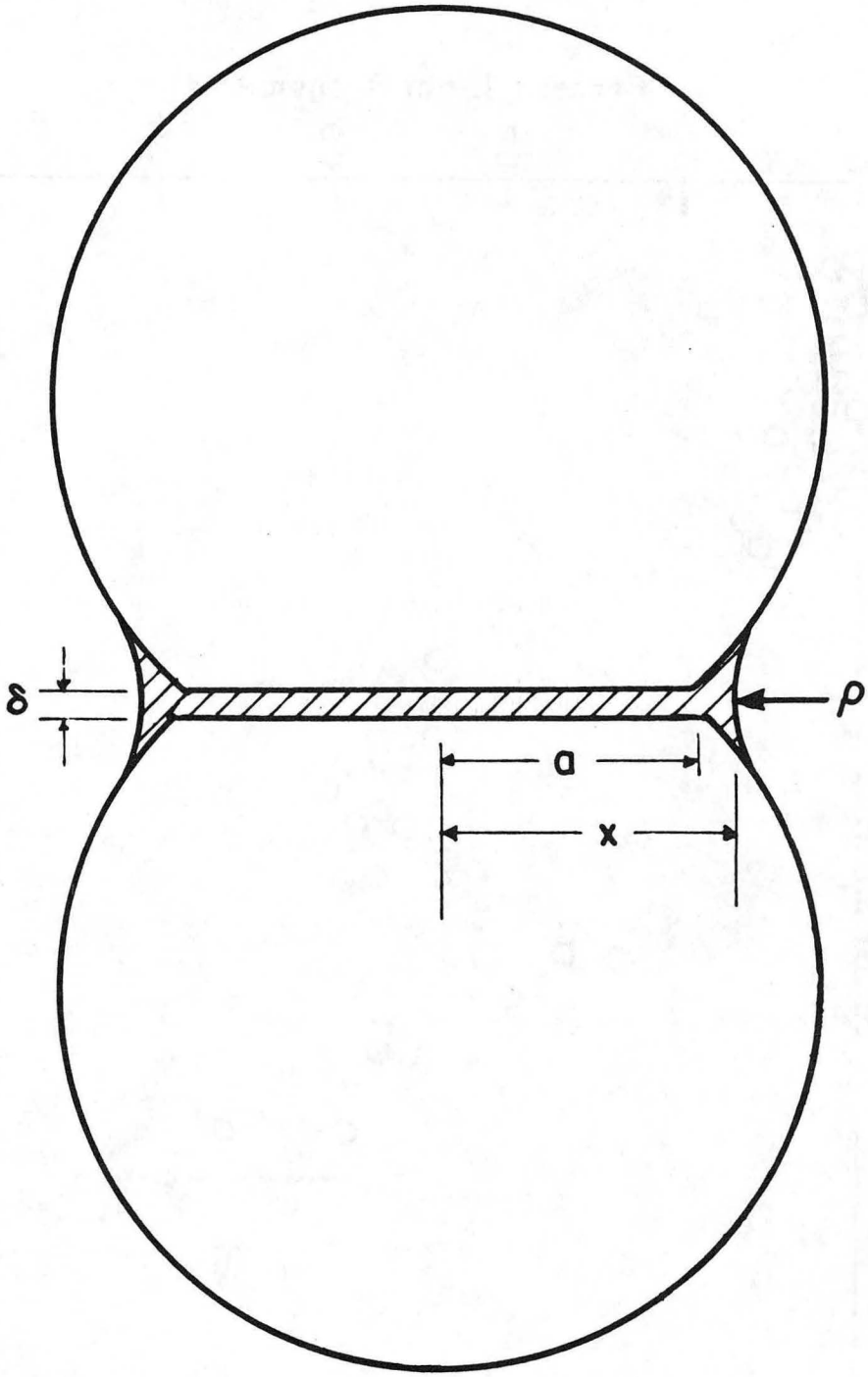

XBL 8410-8220

Figure 4

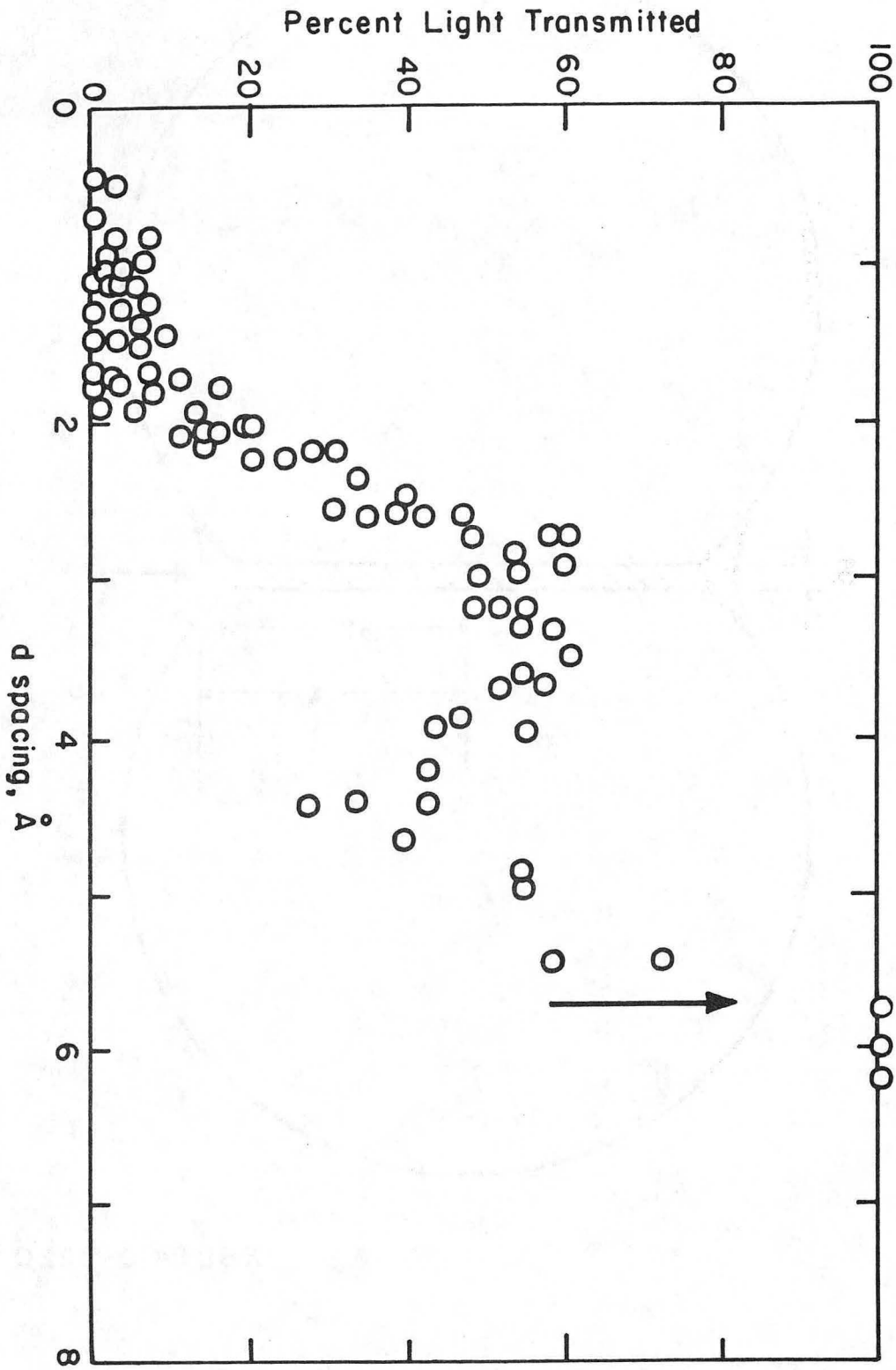

XBL8410-7492

Figure 5a

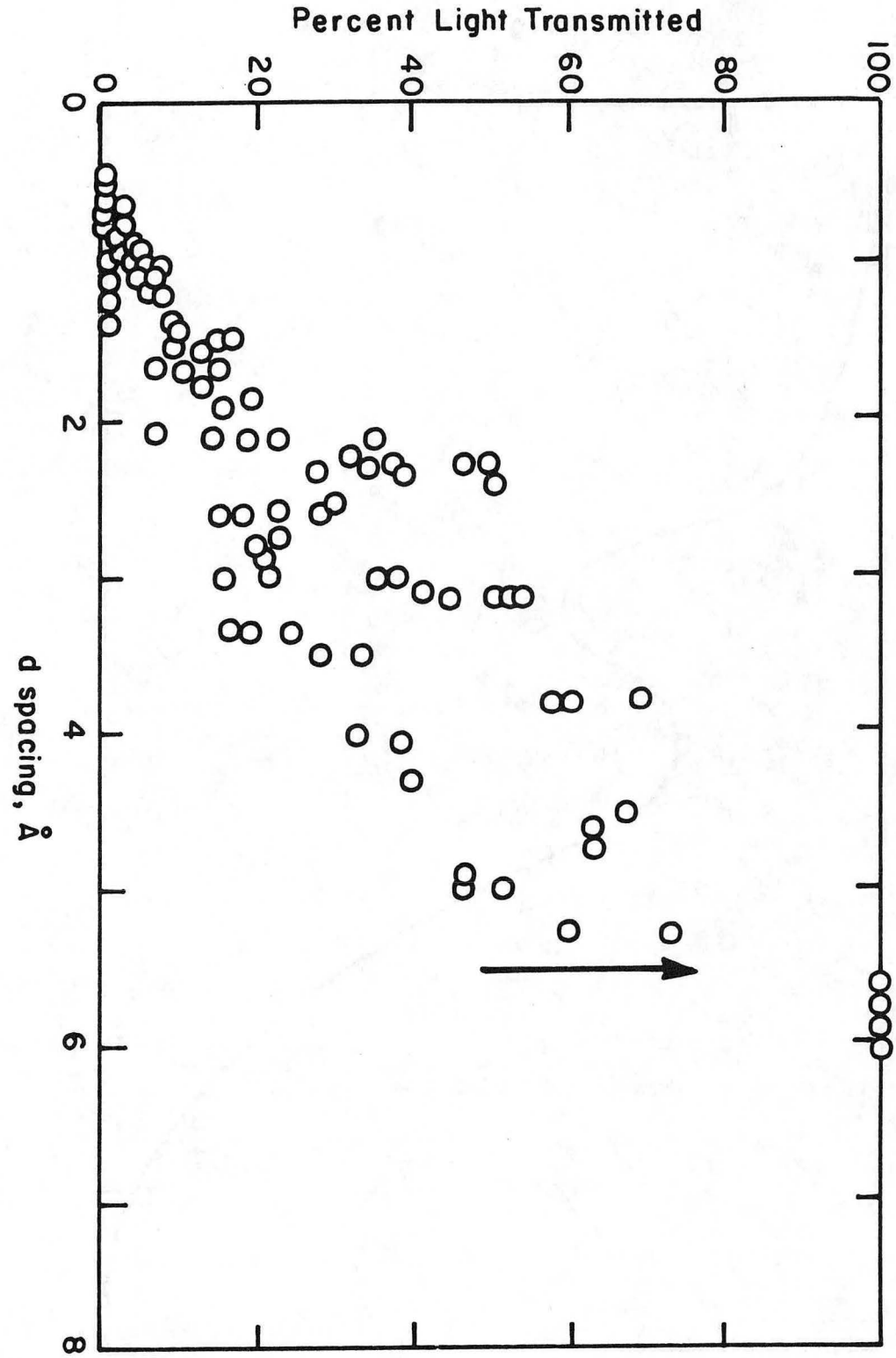

XBL 8410-7493

Figure 5b

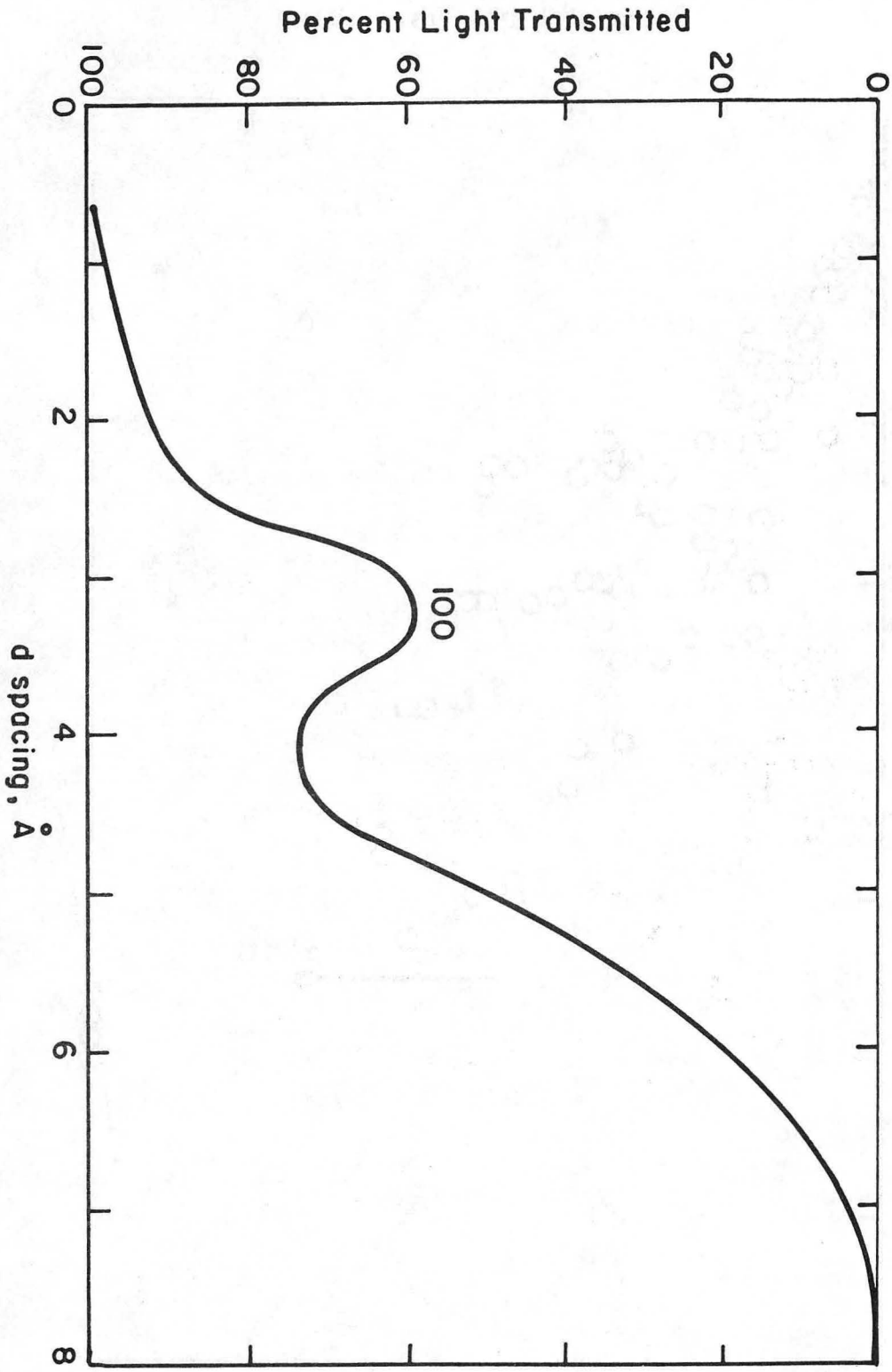
Percent Light Transmitted
0
20
40
60
80
100
100
0
2
4
6
8
d spacing, Å
XBL 8410-7494

Figure 6a

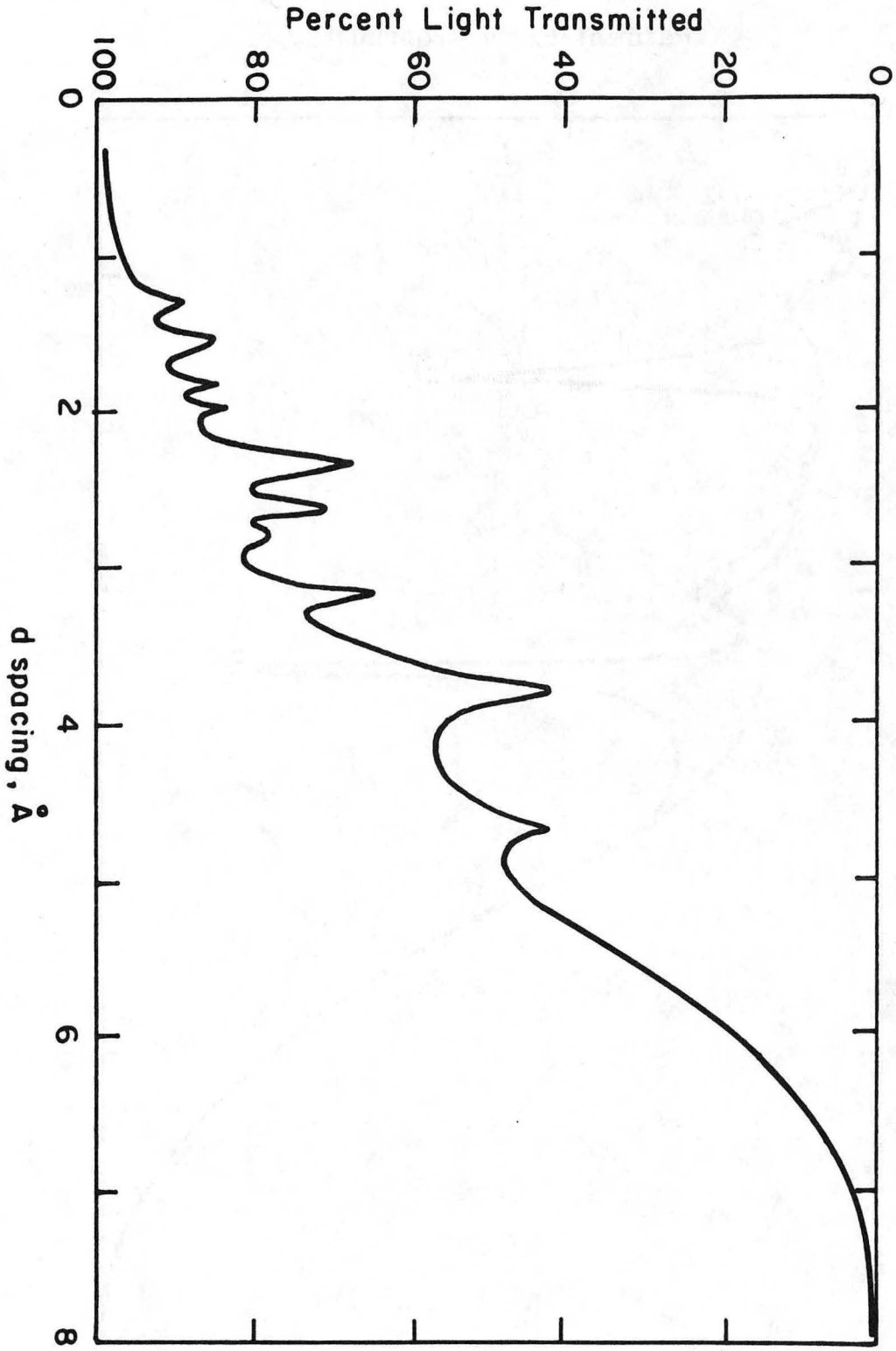
Percent Light Transmitted
0
20
40
60
80
100
0
2
4
6
8
d spacing, Å
XBL 8410-7495

Figure 6b

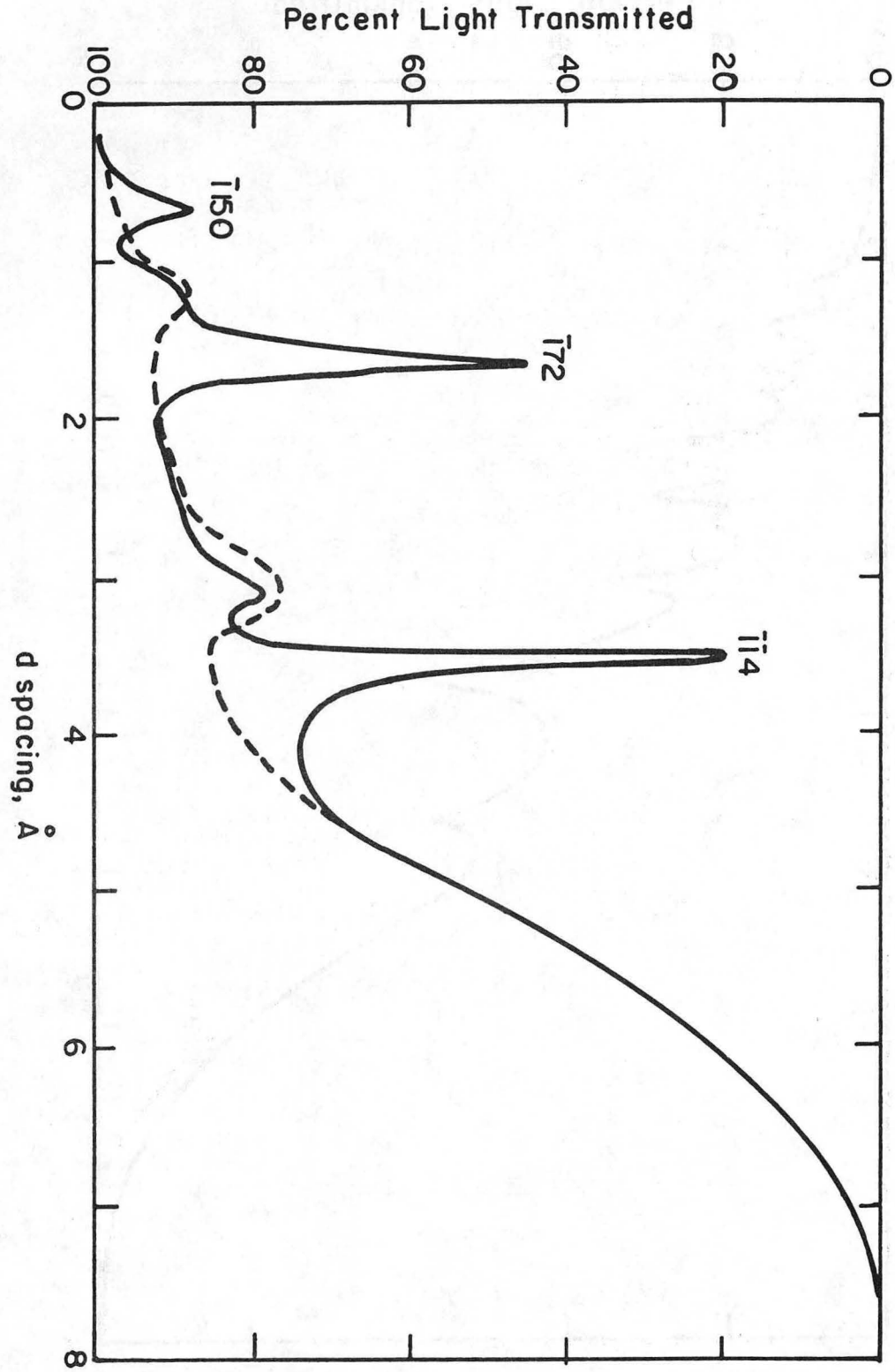

XBL 8410-7496

Figure 6c

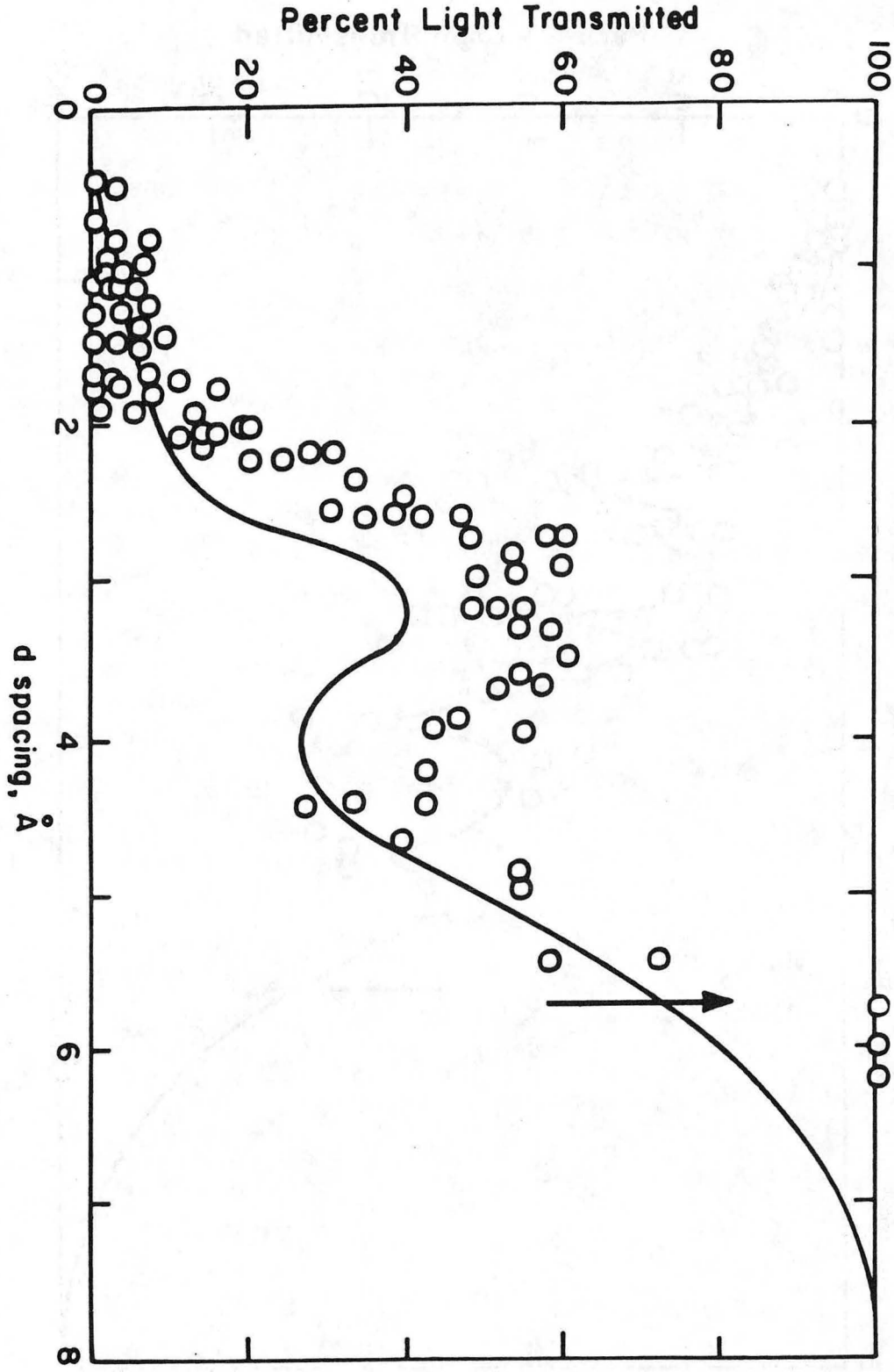

XBL8410-7497

Figure 7a

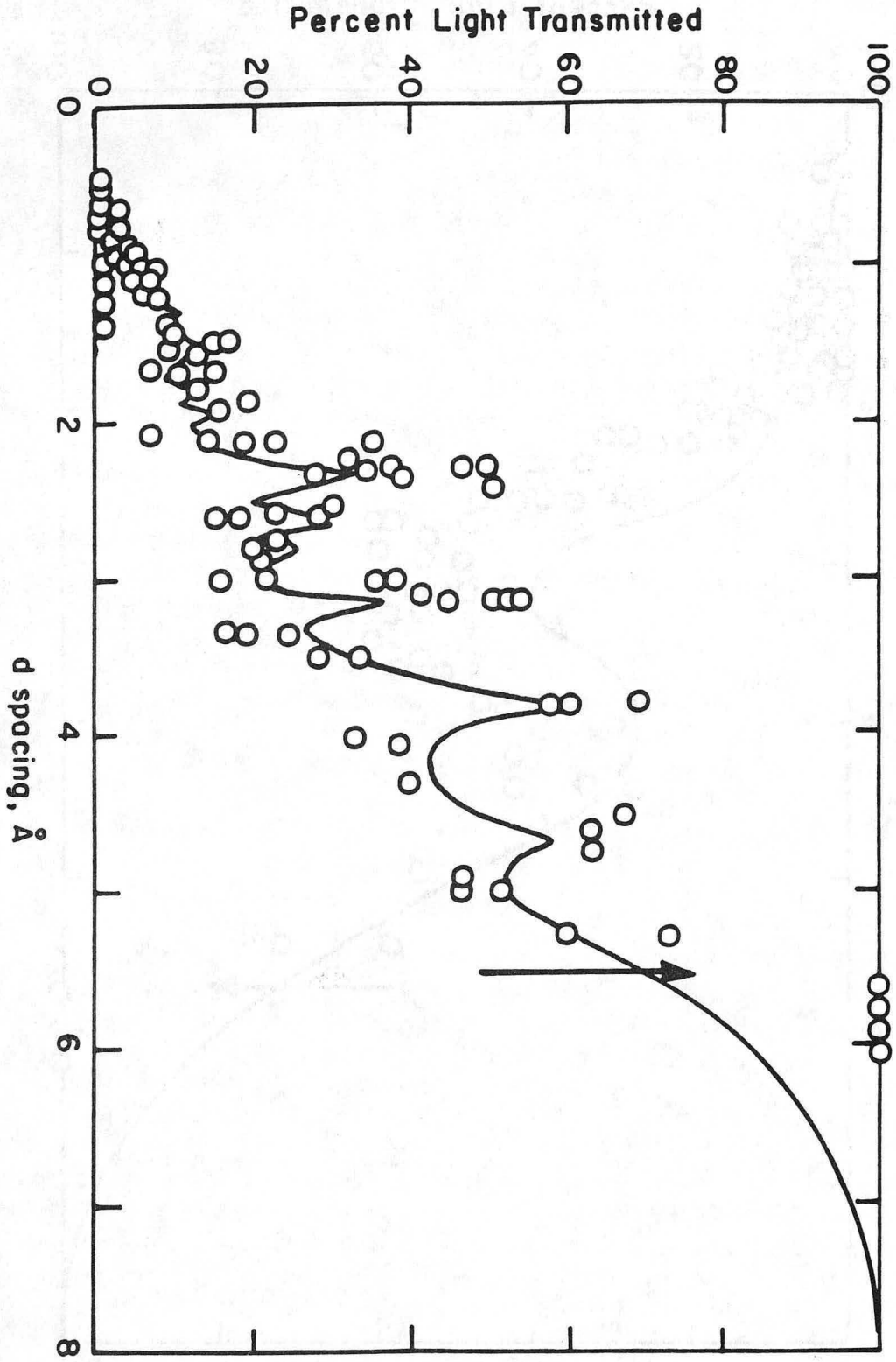

XBL 8410-7498

Figure 7b

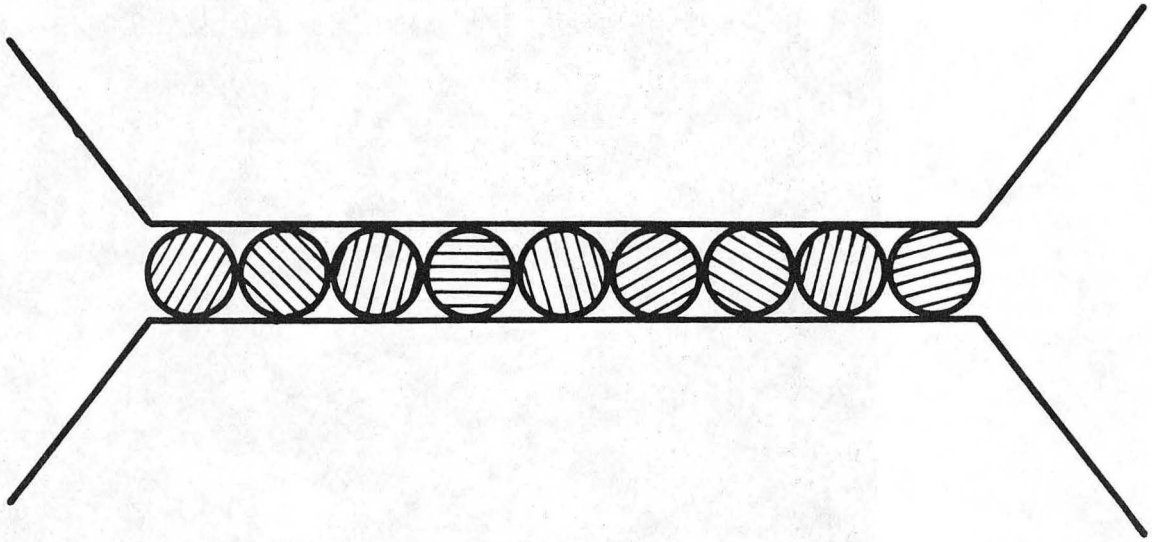

XBL 8410-7499

Figure 8

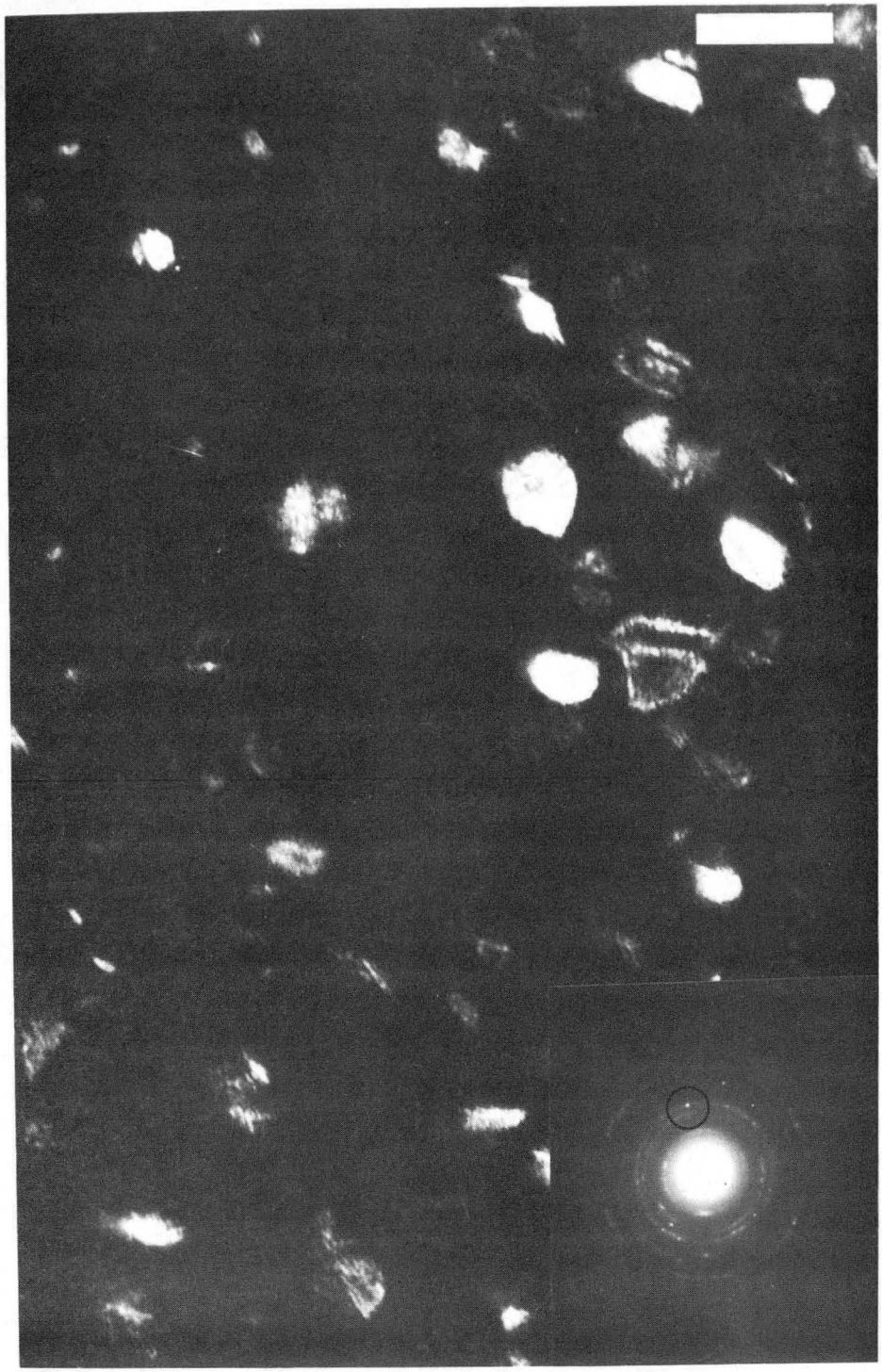

XBB 849-7311

Figure 9

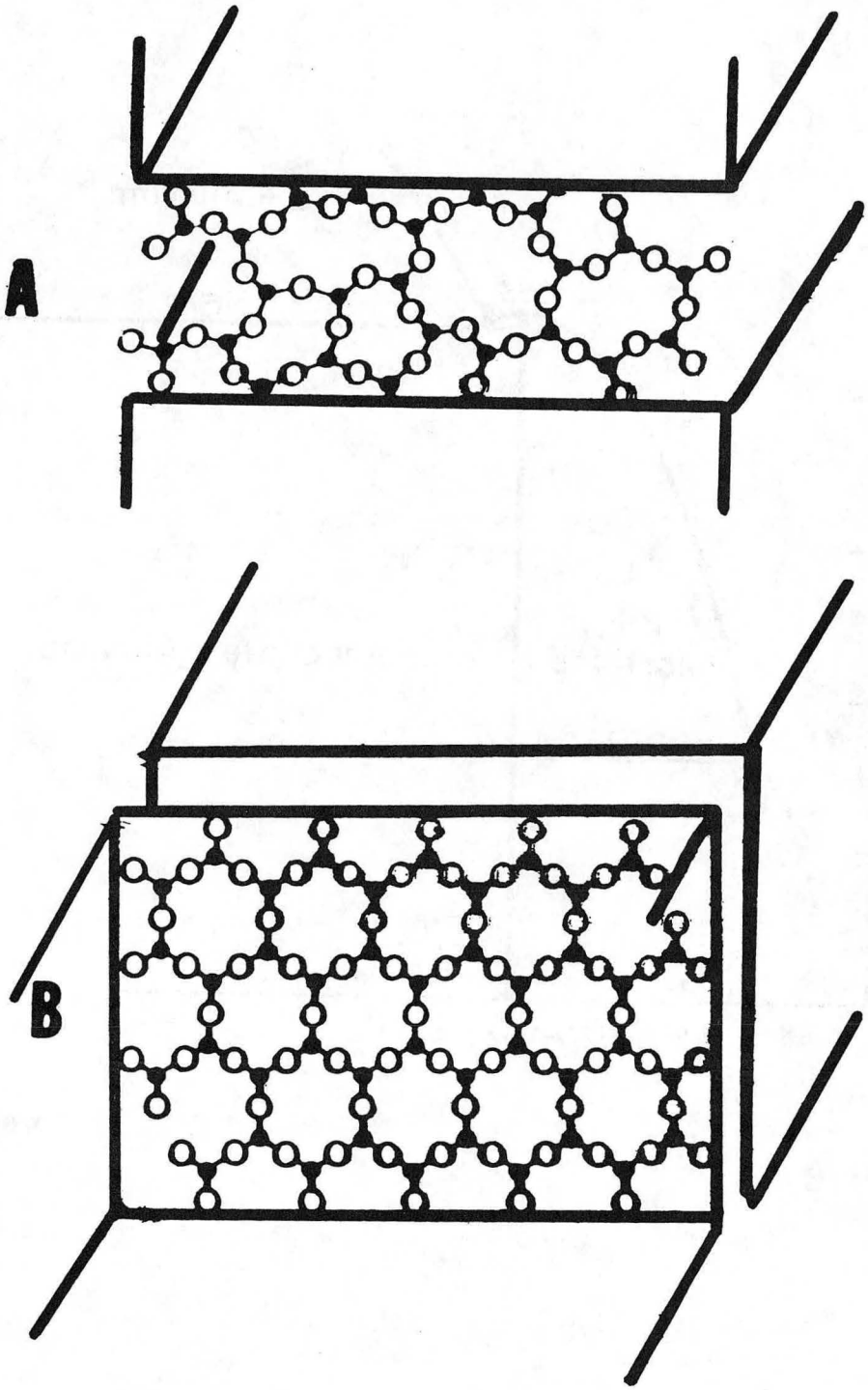

XBL8410 7500

Figure 10

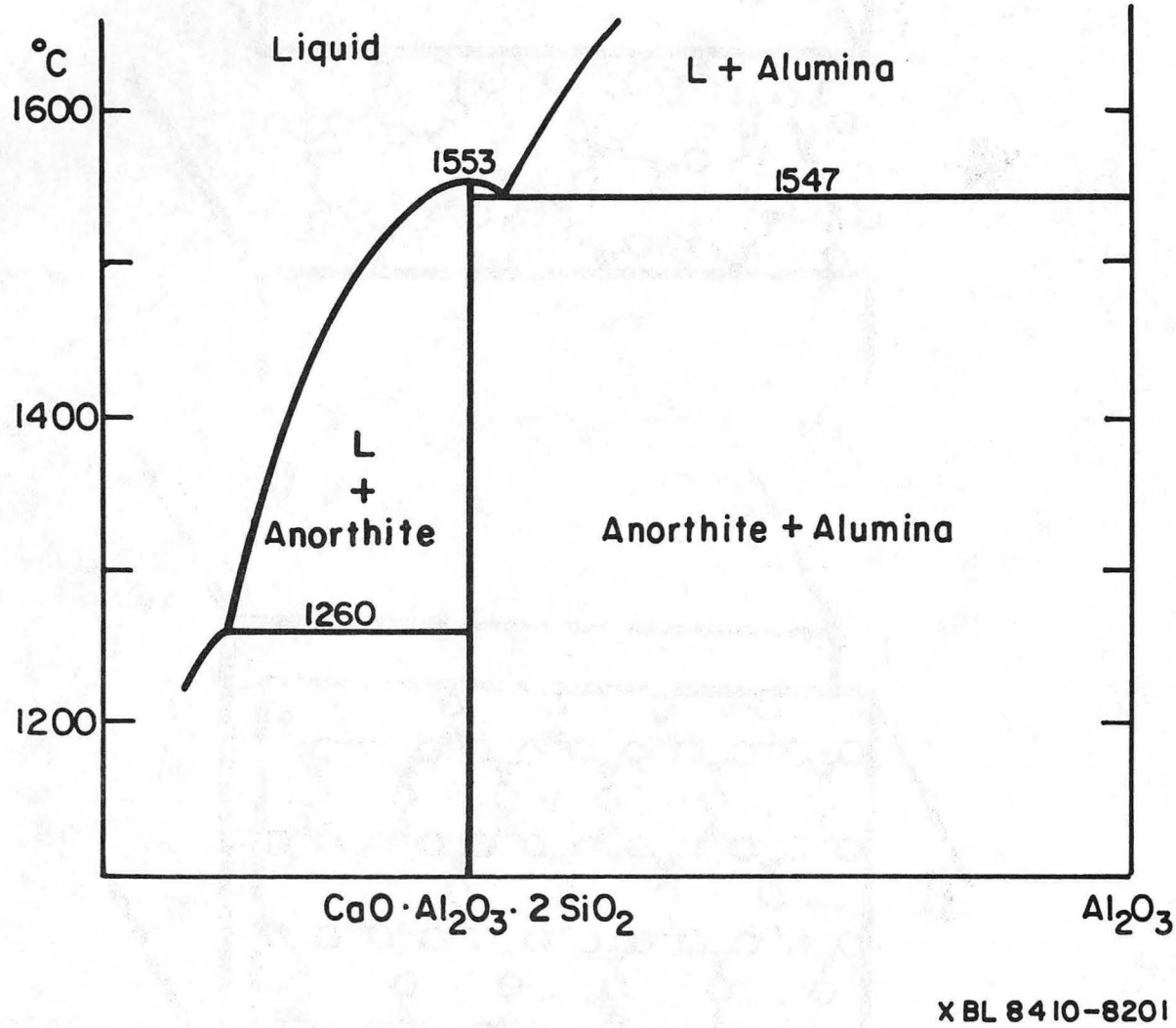
°C
1600
1400
1200
Liquid
L + Alumina
1553
1547
L
+
Anorthite
Anorthite + Alumina
1260
CaO·Al2O3·2 SiO2
Al2O3
XBL 8410-8201

Figure 11

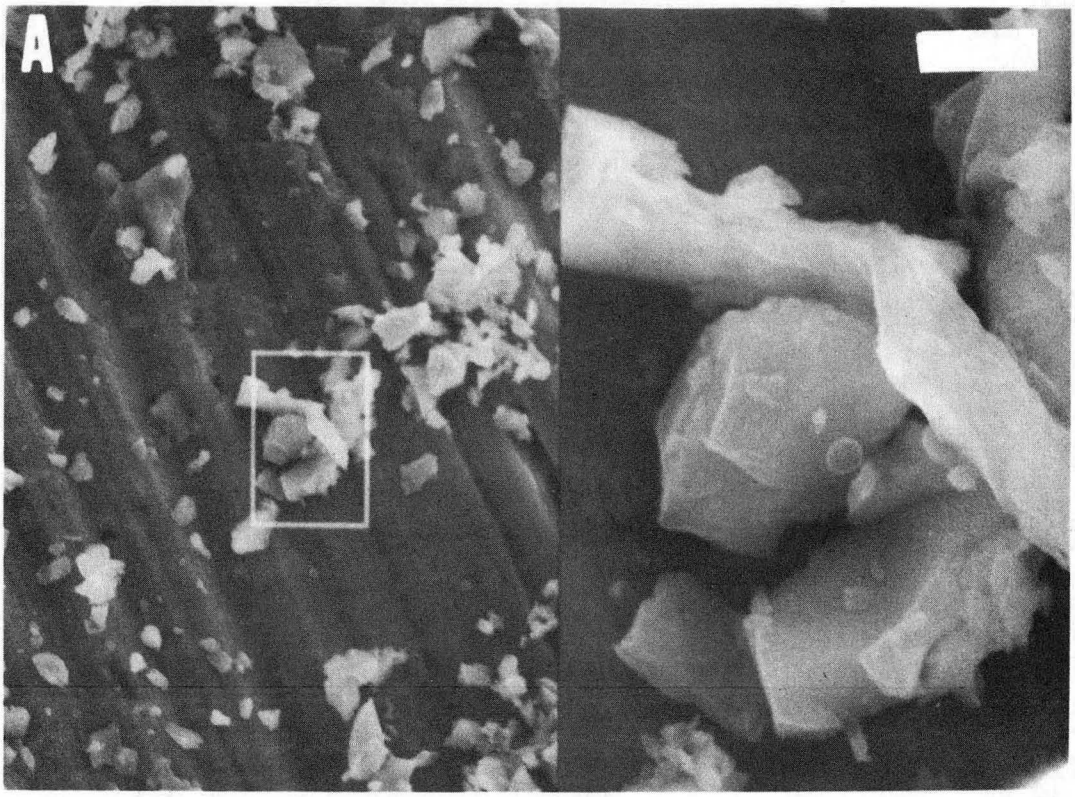

XBB 849-7316

Figure 12a

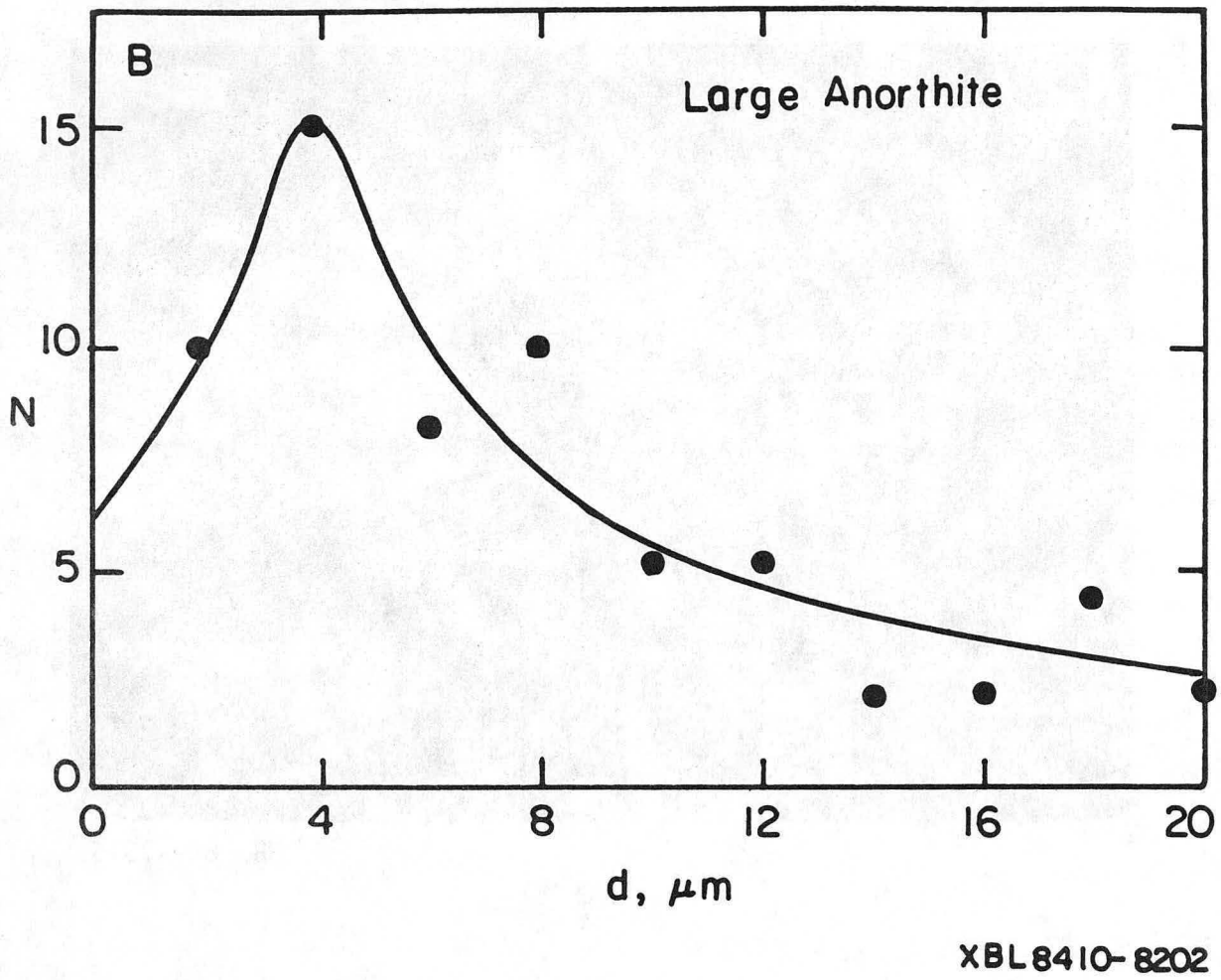

Figure 12b

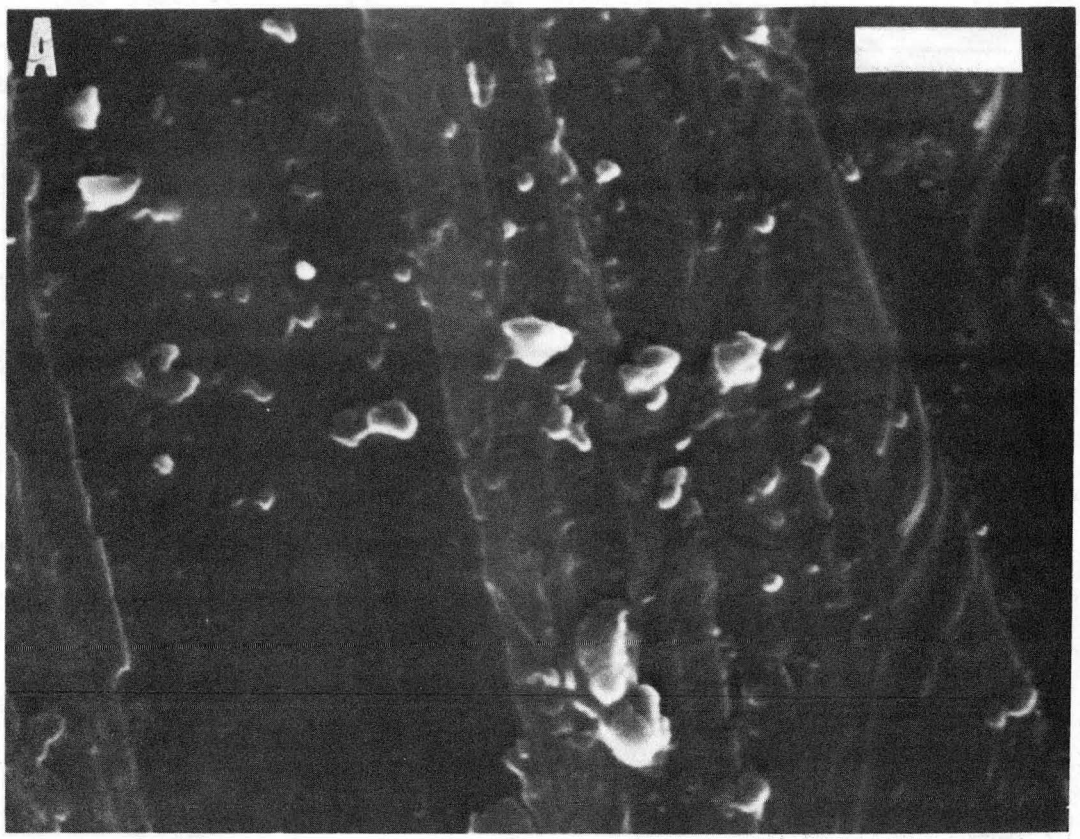

XBB 849-7317

Figure 13a

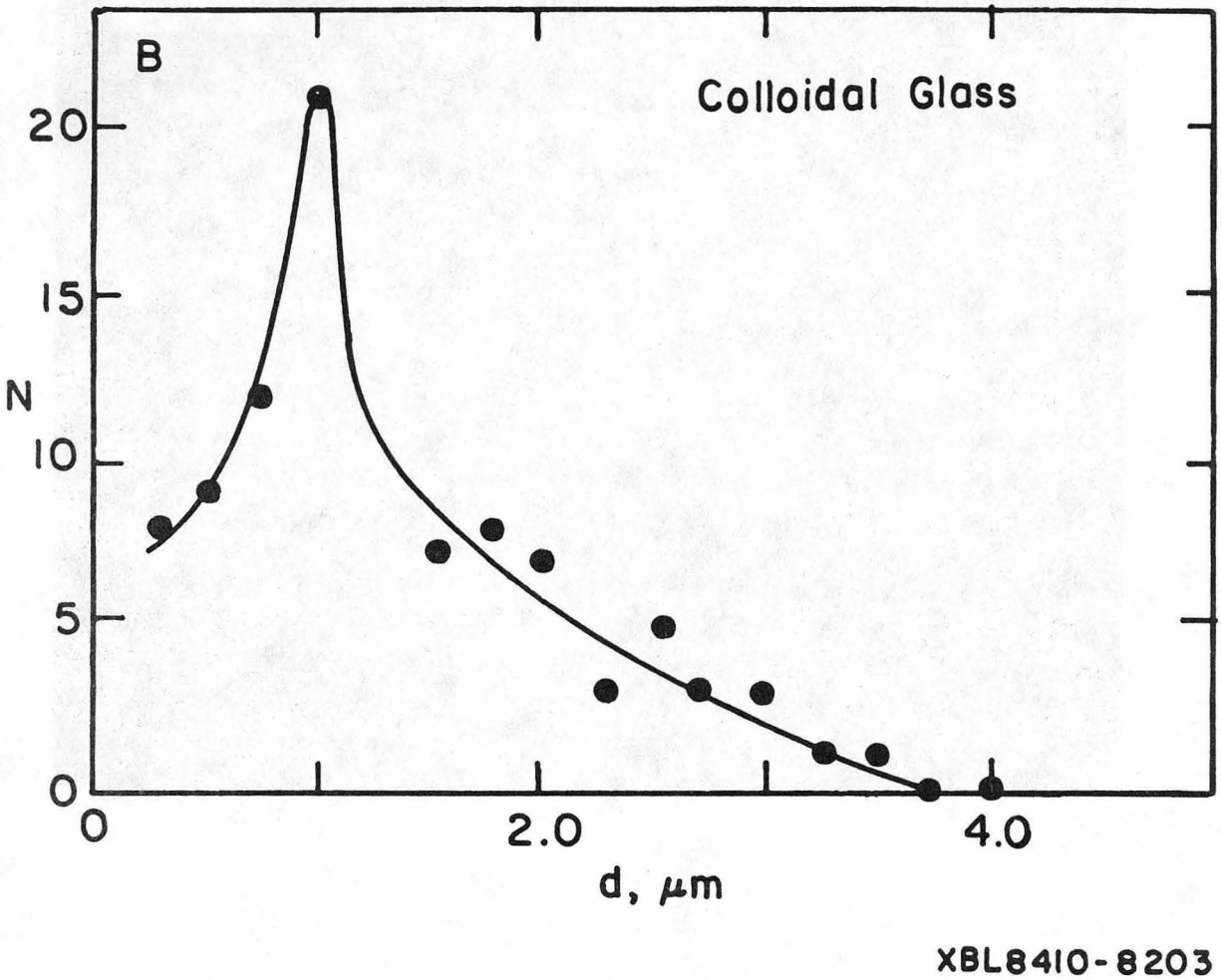

Figure 13b

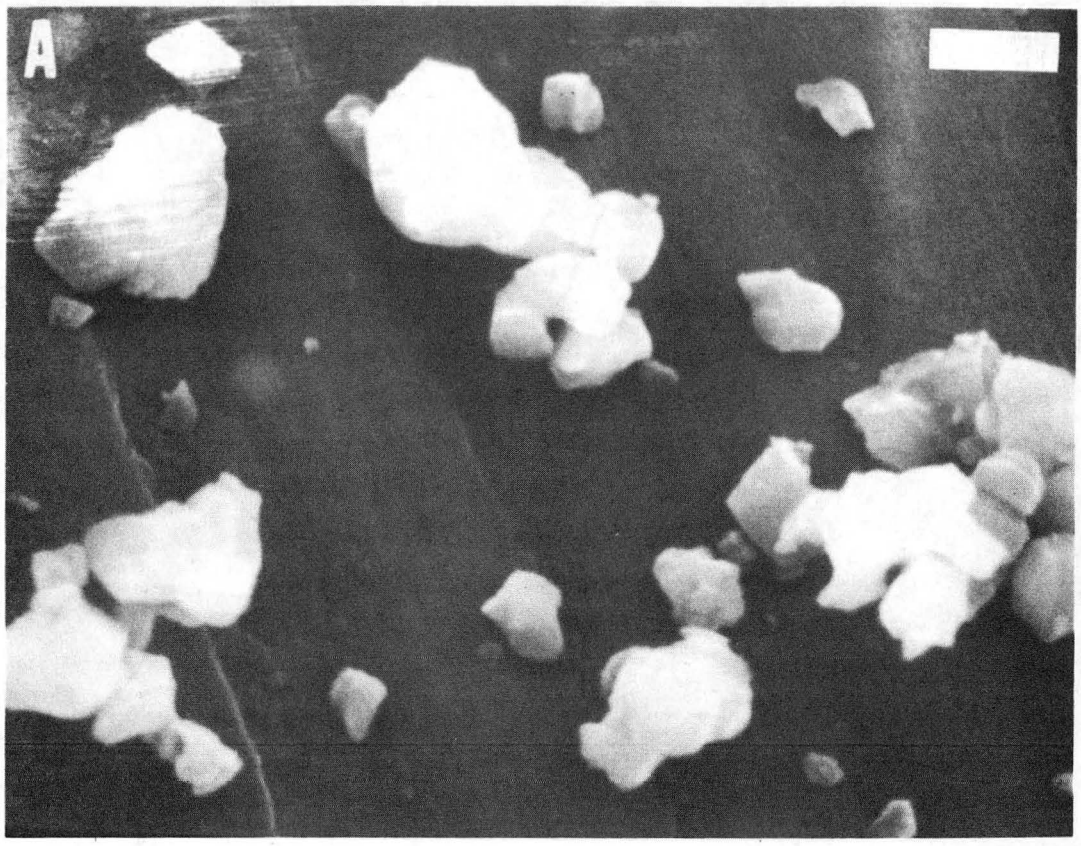

XBB 849-7315

Figure 14a

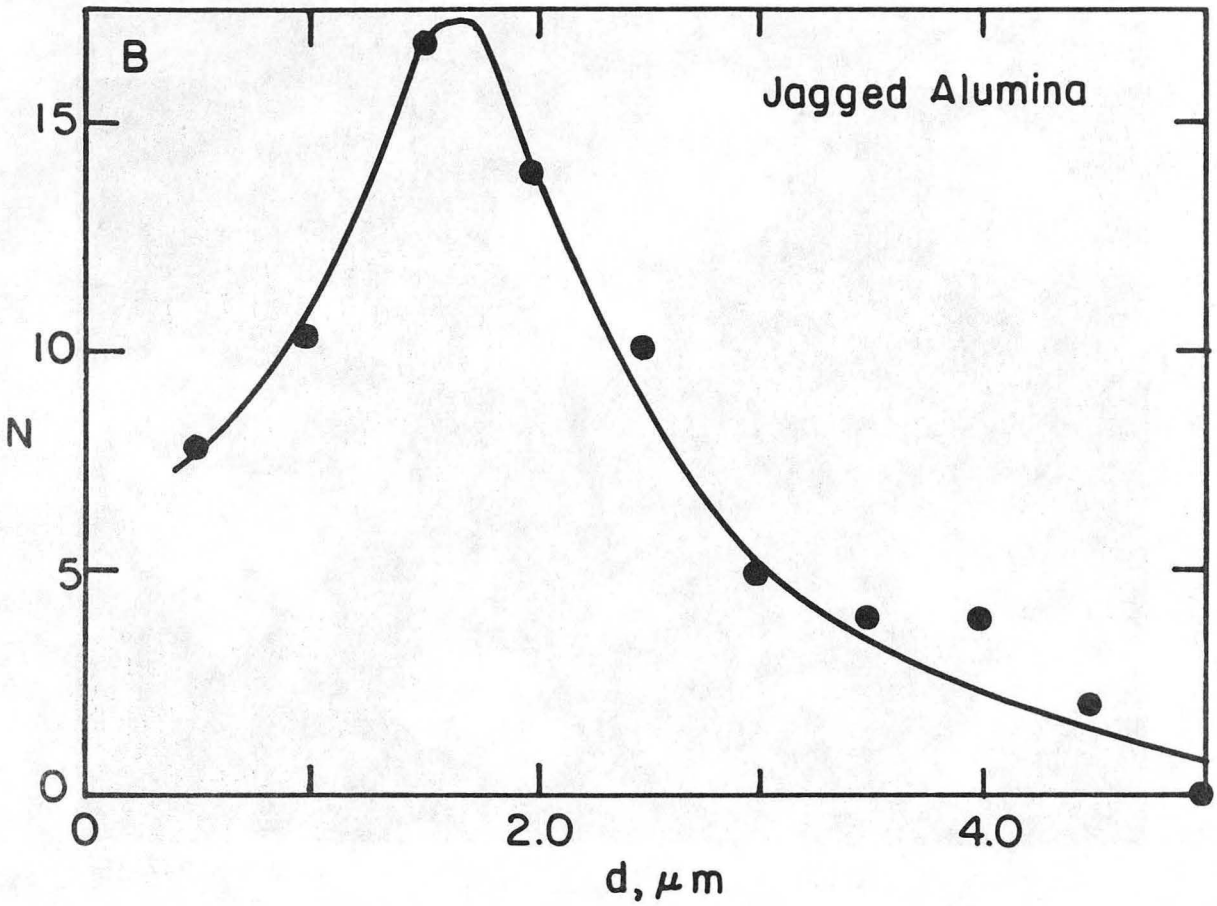

XBL 8410-8204

Figure 14b

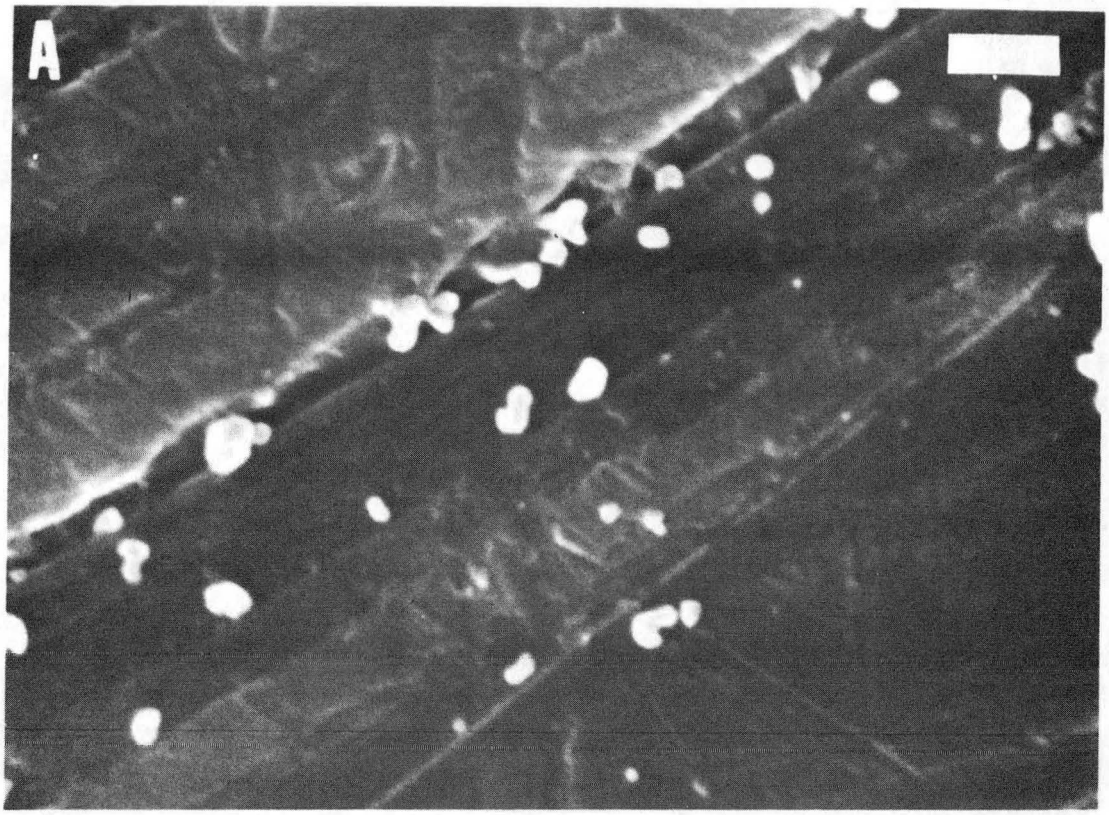

XBB 849-7314

Figure 15a

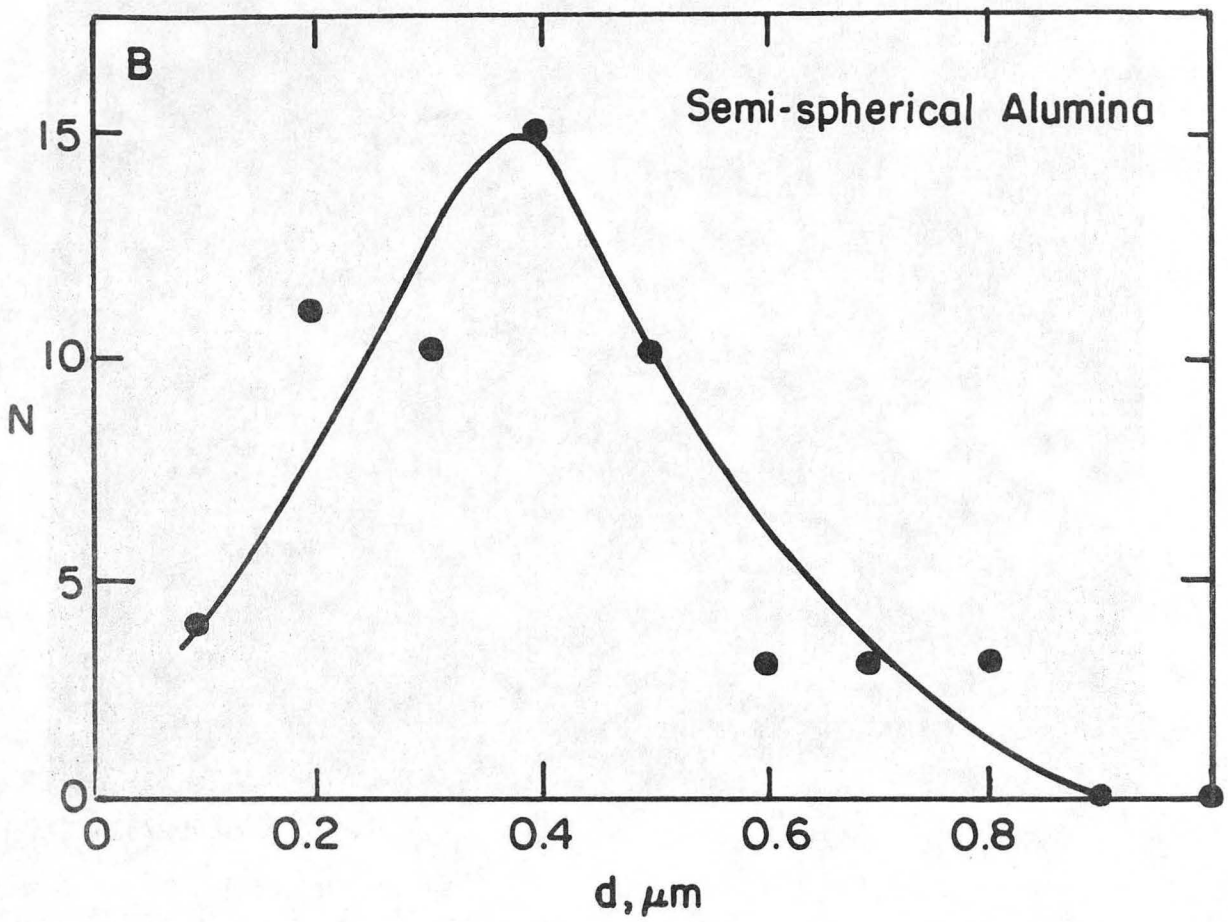

XBL 8410-8205

Figure 15b

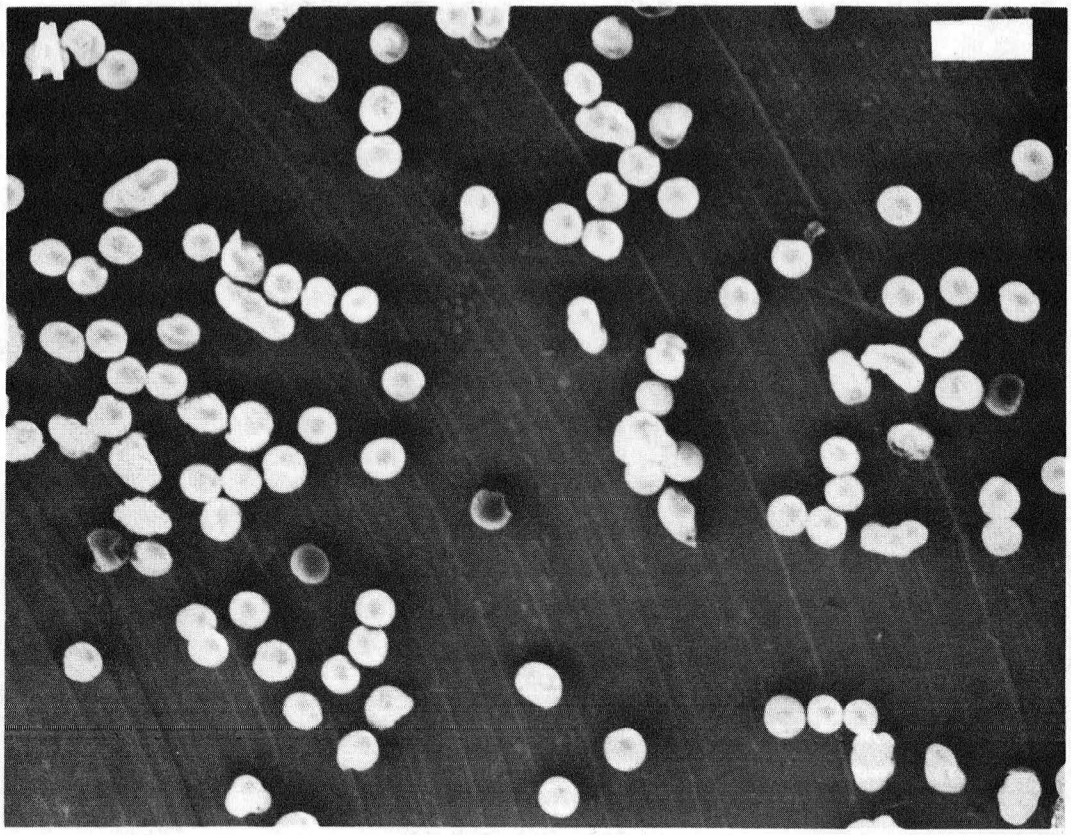

XBB 849-7313

Figure 16a

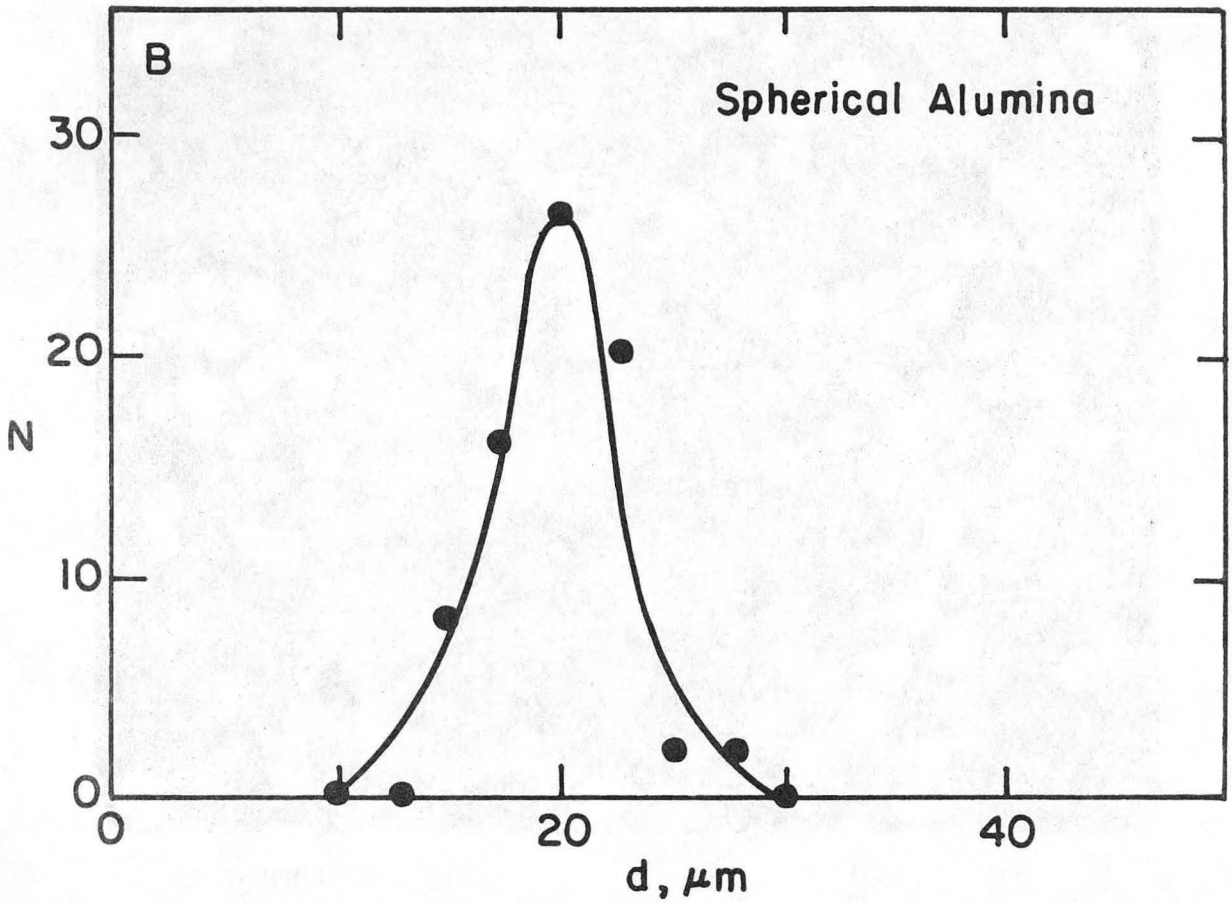

XBL 8410-8206

Figure 16b

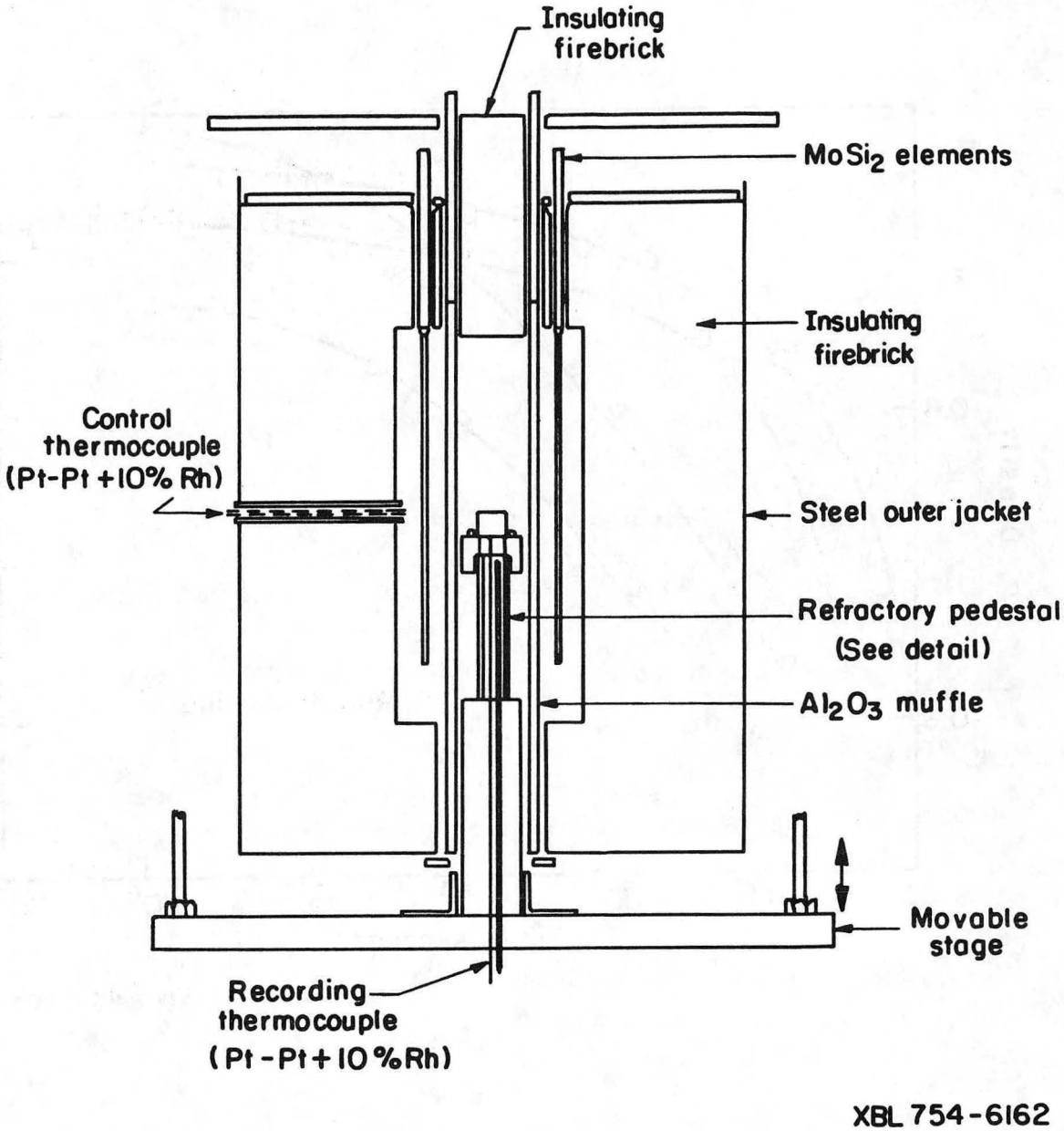
Insulating firebrick
$MoSi_2$ elements
Insulating firebrick
Control thermocouple (Pt-Pt +10% Rh)
Steel outer jacket
Refractory pedestal (See detail)
Al_2O_3 muffle
Movable stage
Recording thermocouple (Pt - Pt + 10 %Rh)
XBL 754-6162

Figure 17

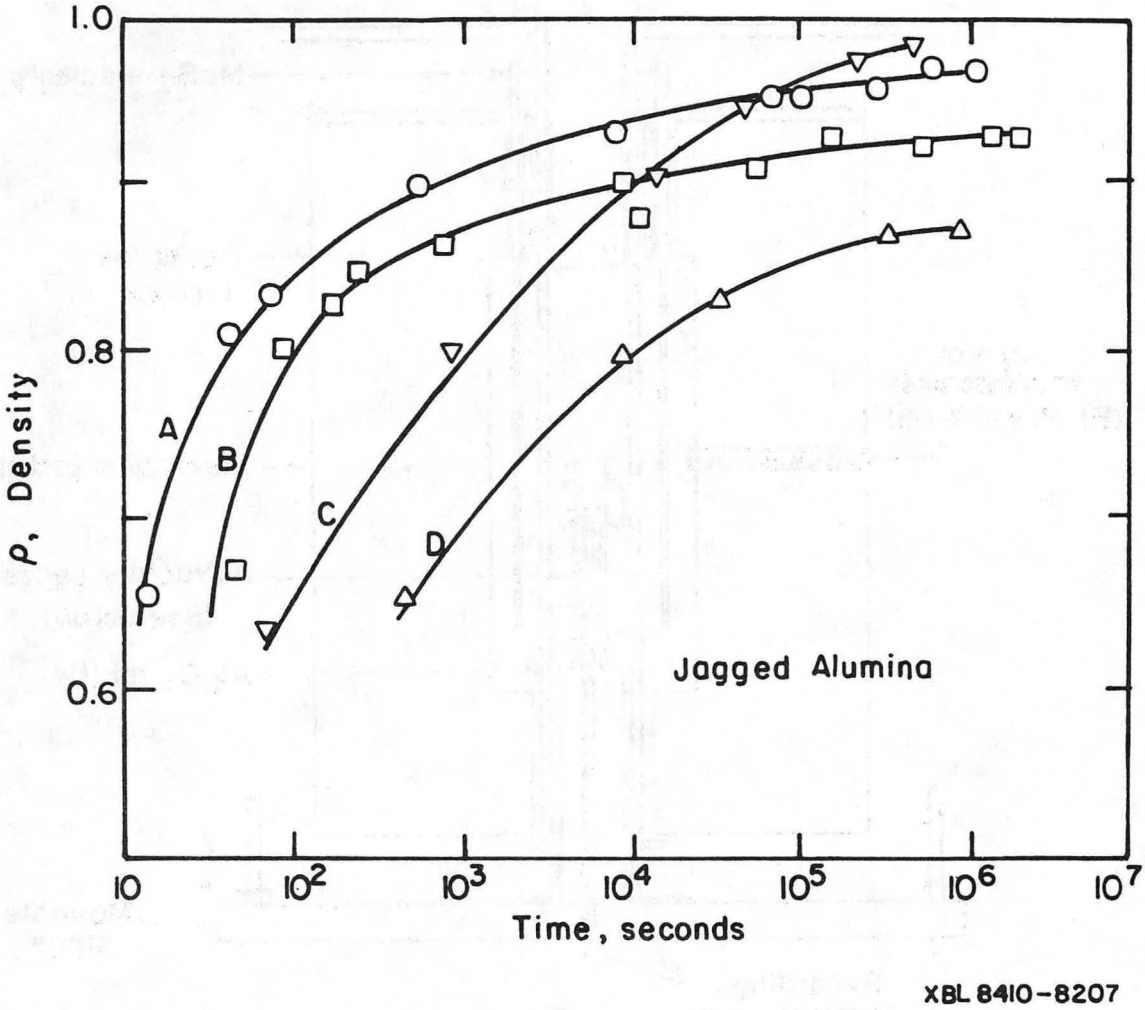
1.0
0.8
0.6
ρ, Density
A
B
C
D
Jagged Alumina
10
10²
10³
10⁴
10⁵
10⁶
10⁷
Time, seconds
XBL 8410-8207

Figure 18

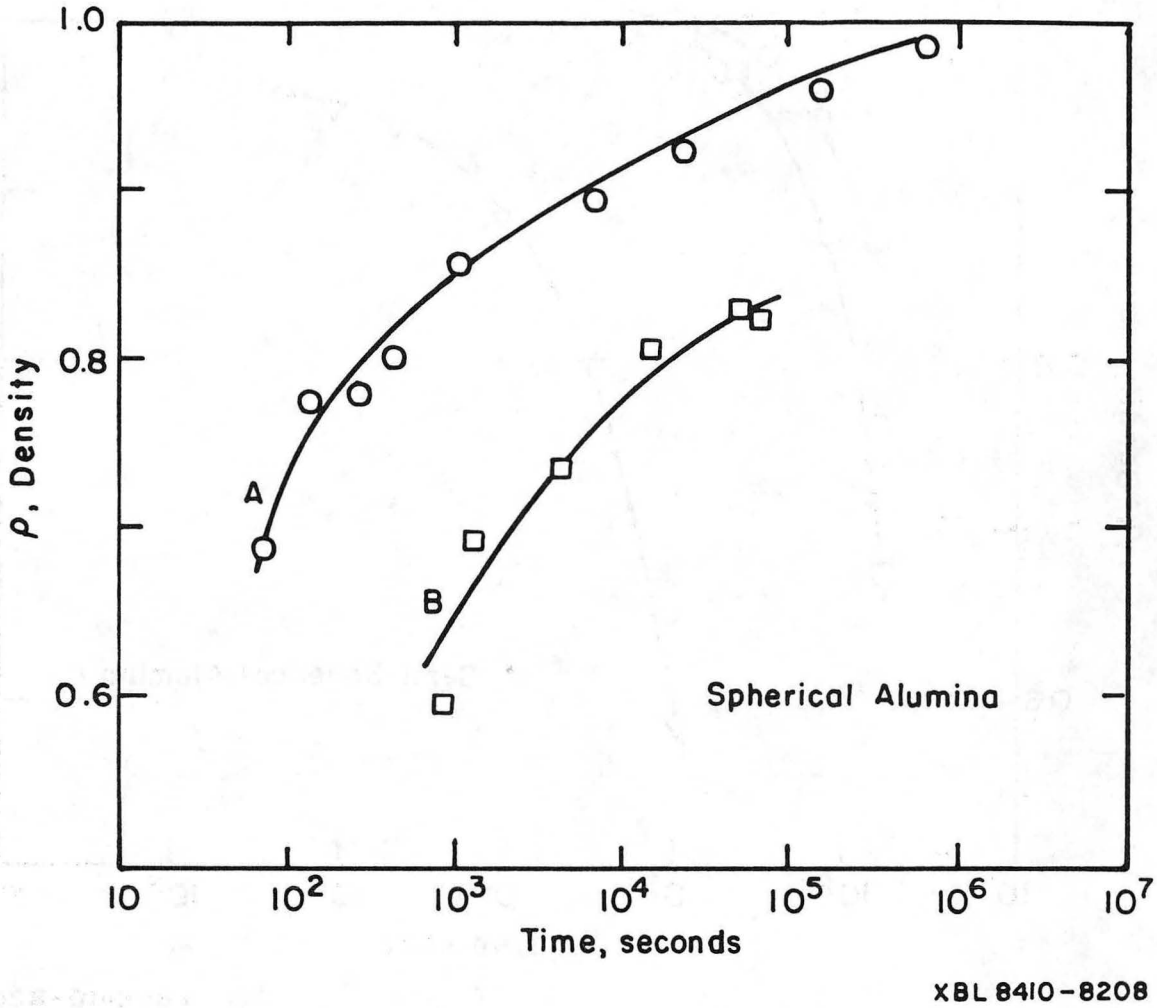
1.0
0.8
0.6
ρ, Density
A
B
Spherical Alumina
10
10^2
10^3
10^4
10^5
10^6
10^7
Time, seconds
XBL 8410-8208

Figure 19

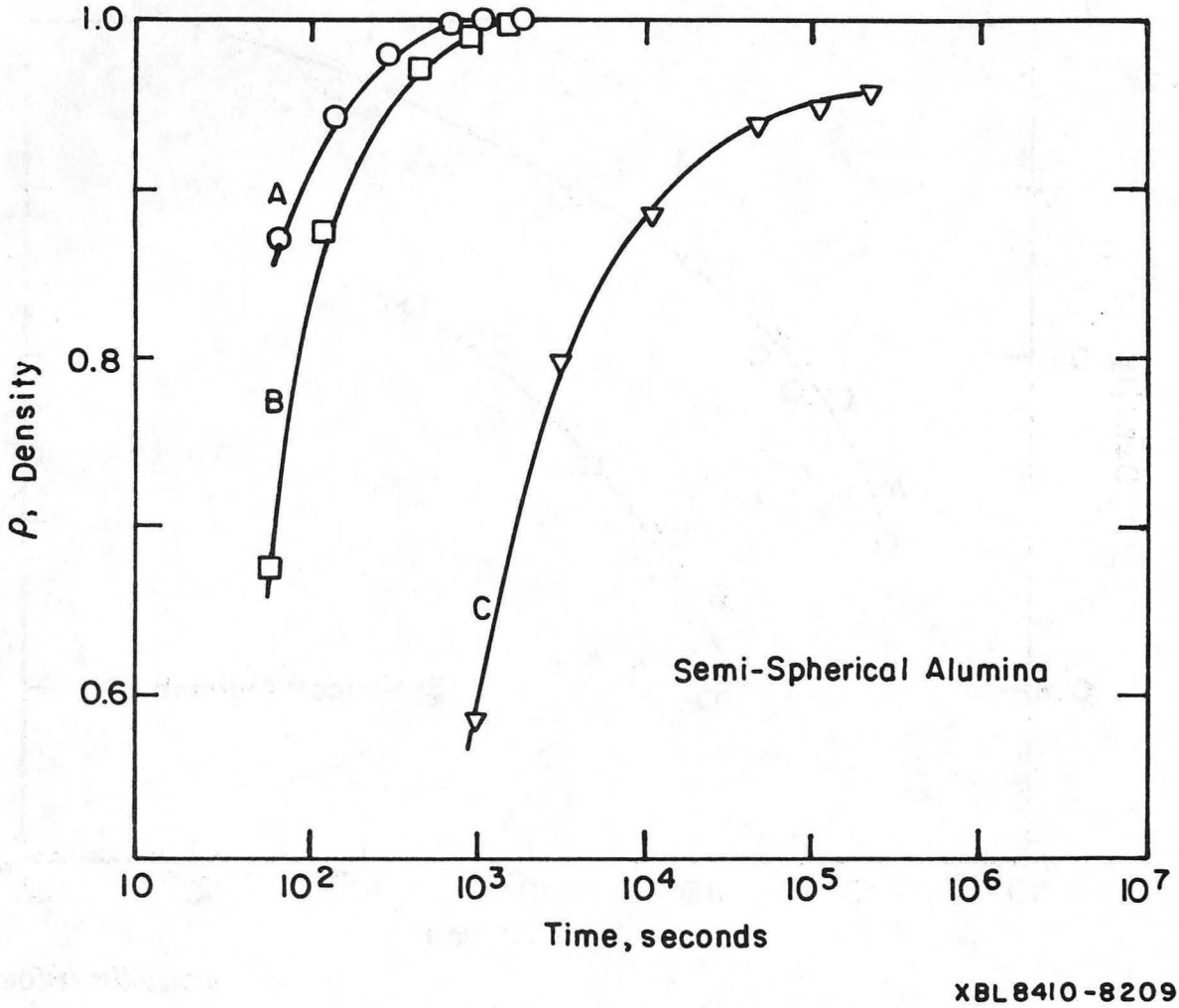
1.0
0.8
0.6
ρ, Density
A
B
C
Semi-Spherical Alumina
10
10²
10³
10⁴
10⁵
10⁶
10⁷
Time, seconds
XBL8410-8209

Figure 20

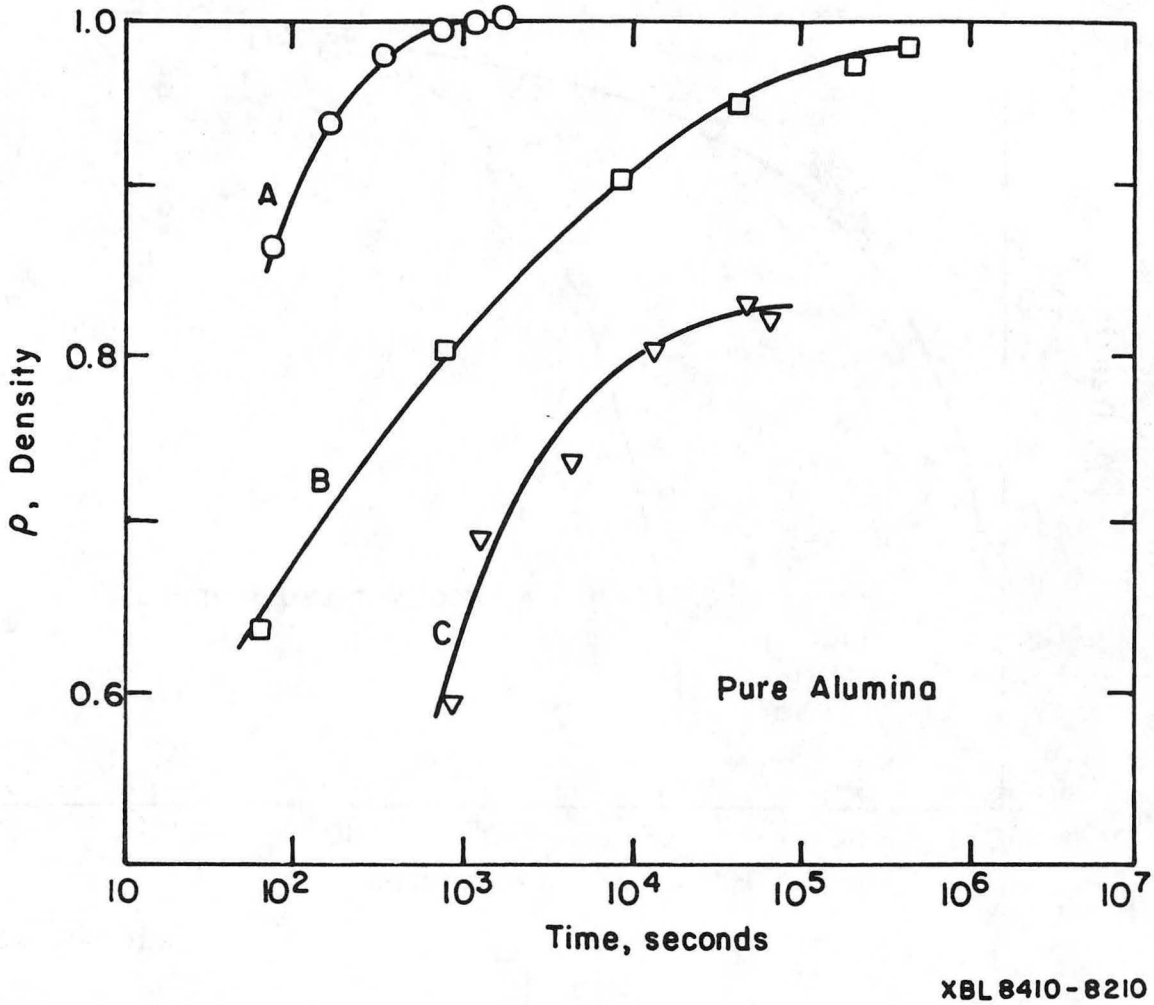
1.0
0.8
0.6
ρ, Density
A
B
C
Pure Alumina
10
10²
10³
10⁴
10⁵
10⁶
10⁷
Time, seconds
XBL 8410-8210

Figure 21

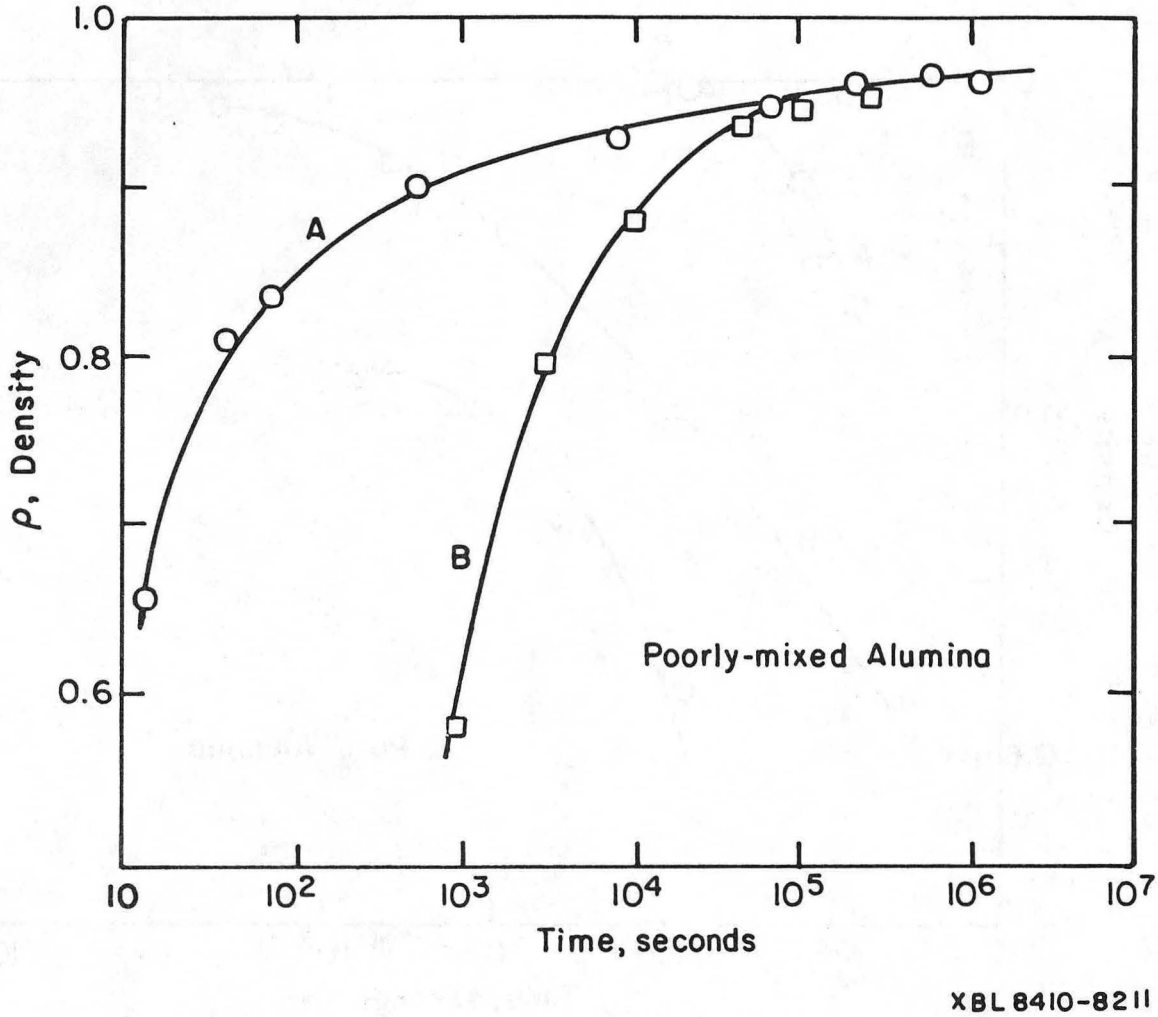
1.0
0.8
0.6
ρ, Density
A
B
Poorly-mixed Alumina
10
10²
10³
10⁴
10⁵
10⁶
10⁷
Time, seconds
XBL 8410-8211

Figure 22

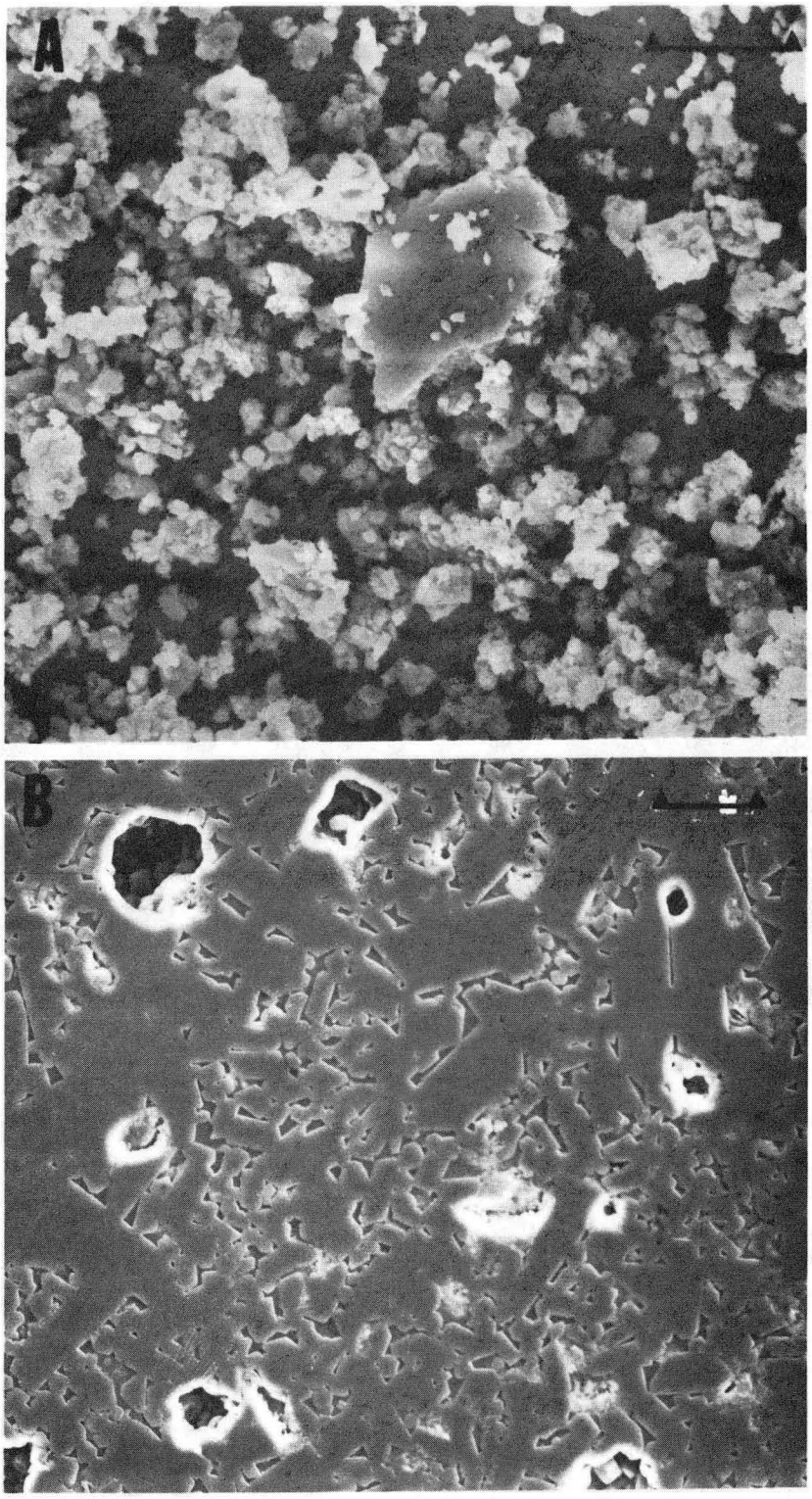

XBB 848-6457

Figure 24

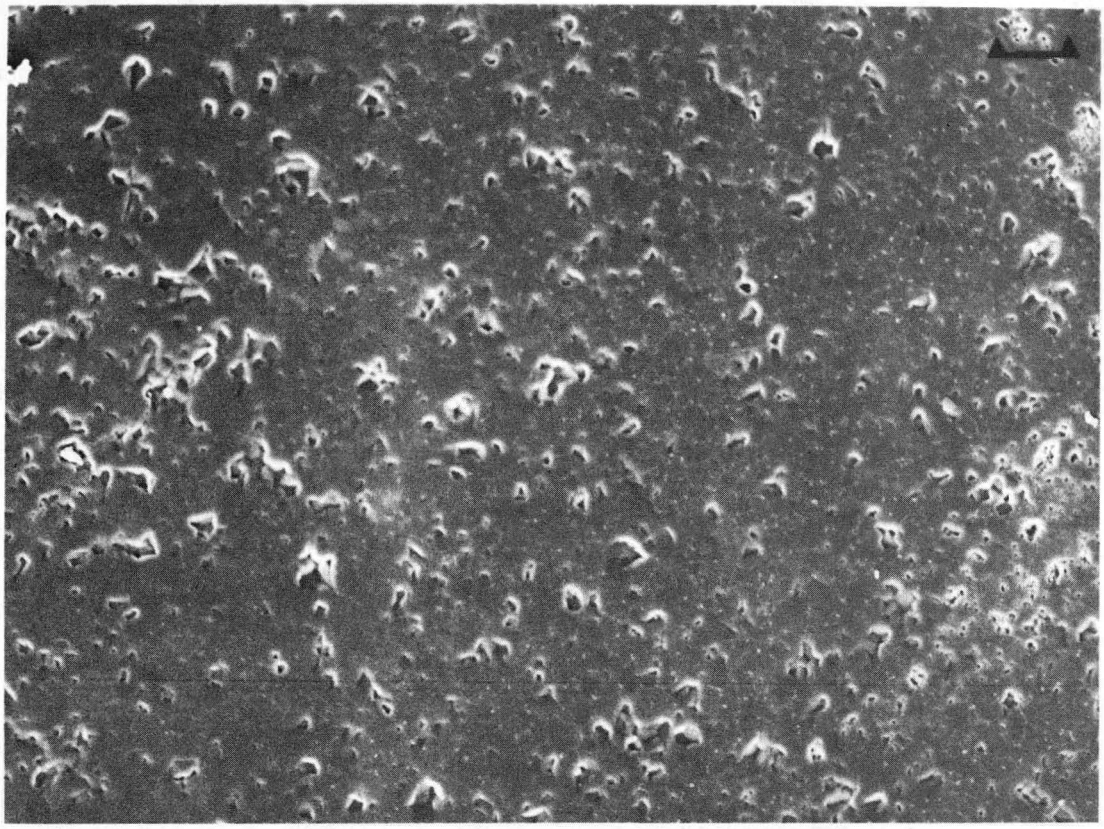

XBB 849-7322

Figure 25

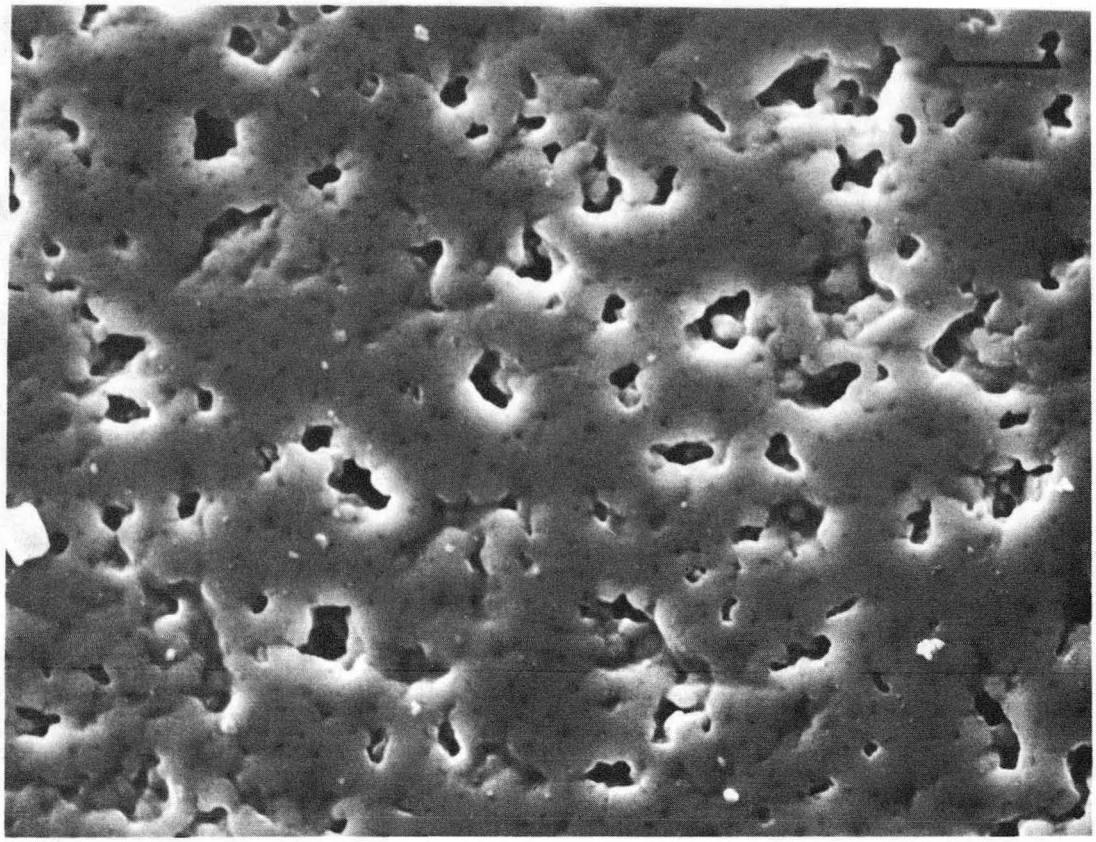

XBB 849-7321

Figure 26

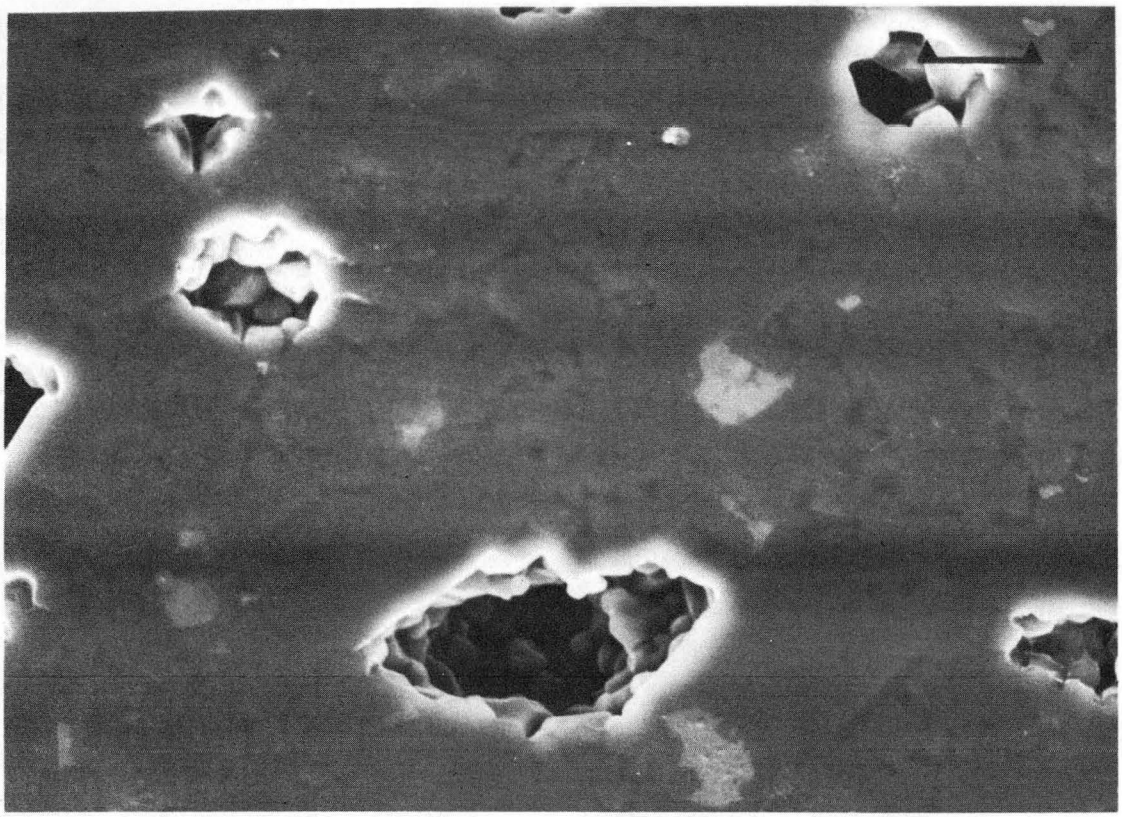

XBB 849-7320

Figure 27

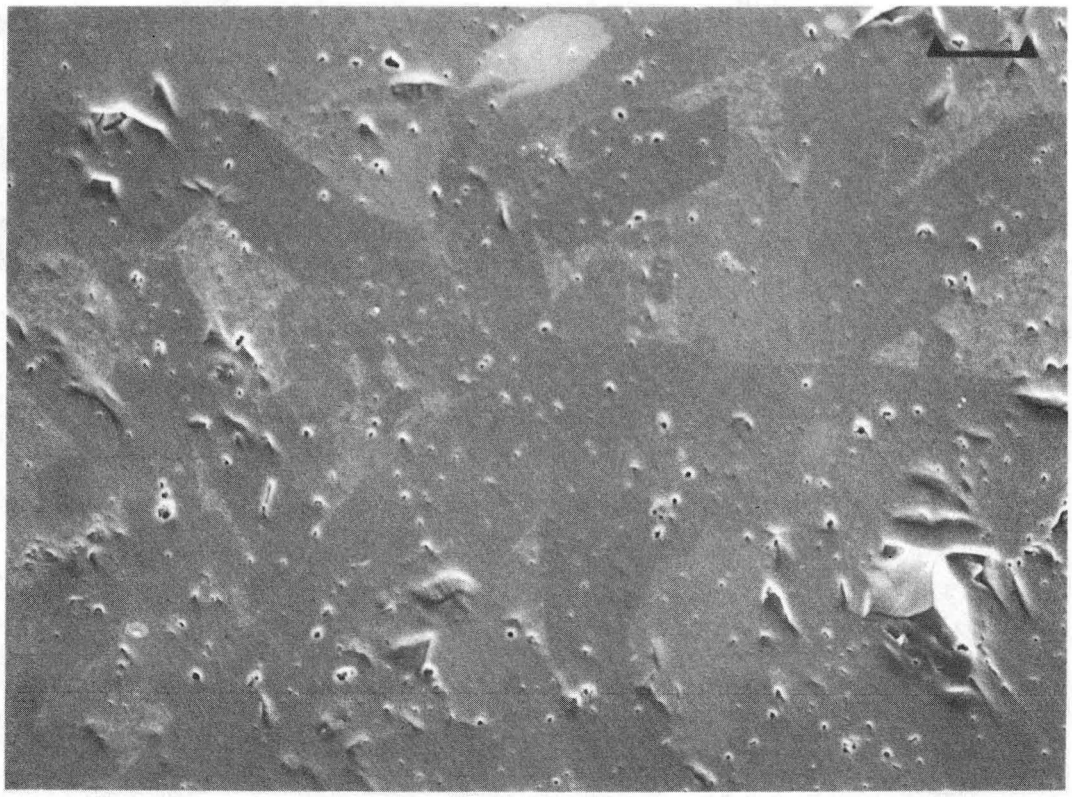

XBB 849-7319

Figure 28

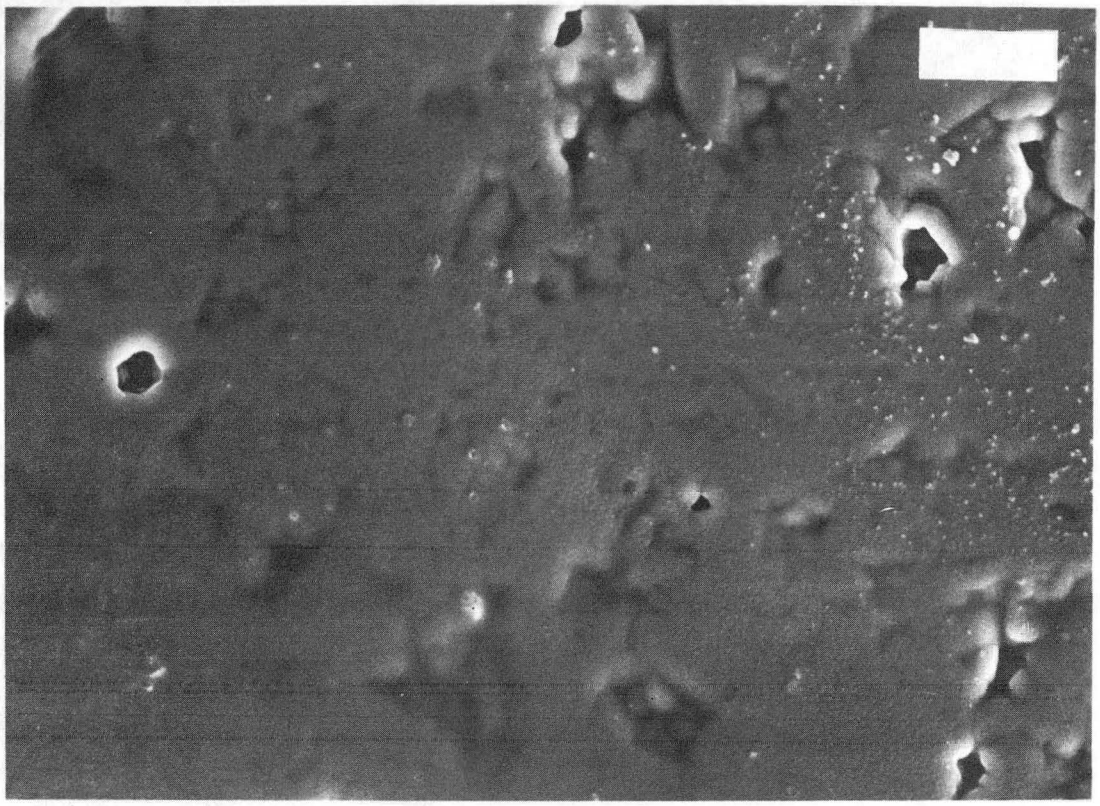

XBB-849-7318

Figure 29

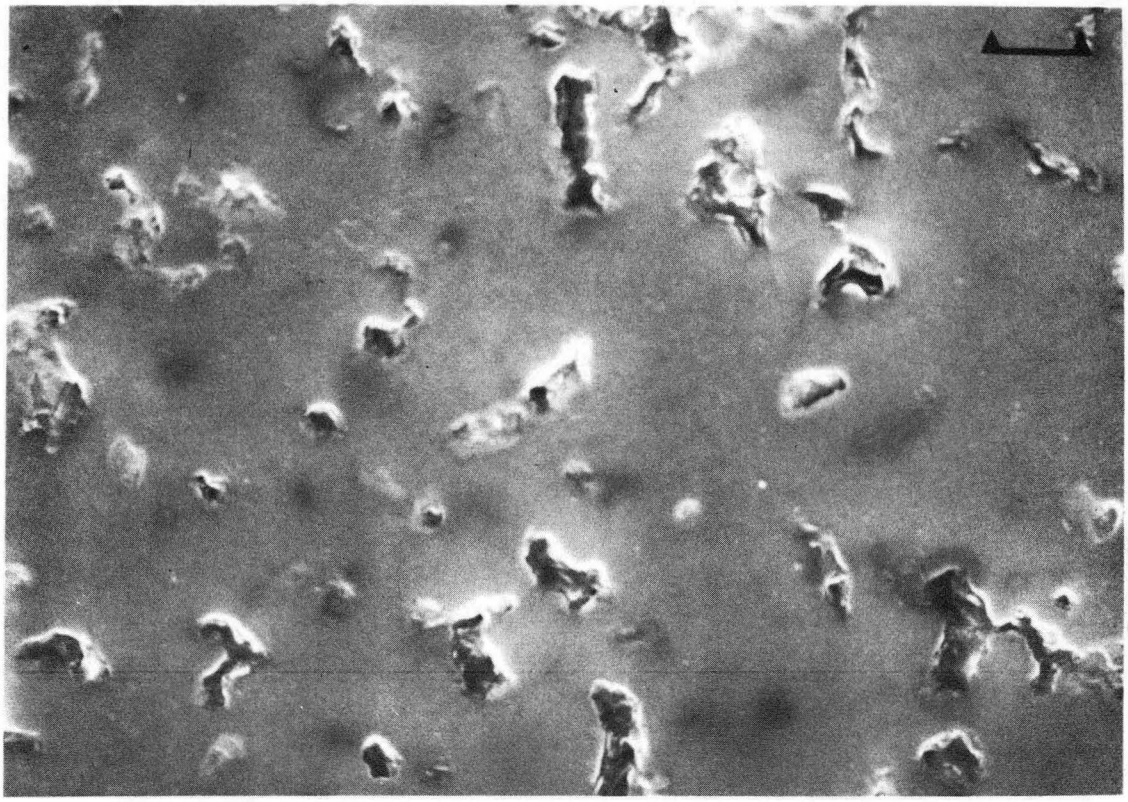

XBB 849-7312

Figure 30

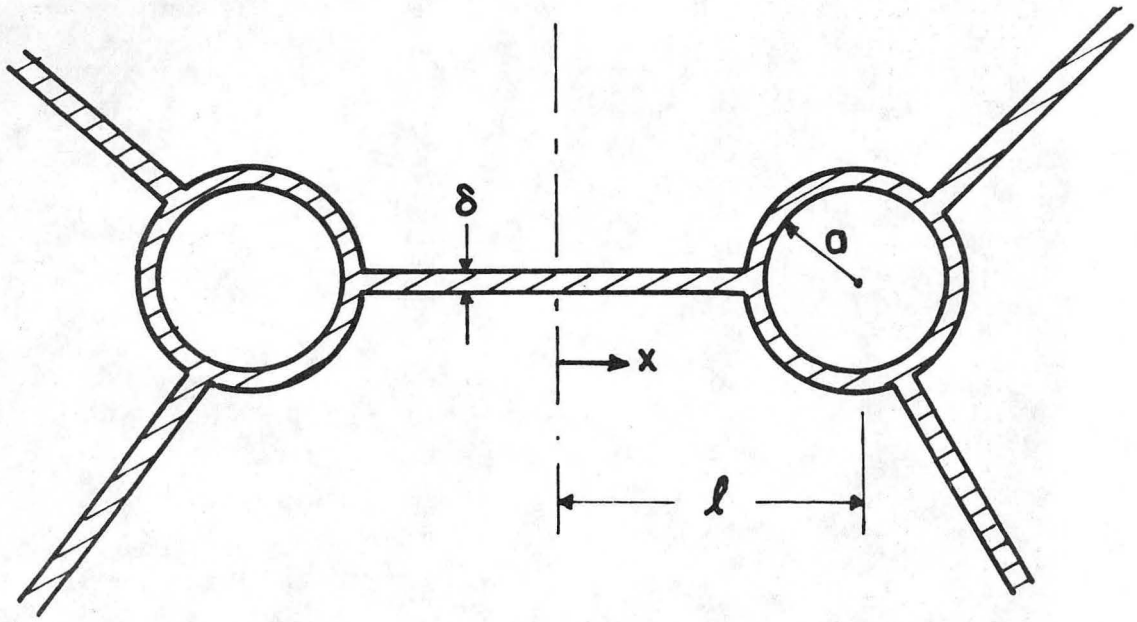

XBL8410-8212

Figure 31

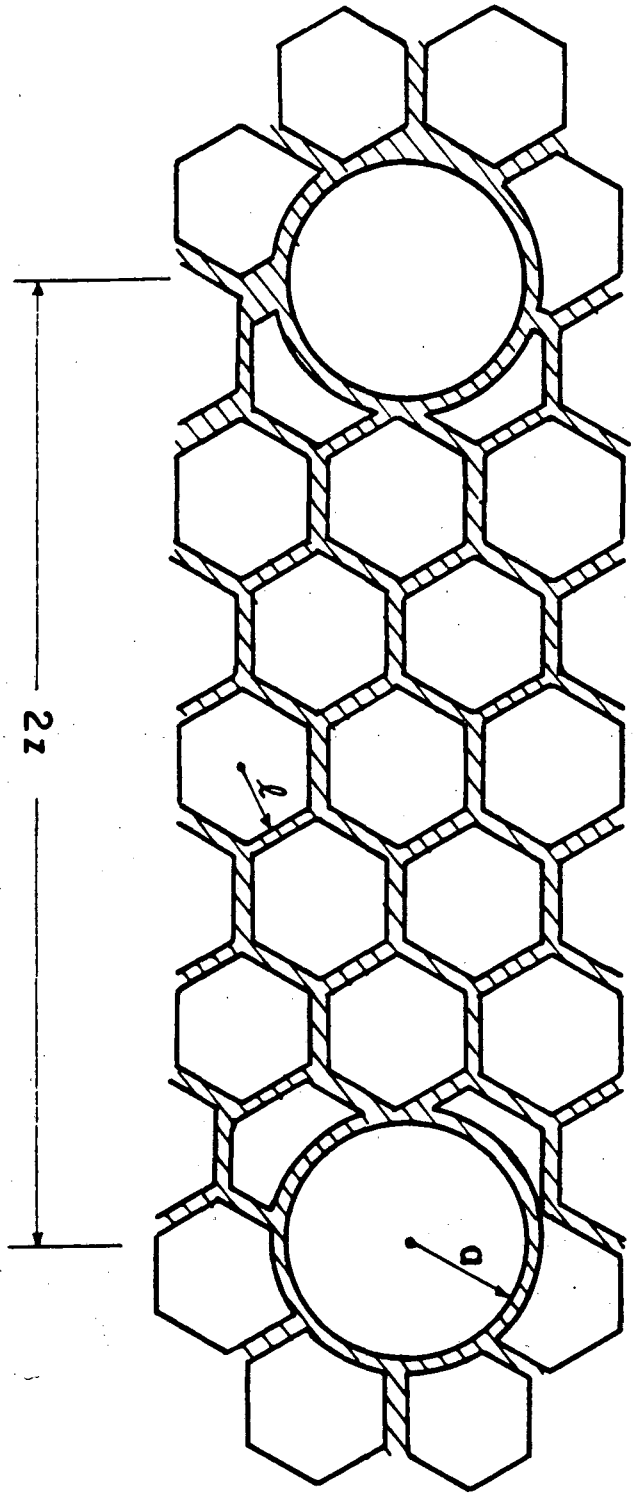

XBL 8410-8213

Figure 32

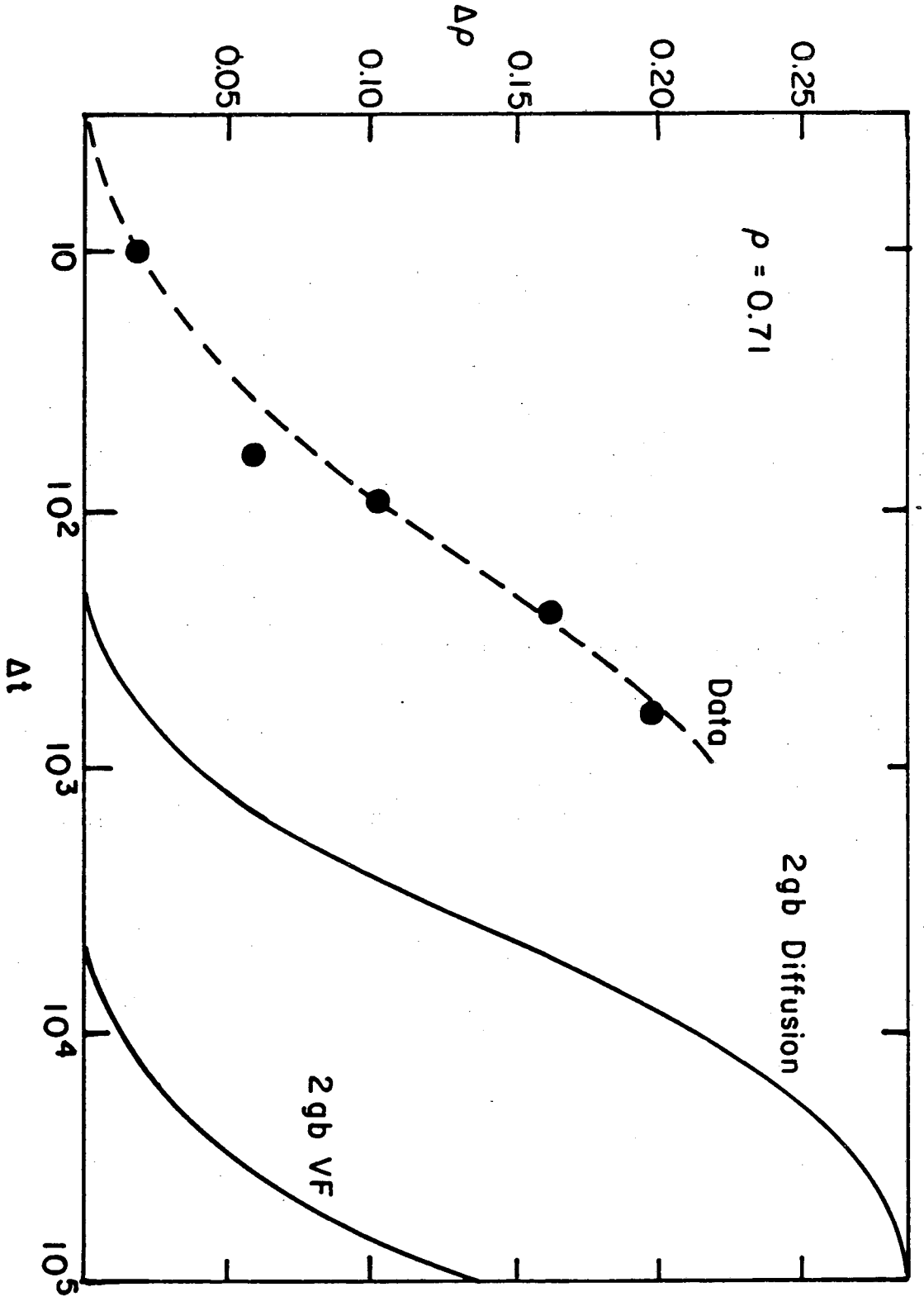

XBL 8410-8214

Figure 33

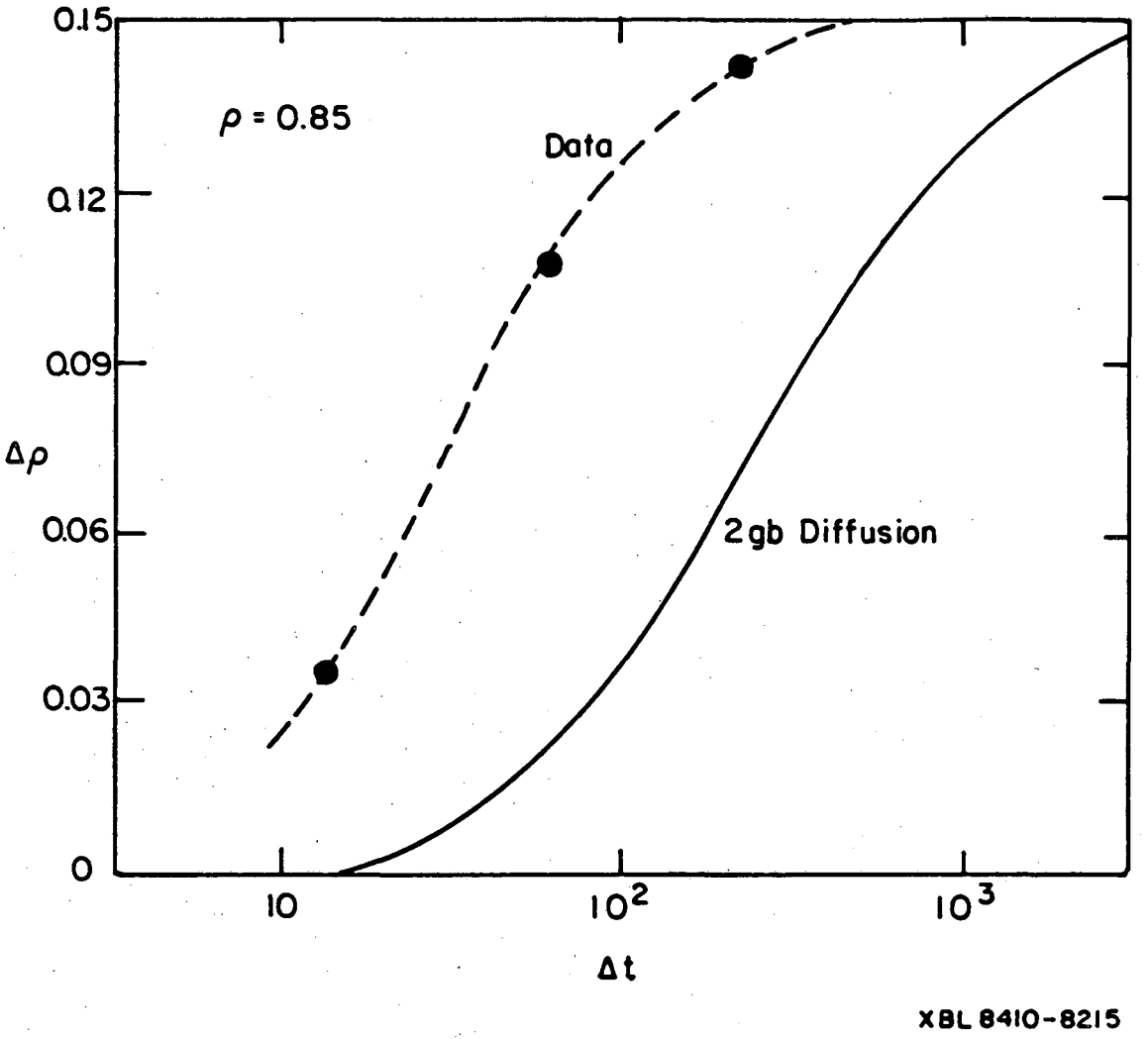
0.15
0.12
0.09
0.06
0.03
0
Δρ
ρ = 0.85
Data
2gb Diffusion
10
10^2
10^3
Δt
XBL 8410-8215

Figure 34

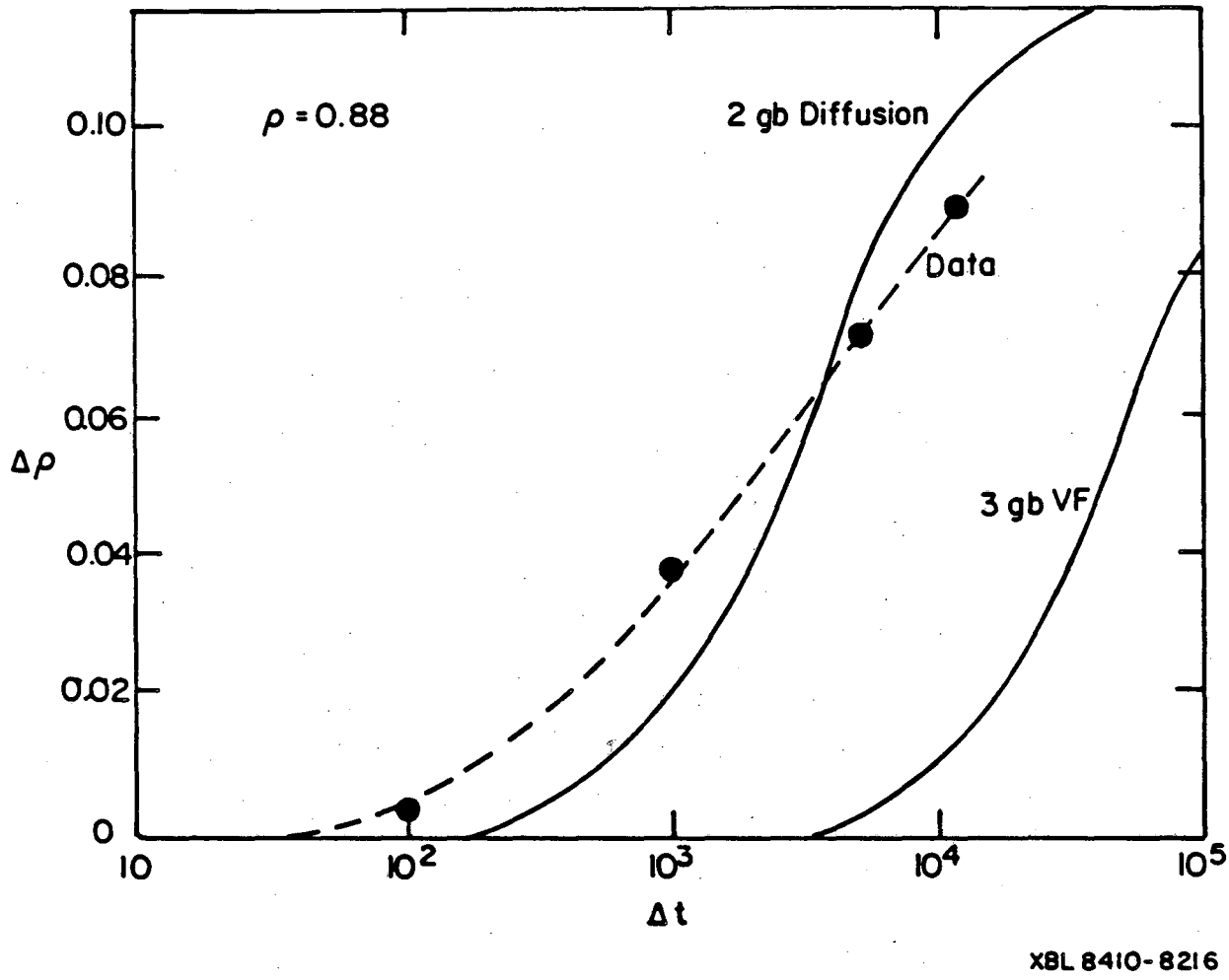
ρ = 0.88
2 gb Diffusion
Data
3 gb VF
0.10
0.08
0.06
0.04
0.02
0
Δρ
10
10²
10³
10⁴
10⁵
Δt
XBL 8410-8216

Figure 35

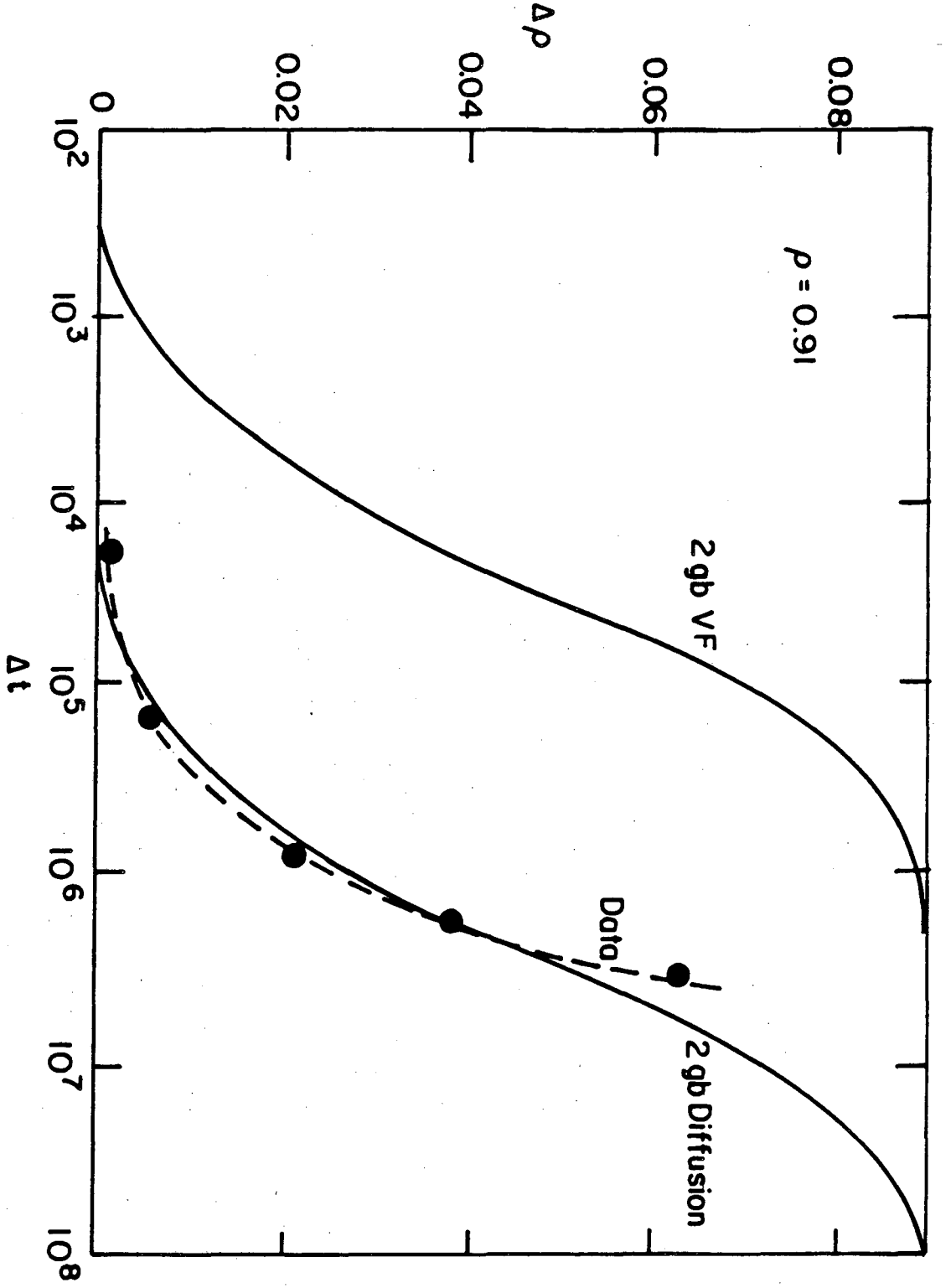

XBL 8410-8217

Figure 36

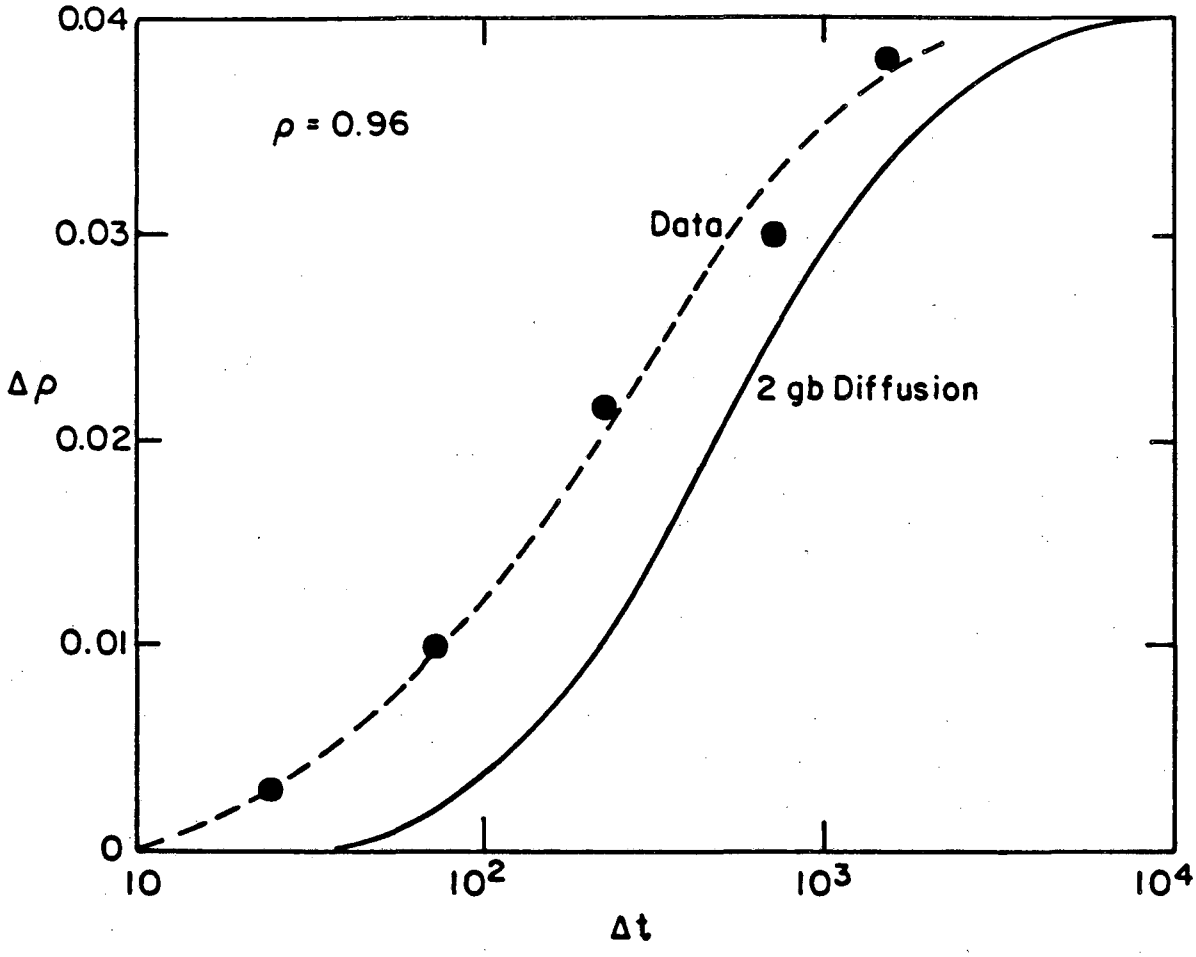

XBL 8410-8219

Figure 37

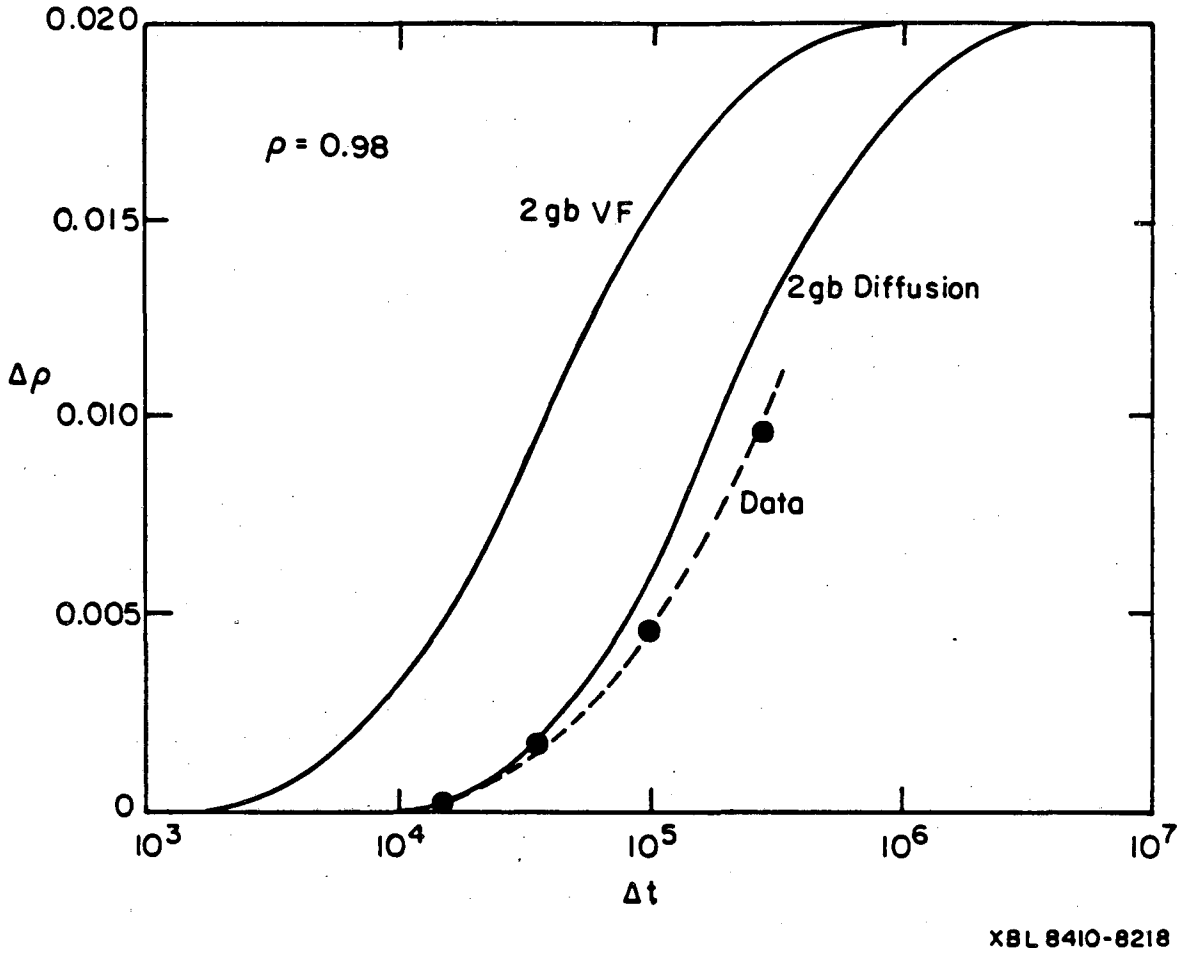
0.020
0.015
0.010
0.005
0
Δρ
ρ = 0.98
2 gb VF
2gb Diffusion
Data
10^3
10^4
10^5
10^6
10^7
Δt
XBL 8410-8218

Figure 37

APPENDIX I

The Capillary Force

Past investigations into liquid-phase sintering have used several different expressions for the interparticle force generated by a penetrating liquid. The exact form of the capillary equation continues to be deliberated, but an instructive and provacative debate on what terms belong in the force equation[1-4] stemmed from a paper by Gillespie and Settineri (1967)[5] claiming that only one or the other of the two usual terms (the hydrostatic stress from the curvature of the liquid, and the surface tension stress) belonged in the capillary force equation because both terms are governed by the liquid vapor interfacial energy and are thus related by Lapaces' equation. The proper expression, and the validity of various approximations, for the force between two spheres that are barely touching, surrounded by a liquid capillary, has been analyzed,[6,7] but since the chemical potential increases to ∞ at the contact point, we prefer to assess the more physically reasonable geometry in which the area of closest sphere approach has already begun to flatten but, as will be shown later, continues to be separated by a thin liquid layer (Fig. 1). For small and moderate amounts of liquid the largest portion of the sintering time is spent in this general configuration.

If a cut is made between the spheres, along a plane perpendicular to the page, the pertinent forces drawing the particles together sum as:

$$\Sigma F = \gamma_{S\ell}(2\pi x) - \Delta P\pi(x^2 - a^2) + \pi a^2 (F_D - F_a). \qquad \text{(A1)}$$

The term $\gamma_{S\ell}(2\pi x)$ is due to the discontinuity in the hydrostatic stress at the liquid meniscus (the surface tension) and acts around the perimeter of the pendular liquid ring. ΔP is the hydrostatic pressure acting across the neck area caused by the liquid curvature, and is given by the Laplace equation

$$\Delta P = \gamma_{S\ell} \left(\frac{1}{x} + \frac{1}{\rho}\right) \tag{A2}$$

where x and ρ are the principle radii of curvature. F_a is the applied force which acts on the flattened area.

The final term, F_D is the force which resists the capillary tension, and any applied compression, F_a. The disjoining force, F_D, is an area integral of the stress over the solid neck, in the absence of liquid. As indicated by observations in Chapters 2 and 3, the capillary tension can be resisted by a thin liquid film along the two grain boundary.

In the absence of an applied force, the net force must equal zero, so

$$\pi a^2 F_D + \gamma_{S\ell}(2\pi x) = \pi\gamma_{S\ell} (x^2 - a^2) \left(\frac{1}{\rho} + \frac{1}{x}\right) . \tag{A3}$$

Heady and Cahn[7] found that, although ρ and x are strictly variables, the error is small in assuming that the minor principal radius is a constant (the circle approximation) for practical amounts of liquid. Hence that approximation is adopted here.

APPENDIX II

Densification by Solution/Reprecipitation

Expressions are given for the total sintering rate, in which both the interface reaction and diffusion are simultaneously considered. The analysis begins with a formulation of the expression for the flux of atoms from the solid grains through a fluid film of thickness δ, having a unit depth. The volume of dissolved solid species entering and leaving a segment of dimension $\delta\Delta x$ during time Δt are

$$V_{in} = j\Omega\delta\Delta t + 2\dot{y}\Delta t\Delta x - \dot{c}\delta\Delta x\Delta t = \tag{A4a}$$

$$V_{out} = (j + \Delta j)\ \Omega\delta\Delta t \tag{A4b}$$

where j is the atom flux, Ω is the atom volume, $\dot{y}$ is the rate of grain center approach, which is related to the overall densification rate, and c is the rate of change in the concentration of atoms from the solid in the liquid at a point distance x from the midpoint of the grain channel.

Volume conservation of atoms from the solid species gives

$$\frac{dj}{dx} = \frac{2\dot{y}}{\delta} - \dot{c} \tag{A5}$$

The chemical potential of atoms from the solid that are now dissolved in the liquid (influenced not only by the concentration within the liquid but also by the state of stress in the liquid) is

$$\mu = \mu_0 - \sigma\Omega + kT\,\ell n(c/c_0) \tag{A6}$$

Differentiation gives the gradient in the chemical potential of atoms within the liquid phase along the grain boundary channel as

$$\frac{d\mu}{dx} = -\Omega\frac{d\sigma}{dx} + \frac{kT}{c}\left(\frac{dc}{dx}\right) \tag{A7}$$

The dissolution rate of solid atoms into the liquid which is now assumed to be a first order reaction (i.e., the rate depends linearly on the difference between the equilibrium and the actual concentration of solid atoms in the liquid) is

$$\dot{y} = k_\ell(c_0 - c)\exp(-\Delta G/kT)\exp\left(\frac{-\sigma\Delta V}{kT}\right) \tag{A8}$$

where c_0 is the equilibrium concentration, k_ℓ is the jump rate constant, ΔV is the activation volume and the other terms have their usual meaning.

For the common case where the activation volume is small [$\Delta V \ll (kT/\sigma)$], Eq. (A8) becomes

$$\dot{y} = \xi(c_0 - c) \tag{A9}$$

where the constant $\xi \equiv k_\ell \exp(-\Delta G/kT)$. We further assume that the grain center approach rate, $\dot{y}$, is independent of position along the grain boundary so that elastic stresses do not develop. Then, by Eq. (A9), the concentration difference must also be position independent. In

such cases, the chemical potential gradient simplifies to

$$\frac{du}{dx} = \frac{-\Omega d\sigma}{dx} \tag{A10}$$

and the grain center approach rate is

$$\frac{d\dot{y}}{dt} = -\xi\frac{dc}{dt} \tag{A11}$$

The expression governing the grain center approach rate is found by combining the standard expression for diffusive flux of solid atoms through a liquid

$$J = \frac{Dc\delta}{kT\Omega}\left(\frac{du}{dx}\right) \tag{A12}$$

with Eqs. (A4), (A10) and (A11) to give

$$\frac{-Dc\delta\Omega}{kT}\left(\frac{d^2\sigma}{dx^2}\right) = \frac{2}{\delta}\frac{dy}{dt} + \frac{1}{\xi}\left(\frac{d^2y}{dt^2}\right) \tag{A13}$$

where D is the diffusivity of the solid through the liquid.

The boundary conditions required to integrate this expression are $d\sigma/dr = 0$ at $r = 0$, $\sigma = \gamma(\frac{1}{\rho} + \frac{1}{a})$ at $r = a$ and $\langle\sigma\rangle = 0$, as required for pressureless sintering.

Integration of Eq. (A13) with $\dot{y}$ independent of x gives

$$\frac{3\gamma D\Omega\delta}{kT}\left(\frac{1}{\rho}\right) = 2\frac{dy}{dt} + \frac{\delta}{\xi}\left(\frac{d^2y}{dt^2}\right) \tag{A14}$$

For sintering, geometry dictates that

$$y \approx a^2/2R \tag{A15}$$

where R is the radius of the solid sphere and hence

$$\frac{\alpha}{y} = 2\dot{y} + \frac{\delta}{\xi}\ddot{y} \tag{A16}$$

where

$$\alpha \equiv \frac{3\gamma DC\ \delta}{2R\ kT}\ \left(\frac{1}{\rho}\right)$$

For specific values of these variables, Eq. (A16) can be evaluated numerically.

APPENDIX III

Thermodynamical Stability of the Intergranular Phase Under a Stress

The purpose of this appendix is to estimate the stress that would be required to force an energetically favored penetrating liquid phase out from between solid grains to form a solid/solid contact.

At some thickness, δ, the solid grains are separated by an amorphous liquid and the boundary energy is given by $2\gamma_{S\ell}$. A stress, σ, is then assumed to be applied normal to the boundary displacing the grains so that the liquid is squeezed out from between the grains giving a dry contact whose energy is then γ_{SS} (Fig. 2). The stress, σ, required to form the dry contact is given by

$$\sigma = \frac{\Delta\gamma}{\Delta t} = \frac{\gamma_{SS} - 2\gamma_{S\ell}}{\delta} \tag{A17}$$

where δ is the observed equilibrium film thickness. Evaluation of the equation for the system studied here (alumina/anorthite; $\gamma_{SS} = 1.5 J/m^2$, $\gamma_{S\ell} = 0.5 J/m^3$, $\delta = 1nm$) gives the stress required to form a solid contact as 500 MPa.

APPENDIX IV

Liquid Phase Sintering: Related Phenomena

A number of considerations related to the microstructual development during sintering in the presence of a liquid phase are considered in this appendix.

A. Sintering of Jagged Particles: The Origin of Low Angle Grain Boundaries

Sintering models based on a two sphere geometry are seductive because the expressions are manageable and are physically and intuitively comprehensible. For the ceramic compacts of technological interest, which are typically composed of jagged and irregular shaped particles (Fig. 3) many of the trends expected from two sphere expressions are observed. However, in many cases behavior predictions for compacts of jagged particles based on two sphere models are fallacious.

In the analysis of jagged particle interactions, if only individual contacts are assessed, the particles would always eventually become face on face, because all other geometries are unstable. For compacts, each particle/particle interaction is not independent and movements caused by the capillary forces on a given particle are subject to the constraint of the surrounding area. In order for rearrangement to to occur, the sum of the forces (from each of a particles contact points) has to be eccentric. If a particle rearranges at all it will be to maximize the number of face to face contacts. However, in model random packings in which the particles are represented by regular polyhedron that have a distribution in the number of faces per particle, the

number fraction of face on face contacts that are possible is less than both the number fraction of corner on face and edge on face contacts, in general accordance with observations.

During early stages of liquid phase sintering there is a tendency for edge on face, and for corner on face contacts, by far the most common geometry in compacts of jagged particles, to rotate in the presence of the liquid so that faces tough. As pointed out by Cahn and Heady[7] the capillary force exerted by a liquid between two spheres will be purely a normal force, but for angular particles, the center of gravity of the interparticle force will not normally lie along the point (or line) of contact. This gives rise to a torque that tends to rotate the particles toward face to face geometries. Since the capillary force is not perpendicular to the contact area, a shear force also arises. Both the normal force and torque terms for corners on faces increases rapidly as liquid enters the boundary, and both shear and torques cause faces to move closer.

Originally a wetting liquid penetrates the contact area if $\gamma_{SS} > 2\gamma_{S\ell}$, but after rotation to face on face, the boundary will often be a low energy boundary and it may be energetically unfavorable for the liquid to remain (Fig. 4). This may account for the relatively large number of low angle grain boundaries observed in which liquid is excluded.

Several other observations are pertinent to this discussion. Qualitatively the propensity for low angle boundaries is higher in the poorly mixed compacts in which far more grain growth has occurred and

the unpenetrated special boundaries are shorter in length than the penetrated high angle grain boundaries in both poorly mixed and well mixed systems. These observations are rationalized in terms of grain boundary mobilities. The mobility of the special boundaries are expected to be much lower than grain boundaries of other orientations so that during grain growth the fraction of low angle grain boundaries will increase as a relatively greater proportion of the high angle grain boundaries are eliminated. Further, the length of the special boundaries will remain short compared to the other boundaries that surround the large grains.

In hot pressing, grain growth often occurs preferentially in a specific orientation to the applied stress. Thus, if large amounts of grain growth are allowed, the probability will increase that grains having similar orientations will end up meeting.

In materials that undergo a phase change during sintering, the number of special boundaries could be higher. For example, during the processing of silicon nitride, the common product containing primarily the β polymorph is manufactured by hot pressing α-Si_3N_4 starting powders in the presence of an oxide fluxing agent. β needles form by solution/reprecipitation and grow preferentially along their c-axis oriented perpendicular to the hot pressing maximum stress axis. As a consequence of this texture, a substantial number of nearly parallel c-axis needles are observed having unpenetrated low angle and coincident-axial-direction grain boundaries, the number being far in

excess of that expected for a polycrystal with randomly oriented grains.*

In materials that exhibit appreciable surface tension anisotropy, there is a tendency during power preparation by comminution to fracture and wear preferentially on certain planes, and not on others. Particles in fine powders of such materials are usually jagged.** When these materials are packed, a moderate number of face on face contacts will develop that have identical, or nearly identical, crystallographic orientation along their boundaries. This creates a set of special boundaries that are of sufficiently low energy that often

$$\gamma_{ss} < 2\gamma_{s\ell} \tag{A18}$$

and hence the liquid will be excluded from these boundaries (Fig. 4). A note on microscopy is pertinent because few of these boundaries have been reported. In a purely random packing where all intercrystal orientations are equally probable, the likelyhood of bordering grain faces being oriented within 1° is less than 10^{-2}. Hence, in order to find a special small angle boundary (misorientation less than 1°) in a randomly oriented solid, one would need to examine over 100

---

*This suggests a method for making glass-free silicon nitride similar to zone refining. A hot zone would be moved along perpendicular to the axial hot pressing direction, transforming random α particles into parallel β needles between which the misorientation is so low that the glassy film is excluded.

**A jagged particle is assumed here to consist of faces, edges and corners.

boundaries. Even though boundaries are not particularly common, they certainly are not a rarity.*

B. Density Relations During Particle Rearrangement

In the presence of a liquid phase the first stage in the sintering process in many ceramic systems begins with the softening of the liquid phase from a solid-like particle to a viscous liquid. Once the liquid phase enters the contact area, a number of important geometrical considerations are pertinent. Shaw[8] has examined the redistribution of liquid during liquid-phase sintering and has shown that for small amounts of a penetrating liquid, the equilibrium configuration will be for the liquid to occupy isolated capillaries separating every solid particle. When the liquid is inhomogeneously distributed, as is the case when it is included in the starting power as discrete solidified particles, there is always a driving force to redistribute the liquid heterogeneously into the contact areas. When the liquid begins to flow into the grain boundaries and the intersticies between solid particles, a very rapid initial increase in density results.

---

* It is unfortunate that no reasonable estimate of how common these boundaries are, could be established, within the confines of justifiable microscope usuage, although certainly the number fraction lies within the range $2x10^{-1}$ to $5x10^{-3}$. In the course of this work, perhaps 10^3 boundaries have been casually observed, and roughly fifty of these special boundaries have been noted, yet no other CSL boundaries have been observed despite an equal probability (in a random packing) of seeing a CSL boundary as of seeing any other particular misorientation. While there exist several possible explanations for this, it is believed that the very low angle boundaries are simply far more common.

Before sintering, the liquid often participates in the compact as solid particles (Fig. 5). The fraction of theoretical density (ρ_f) is then given by

$$\rho_f = \frac{V_s + V_\ell}{V_s + V_\ell + V_v} \quad . \tag{A19}$$

For a system with 10% liquid by weight, a pressed compact might have $V_s = 0.585$, $V_\ell = 0.075$ and $V_v = 0.35$, in which case the theoretical density would change from 65% to about 76% on melting of the liquid, provided that the solid grains then occupy the holes left by the liquid particles in the same packing density as before the liquid melted.*

C. Initial Stage Sintering Rate Equations

Although the portion of the total sintering time expended in the initial stage is generally short compared with the time spent in the other stages, the rate can be estimated by calculating the time taken for the liquid to flow into the capillaries. The equation for the velocity of a fluid with viscosity, η, moving along a capillary with effective radius r is given by Darcy's Law[9]

$$V = \frac{dx}{dt} = K \frac{\Delta P \bar{r}^2}{\eta \ell} \tag{A20}$$

where ΔP is the change in pressure across the meniscus and x is the distance travelled along the capillary, ℓ is the length and K accounts

*This might be the case in mixtures where the size of the solidified liquid particles was slightly smaller or about the same size as the solid particles ($0.2D_{solid} < D_{liquid} < D_{solid}$).

for the tortuousity of the path followed by the flowing liquid. If the dependence of r on x is known, the equation can be integrated to give this portion of the initial stage sintering time. For the case of present interest, (liquid-phase sintering of alumina particles with a silicate glass), the most common geometry in a well-mixed starting powder is the corner of one alumina particle bordering the face of a second alumina particle, with a neighboring glass particle (Fig. 9). Then $r = (\ell - x)\sin\alpha/2$ and $\Delta P \sim 2\gamma/(\ell - x)\sin\alpha/2$ where $\gamma = \gamma_{SV} - \gamma_{S\ell}$. With boundary conditions $x = 0$ at $t = 0$, Darcy's law integrates to

$$t = \frac{\eta x}{K\Delta P \sin(\frac{\alpha}{2})(\ell - x)} \tag{A21}$$

A singularity arises when $x \rightarrow \ell$, hence the model predicts that infinite time is required for the liquid to penetrate materials in which a solid-solid contact is present. Calculations (Appendix III) show that for a variety of common LPS systems the liquid phase energetically prefers to occupy the grain boundaries, and that a substantial increase in the free energy of the system is required to create solid contacts between the grains. Similarly, in experiments preformed here (Appendix VI) and elsewhere,[10] materials that are initially free of a glassy grain boundary phase develop a continous integranular phase when placed in contact with a penetrating liquid. To reconcile the singularity in the kinetic expression for the penetration time with experimental observations it is surmised that the liquid separates the solid boundary by reasonably rapid thermally activated atom exchange in order to achieve the energetically favored penetration within a finite time.

APPENDIX V

Wetting and Penetration

Several experiments are presented in this appendix which explore the conditions under which penetration of a liquid phase into solid grain boundaries occurs. Corallary observations of the wetting angle of glass on alumina are used to estimate the possible range in the solid/liquid interfacial energy.

a. Penetration

A sample of fully dense pure alumina (the pure semi-spherical compact) was examined by high resolution electron microscopy and found to be free of a continous grain boundary phase (Appendix VI). To assess the penetration behavior of a glass phase into this alumina alloy, a small amount of anorthite was placed on the surface of this material and the sample was heated to above the eutectic temperature for one hour. The surface appearance and cross-section (Fig. 7) indicate that the glass had obviously penetrated into the sample. Transmission electron micrographs confirm that the glass phase now separates the two grain boundaries and exists along three grain channels (Fig. 8).

b. Two-sphere Sintering: Penetration Behavior

Sintering of two 120μm diameter sapphire* spheres in the presence of a small amount of anorthite glass was attempted. Furnace

---

*The sapphire spheres are alumina doped with a small amount of Cr_2O_3 in order to give them a slight pink color so that they are more readily visible. The chromium impurity is expected to have a negligible effect on the results presented here.

availability restricted the maximum temperature to 1600°C. Thus within the experimental time frame (one week) only slight densification had occurred. This is not particularly surprising, because the kinetics are inversely related to the cube of the diameter. Still the experiment yielded useful results because the contact angle, θ, the dihedral angle, ψ, and the presence, or absence, of a solid contact could all be assessed despite the lack of significant densification. The question of solid contacts between the spheres was addressed by breaking the spheres apart and examining the neck area for signs of a solid contact (such as dislocations, etc.). This method is believed to be satisfactory, although high resolution electron microscopy would be definitive. Unfortunately, no reliable sectioning method could be devised that would consistently locate the electron transparent area of the thin foil at the suspected location of the small solid contact between the two spheres. Without a reliable method, the detection of an intergranular film would only mean either that there was no solid contact, or that the thin area of the foil simply did not intersect the solid contact. No evidence for solid contacts was found between the spheres in which glass had been introduced.

An experiment to study the penetration behavior of the glass into contacts that had been preformed (in the absence of glass) between two sphere was conducted in which two 120μm spheres were sintered in compression by permitting a portion of the top sphere to extend above the jig and then (Fig. 9) placing a load on the sample to provide a compressive force across the contact. The solid contacts thus formed

fractured when cooled to room temperature but could be identified by a small flattened area and occasionally what appeared to be dislocations (Fig. 10). It was of interest to determine whether or not the grain boundary that had formed between the sapphire spheres would be penetrated when anorthite glass was introduced. This experiment was difficult because the contacts fractured if allowed to cool quickly. To eleviate this problem, the glass was preheated and introduced at temperature (1580°C). The results of these experiments were indistinguishable from the samples in which the glass had been added at the start. Even when no glass was originally present and a solid contact had formed between the spheres, the introduction of a liquid glass dissolved the contacts and formed a continous grain boundary phase.

c. Wetting of Alumina: An Estimate of the Surface Energy Anisotropy

Measurements of the contact angle between anorthite glass and small single crystal sapphire spheres were used to estimate the range in the solid/liquid interfacial energy as a basis for understanding liquid-phase sintering kinetics, and the formation of grain faceting during sintering. Measurements from several pairs of spheres, sintered with anorthite glass sandwiched between them, are shown in Fig. 11. The range in contact angles is between approximately eight and seventy degrees. Using Young's equation

$$\gamma_{S\ell} = \gamma_{SV} - \gamma_{\ell V} \cos\theta$$

we can estimate the range in $\gamma_{S\ell}$. Taking $\gamma_{\ell V} = 0.45$ J/m^2 and $\gamma_{SV} = 0.91$ J/m^2 [10] and assuming that γ_{SV} is orientation independent, then

the solid/liquid interfacial energy is calculated to vary between (at the minimum) 0.46 and 0.76 J/m^2, depending on the orientation of the surface.

APPENDIX VI

Characterization of Microstructures

a. Liquid-Phase Sintered Alumina

The general appearance of the dense alumina/10% anorthite microstructures were similar, regardless of whether the starting powder was jagged, or semi-spherical. The two grain boundaries were typically very thin, and the majority of the glass was found to reside in three grain channels (Fig. 12). The grain structures were typically faceted (Fig. 13). Faceting can occur either because of kinetic limitations on the growth rate of a particular crystalline plane, or, (in equilibrium) because certain orientations have a lower solid/liquid interfacial energy and are thus thermodynamically more stable. The grain facets most often observed were the rhombohedral planes, $\{\bar{1}012\}$. Less common but often encountered are the basal $\{0001\}$ and the prism $\{11\bar{2}0\}$ planes. Grain faces that do not possess these general orientations often have ledges by which these favored orientations are achieved microscopically (Fig. 14).

The frequency of each crystallographic type of faceting was estimated to be the same both in equilibrium and nonequilibrium microstructures. Samples that had been partially sintered and the water-quenched appear similar to samples that had been sintered for several weeks. Also common are dislocation networks (Fig. 15) and low angle grain boundaries (Fig. 16). The latter was usually identifed as a basal plane twin.

b. Pure Alumina

Semi-spherical alumina powder was sintered to full density without additives, and samples for microscopy were prepared in order to assess the presence of solid/solid contacts. The procedure for establishing that no impurity grain boundary film exists between the grains in a polycrystalline material is less straightforward than the now standard procedures for detecting a thin intergranular phase.

A number of approaches have been used in the past to (incorrectly) experimentally determine that contact areas between solid grains are free from a boundary film. The problems with the former procedures generally fall into one of two categories: either the tool used in the investigation had inadequate spatial resolution to detect the narrow impurity channels (e.g. optical or scanning electron microscopy) or the data obtained using the correct aparatus were misinterpretated.[11] Generally, then, if an intergranular phase is detected it is certainly really present, yet if none is detected one must regard the results with suspicion until the procedure by which the results were obtained is reviewed.

In order to assess the presence of a grain boundary film in the high purity alumina sample, six high angle grain boundaries were studied by high resolution electron microscopy. Also three grain functions were inspected for possible glass enclaves.* None were found (Fig. 17).

*In materials that exhibit an intergranular phase along two grain boundaries, the remainder of the glass phase is usually manifest as larger enclaves along three grain channels. Thus, even at low magnification one can often get a sense of whether or not to expect a two grain boundary film by the presence or absence of three grain boundary glassy pockets.

Of the several two grain boundaries examined, none appeared to contain an impurity boundary phase within the 2Å resolution limit of the microscope; Fig. 18 is an example. This boundary was imaged at a variety of orientations with respect to the electron beam within the confines imposed by the tilt stage (±10° in X and Y) and no evidence for an intergranular phase was detected. Some possibility remains that a thin film was present, but was not sufficiently close to perpendicular to the electron beam to be visible. However it is noted that in alloys that contain a glassy phase, the above procedure inevitably enables the microscopists to detect a boundary film.

Of particular interest is the boundary pictured in Fig. 19. The boundary is also free of a detectable grain boundary phase, but is an unusual type of special boundary, never before reported. It appears that between the two major grains, a thin third grain has been created such that both resulting grain boundaries are special boundaries. Thus, two low energy boundaries replace a single high energy boundary.

Without the thin grain, the misorientation is approximately 46° in the plane viewed. Clearly for the observed microstructure to persist, the sum of the two low energy boundaries must be exceeded by the energy of what would be the high angle grain boundary. This fixes the sum of the energies of the two boundaries to about 1.5 J/m^2. Assuming that these boundaries have approximately equal interfacial energy, then these boundaries each have an energy of about 0.75 J/m^2; only slightly larger than the solid/liquid energies predicted in Appendix V.

It is not known to what extent this type of boundary represents a common or highly unusual situation. Certaintly this configuration can permit a lower energy state for a number of high angle, high energy grain boundaries, offering an interesting variation to the traditional areas of concern in the study of coincident lattice site theory.

REFERENCES

1. T. Gillespie, and G. D. Rose, "The Effect of Capillary Liquid on the Fare of Adhesion between Spherical Solid Particles", J. Colloid and Interface Sci. 26 (1967), p. 246.
2. N. L. Cross and R. G. Picknett, Comment on the paper "The Effect of Capillary Liquid on the Force of Adhesion between Spherical Solid Particles", J. Colloid and Interface Sci. 26, (1967) p. 247.
3. H. M. Pricen, "Comments on the Effect of Capillary Liquid on the Force of Adhesion between Spherical Solid Particles", J. Colloid and Interface Sci. 26 (1967), p. 249 and "Comment on the Latest Note by Gillespie and Settineri" (Sic) ibid, p. 253.
4. B. V. Drejaguin, "Concerning the paper: "The Effect of Capillary Liquid on the Force of Adhesion Between Spherical Solid Particles", by T. Gillespie and W. J. Settineri (Vol. 24, No. 2, 1967) J. Colloid and Interface Sci. 26 1967, p. 253.
5. T. Gillespie and W. J. Settineri, "The Effect of Capillary Liquid on the Force of Adhesion between Spherical Solid Particles", J. Colloid and Inter. Sci. 24 (1967), p. 199
6. J. C. Melrose, "Model Calculations for Capillary Condensation" A.I.Ch.E.J. 12 (1966) p. 986.
7. R. B. Heady and J. W. Cahn, "An Analysis of the Capillary Forces in Liquid-Phase Sintering of Spherical Particles" Met. Trans. 1 (1970) p. 185.
8. T. M. Shaw, private communication.
9. See, for instance, A. E. Scheidegger, The Physics of Flow Through Porous Media, University of Toronto Press, 1957.

10. P. L. Flaitz, "Some Aspects of Liquid-Phase Sintering," Ph.D. thesis, University of California, Berkeley (1982).

11. L. K. V. Lou, T. E. Mitchell and A. H. Heuer, Discussion of "Grain Boundary Phases in a Hot-Pressed MgO Fluxed Silicon Nitride", J. Amer. Ceram. Soc. 61 (1978) p. 462.

FIGURE CAPTIONS

Fig. 1. Geometry assumed for capillary force calculation.

Fig. 2. Geometry assumed for solid/solid contact stress calculation. (a) A normal stress is applied to a grain boundary that is penetrated by a liquid phase. (b) When sufficient stress is applied the boundary layer will be squeezed out, leaving a dry contact.

Fig. 3. SEM micrograph of jagged ceramic powder particles (alumina). (Bar = 10 μm)

Fig. 4. Schematic graph of grain boundary energy, γ_{gb}, versus the misorientation between grains. For misorientation angles smaller than the critical angle, θ_c, the grain boundary energy is smallest for a solid/solid contact, because $\gamma_{ss} < 2\gamma_{s\ell}$.

Fig. 5. Schematics illustrating density changes during the early stages of sintering. When the solidified liquid phase particles melt (A) they no longer participate as solid units in the packing so that after rearrangement the powder compacts become much more dense (B). However when the solidified particles are large (C) they can leave large residual voids when they melt (D).

Fig. 6. Schematic illustrating the geometry used in the initial sintering rate calculation.

Fig. 7. SEM micrographs of pure alumina which has been penetrated by anorthite glass.

(A) Low magnification micrograph of the surface appearance (bar = 100 μm).

(B) Cross-section of the sample, showing the area penetrated (at right with voids). The sample surface lies 20 μm to the right edge of the micrograph (bar = 5 μm).

Fig. 8. TEM micrographs of pure alumina, penetrated by anorthite.

(A) The glass phase has penetrated in between the solid grains.

(B) High resolution image showing the three grain channel glass pocket connecting a thin two grain boundary film, continuously separating the solid alumina grains that had previously been unpenetrated.

Fig. 9. Schematic of jib used for two-sphere sintering experiments.

Fig. 10. SEM micrographs of solid contact formed between two spheres in the absence of a glassy phase. (A) (bar = 100 μm).

(B) Detail of features which appear to be dislocations (bar = 5 μm).

Fig. 11. SEM micrographs of two sphere sintering in the presence of a liquid phase.

(A) Low magnification micrograph showing areas for contact angle measurements (bar = 50 μm).

(B) Contact α, contact angle $\theta = 8^\circ$ (bar = 2 μm).

(C) Contact γ, $\theta = 30^\circ$ (bar = 4 μm).

(D) Contact β, $\theta = 26^\circ$ (ba = 5 μm).

(E) Contacts, γ and δ (bar = 20 μm).

(F) Contact δ, $\theta = 70^\circ$ (bar = 2 μm).

Fig. 12. (A) Bright field and (B) Diffuse-dark field TEM micrographs of typical alumina/anorthite microstructures. Large three grain glassy pocket (g) connects thin two grain boundary films. (Bar = 100 μm).

Fig. 13. TEM micrographs of facetted grain structures in liquid-phase sintered alumina/anorthite samples.

(A) Rhombohedral planes on a facetted grain separated from another grain by anorthite glass (g).

(B) Top grain with facets on rhombohedral and basal planes and bottom grain with facets on rhombohedral and prism planes. (Bars = 50 μm)

Fig. 14. (A) BF and (B) DDF TEM micrographs of a three grain pocket and continuous two grain boundary film in alumina/anorthite (bar = 10 nm). (C) High resolution image showing micro-facetting along the boundary.

Fig. 15. TEM micrograph of a dislocation boundary in alumina. Dislocations at (A) are 1/3[0001] burgers vector. At (B) and (C) they are either $(1/3)\langle 10\bar{1}0\rangle$ or $1/3\langle 10\bar{1}1\rangle$ and at D are $1/3\langle 11\bar{2}0\rangle$ although these do not interact with the boundary shown (bar = 3 nm).

Fig. 16. (A) TEM micrograph of a low energy twin boundary (not lying in the basal plane) the two grains share the same $(10\bar{1}0)$ plane but have opposite $\{0001\}$ planes, i.e.,

$$(0001)_A \;//\; (000\bar{1})_B$$

(bar = 200 nm).

(B) High resolution TEM micrograph of two basal plane twins on alumina. Ledges are marked by arrows. The $\{1000\}$ plane spacing is 0.41 nm and the $\{0111\}$ spacing is 0.39 nm.

Fig. 17. TEM micrograph of pure alumina in which no grain boundary phase was found. This bright field micrograph illustrates the absence of three grain glass pockets which are typically found in materials in which an intergranular phase is present. The dislocation (d) has punched through the twin boundary (t). (Bar = 10 nm)

Fig. 18. High resolution TEM micrograph at a grain boundary in pure alumina. The grains share a common $(10\bar{1}3)$ plane but have different orientations. No intergranular phase is present. The interplanar spacings are: $\{11\bar{2}4\}$ and $\{\bar{1}104\}$ are 0.19 nm and $\{10\bar{1}3\}$ are 0.30 nm.

Fig. 19. High resolution TEM micrograph of a grain boundary in pure alumina. A thin grain makes up the misorientation between the two primary grains by forming low angle grain boundaries with both grains. The thin grain has a zone axis $[21\bar{3}0]$ and shares the $(01\bar{1}2)$ with the right hand grain and the $(\bar{1}01\bar{2})$ with the left hand grain. The $(0\bar{1}11)$ is common to all three grains. No intergranular phase is present.

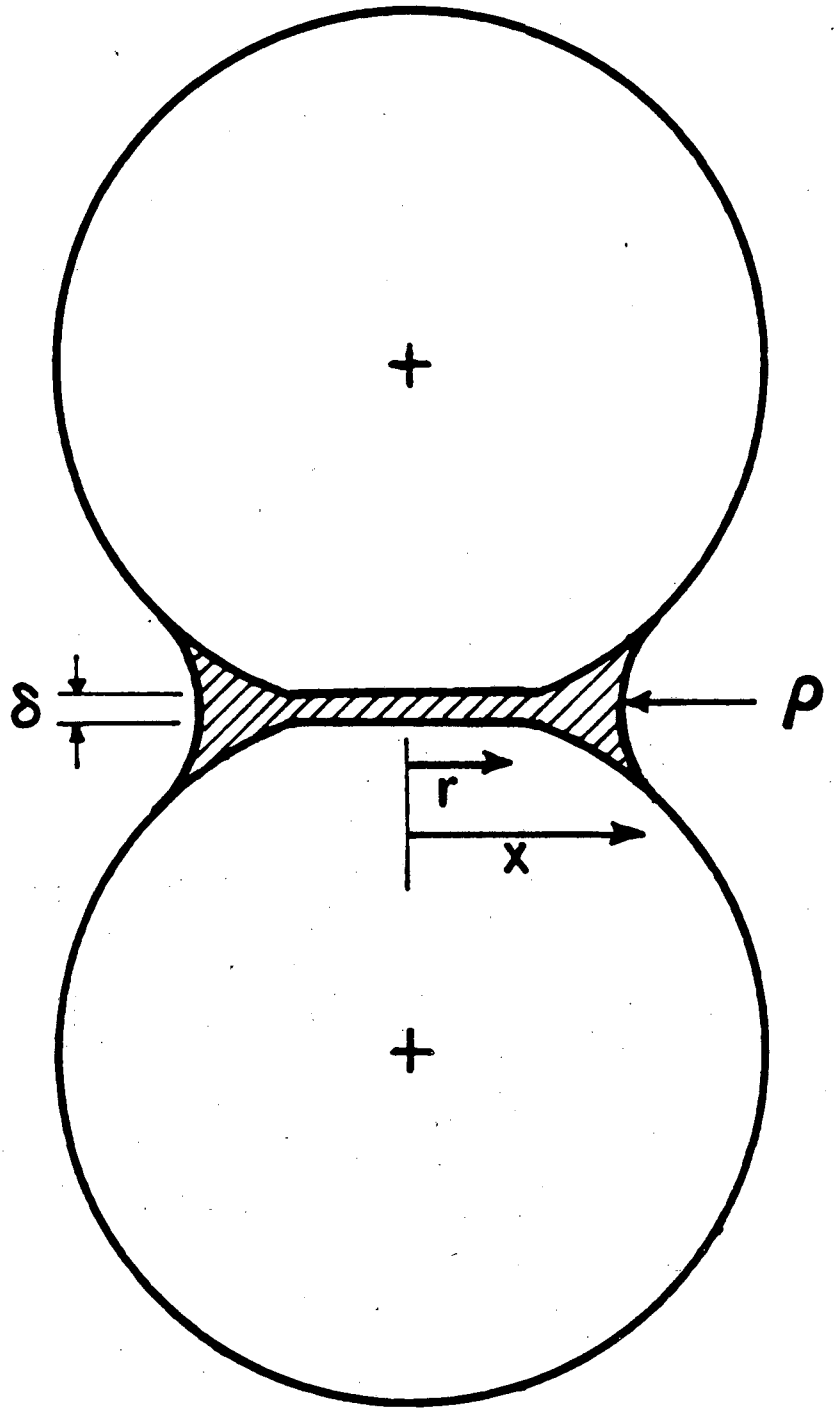

XBL8410-7491

Figure 1

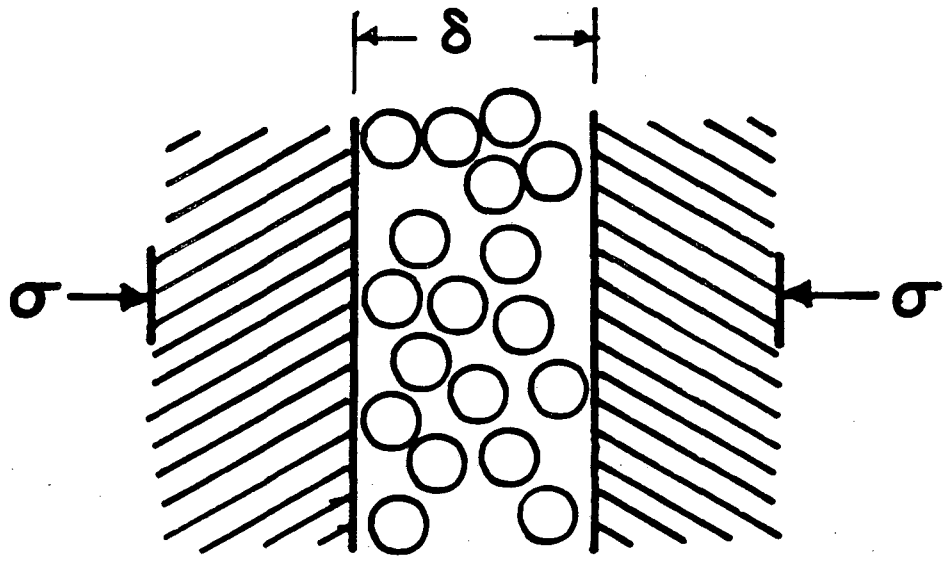

A

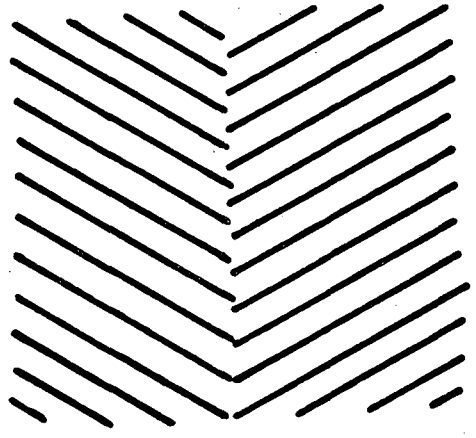

B

XBL 8410-8221

Figure 2

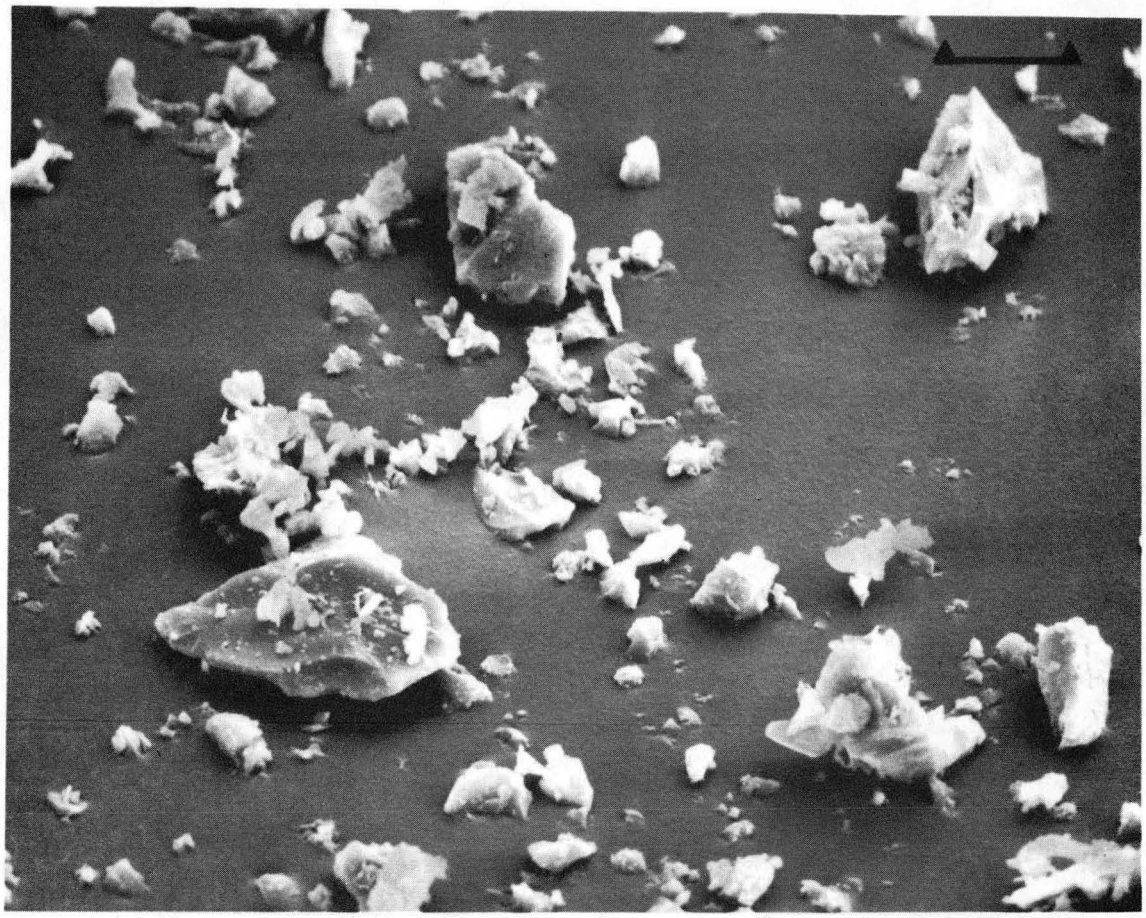

XBB 848-6440

Figure 3

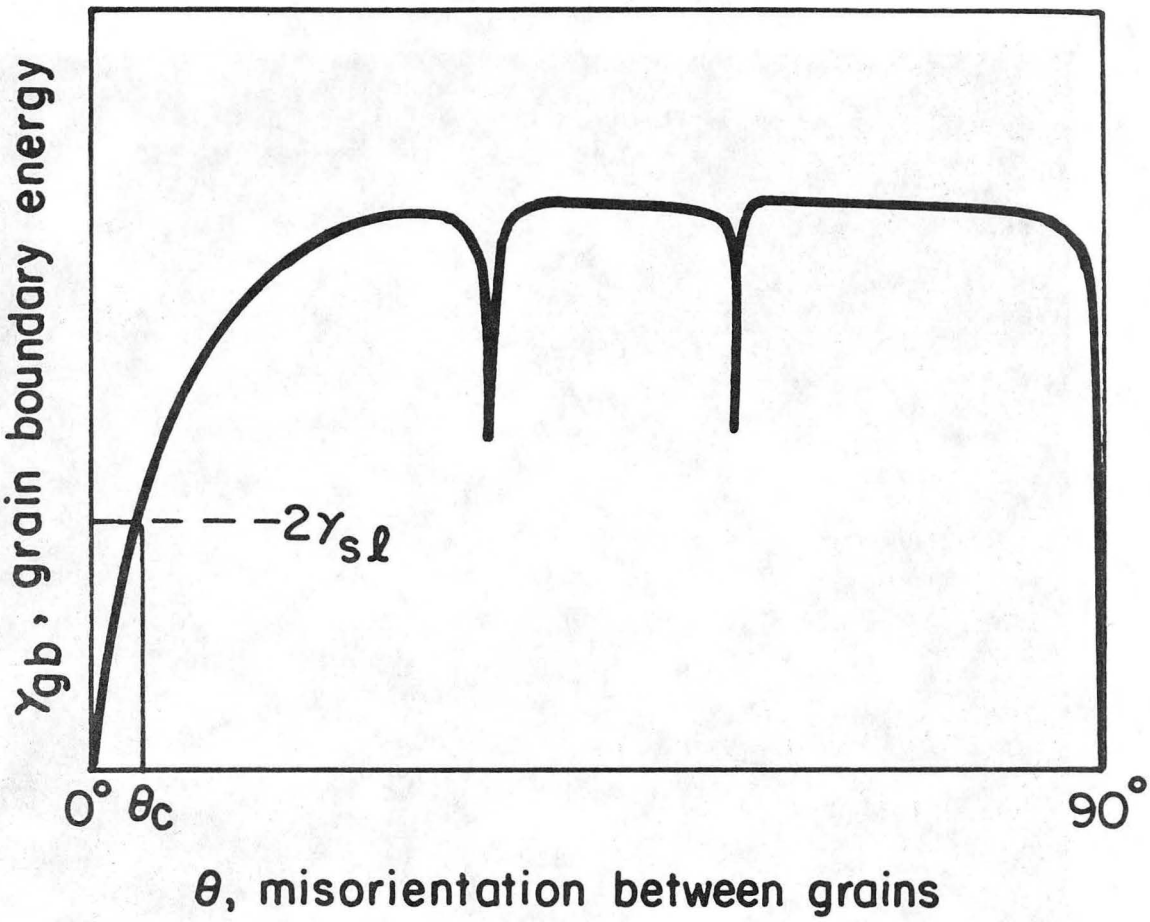

XBL 8410-8222

Figure 4

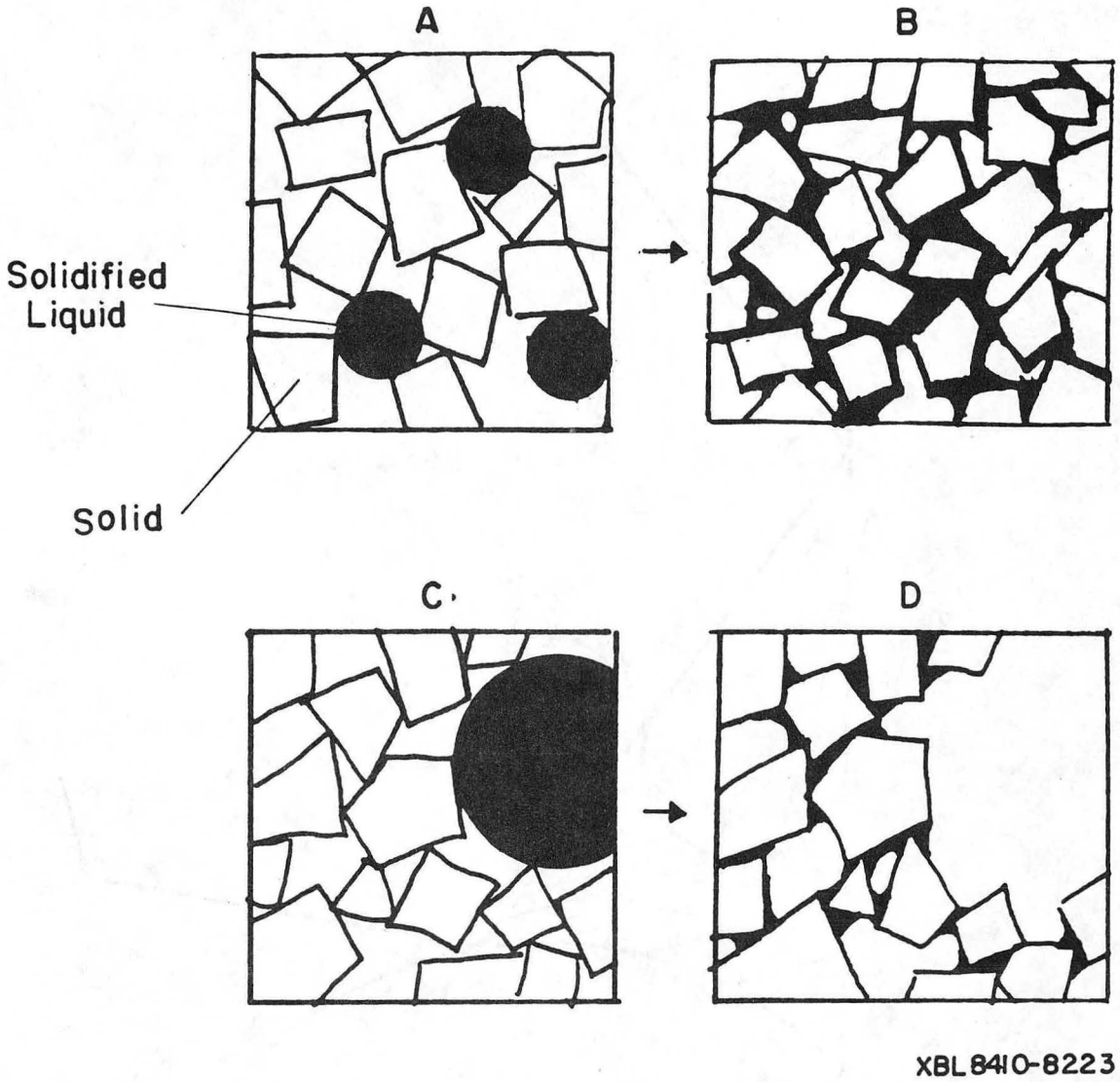

Figure 5

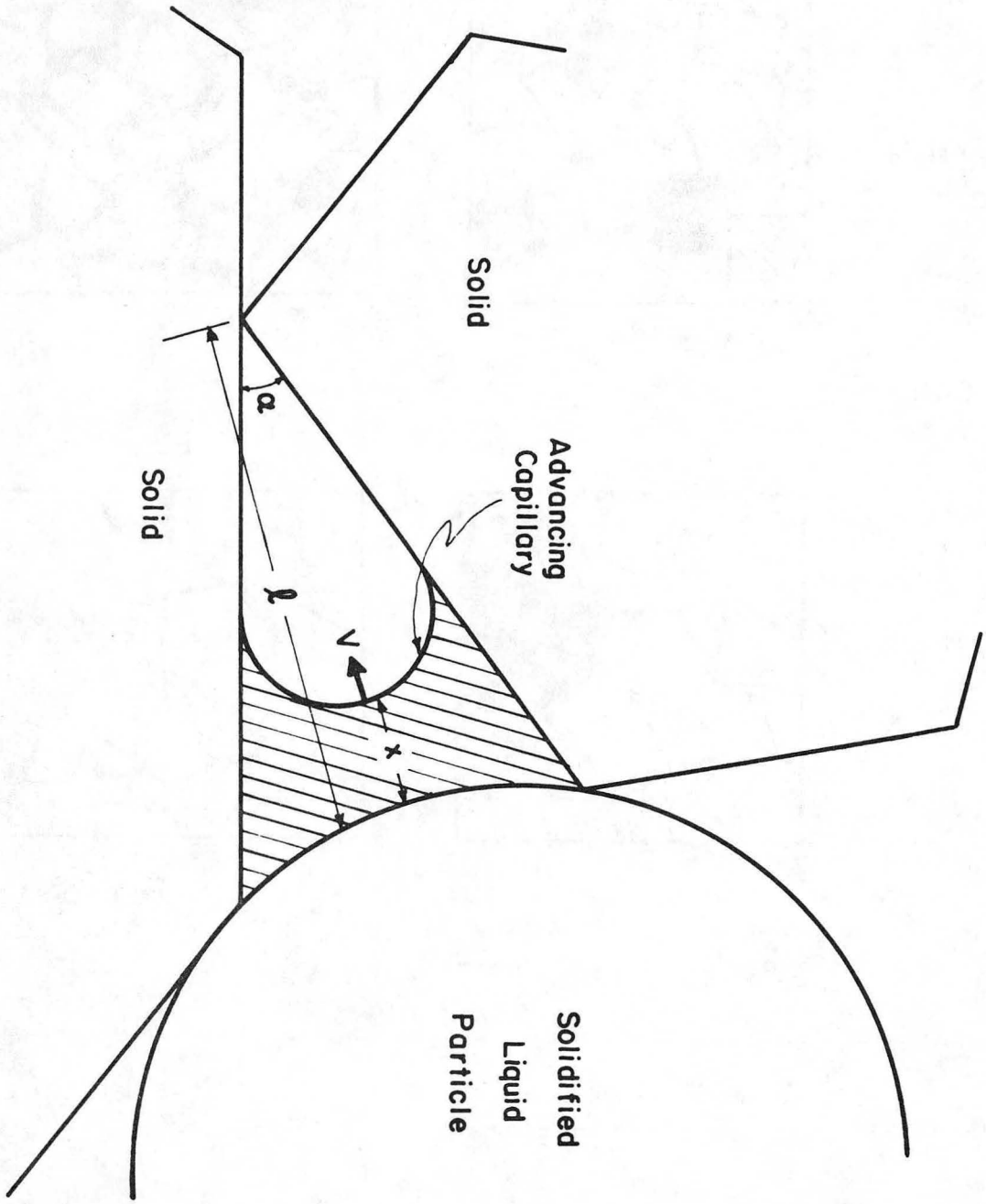

XBL 8410-8224

Figure 6

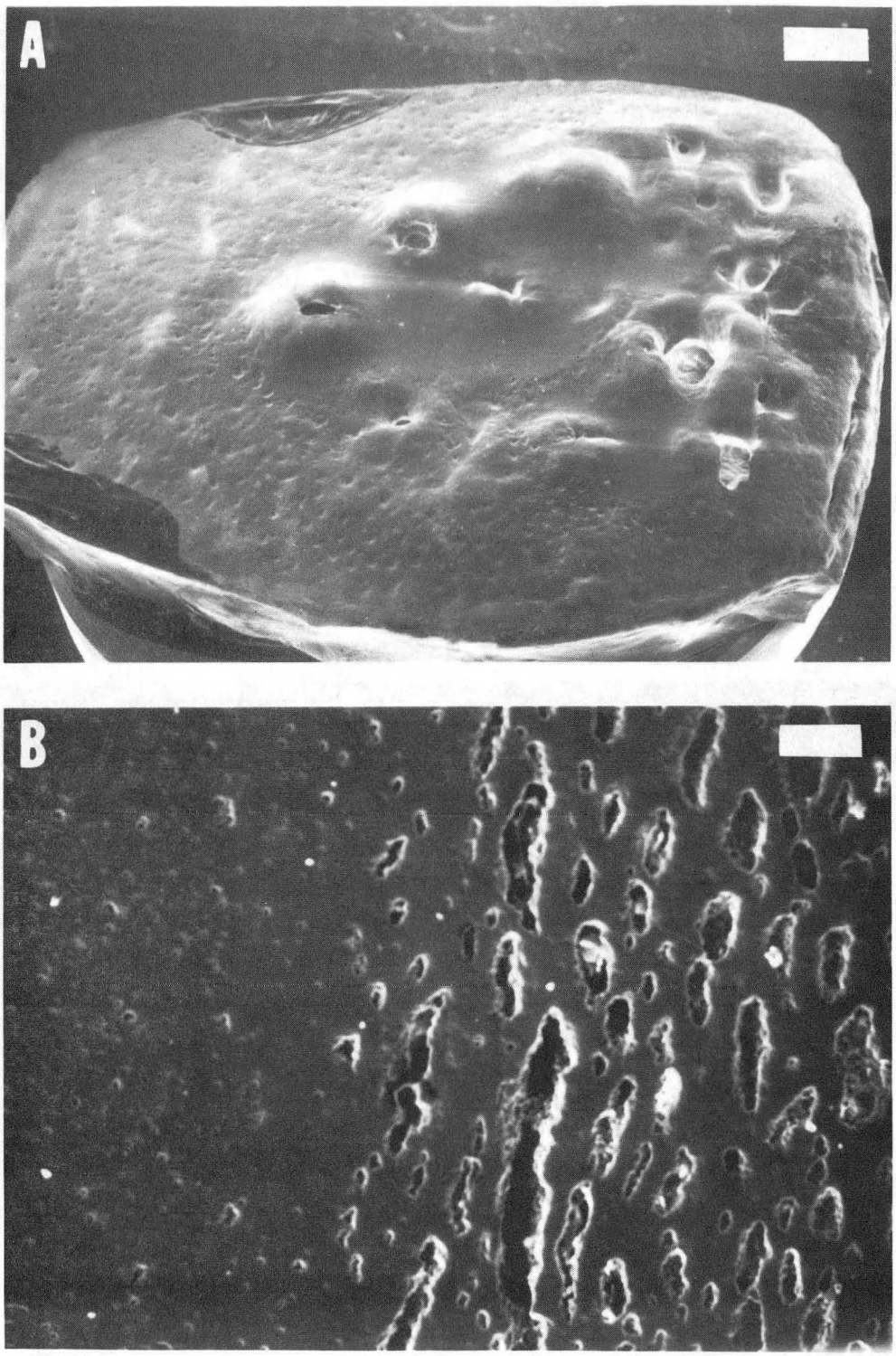

XBB 848-6455

Figure 7

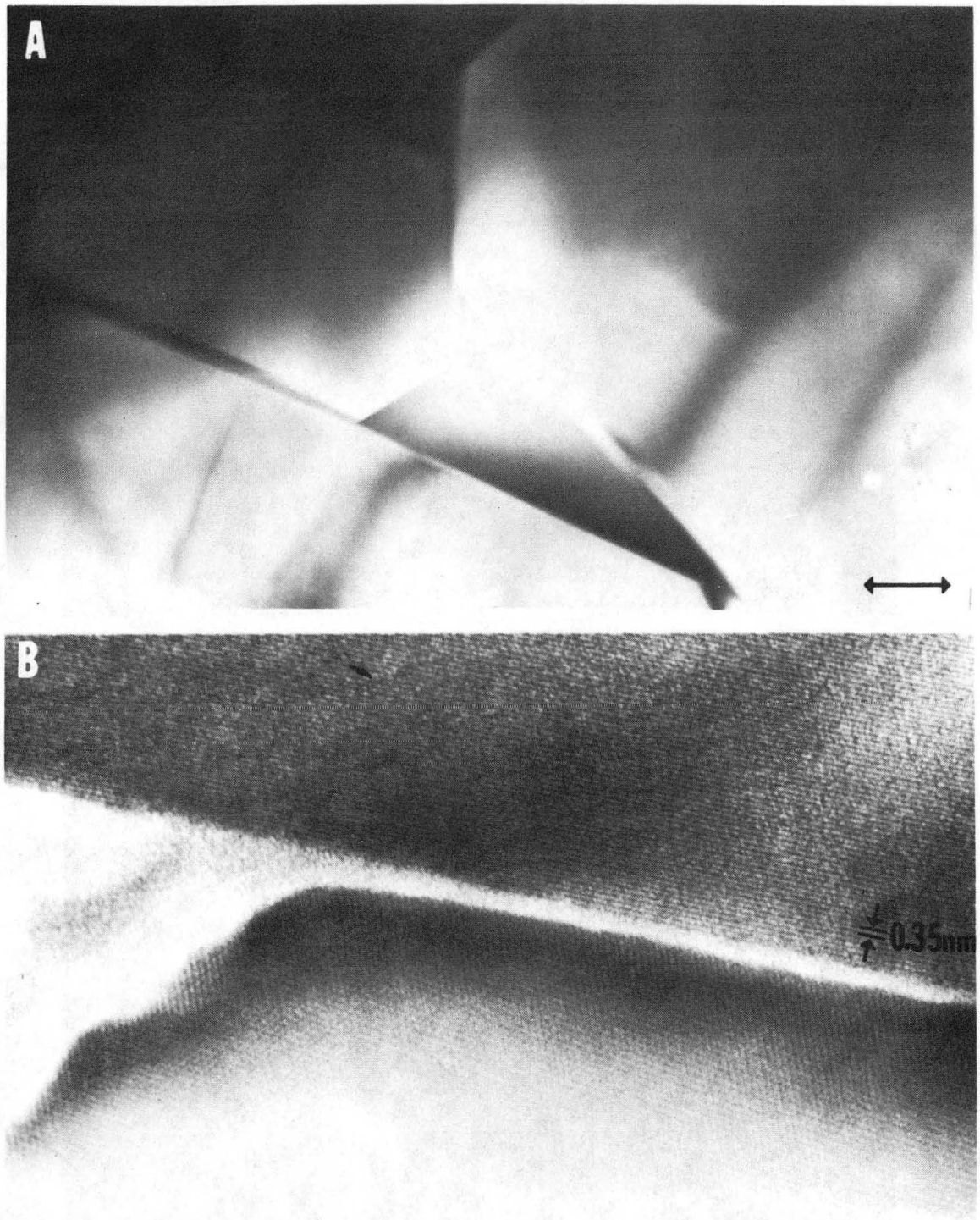

XBB 848-6448

Figure 8

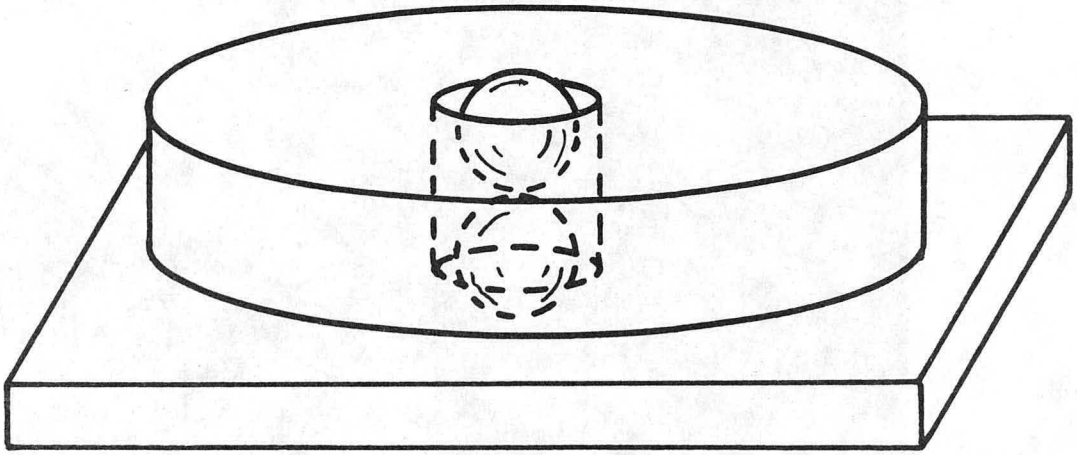

XBL 8410-8231

Figure 9

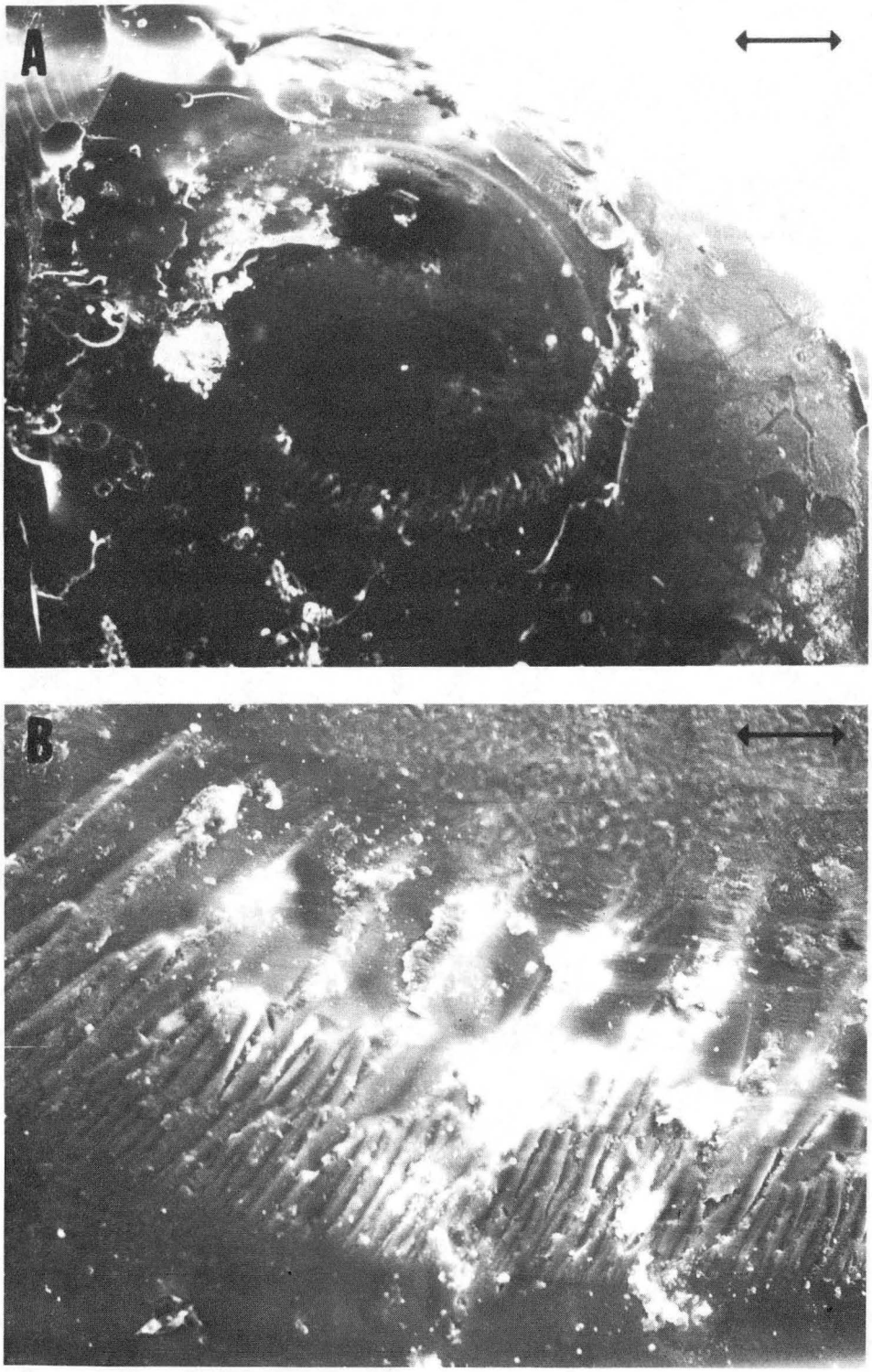

XBB 848-6456

Figure 10

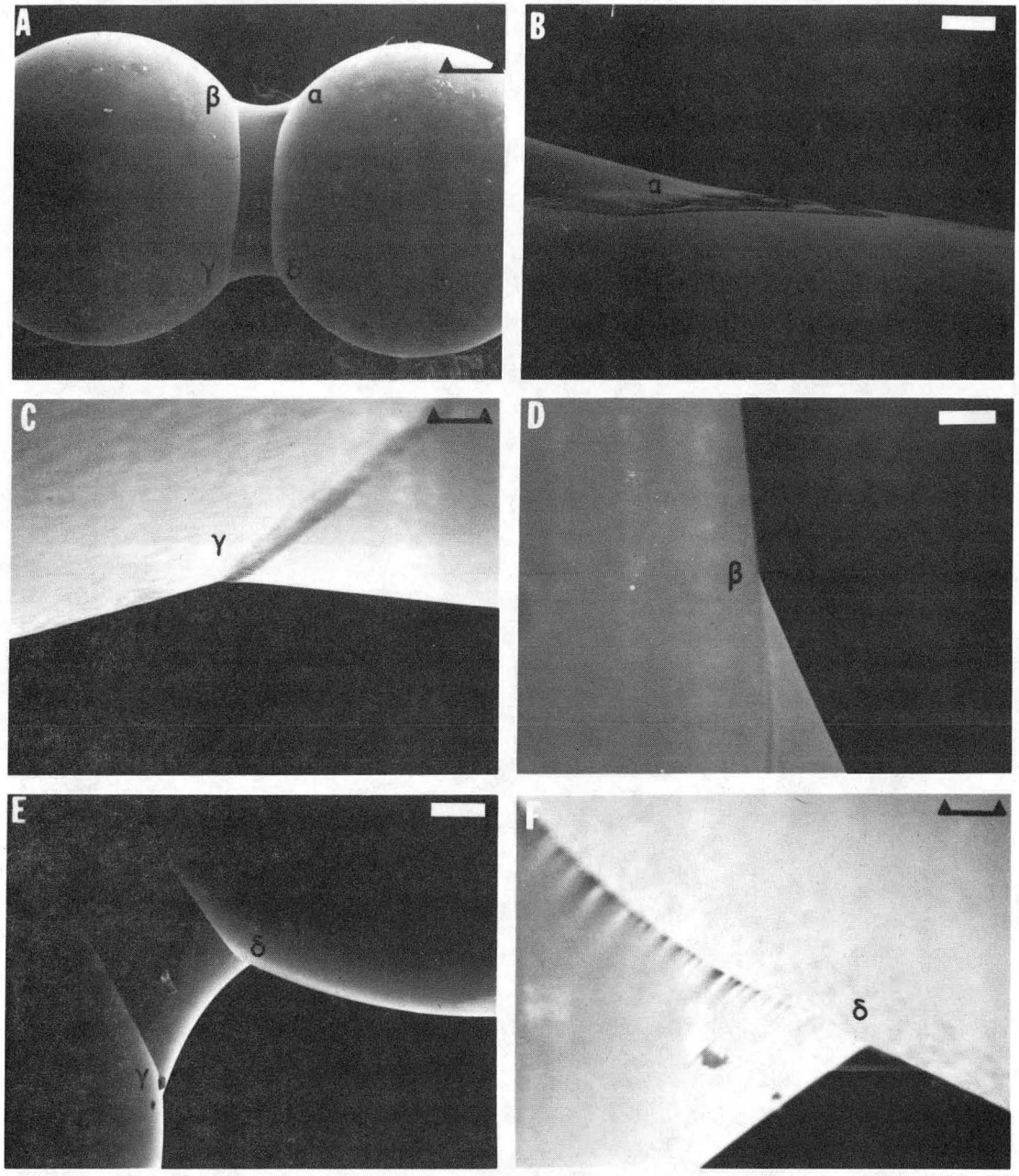

XBB 848-6443

Figure 11

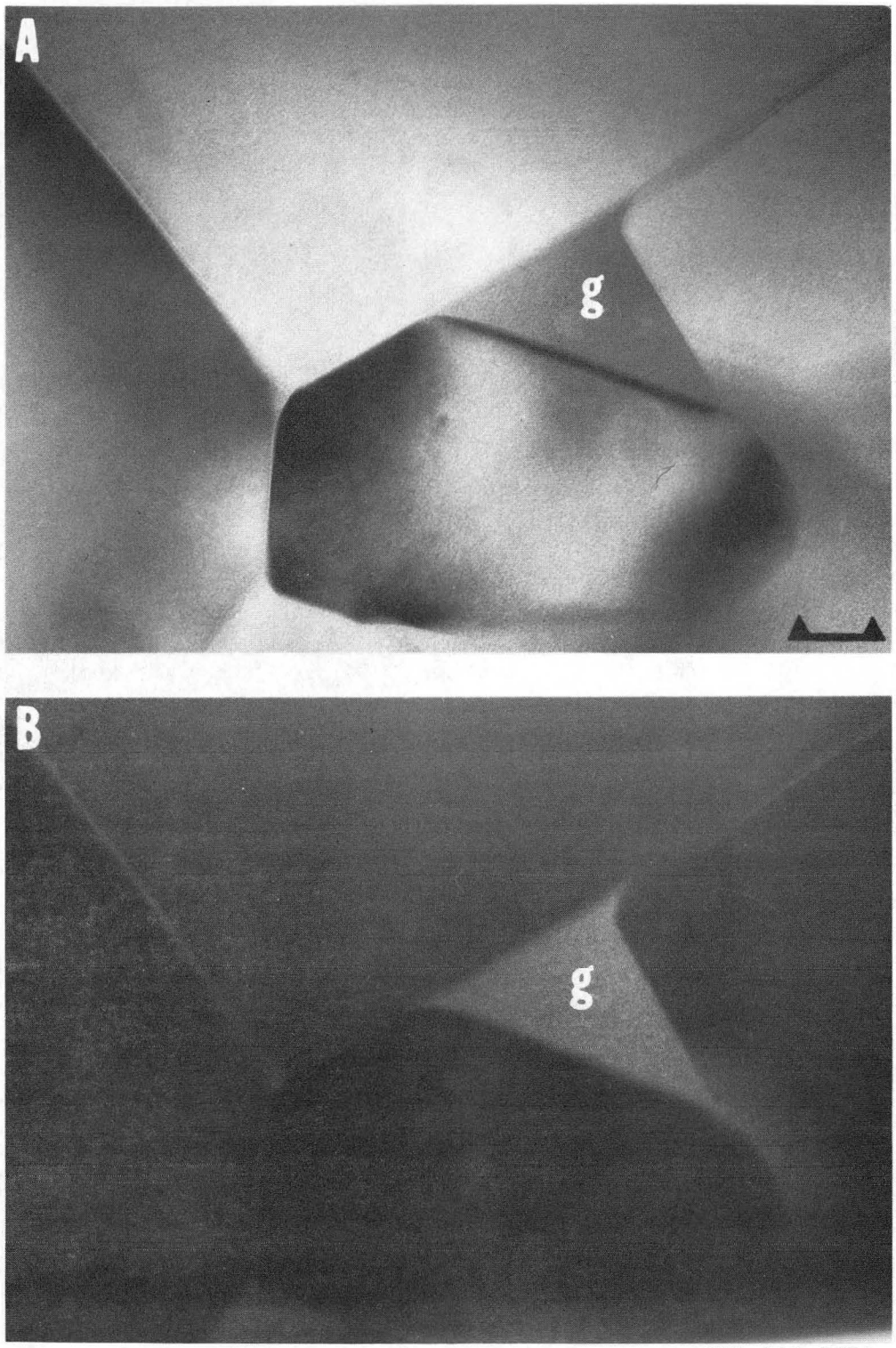

XBB 848-6454

Figure 12

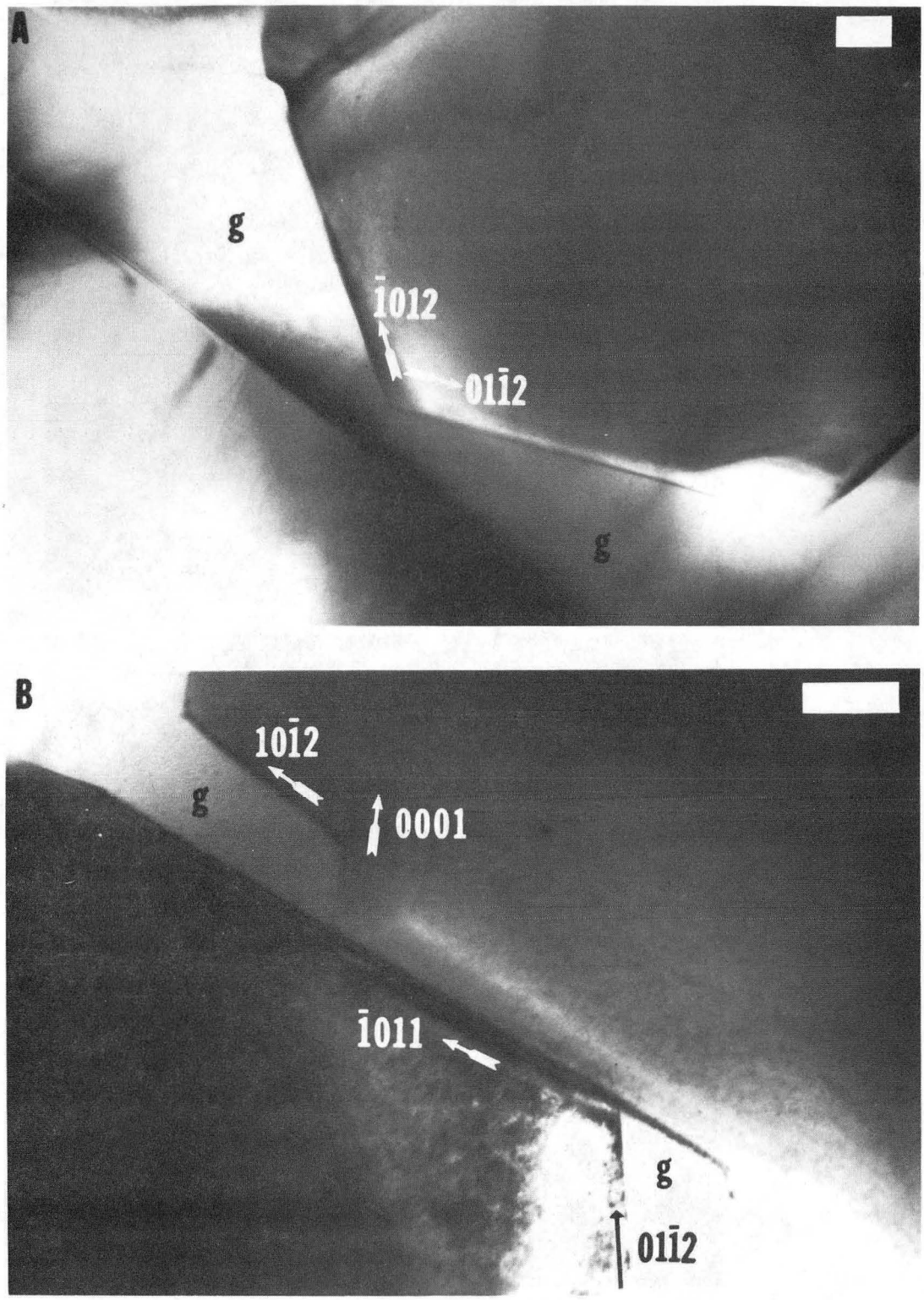

XBB 848-6444

Figure 13

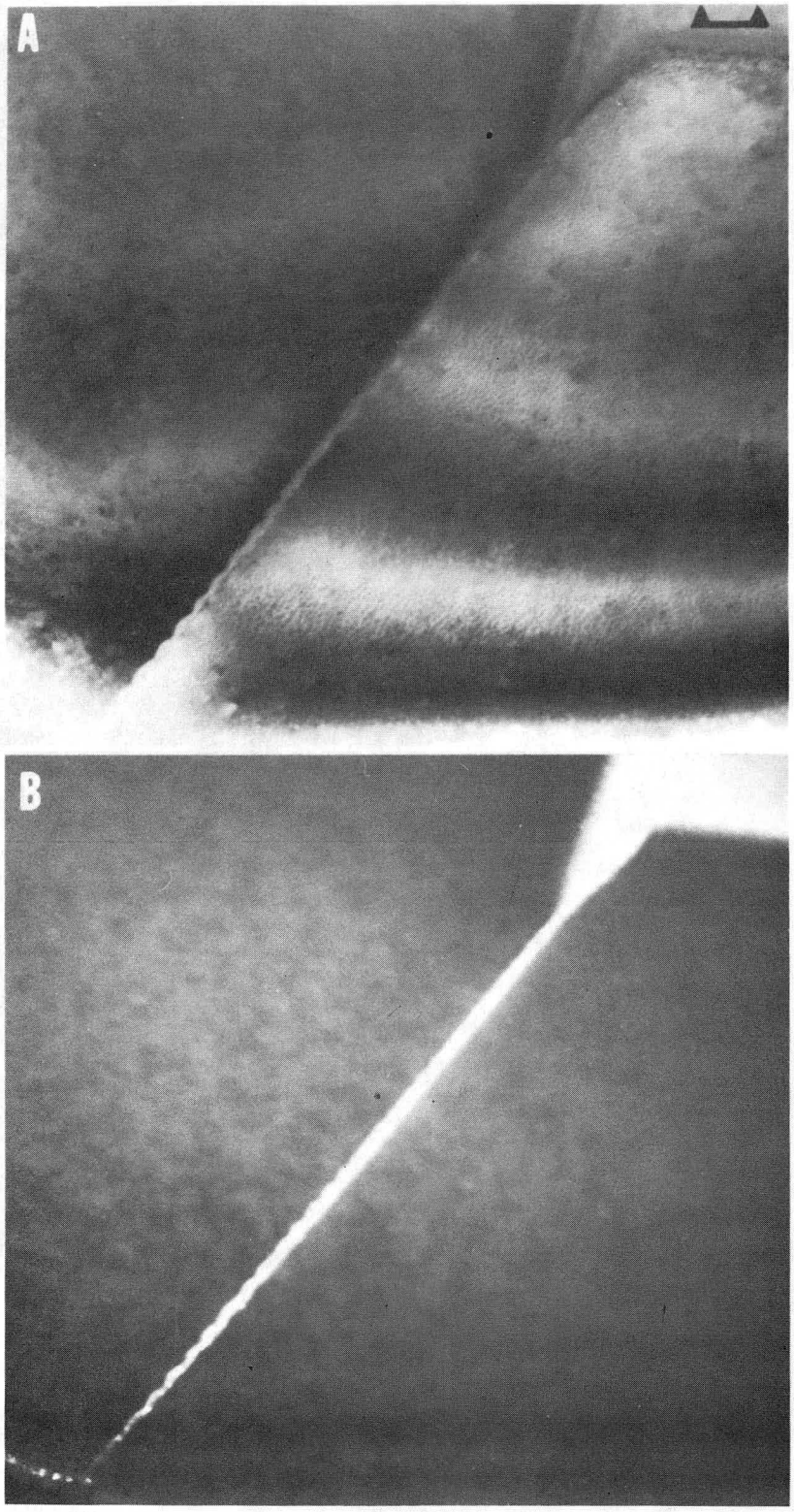

XBB 848-6445

Figure 14a,b

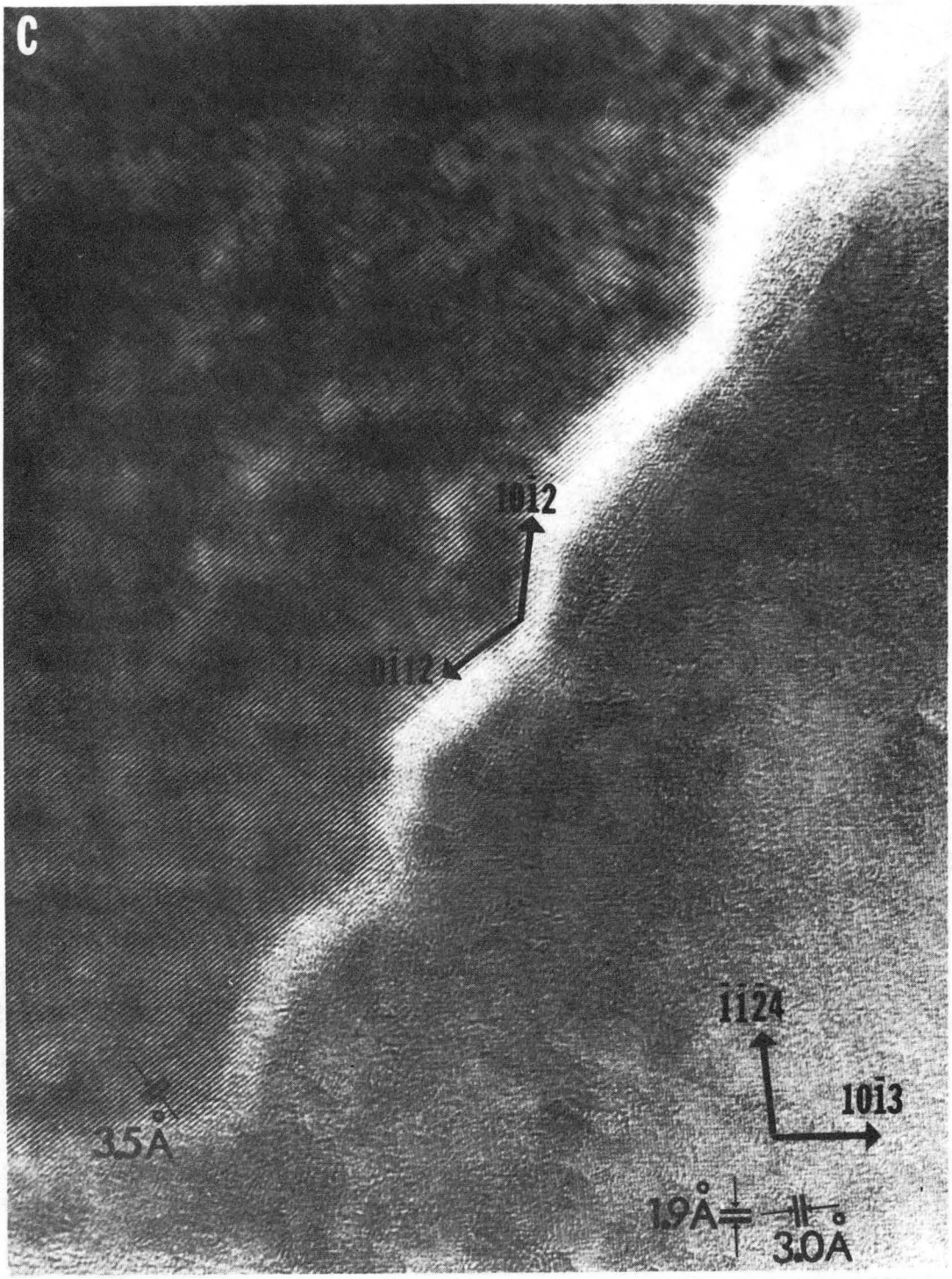

XBB 848-6447

Figure 14c

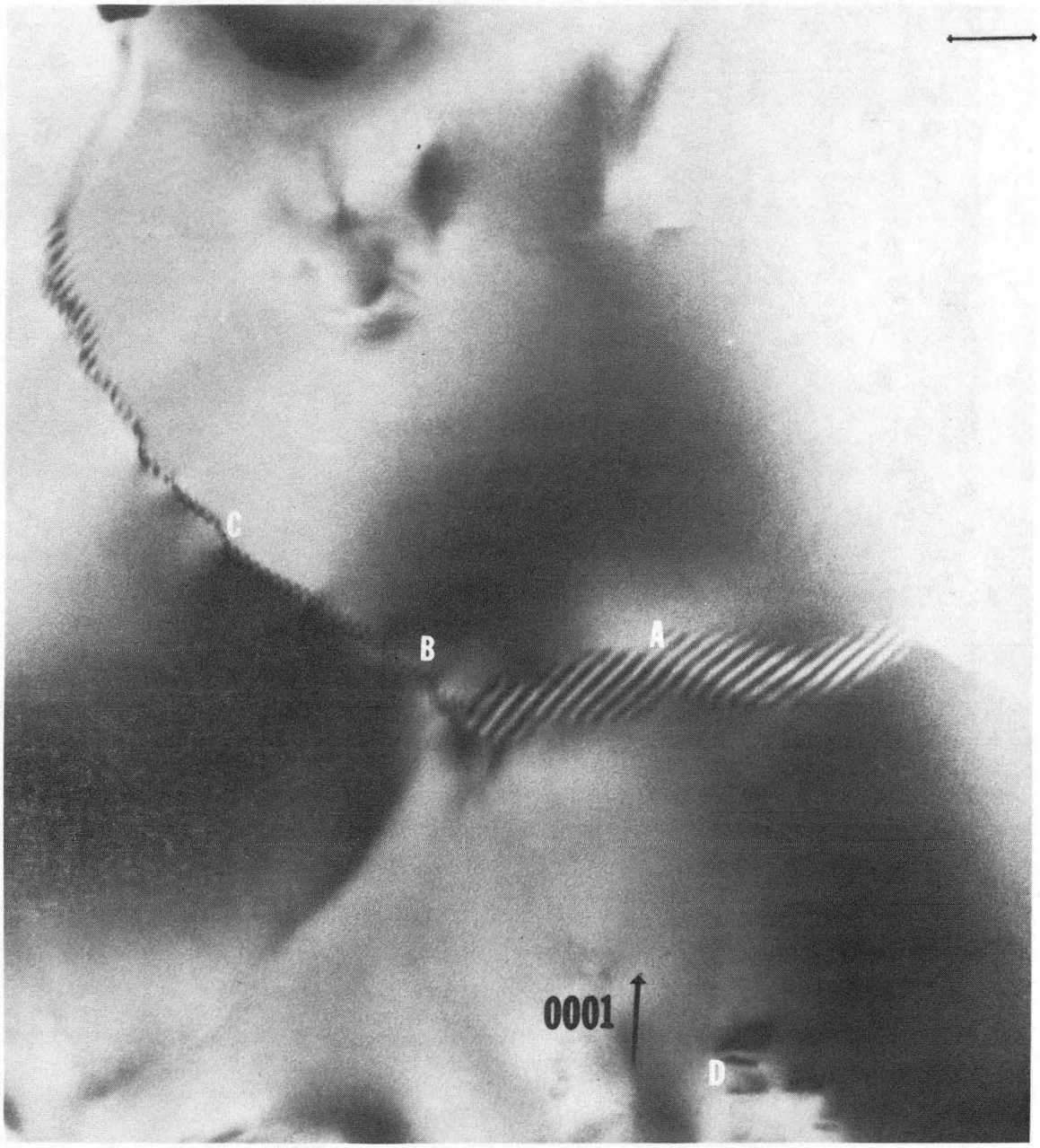

XBB 848-6446

Figure 15

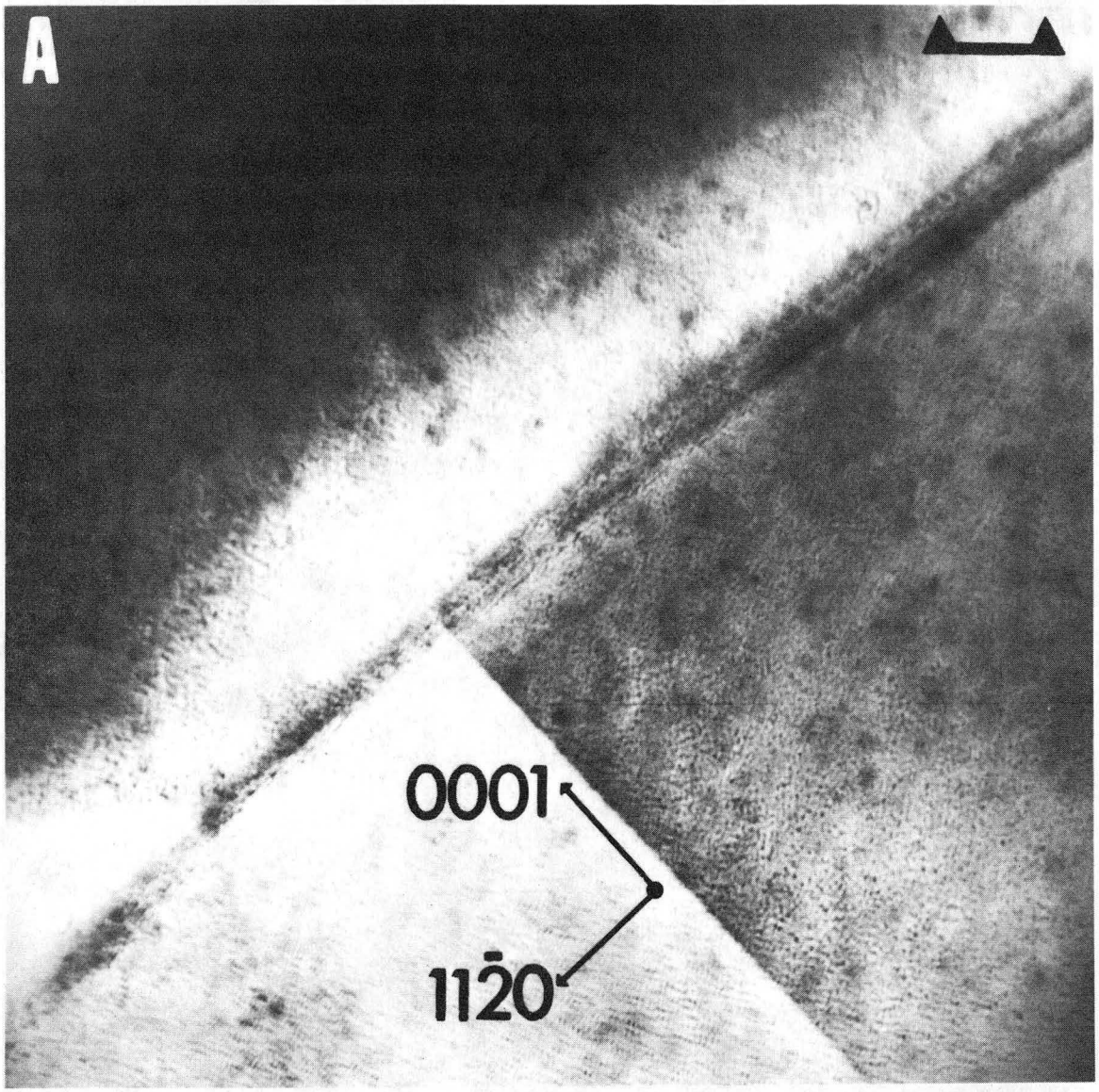

XBB 848-6461

Figure 16a

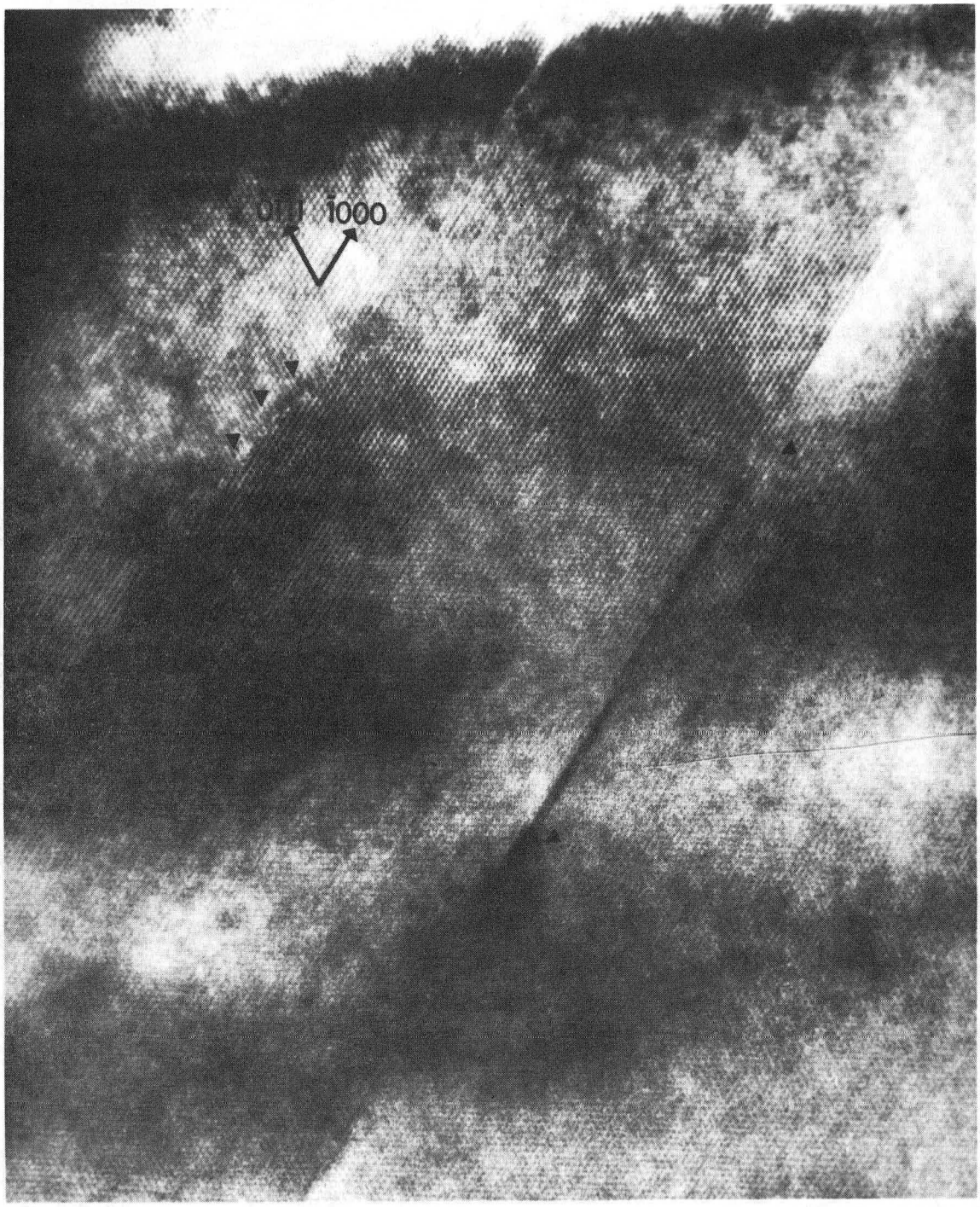

XBB 848-6442

Figure 16b

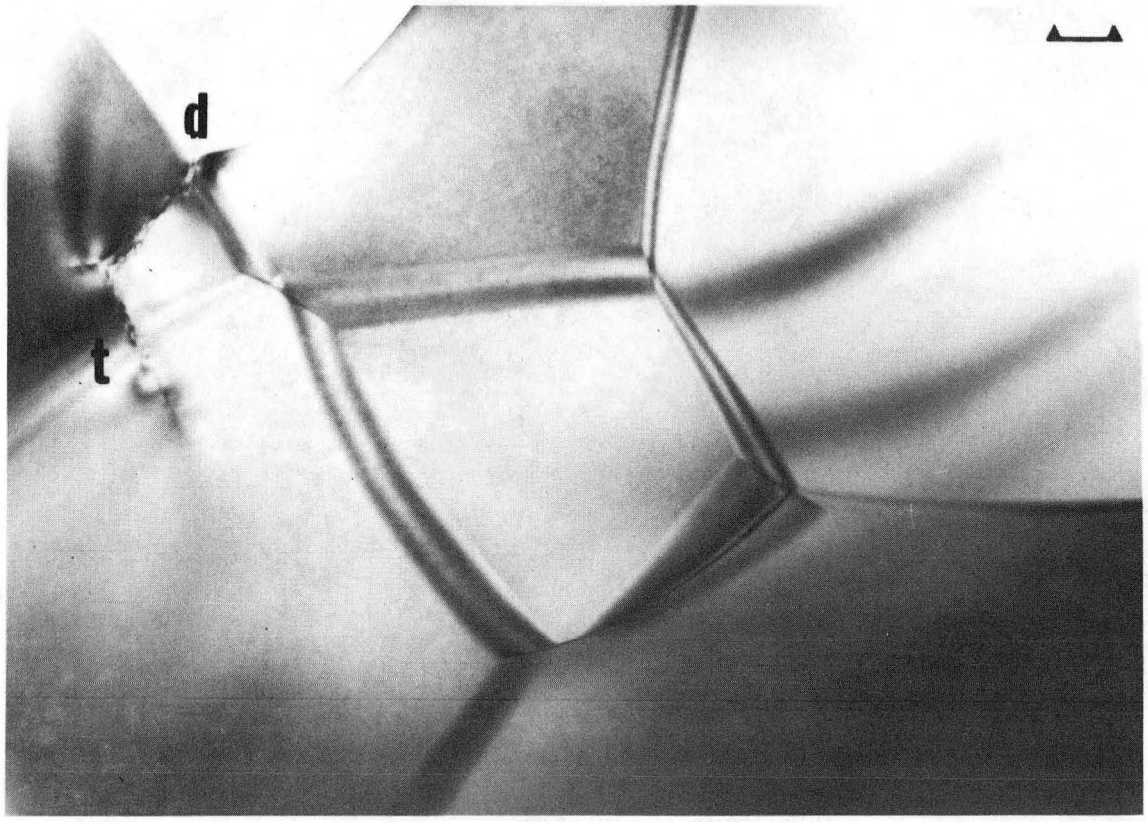

XBB 848-6458

Figure 17

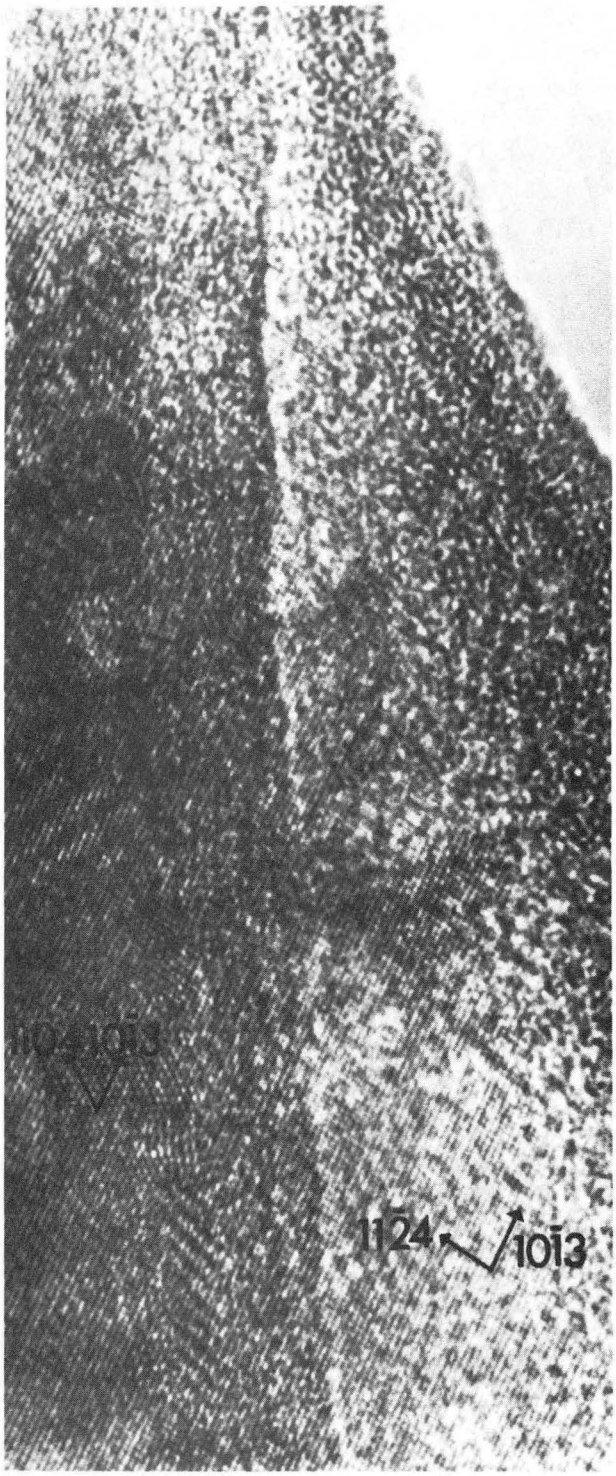

XBB 848-6451

Figure 18

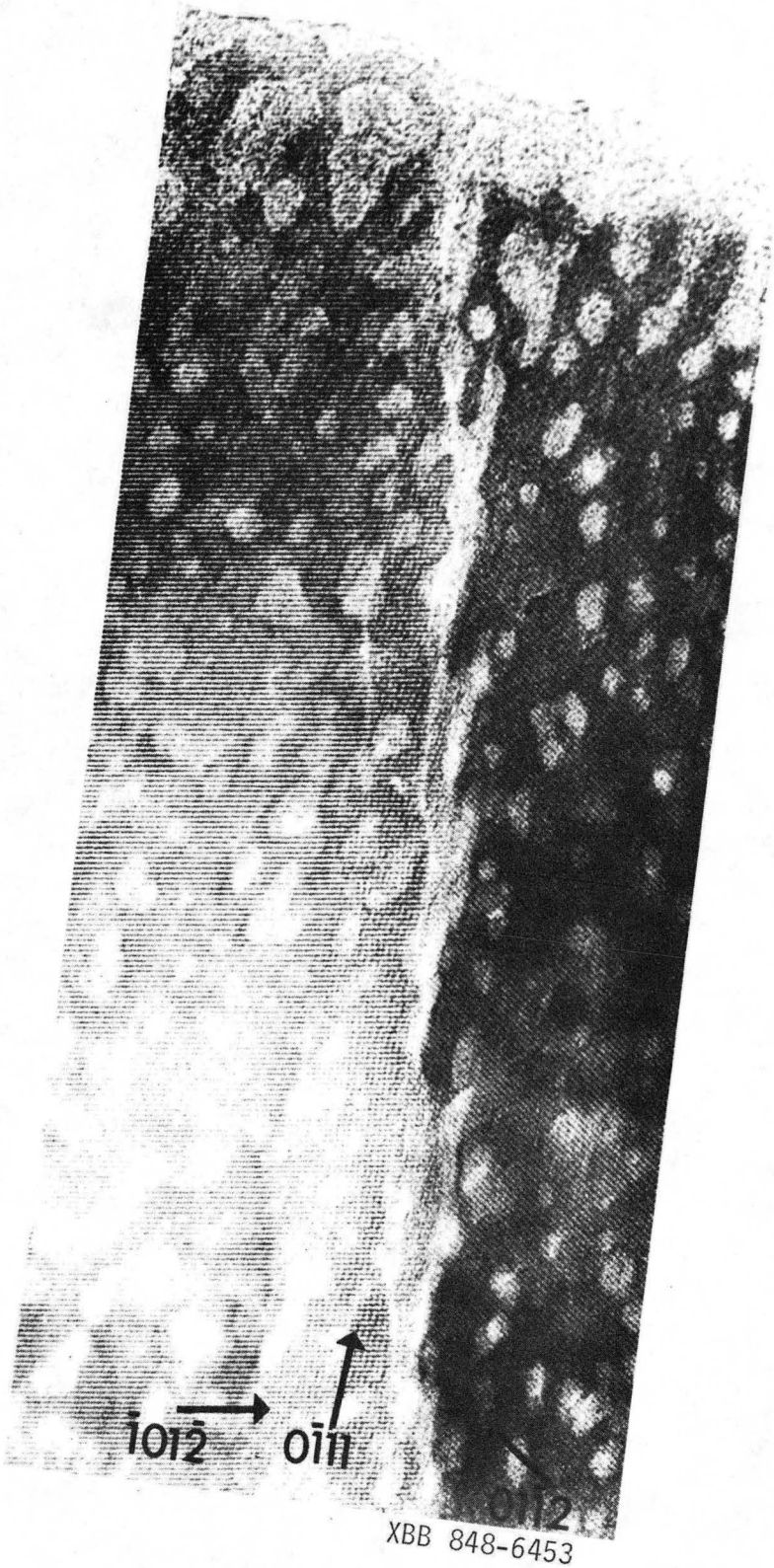

Figure 19

PART II

DEFORMATION IN THE PRESENCE OF A LIQUID PHASE

1. INTRODUCTION

A large number of technologically important materials are prepared by liquid phase sintering. This class of materials is densified with the aid of a second phase that becomes a viscous liquid at the processing temperature (including second phases caused by unintentional impurities). The liquid penetrates between the solid grains at the processing temperature and thus, exists as a continuous, thin intergranular film. The solid has sufficient solubility in the viscous liquid phase that rapid densification is promoted by a solution/reprecipitation mechanism, wherein matrix atoms are dissolved and transported through the liquid.

Ideally, the theoretical understanding of high temperature failure in liquid phase sintered ceramics will become sufficiently mature such that component failure times can be computed from theory. However, current descriptions of failure are confined to empirical expressions for the steady state growth of existing cracks.[1] Yet to be understood are the mechanisms by which creep damage initiates and enlarges. The damage development in such materials is generally governed by the properties of the second phase. While the properties of the second phase are often not entirely homogeneous,[2] observations[3,4] suggest that holes initiate within this phase and that the holes grow and coalesce to form the cracks which induce eventual failure. The observed failure times are determined by the rates at which holes nucleate,

grow and coalesce: both within susceptible regions of the microstructure and ahead of extending cracks.

This portion of the thesis examines the hole evolution sequence associated with the early stages of the failure process. The primary emphasis is on the development of theoretical models of the creep damage process, based on preliminary observations. Specifically, transmission electron microscope observations of creep damage in liquid phase sintered silicon nitride provide the experimental basis for a proposed failure initiation sequence. Physical expressions are derived for the processes of hole nucleation and enlargement into facet-sized cavities by viscous flow and solution/reprecipitation mechanisms. The experimental observations and theoretical analyses together suggest the existence of several alternative cavitation sequences depending on the stress level and the local microstructure. This work constitutes a first step toward the theoretical prediction of high temperate failure times in liquid-phase-sintered ceramics.

2. EXPERIMENTAL PROCEDURES

A number of ceramic materials, known to contain an intergranular phase were deformed in flexure at elevated temperatures to about five percent strain at the outer fiber, and then were frozen under load. The objective of the study was to assess the cavity morphologies as a basis for developing the creep models derived in the next section. The materials investigated were a commercial sintered alumina/silicate, a commercial hot pressed silicon nitride and a hot pressed SiAlON.

The commercial alumina/silicate (Coors AD90) is alumina with approximately 10 volume percent silicate glass. The composition of the glass is proprietary and is not known precisely, but Ca and Na are the primary impurities. The starting powder for the commercial silicon nitride (NC132) is α silicon nitride fluxed with MgO.[5,6] Hot pressing between 1700 and 1800°C causes a transformation from the α polymorph to the β structure by solution/reprecipitation.[7] The SiAlON* lies in the $B'_{60}/Si_3N_4/Y_3Al_5O_{12}$ compatability triangle within the $Si_3N_4/Al_2O_3/Y_2O_3$ phase diagram. The composition was chosen such that a eutectic liquid was an equilibrium phase at the hot pressing temperature of 1750°C, but would (hopefully) crystallize during a short anneal period at 1350°C.[8]

The most satisfactory method for characterizing creep cavity morphologies was transmission electron microscopy. Samples for microscopy were cut from both the tensile as well as compression surfaces of the creep bar near the region of maximum strain and were transformed into circular samples by gluing them to the end of a 3 mm rod and removing the square edges by grinding. Specimens were mechanically abraded to a thickness of about 50 μm on successively finer diamond abrading wheels and thinned in an ion mill until a small hole developed in the specimen center. The electron transparent region bordering the hole was examined in the TEM, after evaporation of a thin amorphous carbon layer onto the foil surface to prevent static charge accumulation under the electron beam.

---

*The samples were kindly provided by T.Y. Tien.

3. DAMAGE OBSERVATIONS

Cavitation was found to be inhomogeneous; (Fig. 1). Single isolated cavities were occasionally observed, but more commonly, clusters of cavities or subcritical cracks were identified. Since the sample deforms uniformly on a macroscopic scale, a significant portion of the strain must be accommodated by solution/reprecipitation. The extent to which cavitation accounts for the macroscopic deformation then must depend on the temperature and stress state, as well as the homogeneity of the microstructure.

A wide variety of cavity geometries and sizes was identified. The very small cavities, less than a grain facet length in dimension, generally provides the evidence necessary to characterize failure initiation in all three materials studied. The following generalizations were found to hold for the materials examined here. Cavities were associated with the amorphous second phase, manifest as pockets at triple grain junctions connected by continuous films along the two grain interfaces (Fig. 2). The three grain pockets were small, generally 5 to 20 nm, and typically triangular in cross-section. Long term oxidation of silicon nitride appeared to remove these pockets (Appendix I). From the limited number of grain boundaries observed, a simple systematic dependence of the grain boundary film thickness on the orientation of the adjoining grains was not found (Fig. 3) with the exception of special low angle grain boundaries, confirming previous studies.[9] (The problem of film width determination is not trivial[9,10]).

Small cavities (considerably smaller than the grain size) were found almost exclusively at triple grain junctions. Only a small proportion were evident along two grain interfaces. The smallest cavities were circular holes, located within three grain pockets (Fig. 4). It was expected that these holes were spherical and completely contained within the glass channel before thinning.* The observational frequency of circular holes was low.

The most commonly observed cavity shape was the triangular wedge (Fig. 5) located at a triple junction, as reported by other investigators.[3,11] In this study, triangular shaped cavities were observed to vary in size from small (7 nm) equilateral triangles (approximately the size of typical triple point glass pockets) to large (100 nm) wedges (about the size of a grain facet). Occasionally these cavities were associated with inclusions (Appendix I). A consistent feature of these triangular cavities was the presence of a thin film of amorphous material continuously coating the perimeter (Fig. 6). The larger cavities with the wedge morphology (Fig. 5b) exhibited consistently smaller values of the cavity angle, ψ, than the triangular-shaped cavities (Fig. 5a). Additionally, full-facet sized cavities were frequently observed (Fig. 5c).

---

*It was necessary to distinguish between holes nucleated during the experiment, and artifacts formed by ion beam thinning. Extensive observations indicated that holes with clearly defined edges located in relatively thick sections of the foil were creep cavities. Holes in thinner section of the foil with irregular, sloped edges were suspect.

The final category of small cavities consists of holes formed along two grain interfaces (Fig. 7). These holes, which assumed an oblate morphology were only detected in the mostly highly strained samples. Oblate holes of this type have been observed in other creep studies of silicon nitride.[3,12] While it is believed that the oblate holes observed here are creep damage, some sample preparation ambiguity remains.

Samples for high resolution electron microscope studies of the grain boundary structures were taken both from near tensile as well as compressive edges of the deformed silicon nitride and sialon bars which had been frozen under load. These were examined to determine whether solid contacts between grains had developed in these alloys when subjected to severe creep strains. Figure 3 illustrates the important point that for all the liquid phase sintered ceramics studied here, a continuous grain boundary film was found at every high angle grain boundary examined, regardless of whether the sample was taken from the compressive or tensile side of the sample. The observations also appeared to be independent of grain orientation with respect to the applied stress. Common to all these liquid phase materials were small angle boundaries that were free of a glassy phase. The nature and origin of these boundaries are discussed in Appendix VII, Part I.

4. MODELS FOR DEFORMATION IN THE PRESENCE OF A LIQUID PHASE

4.1 Introduction

Descriptions for high temperature deformation of liquid-phase sintered materials are proposed in which the high temperature strain is modelled as a parallel process consisting of steady-state creep in locally dense areas by solution/reprecipitation and deformation permitted by the growth of cavities.* The derivation for the strain rate due to mass transport through the liquid phase is a relatively straightforward process involving the identification of the relevant chemical potential gradient which drives the process. However the role of cavitation requires specific reference to the mechanisms by which damage develops within susceptible regions of the microstructure. Transmission electron microscopy of creep damage in several liquid-phase-sintered ceramic alloys provide the experimental basis for the proposed deformation models. The process of steady state creep by solution/reprecipitation in which there is no cavitation (and no failure) as well as processes of hole nucleation and enlargement into facet-sized cavities, by coupled viscous flow and solution/reprecipitation mechanisms, are analyzed, and the observations and analyses together suggest the existence of several alternative creep mechanisms which depend on the stress level and the local microstructure. The physical expressions for the deformation rates and failure times

---

* Viscous flow of the glass phase has been suggested as another possible deformation method. However, observations from before and after severe creep strains indicate that the distribution of the glass phase remains the same throughout creep and hence viscous flow of the glass cannot have contributed to the strain.

associated with each mechanism are derived and the resultant implications for characterizing cavitation prone microstructural regions are discussed.

4.2 Steady State Creep by Solution/Reprecipitation

At stress levels that are insufficient for cavitation, creep deformation is accommodated by solution/reprecipitation. For locally dense regions, the mass transfer is motivated by a chemical potential gradient induced by the stress difference between adjacent grain boundaries due to their relative orientation with respect to the applied stress. Solution/reprecipitation is a series process which involves the rate for solid atoms to be dissolved into the liquid and the rate for matter diffusion through the liquid phase from the grain boundaries in high compression to neighboring boundaries under lower compressive stress. The expression for the creep rate permitted by steady-state solution/reprecipitation are given in Appendix II.

4.3 Hole Nucleation

At high temperatures, but low stress levels, liquid phase sintered materials may deform continuously without failure by solution/reprecipitation. At higher stress, failure occurs by the nucleation and coalescence of cavities. In the absence of pre-existent porosity, the nucleation of holes within the glass second phase may be regarded as the initial step in the failure sequence. Hole nucleation can be analyzed using standard nucleation concepts, involving vacancy coalescence probabilities. The analysis commences with the thermodynamic potential change, $\Delta\phi$, associated with hole formation. For holes that form entirely within the second phase;[13]

$$\Delta\phi = -\sigma\ \Delta V + \gamma\ \Delta A \tag{1}$$

where ΔV and ΔA are the volume and surface area changes induced by the hole, γ is the vapor/liquid-phase surface energy and σ is the net stress acting in the direction of material displacement. A critical nucleus develops when $\Delta\phi/\Delta V=0$, dictating the existence of a critical nucleation stress, σ^*.[14] Specific computation of the critical stress requires determination of the hole nucleation rate from the product of the number of nuclei at the critical size with the probability that the holes will be enlarged to a supercritical size by the addition of vacancies.[15] Two nucleation configurations are of primary interest: spherical holes along the three grain channels (Fig. 4) and oblate holes between two grain interfaces (Fig. 7).

4.3.1 Spherical holes: Nucleation along three grain channels. Observations suggest that three grain channels in typical liquid-phase sintered materials are generally of sufficient size to accommodate a critical nucleus with spherical morphology (Fig. 2). The thermodynamic potential for the nucleation of a spherical hole, radius r, is:[14]

$$\phi = 4\pi r^2\gamma - (4/3)\pi r^3 p \tag{2}$$

where p is the hydrostatic tension in the liquid. The potential exhibits a maximum, ϕ_{max} (at $\partial\phi/\partial r|_p = 0$);

$$\phi_{max} = 16\pi\gamma^3/3p^2 \tag{3}$$

corresponding to a critical nucleus size;

$$r^* = 2\,\gamma/p \tag{4}$$

The number of nuclei, n_c, of the critical size in a unit volume of second phase is:[14]

$$n_c = c_3\, n_o \exp\left[-\phi_{max}/kT\right] \tag{5}$$

where n_o is the number of available nucleation sites in a unit volume and c_3 is the volume fraction of three grain channel second phase, such that $n_o c_3$ is the number of nuclei in a unit volume of the second phase. The time dependent probability of adding a vacancy to a critical nucleus* is:

$$\omega_t = \frac{8\,kT}{3\eta\Omega^{5/3}} \left(\frac{\gamma}{P}\right)^2 \tag{6}$$

where Ω is the molecular volume and η is the viscosity of the second phase.

---

* The result can be derived directly from the Raj and Ashby[15] solution if the diffusivity is replaced by the viscosity using the Stokes-Einstein equation and the hole geometry is appropriately modified.

Combining eqns. (3), (5) and (6), the spherical hole nucleation rate becomes;

$$\dot{n} = \frac{8\ kT\ c_3 n_o}{3\eta\Omega^{5/3}} \left(\frac{\gamma}{p}\right)^2 \exp\left[-\frac{16\pi\gamma^3}{3p^2 kT}\right] \tag{7}$$

The nucleation rate varies rapidly with stress and hence, Eq. (7) can be re-expressed in terms of a 'critical' hydrostatic tension for hole nucleation, p^*[15] (by setting $\dot{n}$ equal to a prescribed nucleation rate, $\dot{n}_o$):

$$(p^*)^2 = \left(\frac{16\pi\gamma^3}{3\ kT}\right) \left[\ell n \left[\frac{8kT\ c_3 n_o \gamma^2}{3\eta\Omega^{5/3}(p^*)^2 \dot{n}}\right]\right]^{-1} \tag{8}$$

To facilitate comparison with the corresponding stress for hole nucleation along a two-grain channel containing a second phase of initial thickness, δ_o, the critical stress in Eq. (8) is re-expressed in terms of the dimensionless critical stress parameter for spherical hole nucleation, $\Sigma_3 = p^*\delta_o/\gamma$,

$$\Sigma_3^2 = \left(\frac{16\pi}{3}\right) \xi \left[\ell n \left[\frac{8c_3 kT}{3\Sigma_3^2 \beta}\right]\right]^{-1} \tag{9}$$

where ξ and β are the dimensionless parameters $\xi \equiv \gamma\delta_o^2/kT$ and $\beta \equiv \eta\ \dot{n}\Omega^{5/3}/n_o\delta_o^2$.

This prediction of the critical stress is contingent upon the maintenance of the stress p^* during the nucleation period (Eq. (3)).

At high local stresses the nucleus is very small (Eq. (4)) and, for relatively large pockets, accommodation can be readily achieved through a minor transfer of matter from the pocket walls (e.g., by solution/reprecipitation)[16] or by slight relaxation of the elastic strain within the grains. However, at lower stress levels, or for small pockets, a stress drop can be expected to accompany hole nucleation, resulting in a suppression of the nucleation event. Equations (8) and (9) then constitute a lower bound nucleation condition.

4.3.2 Oblate holes: Nucleation along two grain channels. The nucleation of oblate holes along two grain channels occurs when the width of the viscous phase is too narrow to admit the formation of stable spherical holes. Since oblate hole formation results in grain displacements normal to the grain interface (Fig. 8), the thermodynamic potential of the hole can be expressed as;

$$\phi = \pi\gamma[2a^2+\pi a\delta+\delta^2] - \pi\sigma_n[a^2\delta+\pi a\delta^2/4+\delta^3/6] \qquad (10)$$

where a is the radius of the hole (Fig. 8) and σ_n is the stress normal to the two grain channel.* In general, δ will increase during nucleation in order to conserve the volume of the second phase, as expressed for each volume element, V, by;

*The normal applies stress presumably dictates the stress within the second phase. Note, however, that viscous flow within a very narrow channel may not be rapid enough to permit equilibration of the hydrostatic tension.

$$V = 2\sqrt{3}\ \delta_o b^2 \equiv \delta[2\sqrt{3}\ b^2-(\pi a^2+\pi^2 a\delta/4+\delta^2\pi/6)] \tag{11a}$$

or

$$\delta = \delta_o \left[1-(\pi/2\sqrt{3})\ (a/b)^2-(\pi^2/8\sqrt{3})a\delta/b^2-(\pi/12\ 3)(\delta/b)^2\right]^{-1} \tag{11b}$$

where 2b is the spacing between holes along two grain boundaries. For the relatively thin films observed ($\delta << a,b$), Eq. (11b) reduces to:

$$\delta = \delta_o \left[1-(\pi/2\ 3)(a/b)^2\right]^{-1} \tag{12}$$

Differentiation of Eq. (12),

$$\frac{d\delta}{da} = \frac{(\pi/\sqrt{3})\ (\delta_o a/b^2)}{[1-(\pi/2\sqrt{3})(a/b)^2]^2} , \tag{13}$$

reveals that the film thickness change is substantially smaller than the increase in hole radius when the hole spacing is relatively large ($b >> a,\ \delta_o$). For this condition, the stress also remains essentially invariant during the nucleation event and the critical size at hole nucleation ($\partial\phi/\partial a|_\sigma = 0,\ \delta = \delta_o$) becomes:

$$a_c = (\pi\delta_o/8)\ [(4\gamma-\sigma_n\delta_o)/(\sigma_n^*\delta_o-2\gamma)] \tag{14}$$

Hole nucleation is thus only feasible in the range, $4\gamma/\delta_o > \sigma_n > 2\gamma/\delta_o$. Within this range the probability of adding a vacancy to the nucleus is

$$\omega_t = \frac{\delta_o(\pi a_c+\delta_o)kT}{6\eta\Omega^{5/3}} \tag{15}$$

The critical stress parameter for oblate hole nucleation Σ^2 ($\equiv \sigma_n^* \delta_o/\gamma$) deduced from the preceding results is plotted in Fig. 9a, and compared with the solution for the spherical hole. Note that the oblate and spherical hole solution coincide for $\Sigma_2 > 4$, because a spherical hole can now nucleate in the two grain channel. However when $\Sigma_2 < 4$, oblate holes exhibit a higher nucleation stress, by virtue of a volume/surface area ratio smaller than that associated with the spherical hole. Specific nucleation stresses pertinent to hot pressed Si_3N_4 are plotted in Fig. 9b.

4.3.3 The role of grain boundary sliding. The nucleation stresses predicted in the preceding section considerably exceed the applied stresses σ at which holes are observed to form (except in regions of large initial film thickness) implying the existence of microstructurally induced stress concentrations. The stress enhancement that develops in the presence of microstructural inhomogeneities (such as large grains or inclusions, Appendix III[17]), and as a consequence of steady state grain boundary sliding, may be inadequate because only about twice the level of the applied stress is reached. However, much larger transient tensile stresses are induced during abrupt grain boundary sliding events,[18] with the magnitude and location of the tensile stresses depending on the planarity of the boundary. For the sliding of planar boundaries, subject to a shear stress σ_{xy}, tensile stresses are induced near the grain edges (Fig. 10) given by;[18]

$$\hat{\sigma} \sim \sigma_{xy}\sqrt{\ell}\,[GD_{\ell}\delta_{o}\Omega t_{\ell}/(1-\nu)kT]^{-1/6} \tag{16}$$

where ℓ is the length of the freely sliding boundary, G is the shear modulus, D_{ℓ} is the diffusivity of the solid phase through the liquid, t_{ℓ} is the duration of the sliding transient, and ν is Poisson's ratio. For nonplanar boundaries transient sliding generates tensile stresses at boundary undulations (Fig. 11) given by;[19]

$$\sigma \sim 3\sigma_{xy}\lambda/4h \tag{17}$$

where λ is the wavelength and h is the amplitude of the undulation (Figs. 9, 11). These stress concentrations can be of adequate magnitude to account for the observed hole formation within the amorphous pockets at grain edges. However, caution should be exercised in applying transient related nucleation concepts until adequate attention has been devoted to both the mechanism of grain boundary sliding transients and the duration of the stress concentration (vis-a-vis, the time needed to nucleate a stable hole). Neither topic has yet been examined in convincing detail.

4.4 Cavity Evolution

The critical stress levels for hole formation within the second phase at three and two grain channels provide the basis for interpreting and predicting the early stages of high temperature failure in ceramics containing an intergranular phase. At local stress levels below the stress needed to nucleate holes at three grain channels, no known failure mechanism exists and the material deforms continuously,

without failure, by solution/reprecipitation. The lower critical stress thus constitutes a failure threshold in fully dense materials, but creep can still occur below this stress. The practical utility of this threshold is dictated by the magnitude of the tensile stress concentration that develop in response to grain boundary sliding, grain rotation, and other stress concentrating mechanisms.

At stresses in excess of this critical level, full-facet sized cavities develop from the hole nuclei. The time, t, needed to form such cavities constitutes an important component of the eventual failure time. This time is dictated by the cavity formation mechanism and by the response of the surrounding microstructure.

When the normal stress is in the range required for nucleation of oblate holes, full-facet cavitation proceeds by the coalescence of these holes, via a viscous flow mechanism (Fig. 12a-c). However, at lower levels of normal stress, but still large enough to satisfy the requirement for spherical hole nucleation within the three grain channels, a more complex sequence occurs. Initially, pocket depletion proceeds by viscous flow of the second phase into the neighboring two grain channels (Fig. 12d-f), in conjunction with cavity enlargement by the diffusive transport of the constituents of the primary phase through the second phase. At the higher stress levels within this range, pocket depletion continues to near completion and enlargement of the cavity to full-facet dimension then proceeds by viscous flow (Fig. 12g). However, at lower stresses, complete pocket depletion is prohibited and full-facet cavitation is dominated by the solution/

reprecipitation rate (Fig. 12h). Each of these effects, schematically summarized in Fig. 12, will be examined in the present section.

The specific rates of hole growth depend upon the local stress level and consequently, on the manner in which the matter displaced from the hole is accommodated by the creep of the surrounding material. Two extremes provide useful insights. When the cavitation occurs uniformly throughout the microstructure, the local stress attains the level of the applied stress, resulting in an unconstrained cavitation time, t^u. Conversely, when cavitation is isolated, the surrounding grains exert a constraint on the cavitating interface, reducing the local stress to;

$$\sigma_\ell/\sigma_\infty \approx 1 - 4\,\dot{\delta}/9\,\dot{\varepsilon}_\infty \tag{18}$$

where $\dot{\delta}$ is the rate of displacement of the centers of the neighboring grains, in the direction of the applied stress, and $\dot{\varepsilon}_\infty$ is the creep-rate of the surrounding material (at the level of the applied stress). The reduced local stress increases the cavitation time by an amount t^c, such that the total time, t, has the form;

$$t = t^u + t^c \tag{19}$$

The constrained component, t^c, can always be expressed as a product with $\dot{\varepsilon}_\infty$, by virtue of the dependence of σ_ℓ on $\dot{\varepsilon}_\infty$ given in Eq. (18). This product, $t^c\dot{\varepsilon}_\infty$, depends primarily on the geometric changes that accompany cavitation (independent of the mass transport mechanism) and

is thus relatively mechanism insensitive. Conversely t^u is expected to exhibit appreciable mechanism sensitivity. Detailed computations of t^u and t^c for each of the mechanisms discussed above are presented in Appendix IV.

4.4.1 Oblate hole coalescence. At stress levels above that needed to nucleate holes within two grain channels (Fig. 9, Eq. (15)), facet-sized cavities develop by the growth and coalescence of the oblate holes within the channel (Figs. 7, 8). The growth rate of oblate holes can be computed from standard expressions for the pressure distribution that develops within a parallel sided channel containing a flowing viscous fluid;[20]

$$\nabla^2\sigma(r_x) = 12\eta\dot{\delta}/\delta^3 \tag{20}$$

where σ is the stress at a distance r_x from the hole center (Fig. 8). If the liquid phase penetrates the solid (as required for liquid phase sintering) and contains an array of holes with spacing 2b and radius a, the boundary conditions needed to solve Eq. (20) can be specified as follows: symmetry at the mid-position between holes requires that $d\sigma/dr_x = 0$ at $r_x = b$ and chemical potential continuity at the hole surface demands that $\sigma = \gamma(1/a + 2/\delta)$ at $r_x = a$. Then, imposing volume conservation (Eq. (11a)) the solution to Eq. (20) can be expressed in terms of the hole growth rate as;[21]

$$\dot{\alpha} = \left(\frac{\delta_0^2}{5b^2\eta}\right)\left[\frac{(1-0.9\alpha_0^2)[\sigma_\ell - \gamma_\ell(1/\alpha b+2/\delta)(a-0.9\alpha^2)]}{\alpha(1.1-\alpha^2)[0.96\alpha^2-\ell n\alpha-0.72-0.23\alpha^4]}\right] \tag{21}$$

where $\alpha = a/b$ (α_0 is the initial value at hole nucleation) and δ_0 is the initial channel thickness. The pertinent local stress can be deduced by combining Eqs. (13) and (18) to obtain (for a boundary normal to the applied stress);

$$\sigma_\ell/\sigma_\infty = 1 - 16\sqrt{3}\pi\ \delta_0\alpha\dot{\alpha}/9\ (2\sqrt{3} - \pi\alpha^2)^2\ \dot{\epsilon}_\infty \tag{22}$$

Inserting the local stress into Eq. (21) and integrating between α_0 and 1 gives the fully-constrained time;

$$t_p^c\ \dot{\epsilon}_\infty = (8\sqrt{3}/9\pi)\ (\delta_0/\ell)\ T_1^c \tag{23a}$$

where T_1^c is a function of a_0/b and the critical stress parameter, Σ_2. For the important case where $\delta < a_0$, and $\Sigma_\infty(\equiv(\sigma_\ell\delta_0/\gamma_\ell) >> 1$;

$$T_1^c = 10 - [1.1 - \alpha_0^2]^{-1} \tag{23b}$$

The equivalent result for unconstrained hole growth is obtained by numerical integration of Eq. (21) between α_0 and 1, with $\sigma_\ell = \sigma_\infty$. The coalescence times for unconstrained conditions are given by

$$t_p^u\ \sigma_\infty/\eta = T_1^u \tag{24}$$

where T_1^u is a function of b/δ_o and a_o/b, plotted in Fig. 13. Note that the hole spacing b has a relatively minor influence on t_p^c (at least when $a_o << b$) and that the $t_p^c\varepsilon$ increases as δ_o increases. However, t_p^c may not increase as δ_o increases because $\dot{\varepsilon}_\infty$ exhibits an inverse dependence on δ_o.[16]

4.4.2 Pocket depletion. At stress levels below that required to nucleate holes on two grain interfaces, but above that needed to nucleate holes within pockets, the firs event to initiate during creep rupture is the viscous expansion of the hole within the pocket. This leads to the essential depletion of the pocket (Fig. 14a), by viscous flow of the amorphous phase into the surrounding two grain channels, resulting in an increased film thickness along the two grain interfaces. The process is controlled either by the stress at the hole surface or by the flow rate into the channel. Specific results can be obtained by considering the case where the three grain channel is triangular in cross section* and the grains displace by flow of the second phase.

Viscous flow along the boundary channel is characterized by the two-dimensional equivalent of Eq. (20);

$$\frac{d^2\sigma(x)}{dx^2} = \frac{-12\eta\dot{\delta}}{\delta^3} \tag{25}$$

* The included angle at the three grain channels (ψ in Figs. 5 and 14b) in the presence of complete penetration between the solid by the liquid phase must be dictated by anisotropy of the solid/liquid interface energy.

Here x is the distance from the grain corner. Symmetry requires that $d\sigma/dx = 0$ at the grain facet center ($x=\ell/2$; Fig. 14a) while the stress at the mouth of the channel ($x=d$) is governed by the stress at the surface of the hole,

$$\sigma(d) \approx \Upsilon\gamma / r_c \tag{26}$$

where r_c is the radius of curvature of the hole and Υ ranges between 2 (when the hole is spherical) and 1 (when the hole becomes cylindrical). This stress prevails at the channel mouth provided that viscous flow within the pocket occurs at a sufficiently rapid rate that the stresses in the region between the hole and the channel opening are equilibrated. Integration of Eq. (25) subject to these boundary conditions gives the stress distribution within the channel as;

$$\sigma(x) = \frac{6\eta\dot{\delta}}{\delta^3}[d^2-x^2] + (x-d)] + \frac{\Upsilon\gamma}{r_c} \tag{27}$$

and the separation rate becomes,

$$\dot{\delta} = \frac{\delta^3[\sigma - \Upsilon\gamma(1-2f)/r_c]}{\eta\ell^2[1-6f + 18f^2 - 14f^3]} \tag{28}$$

where $f = d/\ell$. The surface tension term, γ/r, is of significant magnitude (relative to the local stress) during the two extremes of the depletion process: both immediately after nucleation of the hole and as complete hole deplection is approached. Since in the presence of stress concentrations the initial expansion of the cavity occurs

rapidly, it is surmised that the surface tension term does not significantly affect the depletion rate until depletion of the channel is nearly complete (when the surface tension stress increases continuously as the second phase is drawn into the mouth of the two grain interface (Figs. 6,14b)). This process exhibits a characteristic relaxation time t_d (Appendix III). When $t \ll t_d$, the retardation effects that occur in the final stage can be neglected, and the time t_d for 'depletion' of the pocket can be expressed directly in terms of the displacements, from Eqs. (18) and (28), as ($\gamma\gamma/r_c = 0$);

$$t_d^c \dot{\epsilon}_\infty = (4/9)\ (\delta_d - \delta_o)/\ell \quad , \tag{29a}$$

$$t_d^u \sigma_\infty/\eta = \ell^2[1-6f + 18f^2 - 14f^3]\ [1/\delta_o^2 - 1/\delta_d^2] \tag{29b}$$

where d is the pocket size (Fig. 14), f is the three grain cavity size ratio (d/ℓ), δ_d is the thickness of the two grain channel at depletion given by;

$$\delta_d \approx \delta_o + d^2 \tan(\psi/2)/\ell(1 - f) \tag{30}$$

and ψ is the angle contained by the triangular pocket (Fig. 14b). The 'depletion' time, t_d, is the time that expires while sufficient material is removed from the pocket that the increase in curvature of the liquid surfaces causes the surface tension stress to increase to a significant fraction of the local stress. It should thus be recognized that a small quantity of residual liquid, in excess of that required

for wetting, may remain within the pocket, for a period $t \gg t_d$. In fact, the presence of residual liquid, as influenced by the level of the local stress, has a direct association with the next step in the failure sequence, which may occur either by viscous hole extension into the two grain channel or by solution/reprecipitation.

4.4.3 Meniscus propagation. When the local stress after hole depletion exceeds $2\gamma/\delta_d$, the liquid meniscus can be drawn into the channel mouth (Figs. 6,14b), by allowing a positive pressure gradient to be retained within the liquid. Under these conditions, the thickness of the liquid film increases, as the meniscus enters the channel. Hence, the meniscus continues to be drawn into the channel, resulting in a meniscus velocity;

$$\dot{\rho} = \frac{(\delta_d/\ell)^2(1-d/\ell)^2\ \sigma - \gamma(1-\rho)^2/\delta_d(1-d/\ell)}{\eta(1-\rho)\ (1-6\rho+18\rho^2-4\rho^3)} \tag{31}$$

where $\rho = w/\ell$, such that w is the distance from meniscus tip to the grain corner (Fig. 14b).

However, the continuous increase in meniscus velocity as it progresses along the channel is likely to induce a meniscus instability and the consequent formation of a finger-like perturbation (Figs. 15,16).[22] Finger formation is characterized by a critical wavelength;

$$\lambda_c = \pi\left(\frac{\gamma\delta^2}{3\eta\dot{w}}\right)^{1/2} \tag{32}$$

The meniscus is capable of developing instabilities when λ_c is appreciably smaller than the total width, z, of the cavity front, e.g., when $\lambda_c < z/4$. Hence, for cavities emanating from three grain pockets, with a cavity front width $z \approx \ell$, insertion of the meniscus velocity from Eq. (31) into Eq. (32) predicts a critical dimension, ρ_c ($\equiv w_c/\ell$), for the onset of finger formation. For unconstrained conditions;

$$\sigma_\infty \ell/\gamma \approx [16\pi^2/3]\ (1-\rho_c)(1-6\rho_c+18\rho_c^2-4\rho_c^3) \tag{33}$$

Once finger formation initiates, at ρ_c, cavitation along the grain facet proceeds very rapidly and the time expired at the onset of finger formation can be essentially equated to the cavitation time.

4.4.4 Solution/Reprecipitation. When the local stress is not high enough to induce full-facet cavitation by viscous flow mechanisms, the depleted three grain junction holes extend (more slowly), by solution/reprecipitation. In this case, the transport of material is motivated by a stress difference between the liquid film on the cavity surface and the liquid within the channel and entails the transport of the solid phase through the liquid, from cavity surface onto the grain surfaces within the channel. Hence, further redistribution of the liquid phase is not necessarily involved. As discussed earlier, the process can be either diffusion controlled or interface controlled. Before proceeding, it is noted that solution/reprecipitation is expected to occur concurrently with pocket depletion (by

viscous flow). A rigorous analysis would examine this concurrence. However, for simplicity, solution/reprecipitation is considered to initiate when hole depletion is essentially complete because, for most practical systems, the solution/reprecipitation process is the slowest constituent of full-facet cavitation.

Diffusion controlled solution/reprecipitation requires that a chemical potential gradient exist along the channel to drive migration of the solid phase. This can only be achieved in the presence of a pressure gradient within the liquid. For this geometry a suitable pressure gradient exists if the liquid phase continues to flow within the channel, throughout the process. Viscous flow thus may be a necessary accompaniment to solution/reprecipitation.*

The rate of mass transport along a grain channel is given by the differential equation

$$\frac{d^2\sigma(x)}{dx^2} = -\frac{12kT\dot{\Delta}}{\Omega D_\ell C_\ell \delta_\ell} \tag{34}$$

where $\dot{\Delta}$ is the rate of separation of the grain centers induced by matter deposition away from the grain surfaces, D_ℓ is the diffusivity

* The viscous flow prerequisite may be obviated in the presence of grain boundary ledges that substantially impede viscous flow through the channel, or in boundaries where the intergranular phase is sufficiently constrained that it can sustain normal stress gradients.

of the solid phase in the liquid and C_ℓ is the solubility of the solid in the liquid. Integration of Eq. (34), subject to the same boundary conditions pertinent to the viscous flow in the channel, gives;

$$\sigma(x) = \left(\frac{kT\dot{\Delta}}{2\Omega D_\ell C_\ell \delta_\ell}\right)\left[\left(d^2 - x^2\right) + (x-d)\right] + \frac{\Upsilon\gamma}{r_c} \tag{35}$$

Comparison of Eqs. (27) and (35) indicates that;

$$\frac{\dot{\Delta}}{\dot{\delta}} = \frac{12\Omega D_\ell C_\ell \eta}{kT\delta^2} \tag{36}$$

Combining Eqs. (18), (28), and (36) and recognizing that the local stress (Eq. (18)) is dictated by the sum, $\dot{\delta} + \dot{\Delta}$, the differential equation describing the grain separation rate due to matter deposition becomes,

$$\dot{\Delta}(t)\left\{\frac{\ell^2 kT[1-6f(t) + 18f^2(t) - 14f^3(t)]}{12\Omega D_\ell C_\ell \delta_\ell(t)} + \frac{4\sigma_\infty}{9\dot{\varepsilon}_\infty}\left[1 + \frac{kT\delta^2(t)}{12\Omega D_\ell C_\ell \eta}\right]\right\}$$
$$= \sigma_\infty - \Upsilon\gamma(1-2f)/r_c \tag{37}$$

Cavity growth is controlled in this instance by the rate of transport of the solid phase through the liquid that exists within the two grain channel (thickness, δ_d) and along the cavity surface (thickness, δ_s). Specifically, domination of the cavity growth rate by diffusion through the liquid over the cavity surface, vis-a-vis diffusion along the channel, is presumed to be dictated by the relative film thickness, δ_s/δ_d,

at the two locations (the role of δ_s/δ_d being analogous to that of the diffusivity ratio $D_s\delta_s/D_b\delta_b$ in single phase systems). However, for the present problem, the requirements on the contained angle, ψ, are not readily specified. It is tempting to propose that diffusion through the fluid film over the cavity surface is rapid enough to maintain a constant contained angle, ψ, during cavity growth. However, this assumption yields an inadmissible solution for unconstrained cavity growth; as well as being at variance with the microstructural observations (Fig. 5), which suggest that ψ decreases as the cavity expands. Instead, the observations suggest that cavities only extend along boundaries normal to the applied stress and do not progress along the inclined boundaries. Adopting that assumption, volume conservation of the solid phase (the liquid phase volume is necessarily constant) permits the grain separation rate, $\dot{\Delta}$ to be expressed as;

$$\dot{\Delta} = \ell f_o \dot{f} \tag{38}$$

Solutions for t_p can, in principle, be obtained by combining Eqs. (25), (37), and (38), but the expressions are unwieldy. In seeking physically reasonable simplifications it is noted that Eq. (36) can be rearranged using the Stokes-Einstein equation. Evaluating that expression for measured values of the film thickness illustrates the trend that $\dot{\Delta} >> \dot{\delta}$. For levels of the applied stress at which cavitation is observed, the surface tension term is relatively insignificant

($\sigma_\infty >> \gamma\gamma/r_{c'}$). Both the implied loss of driving force and neglect of the stress at the channel mouth give lower bound cavitation time results;

$$t_p^c \dot{\varepsilon}_\infty > (2/9)\ (f_o)\ [1-2f_o] \tag{39a}$$

$$t_p^u \sigma \left(\frac{C_\ell D_\ell \delta \Omega}{kT\ell^3}\right) > \left\{(f_o/192)\left[1-16(f_o)+48(f_o)^2-48(f_o)^3+16(f_o)^4\right]\right\} \tag{39b}$$

where $f_o(\ d_o/\ell)$ is the ratio of the initial pocket size to the grain facet length. The constrained time t_p^c (being insensitive to the atom transport rate) can be expected to exceed the lower bound by up to ~2, (as obtained when $\dot{\delta} = \dot{\Delta}$) for the same geometric assumption. However, the corresponding unconstrained time could be substantially in excess of the lower bound.

If cavity growth by solution/reprecipitation is <u>interface</u> limited,[16] the stress within the liquid layer at the grain interface can equilibrate at the level of the locally applied stress; except near the cavity tip where the stress must decrease to about zero as the cavity surface is approached. Assuming that the stress gradient within the liquid can be supported either by the intergranular film itself or by fluid flow into the channel mouth and over the cavity surface, the matter deposition rate along the grain interface is simply;

$$\Delta\dot{V}_{int} = \sigma_\ell \Omega k_\ell \ell (\ell - d_o)/kT \tag{40}$$

where k_ℓ is the rate of condensation of atoms from the liquid film onto the grain surface (a parameter that can be determined from crystallization or creep studies).[16] Then, subject to volume conservation (Eq. (38)), the cavitation time for equilibrium shaped cavities, when $\dot{\Delta} >> \dot{\delta}$, becomes,

$$t_p^c \dot{\varepsilon}_\infty = (2/9)\ (f_o)\ [1-2f_o] \quad , \tag{41a}$$

$$t_p^u \sigma_\infty k_\ell \Omega / kT = \ell [1-f_o] \quad . \tag{41b}$$

Note that the constrained result is necessarily the same as that for the diffusion controlled process.

4.4.5 Comparison of cavitation times. Comparison of the cavitation times for each of the prospective processes suggests that, under fully-constrained conditions (when only the cavity morphology and matter conservation requirements are important) the cavitation times are similar for all processes; with distinctions between mechanisms depending on specific hole spacings, pocket shapes and sizes, film thicknesses etc. Some typical choices for liquid phase sintered Si_3N_4, indicate that the fastest constrained process for this material is pocket depletion, while solution/reprecipitation is the slowest. When the constraint relaxes, during subsequent cavity growth, appreciably different cavitation rates can be attributed to the various growth mechanisms, depending on η, D_ℓ, b, C_ℓ, etc.

5. DISCUSSION AND IMPLICATIONS

Transmission electron microscopy of an L.P.S. silicon nitride, deformed at high temperature, lead to the identification of early stage failure mechanisms. Growth and coalescence of oblate holes along two grain boundries was considered responsible for interface failure at the highest local stress. At lower stress levels, below a critical value, the material deformed continuously without failure by solution/reprecipitation. At intermediate stresses failure was considered to initiate by the formation of spherical holes along three grain channels, which were then depleted by viscous flow of glass into neighboring two grain interfaces. Subsequent full-facet-sized cavity formation was predicted to occur either by continued viscous flow, at intermediate stresses, or by solution/reprecipitation at low stresses. In the former case, the liquid meniscus was drawn into the two grain channel, until the film thickness was sufficiently enhanced to permit either hole nucleation or the formation of finger-like perturbations. Otherwise, the depleted three grain channels expanded, more slowly, by solution/reprecipitation. Nevertheless, the time required to form isolated full-facet cavities, being subject to constraint, was shown to be relatively mechanism insensitive. The primary controlling variables in this process are the creep-rate of the material and the geometry of the cavity.

The steady-state deformation rate of liquid phase sintered materials is determined by solution/reprecipitation with only small transient strains occurring by viscous flow. The specific viscosity

of the second phases is thus relatively unimportant in the initial cavitation process, even when the cavitation mechanism themselves involve viscous flow. The most important parameters are the diffusivity of the major constituents within the second phase and/or the surface condensation rate of atoms of the major phase in the presence of the minor phase. These solution/reprecipitation related mass transport parameters are not overtly related to the viscosity of the second phase. However, some interdependence between η, D_ℓ, and k_ℓ may reasonably be expected, even though the Stokes-Einstein relation* may be misleading when applied to the narrow channels encountered here. The determination of D_ℓ, C_ℓ, and k_ℓ from creep and crystallization studies on this class of materials emerges from this study as a prime requirement for the interpretation and prediction of the early stages of failure.

The geometric aspects of full-facet cavitation are intimately associated both with the microstructure, the local stress and the local deformation rate. The presence of microstructural inhomogeneities, such as large grains or inclusions, influences the local creep rate and can induce stress concentrations up to $\sim 2\sigma_\infty$.[23] The enhanced stress encourages the nucleation of holes along two grain channels. Premature cavitation at three grain interfaces can also occur along exceptionally thick second phase channels, especially where chemical composition fluctuations[24] or surface tension anisotropy favor a low local surface energy, or in the presence of

---

*$D_\ell = kT/6\pi\eta\Omega^{1/3}$.

inclusions. In several materials of this class, phase separation within three grain boundaries has been observed.[25-27] This heterogenity results in a lower stress being required for nucleation of cavities within these regions.

More generally, the thin second phase films prohibit hole nucleation along two grain channels in the absence of substantial stresses from grain boundary sliding transients. Consequently, hole nucleation within three grain channels is more likely followed by pocket depletion and growth by solution/reprecipitation. This process results in relatively wide cavities and appreciable constraint, thus minimizing the influence of such cavities in eventual failure. Note, however, that relatively large second phase pockets are capable of inducing a sufficient thickening of the second phase along the two grain channels, during pocket depletion, that rapid viscous formation of a facet-sized cavity may ensue. Hence, the size, disposition and heterogeniety of the second phase pockets (which is related to the grain size, the volume fraction and chemical composition of the second phase, and the prior thermal history) also constitute an important microstructural feature.

Subsequent stages of the failure process involve the coalescence of facet-sized cavities to form a discrete crack and the subsequent extension of the crack to critical dimensions required for spontaneous fracture. The advance of sub-critical cracks proceeds by the nucleation and growth of cavities in the concentrated stress field ahead of the crack. The local stresses in the crack field may then be large

enough to induce holes along two grain channels, and the constraint may become sufficiently small that cavitation may progress by viscous hole coalescence, without significant dependence on the creep relaxation properties of the material. Thus, once cracks begin to grow a transition occurs and the critical hole nucleation stress and the viscosity of the second phase then exert a dominant influence on the crack growth rate.

Ultimately, the time required for failure of critical components in high temperature environments will be computed from theory. The models proposed here for the early stages of failure of elevated temperature comprise a first step in a complete theoretical description of high temperature failure in liquid-phase sintered ceramics.

REFERENCES

1. S.M. Wiederhorn, "Subcritical crack growth in ceramics," from Fracture Mechanics of Ceramics, Vol. 2, eds. R.C. Bradt, D.P.H. Hasselman and F.F. Lange; (Plenum Press, 1974), p. 613.
2. C.C. Ahn and G. Thomas, "Microstructure and Grain-Boundary Composition of Hot-Pressed Silicon Nitride with Yttria and Alumina," J. Amer. Ceram. Soc. 66, 1983, p. 14.
3. F.F. Lange, D.R. Clarks, B.I. Davis, "Compressive Creep of Si_3N_4/MgO alloys. Part I: Effect of Composition," J. Mater. Sci., 15, 1980, p. 601.
4. M.H. Lewis, B.S.B. Karunaratne, J. Meredith, and C. Pickering, "Mechanisms of creep deformation and fracture in single and two-phase Si-Al-O-N ceramics," from Creep and Fracture of Engineering Materials and Structures, eds. B. Whilshire and D.R.J. Owens; (Pineridge Press, Swansea, UK), p. 365.
5. P. Grieveson, S. Wild, and K.H. Jack, "Nitrogen Ceramic Structures" in Special Ceramics, 4, ed. P. Popper (Stoke-on-Trent) Brit. Ceram. Res. Assoc., (1972), p. 385.
6. S. Prochaska and C. Grescovich, "Synthesis and Characterization of Pure Silicon Nitride Powder, Ceram. Bull., 57, (1978), p. 579.
7. P. Drew and M.H. Lewis, "The Microstructure of Silicon Nitride Ceramics During Hot Pressing Transformations," J. Mat. Sci., 9, (1974), p. 261.
8. T. Y. Tien, private communication (1982).

9. O.L. Krivanek, T.M. Shaw, and G. Thomas, "Imaging of thin intergranular phases by high resolution electron microscopy," J. Appl. Phys. 50 (6). June 1979, p. 4223.

10. D.R. Clarke, "On the detection of thin intergranular films by electron microscopy," Ultra Microscopy 4, 1979, p. 33.

11. R.M. Arons and J.K. Tien, "Creep and strain recovery in hot pressed silicon nitride," J. Mat. Sci. 15, 1980, p. 2046.

12. N.J. Tighe, "Analysis of Creep Microstructures in Silicon Nitride by AEM,": from Electron Microscopy 1982, 10th Int. Cong. on Electron Microscopy, V. 2, 1982, p. 399.

13. J.P. Hirth and G.M. Pound, Condensation and Evaporation - Nucleation and Growth Kinetics, (Pergamon Press, The MacMillan Company, New York, 1963).

14. J.C. Fisher, "The fracture of liquids," J. Appl. Phys. 19, November 1948, p. 1062.

15. R. Raj and M.F. Ashby, "Intergranular fracture at elevated temperatures," Acta Met., 23, 1975, p. 653.

16. R. Raj and C.K. Chyung, "Solution-reprecipitation creep in glass ceramics," Acta Met. 29, 1981, p. 159.

17. S.M. Johnson, "The role of microstructural inhomogenities in high temperature failure," Ph.D. Thesis, U.C. Berkeley, 1982.

18. A.G. Evans, J.R. Rice, and J.P. Hirth, "Suppression of cavity formation in ceramics: prospects for superplasticity," J. Amer. Ceram. Soc. 63, No. 7-8, p. 368 (1980).

19. R. Raj and M.F. Ashby, "On grain boundary sliding and diffusional creep," Met. Trans. 2, 1971, p. 1113.

20. A.H. Cotrell, Mechanical Properties of Matter, Wiley, 1964, p. 223.

21. R. Raj. and C.H. Dang, "De-adhesion by the growth of penny-shaped bubbles in an adhesive layer," Phil. Mag. 32, 1975, p. 909.

22. R.J. Fields and M.F. Ashby, "Finger-like crack growth in solids and liquids," Phil. Mag., 33, 1976, p. 33.

23. C.H. Hseuh and A.G. Evans, "Creep fracture in ceramic polycrystals," Acta Met., 29, 1981, p. 1907.

24. D.R. Clarke, "Densification of Silicon Nitride: Effect of Chlorine Impurities," J. Amer. Ceram. Soc., 62, 1982, p. C21.

25. C.C. Ahn and G. Thomas, "Microstructure and Grain-Boundary Composition of Hot-Pressed Silicon Nitride with Yttria and Alumina," J. Amer. Ceram. Soc. 66, 1983, p. 14.

26. G. Thomas, C. Ahn, and J. Weiss, "Characterization and Crystallization at Y-Si-Al-O-N Glass, ibid. 65 (1982), p. C185.

27. T.M. Shaw, G. Thomas and R.E. Loehman, "The Formation and Microstructure of Mg-Si-O-N Glasses."

FIGURE CAPTIONS

Fig. 1. Scanning electron micrograph of a cavitation prone area in silicon nitride.

Fig. 2. Transmission electron micrograph showing a three grain channel glass pocket between β and α-Si_3N_4 grains connected by a continuous amorphous phase along two grain interfaces. $(10\bar{1}0)$ lattice fringes are excited in all three grains (plane spacings is 0.66 nm in β-Si_3N_4 and 0.46 nm in α-Si_3N_4). $\{10\bar{1}1\}$ cross fringes are visible in the right-hand grain.

Fig. 3. Transmission electron micrographs of grain boundaries in deformed liquid phase sintered ceramics. (Arrows indicate axis of applied stress.)

(a) Grain boundary in silicon nitride from the tensile surface of the creep bar, nearly perpendicular to the axis of applied stress.

(b) Grain boundary in Sialon from the compressive edge of the creep sample, nearly perpendicular to the axis of stress.

(c) Grain boundary in alumina from near the compressive surface of the creep sample; note facets.

Fig. 4. A hole nucleated completely within a three-grain glass pocket.

The steep, smooth sides of this hole, and the location in a relatively thick section of the foil, indicate that it is not an artifact, and that it was nucleated during creep deformation.

Fig. 5. (a) Small triangular depleted three grain channel with a large cavity angle.

(b) Large wedge-shaped three grain cavity with smaller cavity angle.

(c) Full facet-sized cavity.

Fig. 6. Diffuse dark field micrograph of the liquid meniscus being drawn into the two grain interface (arrow). The image is formed by electrons that have been diffusely scattered by the amorphous phase, and shows a thin film of glass which continuously coats the cavitating three grain pocket.

Fig. 7. (a) Scanning electron micrograph of a two grain boundary showing glass fibrils connecting cavitating grains.

(b) Transmission electron micrograph of holes formed within the glass phase along a two grain boundary which have an oblate morphology.

Fig. 8. Schematic of the assumed oblate hole geometry along a two grain boundary. (a) Edge on view and (b) plan view.

Fig. 9. Plots of critical nucleation stresses for spherical and oblate holes (a) in normalized coordinates, (b) results specific to hot-pressed Si_3N_4 (δ_0 = 1.5 nm, γ = 0.2 J/m^2).

Fig. 10. Schematic of the stress redistribution along the two grain interfaces due to grain boundary sliding and diffusive flow.

Fig. 11. Schematic of boundary undulations creating normal stresses in the presence of a shear stress.

Fig. 12. Schematic illustrating the cavity formation sequence. (a) uncavitated interface, (b) nucleation of oblate holes along the two grain boundary at $\sigma_\infty > \sigma_c^2$, (c) coalescence to a full-facet cavity, (d) an uncavitated three grain pocket, (e) nucleation of a spherical hole in the glass at $\sigma_\infty > \sigma_c^3$, (f) depletion of the pocket by viscous flow (g) expansion to full facet size by viscous flow at high local stress (h) growth to full facet size by solution/reprecipitation at low local stress.

Fig. 13. Plot of the unconstrained hole coalescence time for nucleation of oblate holes as a function of the initial film thickness for several choices of the hole size at nucleation.

Fig. 14. Schematics showing (a) the geometry of a depleted three grain channel, (b) the cavity being drawn into the two grain boundary.

Fig. 15. Scanning electron micrograph of finger-like perturbations in advancing cavity fronts on the fracture surface of a L.P.S. alumina subjected to creep strains, frozen under load and fractured at room temperature. Courtesy of D.R. Clarke.

Fig. 16. (a) Two- and (b) three-dimensional schematics of finger-like perturbations on a cavity front advancing from left to right.

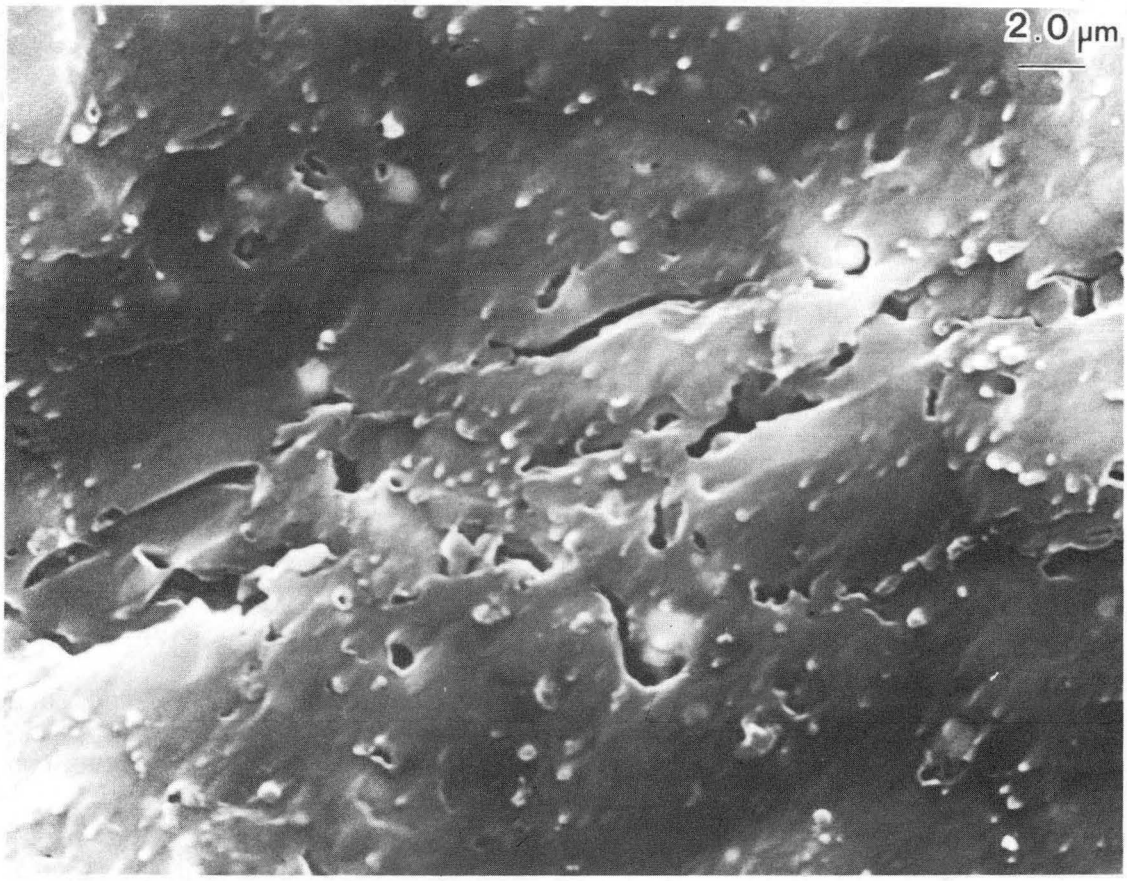

XBB 832-1774

Figure 1

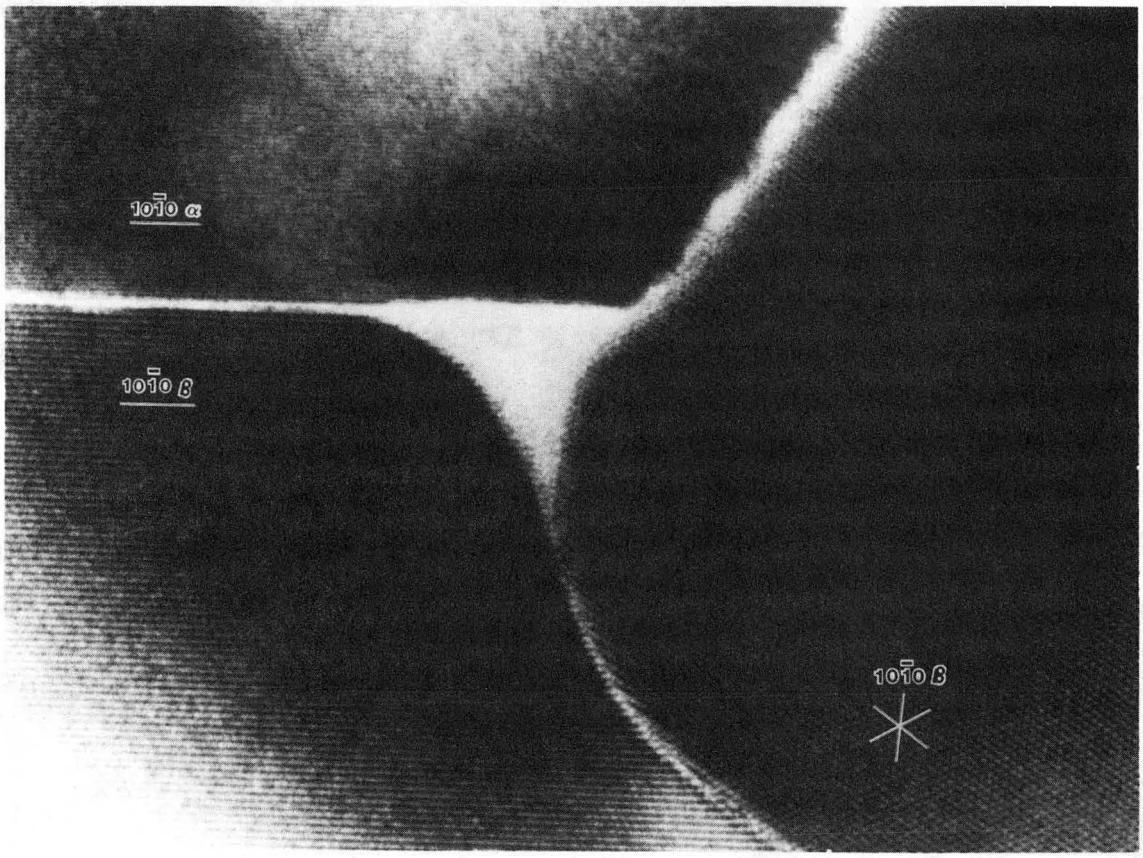

XBB 820-9092

Figure 2

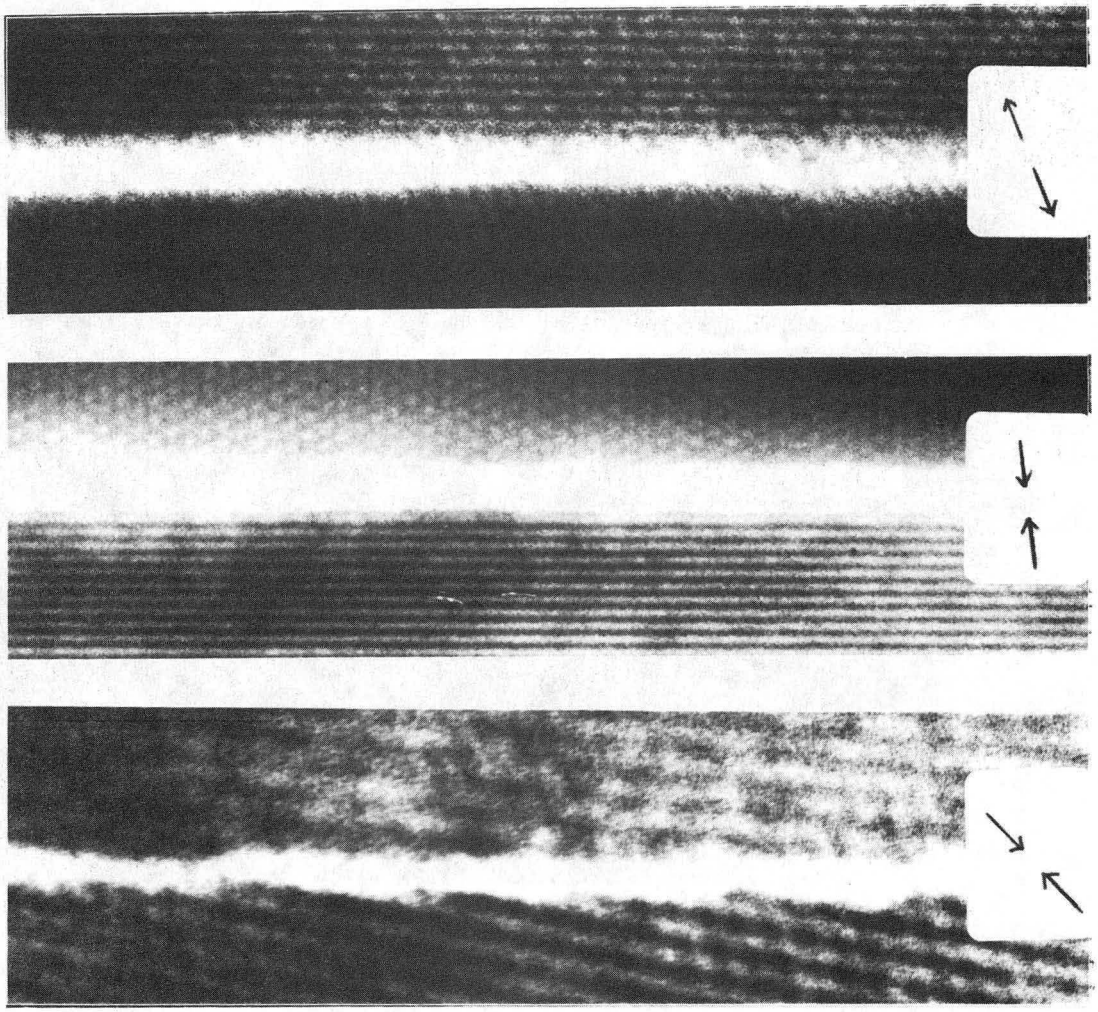

XBB 840-8001

Figure 3

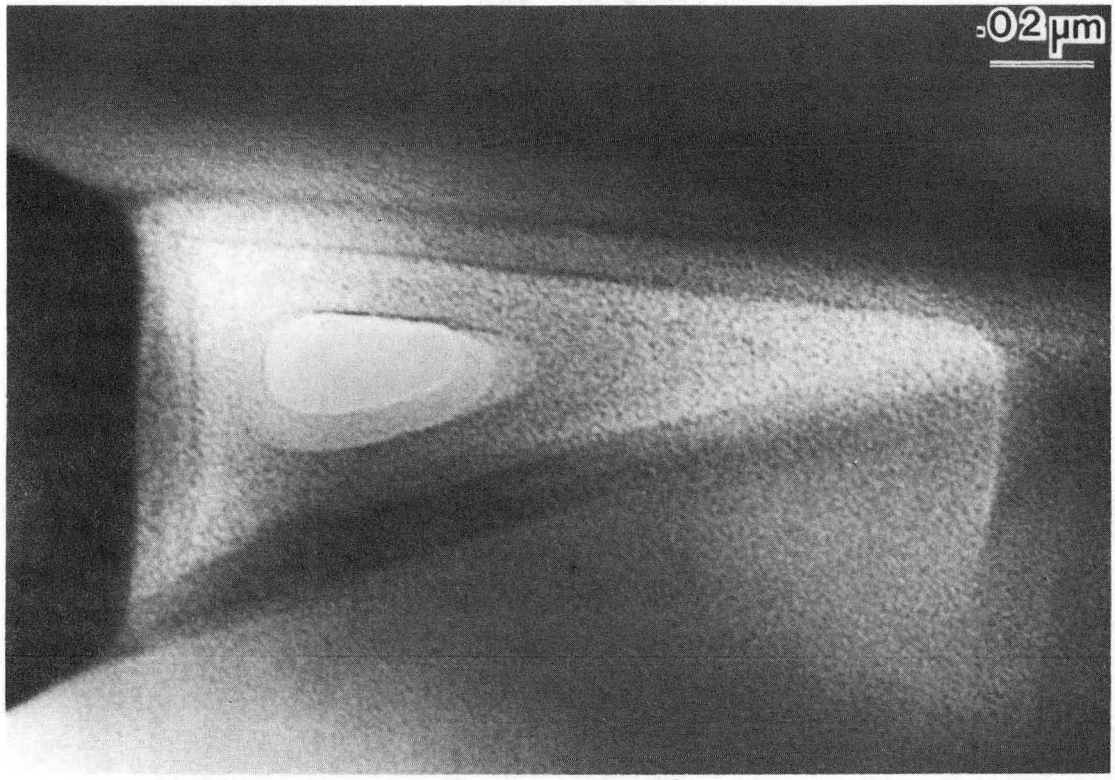

XBB 820-9088

Figure 4

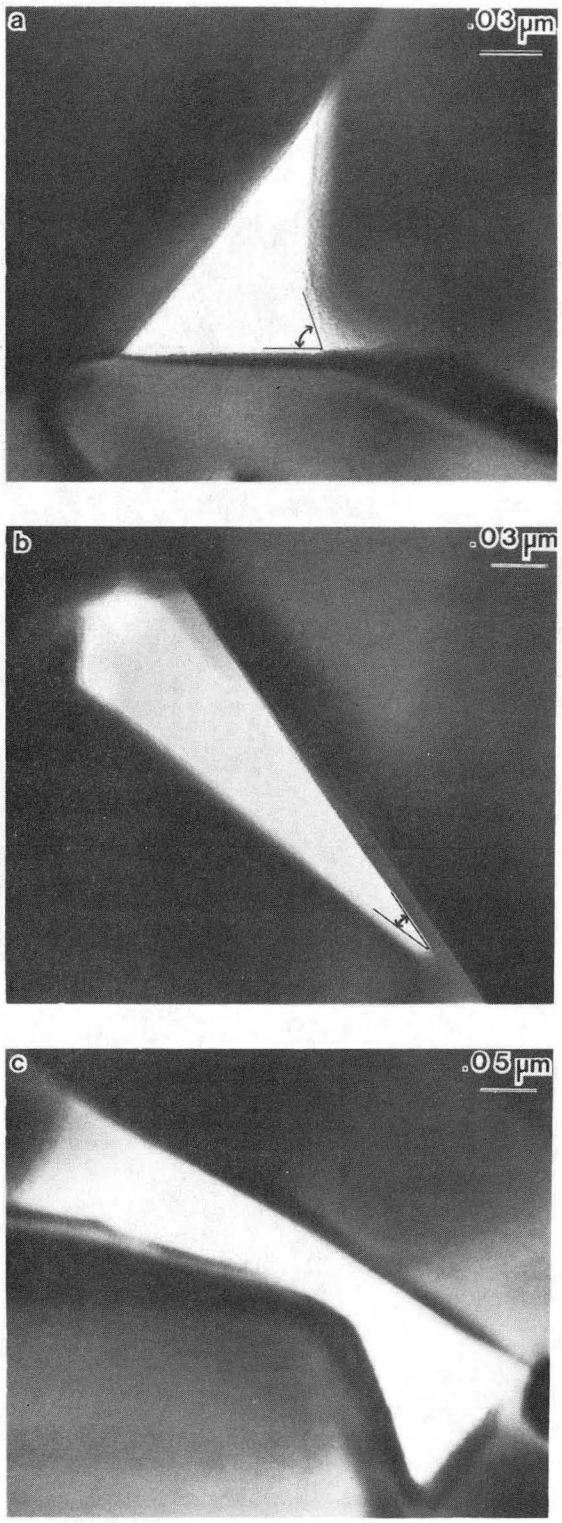

XBB 832-1772

Figure 5

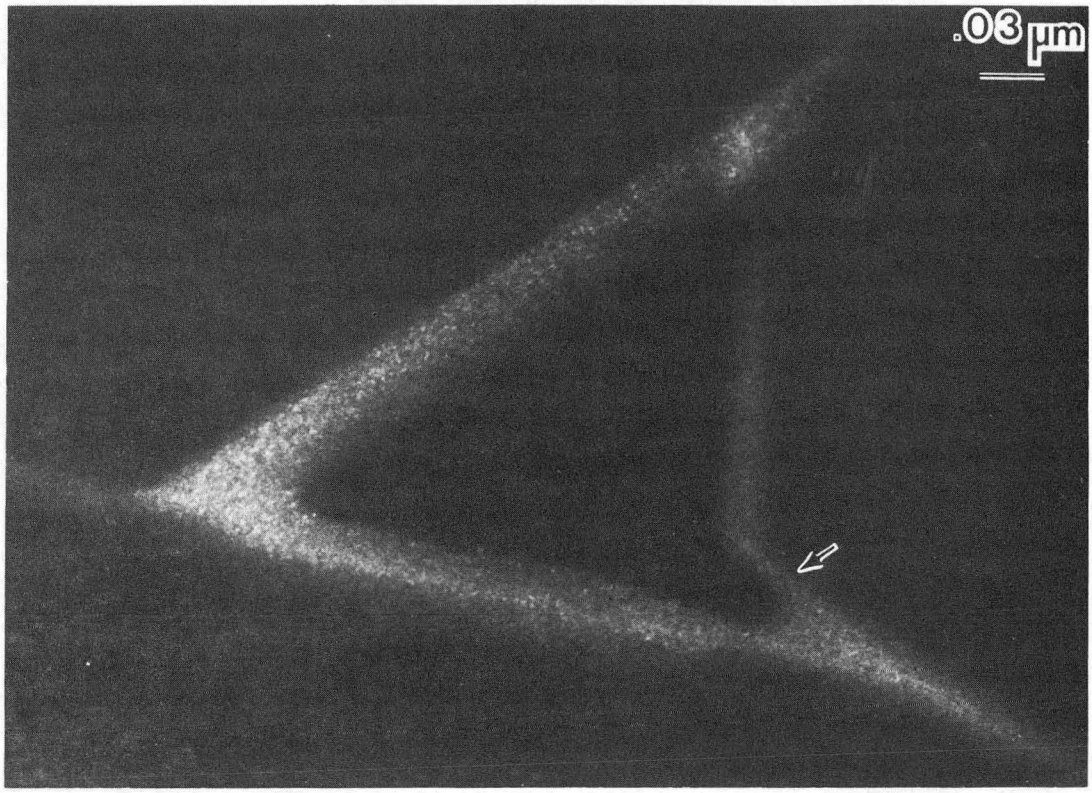

XBB 832-1770

Figure 6

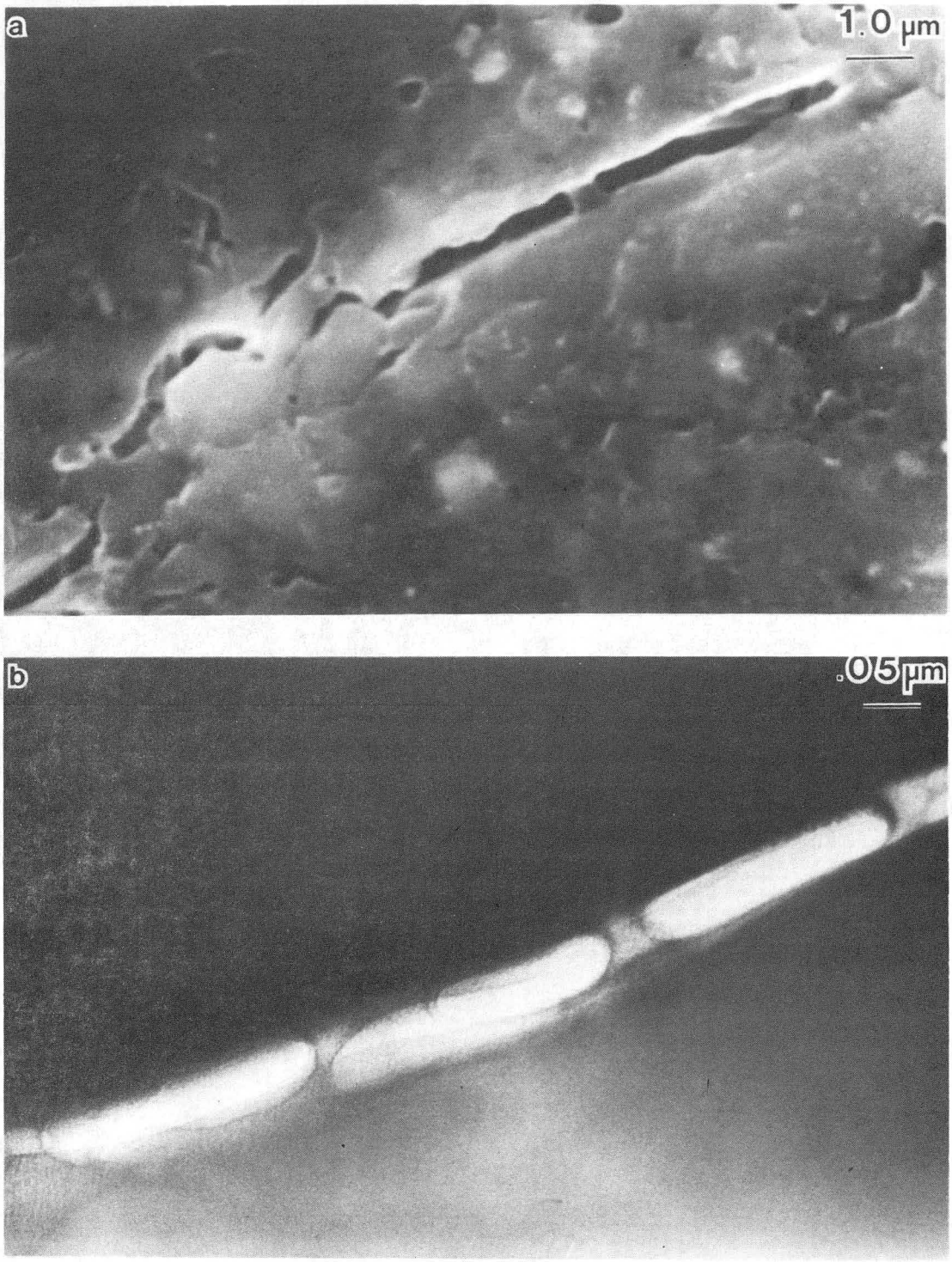

XBB 832-1773

Figure 7

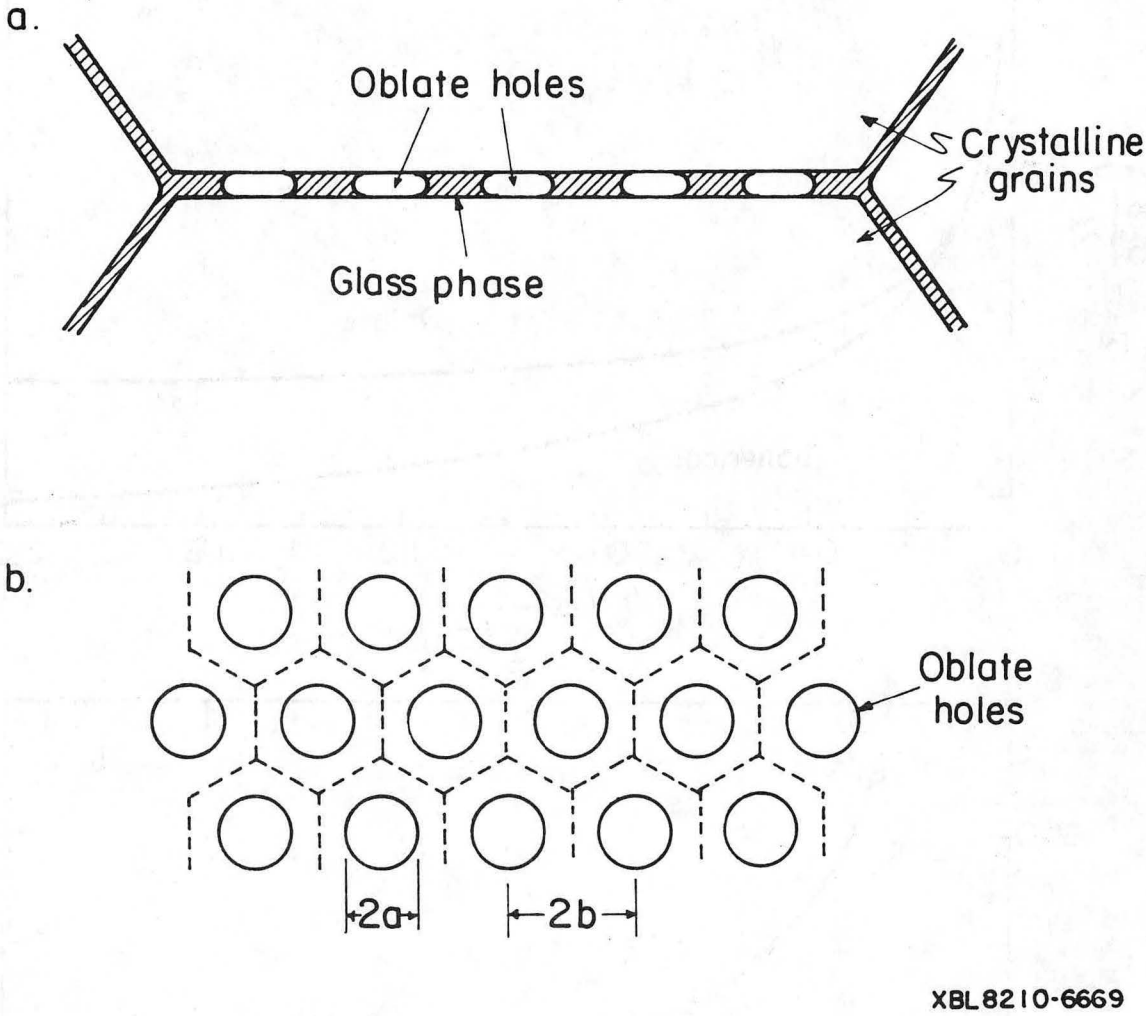
a.
Oblate holes
Crystalline grains
Glass phase
b.
Oblate holes
2a
2b
XBL8210-6669

Figure 8

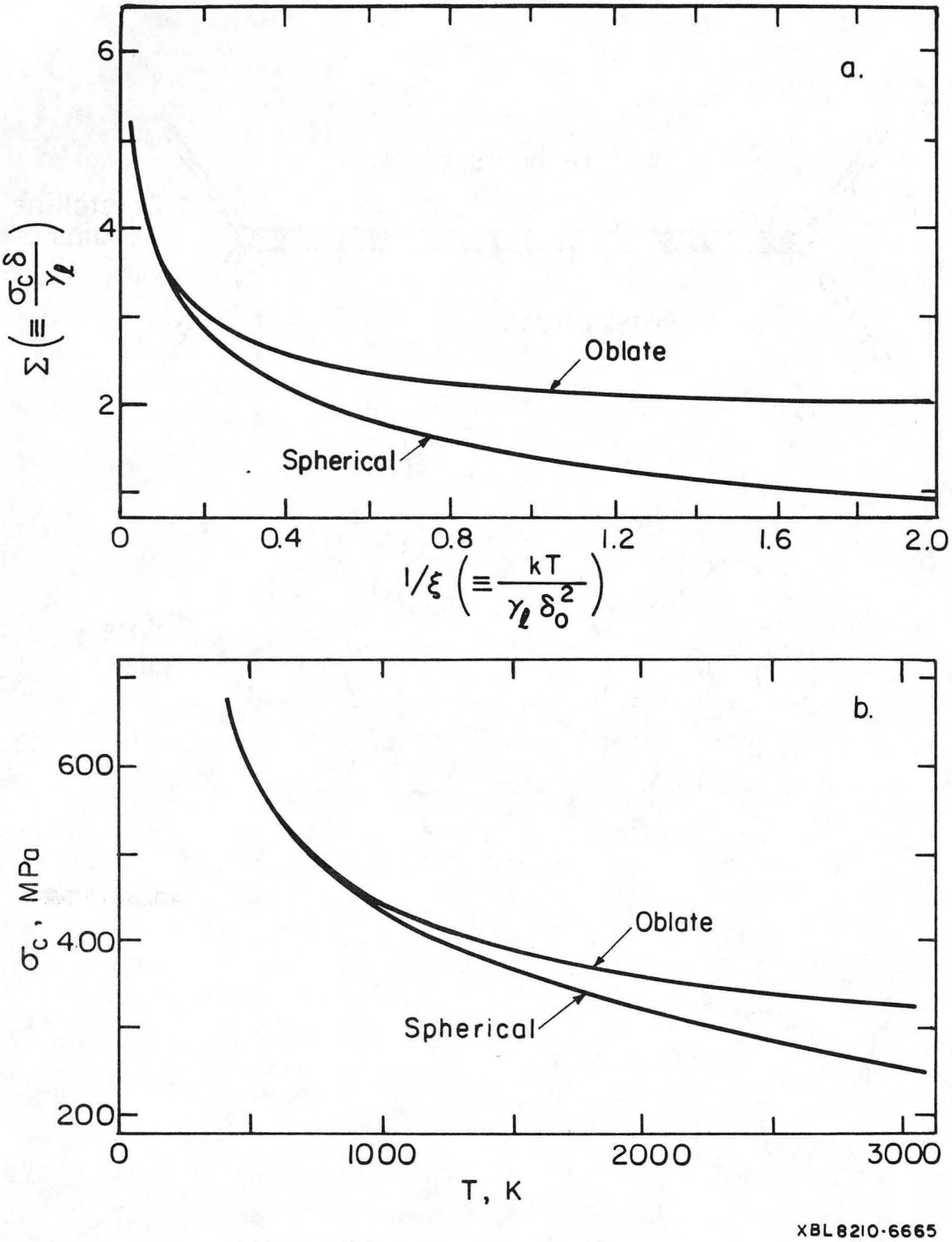
a.
6
4
2
$\Sigma \left(\equiv \frac{\sigma_c \delta}{\gamma_\ell}\right)$
Oblate
Spherical
0
0.4
0.8
1.2
1.6
2.0
$1/\xi \left(\equiv \frac{kT}{\gamma_\ell \delta_0^2}\right)$
b.
600
400
200
σ_c, MPa
Oblate
Spherical
0
1000
2000
3000
T, K
XBL8210-6665

Figure 9

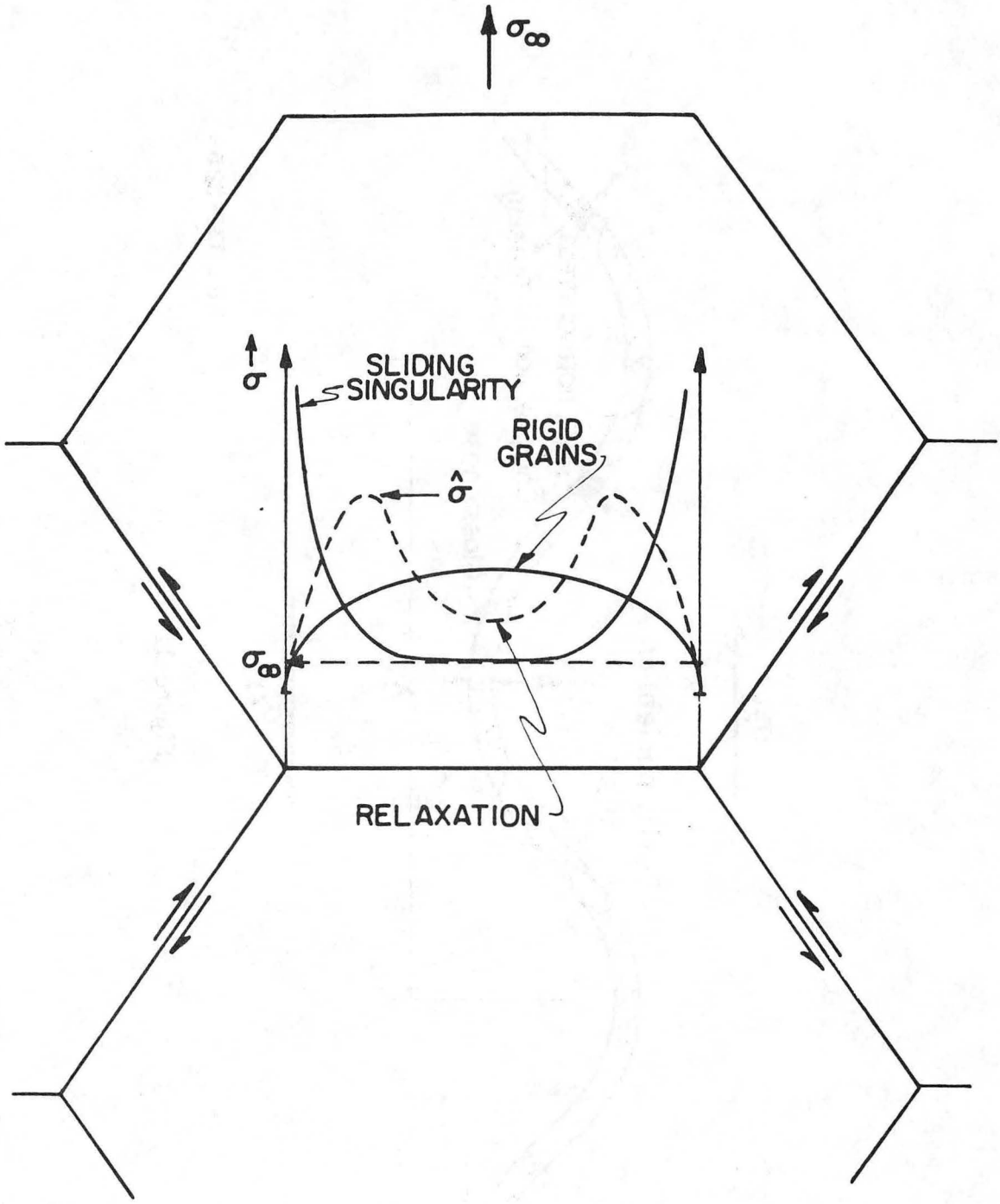

XBL 822-5268A

Figure 10

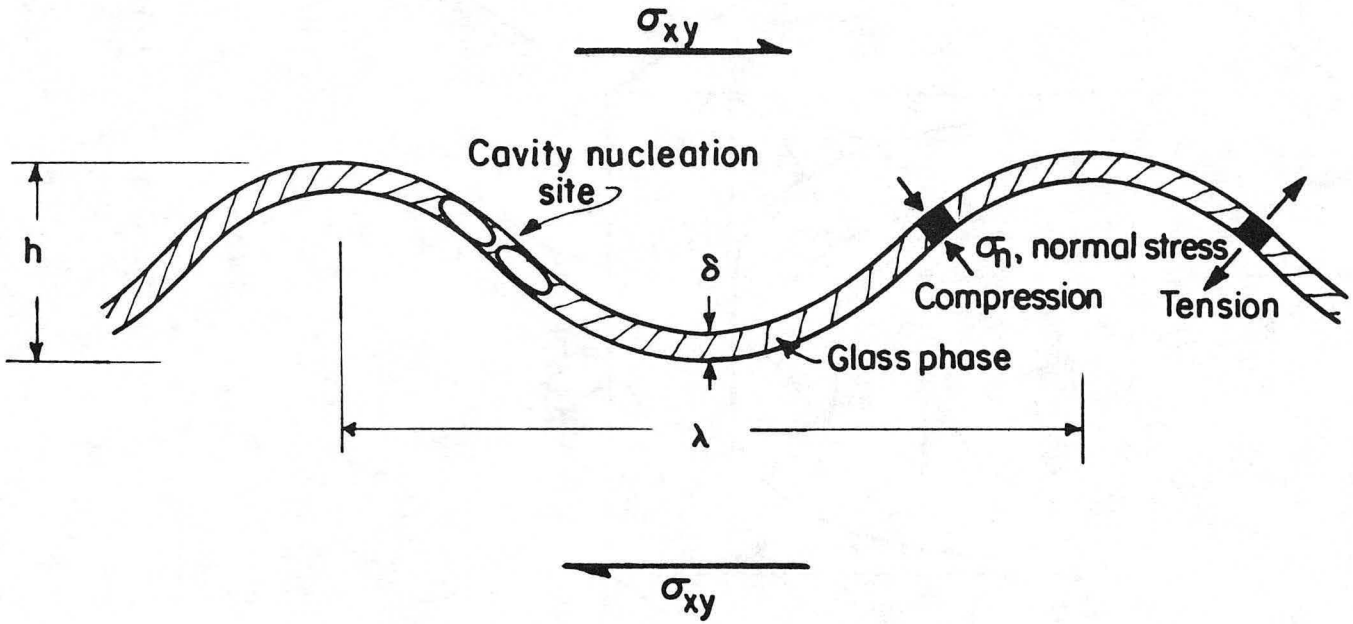

XBL 832-5259

Figure 11

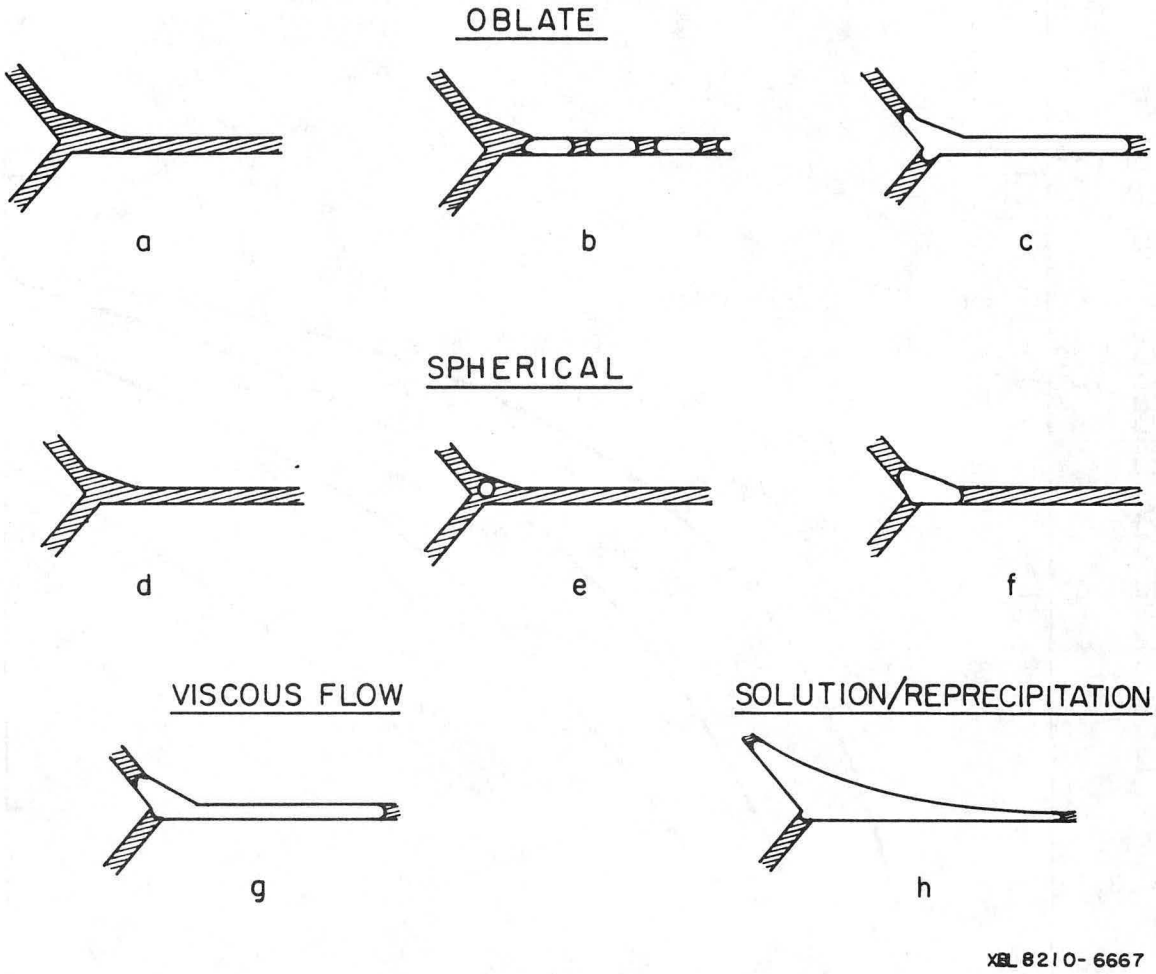
OBLATE
a
b
c
SPHERICAL
d
e
f
VISCOUS FLOW
g
SOLUTION/REPRECIPITATION
h
XBL 8210-6667

Figure 12

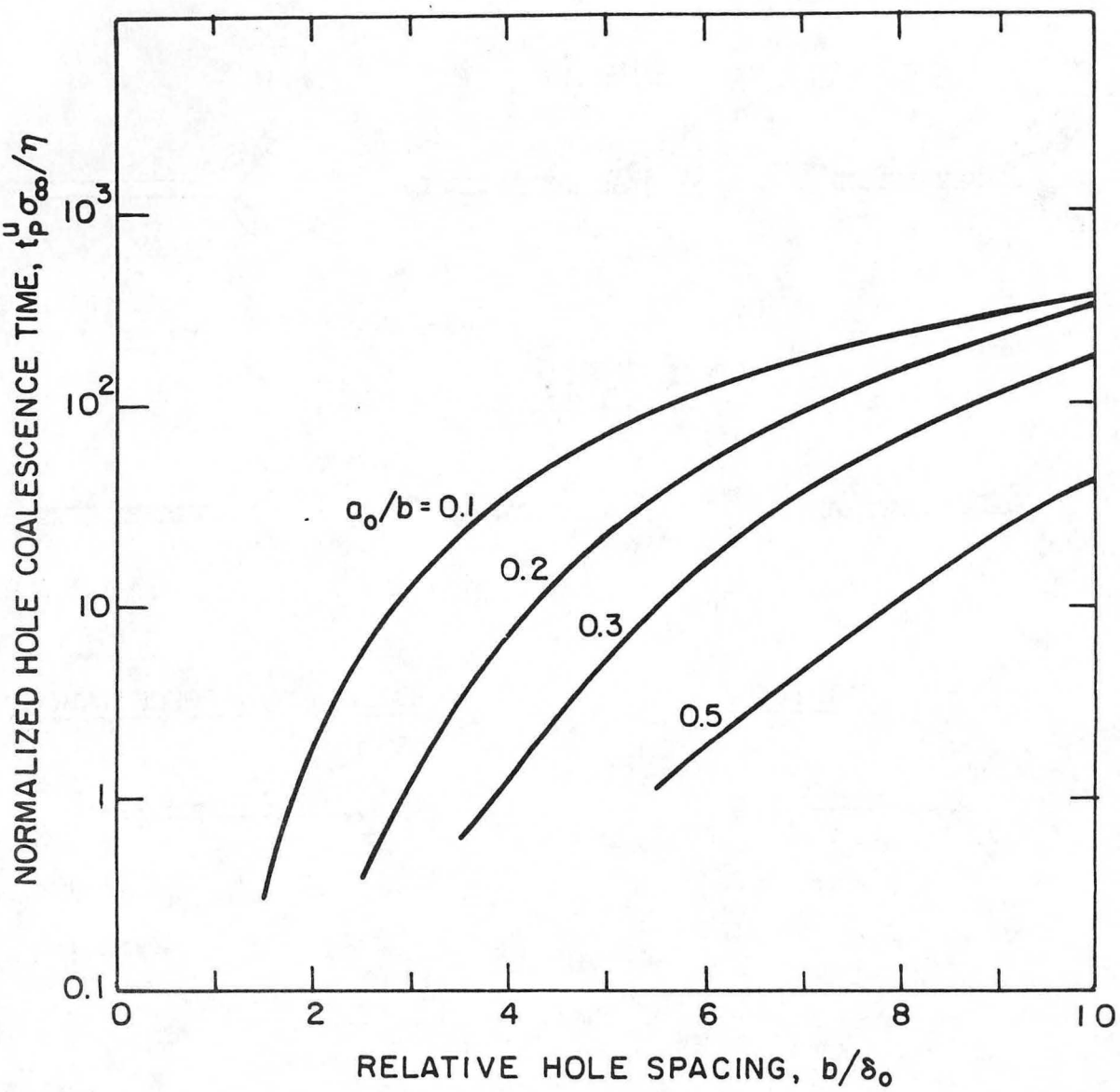

XBL 822-5273

Figure 13

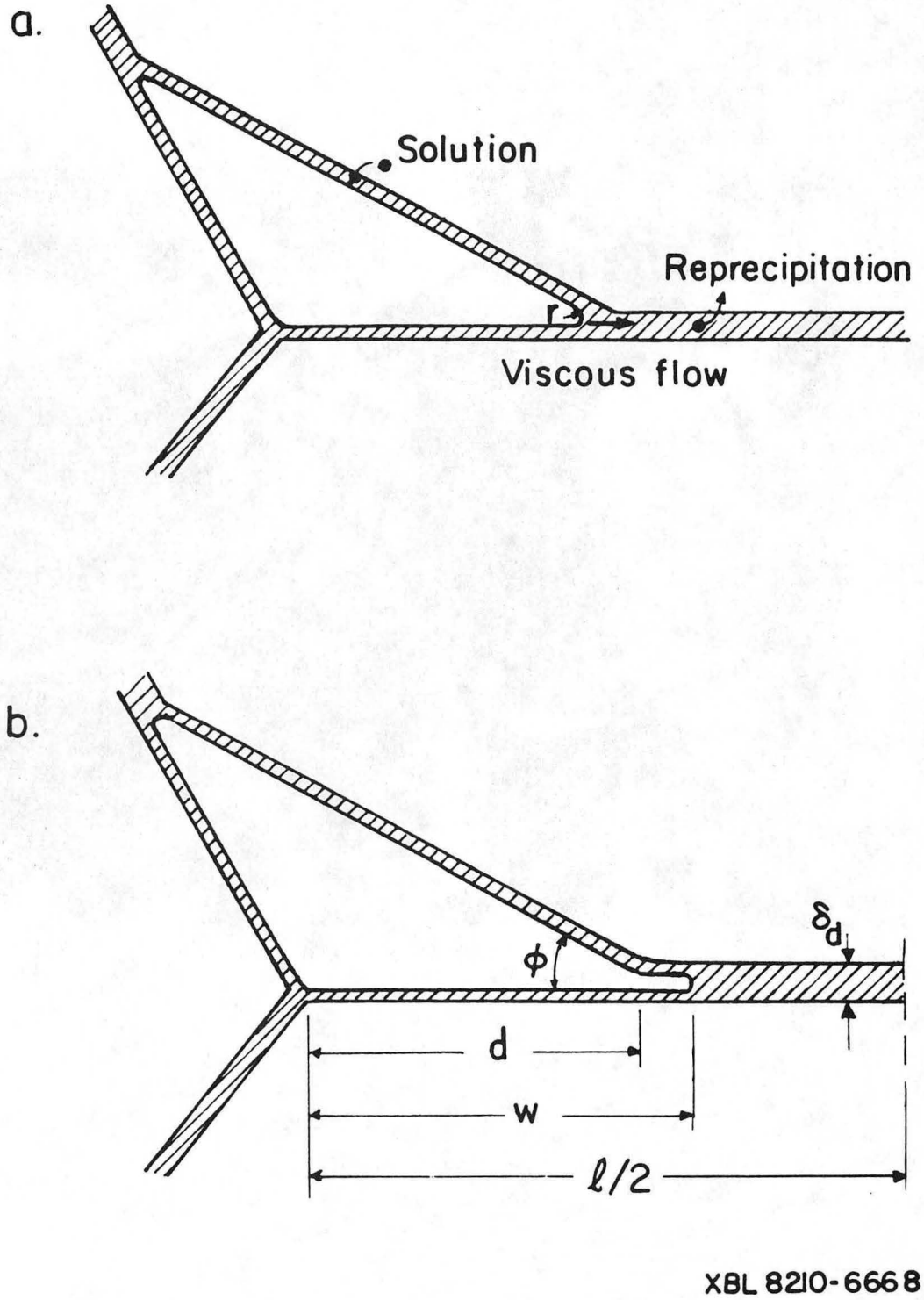
a.
Solution
Reprecipitation
r
Viscous flow
b.
δ_d
ϕ
d
w
$\ell/2$
XBL 8210-6668

Figure 14

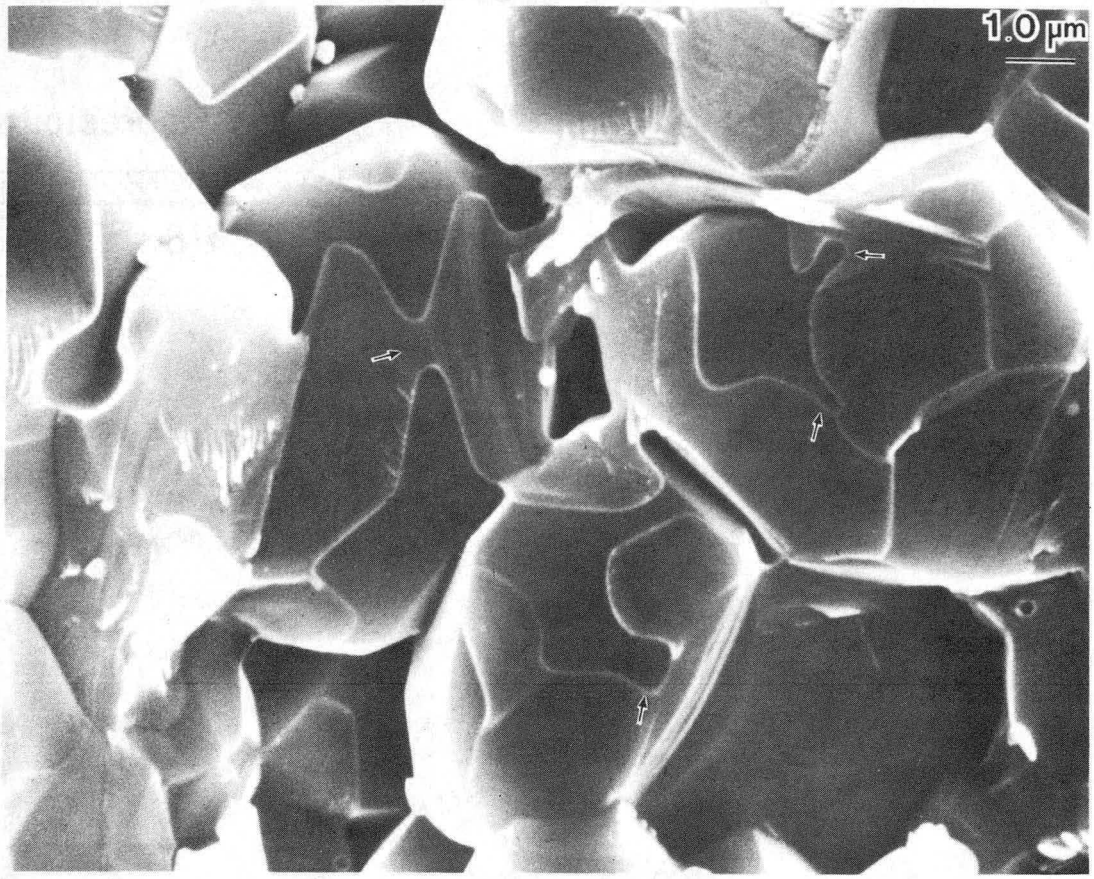

XBB 832-1771

Figure 15

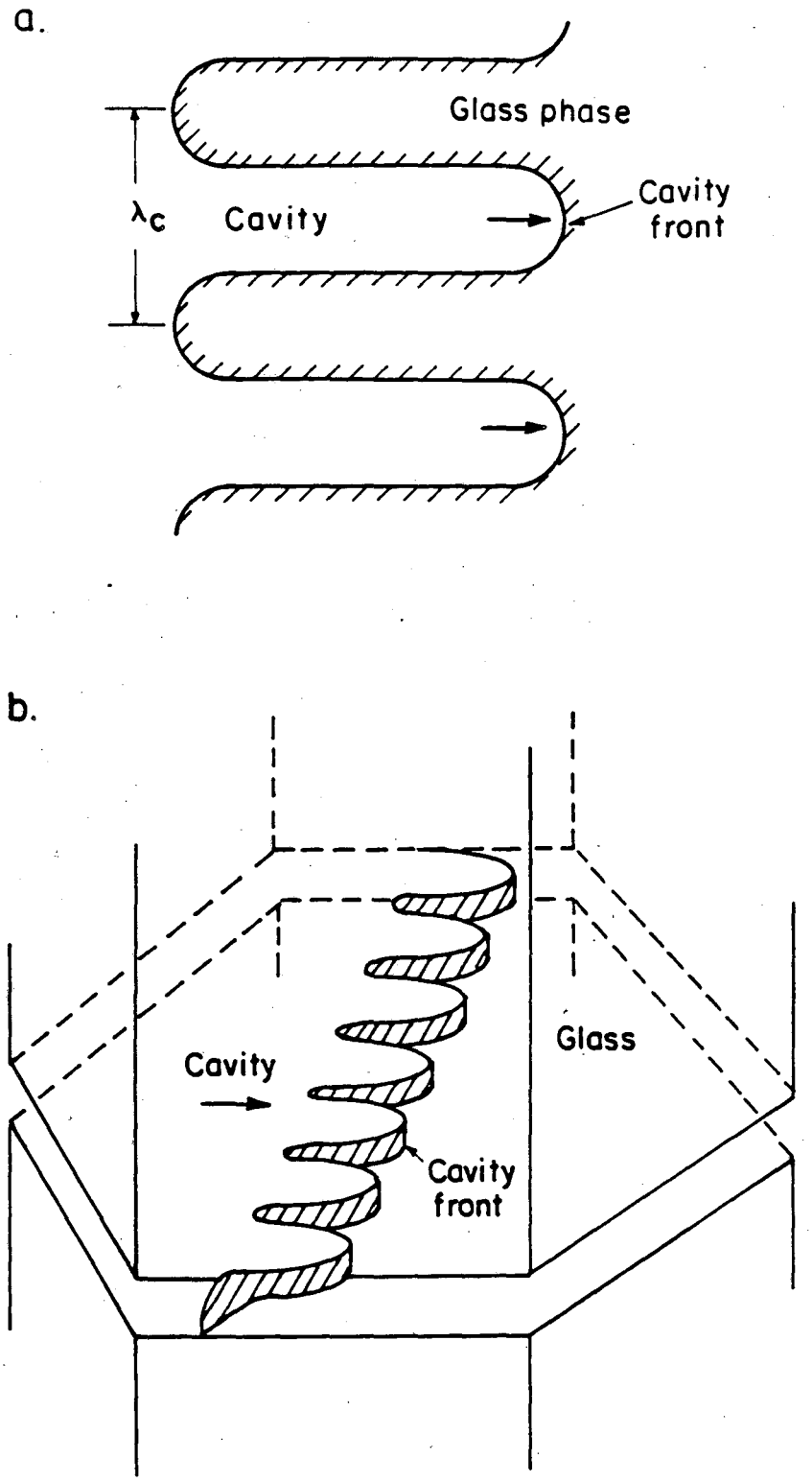

XBL 8210-6666

Figure 16

APPENDIX I

The Origin of the Strengthening Effect of Silicon Nitride by Oxidation

Commercial liquid phase sintered ceramics are typically processed by hot pressing with one to ten weight percent of a metal oxide additive which promotes densification at the processing temperature by forming a liquid phase in which matter transport by solution/reprecipitation can occur. In the dense microstructure the glassy phase is isolated along two grain boundaries as a film approximately 1.2 nm in thickness, connecting larger three grain channels which contain the remainder of the glassy phase. A serious decrease in strength at elevated temperatures is attributed to softening of this glassy phase. However, the high temperature strength of several liquid phase sintered ceramics, particularly silicon nitride has been improved dramatically by long term oxidation.[1]

A variety of mechanisms have been advanced to explain this recent observation. The theories include the development of a surface compressive stress, a reduction in the impurity level in the glass phase, and a decrease in the overall volume fraction of the glassy phase. The purpose of this appendix is to examine each of these theories in light of published studies and experimental work performed here and to discuss the conclusions in relation to the creep models proposed in the main text of the thesis.

Compressive surface stresses can enhance the strength of brittle solids by preventing the surface cracks (which often lead to failure)

from propagating. Oxidation of silicon nitride gives rise to compressive surface stresses by the formation of a gradient from the surface into the bulk in the volume fraction of intermediate oxidation products which give a volume expansion upon formation. McDonough[2] has observed such a gradient in the concentration of silicon oxynitride in a silicon nitride alloy which was oxidized at 1400°C for 100 hours (a relatively moderate treatment). However, Mendiratta and Petrovic[3] have examined residual stresses in silicon nitride at elevated temperature; his studies indicate that residual stresses are rapidly relieved after short anneal treatments (1200°C, 1 hour). Similarly Clarke and Lange,[1] using a surface indentation technique which measures apparent toughness at the surface, have found that very short anneal periods resulted in a toughness decrease. It therefore appears that surface compression cannot account for the observed strengthening effect.

The two other possible mechanisms are now examined. Impurity flux (Ca, Mg) to the surface scale during oxidation is observed by Xray.[1] This suggests that either the concentration of impurities in the intergranular phase, or the volume fraction of the glassy phase is being reduced (or both).* In order to explore which of these mechanisms are responsible for the observed strengthening effect, a comparitive TEM study of both oxidized and unoxidized materials was undertaken.

---

* One further possibility is that the impurity phase is being incorporated into the grains by a chemical reaction. However, solid solubility of these impurities in silicon nitride is extremely low. This highly covalent material is expected to exclude impurities and become more pure over the period of the anneal.

Silicon nitride (NC 132) was subjected to long term oxidation at high temperature (400 hours at 1500°C). Samples for TEM were taken from below the oxide scale and were prepared in the standard manner.[4] These results were compared to previous characterization of unoxidized samples of the same material.

The observations suggest that the volume fraction of the intergranular phase is indeed reduced, particularly along three grain channels where the largest glass enclaves are normally segregated (Fig. 1). The impurity phases along the three grain channels appear to have been reduced to the approximate thickness of the two grain boundaries, but the thickness of the two grain boundaries have remained essentially unchanged.

From the discussion on hole nucleation (Part II, Section 4.3) it is clear that a reduction in space available for hole formation will cause a higher critical hole nucleation stress and thus tend to suppress the early stages of failure. This suggests that the observed reduction in the volume fraction of the glassy phase would be important in reducing the high temperature deformation rate only in the stress/temperature regime where cavitation occurs. Elimination of large three grain glass enclaves would also elevate the stress level required to initiate failure.

Yet to be examined are the relative impurity levels in the glassy phase in samples before and after oxidation treatment. Xray spectroscopy was performed in an electron microscope* fitted with an energy

---

* Phillips, Electronic Instruments, Mount Vernon, NY, Model EM400.

dispersive detector.* For comparison of the impurity levels, the CaK_α peak was used; a large Ca peak is found in the three grain boundaries of the unannealled specimen, and a small Ca peak, just above the detectable limit was found in the reduced sized three grain pockets in the oxidized material. However, the probe diameter exceeded the pocket size considerably, so this does not conclusively indicate a lower fraction of Ca in the glass at the triple points in the oxidized material. Small Ca signals were detected in the two grain boundaries of both the oxidized and unoxidized materials, but after stripping, there was no statistically significant difference in the Ca peak heights of the two materials. The level of Ca impurity is so near the detection limit that the results concerning the differences in the Ca impurity levels are considered to be indefinite. Therefore, a macroscopic measurement technique was devised which definitively separated the relative contributions to strengthening from the two remaining mechanisms. Those experiments are now described.

For low and moderate stress levels, at temperature, silicon nitride can deform continuously by solution/reprecipitation, without cavitation. This diffusional creep can be identified by a stress exponent, n, of unity in the generalized creep equation;

---

*Kevex Corp., Burlingame, CA.

$$\dot{\varepsilon} = \sigma^n F(T,S) \tag{A1}$$

where σ is the stress, and T and S are temperature and microstructural parameters. Assuming a constant microstructure over the period of the creep test

$$\dot{\varepsilon} = A\sigma^n \exp(-Q/kT) \tag{A2}$$

where Q is the activation energy and A is a constant. At higher stress levels, cavitation adds a component to the creep strain rate, giving a stress exponent greater than unity.

In order to assess the effect due to a reduction in the impurity level of the liquid phase, the creep behavior was compared between oxidized and unoxidized samples at stresses below the critical cavitation stress. If the creep rate was found to be the same for both samples, one could conclude that the mechanism of impurity reduction in the intergranular phase has little effect.

Creep bars were cut from the billet, transverse to the hot pressing direction. High temperature deformation was performed in air at a constant strain rate of 2×10^{-4} inches per minute. The stress supported by the sample was continuously monitored as was the temperature at the surface of the sample.

Analysis of data obtained from bend specimens, as used in this experiment, has been criticized because of the inhomogeneous stress state within the sample. Certainly dead-load, uniaxial tests would be preferred, but sample preparation expenses preclude the use of this

technique. In any case, for the materials of interest here, Karunaratne and Lewis[5] have compared data from bend tests and uniaxial compression and indicate essentially identical results from both methods.

The procedure for analysis of bend bar measurements outlined by Blumenthal[6] was used here to generate the data listed in Table 1.

Due to large variations in properties between different billets of nominally the same material, all measurements were confined to samples cut from one billet. This limited the number of observations to eighteen.

At low temperatures (900 and 1100°C) the stress exponent for both the oxidized and unoxidized samples (as well as the density change during the creep test) are essentially the same. It appears then that neither sample cavitates significantly. However, the activation energy for the oxidized samples are about twice that for the unoxidized material. Apparently, although no cavity nucleation is involved, the creep rate is high because diffusion along the "impure" intergranular phase in the unoxidized samples is significantly easier than along the cleaner grain boundary films in the treated material.

At higher temperatures in the regime where cavitation is primarily responsible for the deformation, the stress exponent and density charge are both much higher in the unoxidized sample; the oxidized sample is less prone to cavitation.

Next, the threshold conditions for hole nucleation are estimated from the creep data to determine the conditions under which cavitation

Table 1. Creep Data

Oxidation Treatment	No. of Test Samples	Test Temp. °C	Stress Exponent, n	Activation Energy Q kJ $mole^{-1}$	Density ρ before oxidation*	Density ρ after oxidation**
none	3	900	1.0	340 ± 14	.99 ± .01	.99 ± .01
1500°C, 400 hr.	2	900	1.0	780 ± 50	1.00 ± .01	1.00 ± .01
none	2	1100	1.1	370 ± 17	.99 ± .01	.98 ± .01
1500°C, 400 hr.	2	1100	1.0	810 ± 60	1.00 ± .01	1.00 ± .01
none	2	1300	1.6	460 ± 20	.99 ± .01	.95 ± .01
1500°C, 400 hr.	3	1300	1.2	800 ± 30	1.00 ± .01	.99 ± .01
none	2	1500	2.1	520 ± 21	.99 ± .01	.91 ± .01
1500°C, 400 hr.	2	1500	1.6	830 ± 60	1.00 ± .01	.95 ± .01

*Fraction of theoretical density based on 3.19 = gm/cm^3.

**Measurement taken after the surface scale was mechanically removed.

occurs in the two alloys. Some changes in the stress exponent and density were found at 1100°C in the untreated samples, and this became significant at 1300°C; from these data the onset of widespread cavitation is estimated to be about 1150°C in the unoxidized sample. On the other hand the data suggest that cavitation becomes significant in the oxidized sample at about 1300°C. The threshold for nucleation of cavities is therefore estimated to be about 150°C higher in the oxidized sample. One final observation is that the activation energy of the unoxidized samples increased as the test temperature was increased. This is attributed to the temperature sensitivity of the oxidation kinetics which results in a higher degree of oxidation in the untreated samples which were tested at high temperature.

These observations are rationalized as follows. At high temperatures, cavitation is suppressed in the oxidized samples because the size of the three grain enclaves has been reduced, preventing ready nucleation of voids. At lower temperatures, where none of the samples cavitate, the creep rates of the unoxidized samples are higher because diffusion along the highly modified grain boundary silicate layers are faster than diffusion along the grain boundaries in the oxidized samples which contain less impurities. At some intermediate temperature (~1250°C) the oxidized sample is far superior because it has both a lower diffusional creep rate and does not cavitate significantly.

APPENDIX II

Creep Rate Due to Solution/Reprecipitation

The analysis for the creep strain rate permitted by solution/reprecipitation is identical (with a change in the sense of the stress) to the analysis for densification given in Appendix II, Part I, except the boundary conditions for integration of the differential equation governing the grain center separation rate require modification.

That equation

$$\frac{-Dc\delta}{kT}\left(\frac{d^2\sigma}{dx^2}\right) = \frac{2}{\delta}\frac{dy}{dt} + \frac{1}{\xi}\frac{d^2y}{dt^2} \tag{A3}$$

is now integrated subject to the boundary conditions

$$\frac{d\sigma}{dx} = 0 \quad \text{at} \quad x = 0 \quad ,$$

$$\sigma = \zeta\sigma_a \quad \text{at} \quad x = \ell$$

where σ_a is the applied stress and ζ is a constant that varies between 0 and 1 depending on the orientation of the neighboring grain boundry (at $x = \ell$) to the applied stress, and 2ℓ is the length of the grain facet. The average stress on the boundary, $\langle\sigma\rangle$, is set at the level of the applied stress. The assumption is made that matter transport is sufficiently rapid that elastic stresses do not develop in the solid grain; hence $\dot{y}$ is independent of position along the grain boundary. Integration of Eq. (1) can now proceed yielding;

$$\frac{3Dc\delta\Omega\sigma_a}{2kT\ a^2y}\ (\zeta-1) = 2\frac{dy}{dt} + \frac{\delta}{\xi}\frac{d^2y}{dt^2} \tag{A4}$$

By geometry, the amount of center approach, y, is related to the neck size, a, and the particle radius, R, as

$$y = a^2/2R \tag{A5}$$

so that

$$\frac{c}{y} = 2\dot{y} + \frac{\delta}{\xi}\ddot{y} \tag{A6}$$

where

$$c = \frac{3Dc\Omega\delta\sigma_a}{4kT\ R}\ (\zeta-1)$$

For a specific system, the solution to Eq. (A6) can be found by numerical integration.

APPENDIX III

Related Observations

Several other observations are of interest to these deliberations on creep in liquid-phase-sintered materials. In particular, specific observations of stress concentrating microstructural features are discussed here. In both silicon nitride and sialon, a number of the three grain boundaries contained crystallites (Fig. 2). STEM analysis showed that inclusions in the silicon nitride are tungsten rich (Fig. 3); these are expected to be either WSi_2 or WC. WC is not thermally stable at the creep temperature[7] yet small WC inclusions have been reported in this material.[8] The STEM profile indicates a significant amount of silicon; while it is possible that this is from the surrounding silicon grain, it is believed that these inclusions are WSi_2. These inclusions were occasionally the site of the cavitation (Fig. 4).

In the sialon, the crystallies are aluminum and yttrium rich. Microdiffraction patterns from these crystals could not be indexed, except the small round dots in Fig. 2b were found to be YAG. No mellite was found and the morphology of the crystallites was considerably different than that previously reported for sialons.[9] Unlike the WSi_2 inclusions in silicon nitride, cavitation along three grain channels containing these crystallites in the sialon was not observed.

Surveying the silicon nitride in the TEM, occasionally silicon oxynitride grains were observed. In the as-received materials, these grains had no distinguishing features that set them apart from the

silicon nitride grains and were only identified from diffraction patterns. However, in the samples which had been frozen under load after severe creep strains had been applied, these grains were found to often contain high dislocation densities which typically appeared as tangles (Fig. 5). It is presumed that the dislocations arise because the fracture toughness of Si_2ON is less than silicon nitride but the thermal expansion coefficient of silicon oxynitride is higher.

Both inclusions and intermediate oxidation products are capable of inducing cavitation by elevating the level of the local stress above the applied stress. These observations are therefore important from an engineering design standpoint because they illustrate several specific ways in which stress is concentrated in these brittle solids.

APPENDIX IV

The Final Stage of Hole Depletion

Removal of the remnant liquid from a three-grain channel occurs in accord with the relation (Eq. (27)),

$$\sigma_\ell - (\gamma_\ell / r_c)\ (1-2f) \ = \ \eta \dot{\delta}_\ell^{\,2} F(f)/\delta^3 \tag{A7}$$

where r_c is the radius of curvature of the liquid at the channel opening, and $F(f) = 1\ 6f + 9f^2\ 4f^3$. Volume conservation of the second phase requires that:

$$d^2 \tan(\psi/2) - r_c^2\ [\cot\ (\psi/2) - \pi/2 + \psi/2] \ = \ (\delta-\delta_o)\ (\ell-d) \tag{A8}$$

and hence, that

$$\dot{\delta}(\ell-d) \ = \ -2r_c\dot{r}_c\ [(\cot\ (\psi/2) - \pi/2 + \psi/2] \tag{A9}$$

$$-2r_c\dot{r}_c\ \Psi(\psi)$$

where $\Psi(\psi) \equiv (\cot\ (\psi/2) - \pi/2) - \pi/2 + \psi/2$. Combining Eqs. (A7), (A8), and (A9) gives

$$\sigma_\ell - (\gamma_\ell / r_c)(1-f) \ = \ - \frac{2\eta\ell^2 F(f)\Psi(\psi)/(\ell-d) r_c \dot{r}_c}{\left\{[d^2\ \tan(\psi/2) - r_c^2 \Psi(\psi)]/(\ell-d) + \delta_o\right\}^3} \tag{A10}$$

For the case of present interest, $\sigma_\ell < \gamma_\ell/\delta_d$, final depletion occurs slowly. Then, σ_ℓ is approximately time invariant, and for long times

($r_c << d$, $\delta >> \delta_o$, $r_c \rightarrow \gamma / \sigma_\ell$), the time dependence of the meniscus radius becomes;

$$r_c \sim \gamma_\ell (1-f)/\sigma_\ell + \exp - \left[\frac{t\sigma^3 d^2 \tan^3(\psi/2) f^4}{2\eta\gamma_\ell^2 (1-f)^4 F(f)[\cot(\psi/2) - \pi/2 + \psi/2]} \right] \quad \text{(A11)}$$

corresponding to an effective relaxation time,

$$\tau_d = 2(\eta\gamma_\ell^2/\sigma_\ell^3 d^2) F'(f) G(\psi) \quad \text{(A12)}$$

where $F'(f) = F(f)\ (1-f)^4/f^4$ and $G(\psi) = [\cot(\psi/2) - \pi/2 + \psi/2]/\tan^3(\psi/2)$.

REFERENCES

1. D.R. Clarke, F.F. Lange and G.D. Schnittgrund, "Strengthening of a Sintered Silicon Nitride by a Post-Fabrication Heat Treatment," J. Amer. Ceram. Soc. 65, p. C51 (1982).
2. W.J. McDonough, C. Cm. Wu, and P.E.D. Morgan, "Internal Phase Changes in Dense Si_3N_4 Associated with High-Temperature Oxidation," ibid. 64, p. C45 (1981).
3. G. Mendiratta and J.J. Petrovic, "Slow Crack Growth from Controlled Surface Flaws in Hot-pressed Silicon Nitride," ibid. 61, p. 226 (1978).
4. J.E. Marion, A.G. Evans, M.D. Drory and D.R. Clarke, "Overview No. 28: High Temperature Failure Initiation in Liquid Phase Sintered Materials," Acta. Metall. 31, p. 1445 (1983).
5. M.H. Lewis, B.S.B. Karunaratne, J. Meredith and C. Pickering, Creep and Fracture of Engineering Materials and Structures, eds. B. Whilshire and D.R.J. Owens, Pineridge Press Swansea, p. 365, 1977.
6. W.R. Blumenthal, "Mechanical Response of Ceramics to Creep Loading," Ph.D. Thesis, U.C. Berkeley, 1983.
7. D.R. Clarke, private communication (1980).
8. O.L. Krivanek, T.M. Shaw and G. Thomas, "The Microstructure and Distribution of Impurities in Hot-pressed and sintered silicon nitride," J. Amer. Ceram. Soc. 62, p. 585 (1979).
9. G. Thomas and C.C. Ahn, "Characterization and Crystallization of Y-Si-Al-O-N glass," ibid. 65, p. C185 (1982).

FIGURE CAPTIONS

Fig. 1. (A) TEM micrograph of oxidized silicon nitride showing a three grain channel that has been reduced to the size of the two grain boundaries (between 1 and 2 nm).

(B) High Resolution TEM micrograph of unoxidized silicon nitride showing a large amorphous three grain pocket, marked A, (about 20 nm). (Bar = 5 nm)

Fig. 2. TEM micrographs of inclusions in (A) silicon nitride (WSi_2) and (B) in SiAlON (black dots are YAG) (bars = 10 nm).

Fig. 3. STEM profiles of inclusion in silicon nitride pictured (2A).

(A) W and Si peaks, along with system peaks and

(B) A comparison of matrix and inclusion showing no W in the matrix.

Fig. 4. TEM micrograph of a cavity formed near an inclusion in Si_3N_4 (bar = 50 nm).

Fig. 5. TEM micrograph of Si_2ON grain in Si_3N_4 showing dislocation tangles. (Bar = 100 nm)

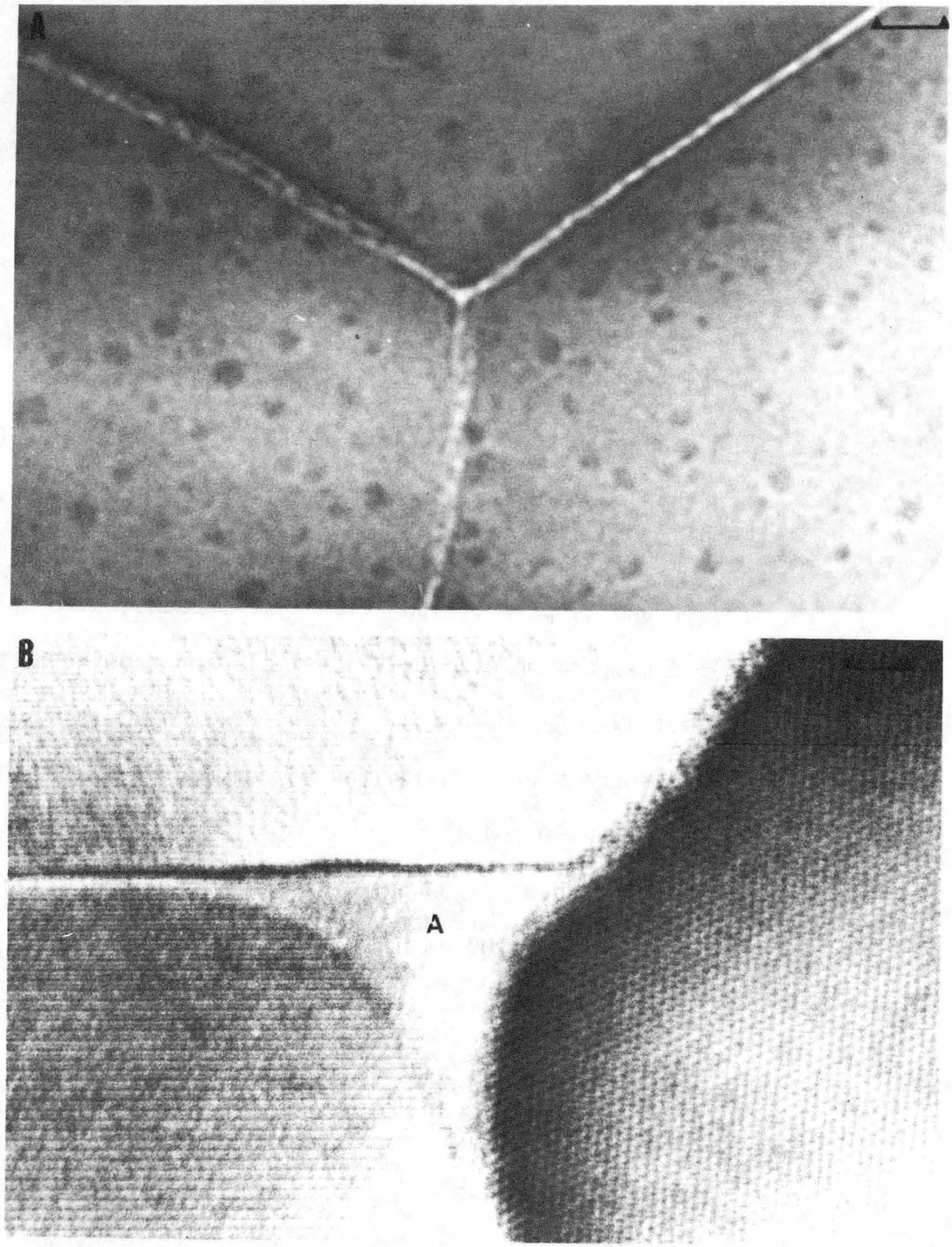

XBB 848-6450

Figure 1

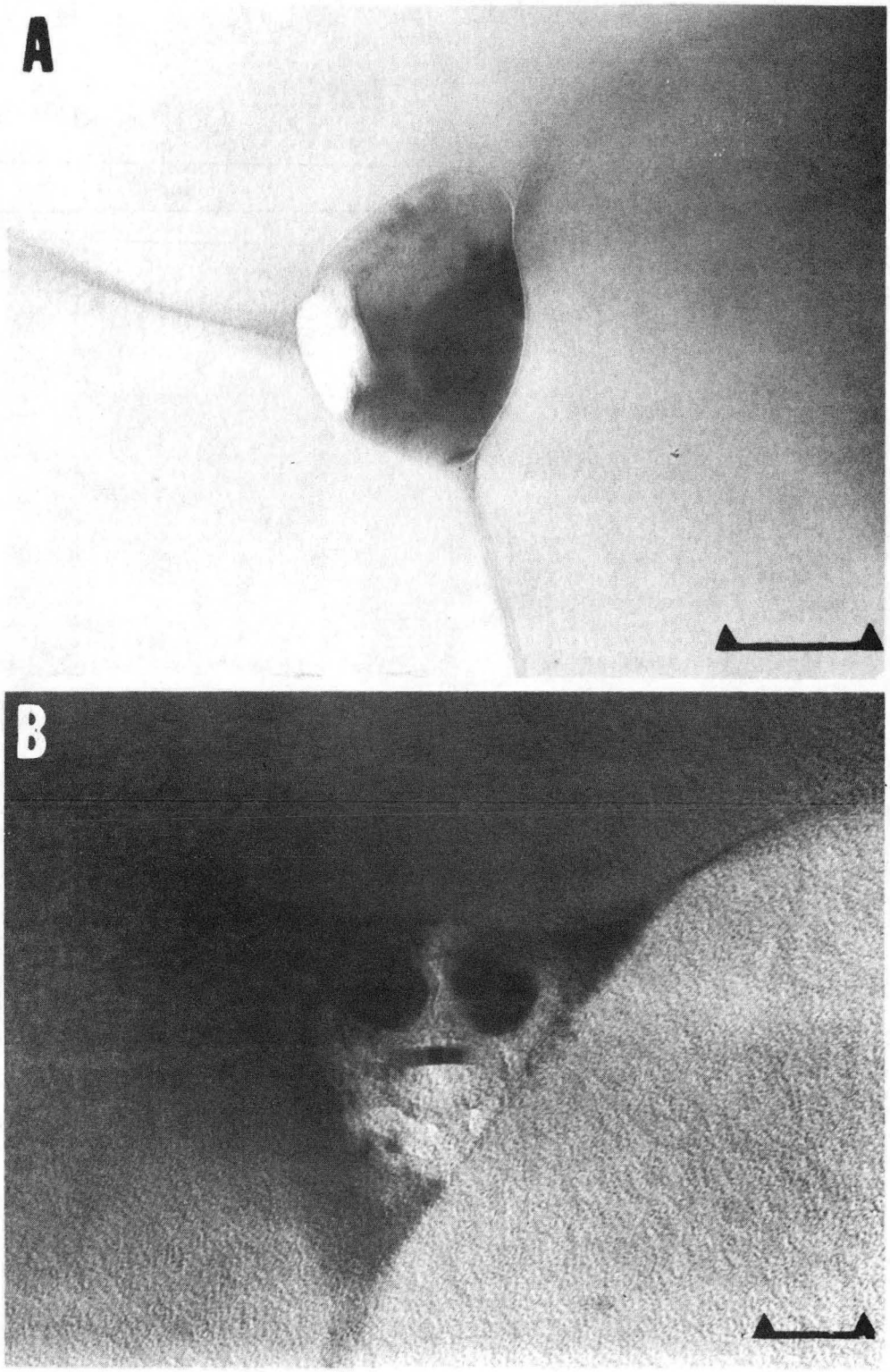

XBB 848-6460

Figure 2

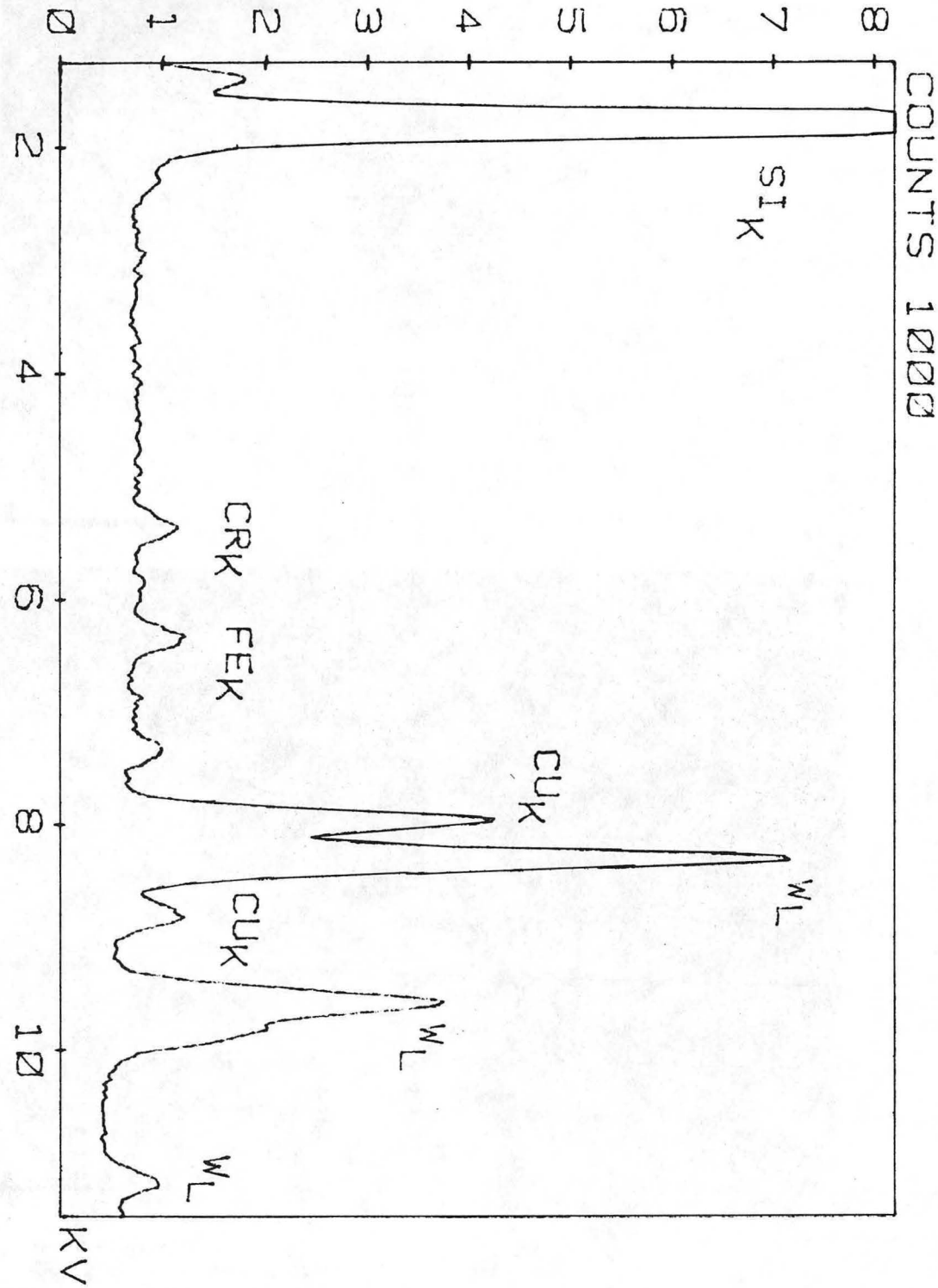

XBL 848-3605

Figure 3b

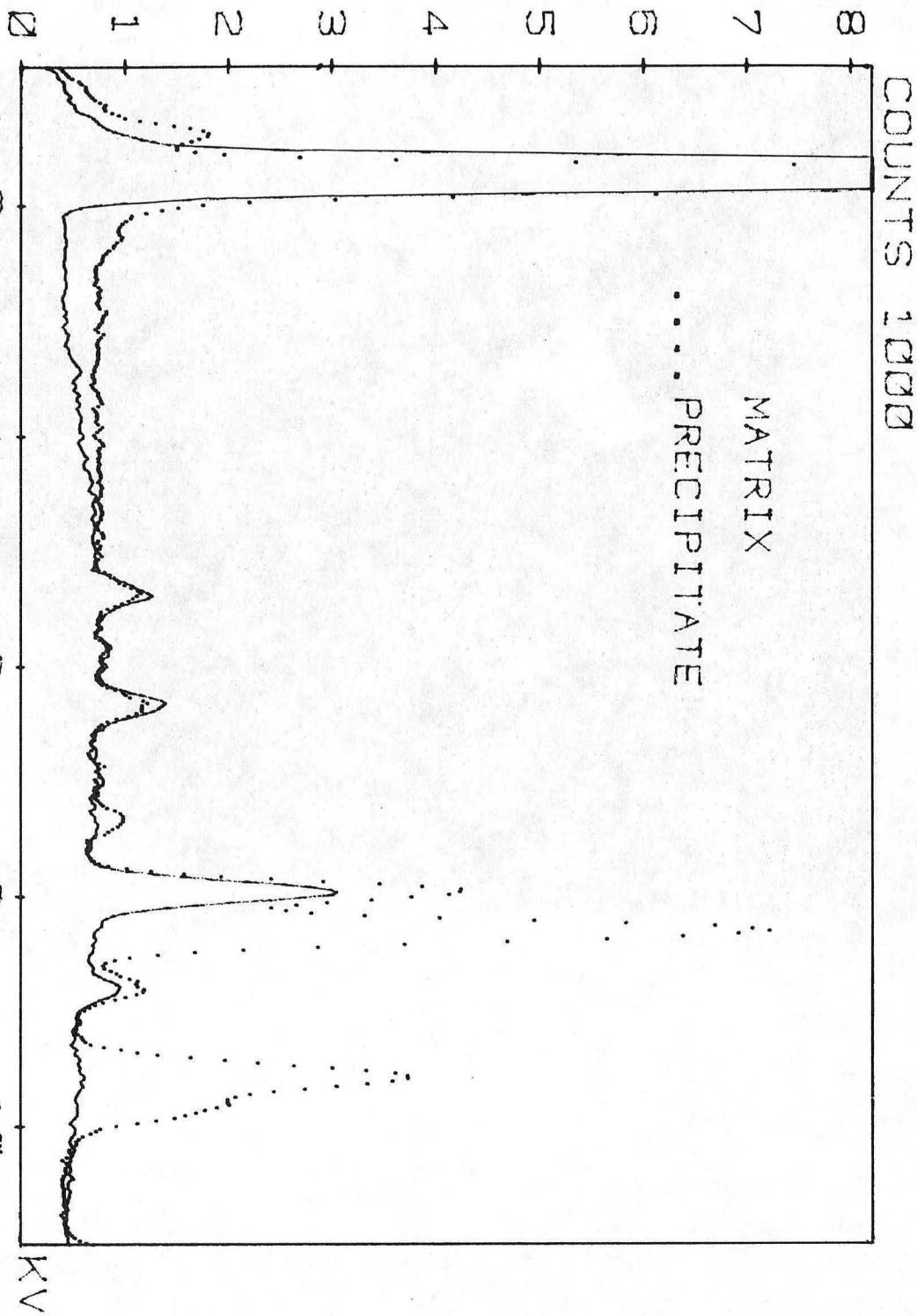

XBL 848-3604

Figure 3b

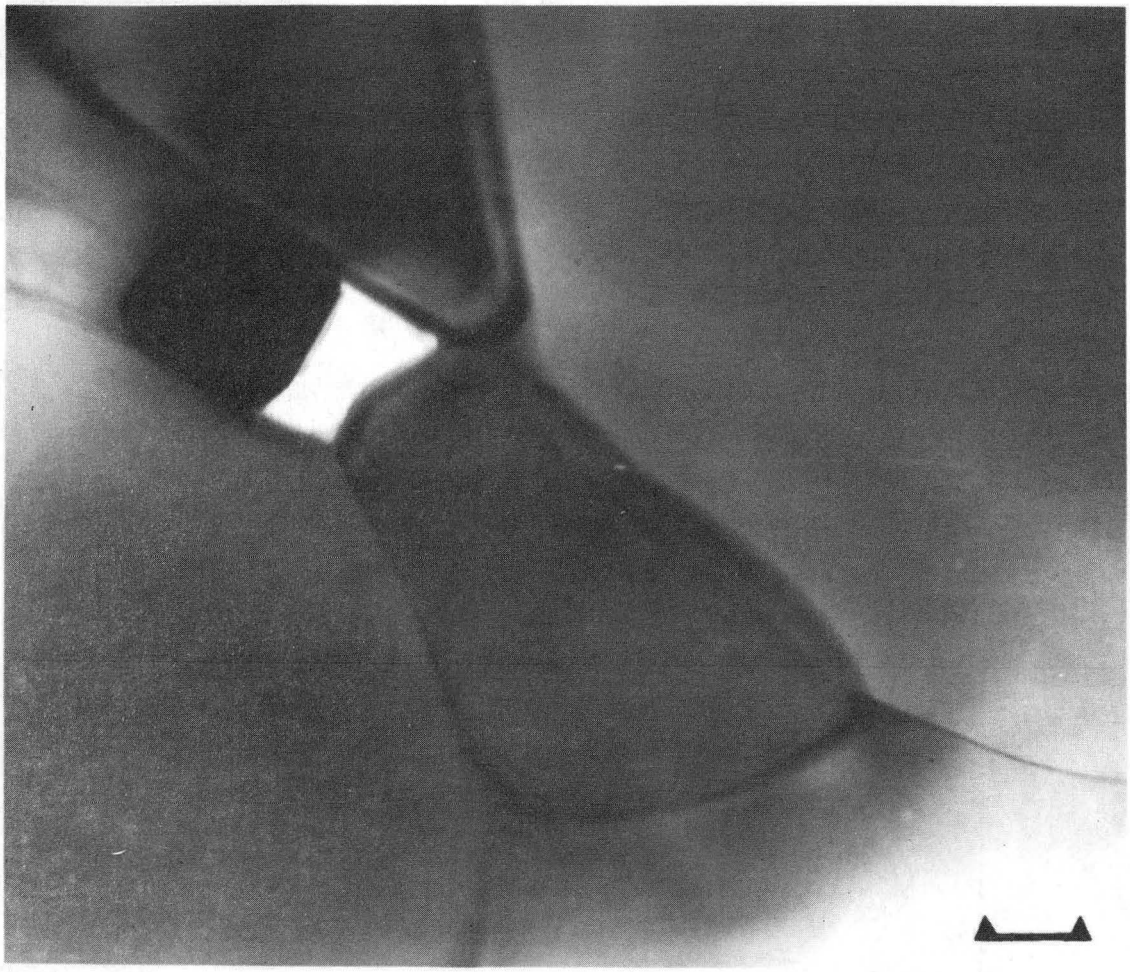

XBB 848-6439

Figure 4

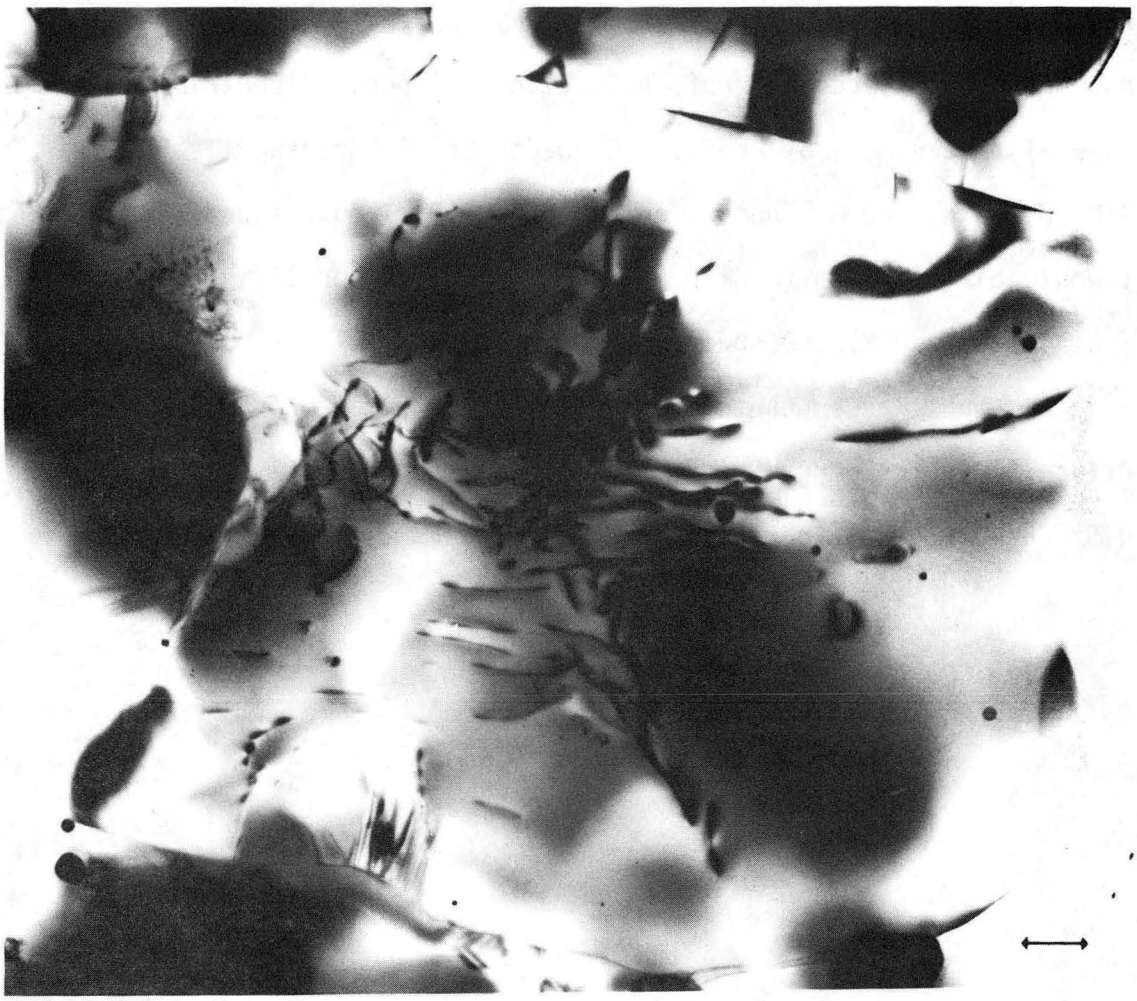

XBB 848-6441

Figure 5

ACKNOWLEDGMENT

This thesis would not have been possible without the support of a number of individuals. I particularly appreciate the continued support and patience of Prof. A.G. Evans. Important contributions have also been made by Profs. L.C. DeJonghe, R. Gronsky, I. Finnie, A.M. Despain, and G. Thomas, and by Drs. M.D. Thouless and D.R. Clarke. I would also like to thank D.D. Marion, J.E. Marion III, J.E. Marion I, E.G. Marion and M.C. Despain.

This work was supported by the Director, Office of Energy Research, Office of Basic Energy Sciences, Materials Sciences Division of the U.S. Department of Energy under Contract No. DE-AC03-76SF00098.

This report was done with support from the Department of Energy. Any conclusions or opinions expressed in this report represent solely those of the author(s) and not necessarily those of The Regents of the University of California, the Lawrence Berkeley Laboratory or the Department of Energy.

Reference to a company or product name does not imply approval or recommendation of the product by the University of California or the U.S. Department of Energy to the exclusion of others that may be suitable.

TECHNICAL INFORMATION DEPARTMENT
LAWRENCE BERKELEY LABORATORY
UNIVERSITY OF CALIFORNIA
BERKELEY, CALIFORNIA 94720